

1 2 9 0



UNIVERSIDADE D
COIMBRA

Filipe Augusto Coelho Ramos Rodrigues

**BUCKLING RESISTANCE OF HIGH
STRENGTH STEEL BEAMS**

**PhD Thesis in Steel and Composite Construction supervised by
Professor Luís Alberto Proença Simões da Silva and Professor
Trayana Stoykova Tankova, and submitted to the Department of
Civil Engineering, Faculty of Sciences and Technology of the
University of Coimbra.**

April 2023



FACULDADE DE
CIÊNCIAS E TECNOLOGIA
UNIVERSIDADE DE
COIMBRA

DEPARTAMENTO
DE ENGENHARIA
CIVIL



Institute for Sustainability and
Innovation in Structural Engineering

Filipe Augusto Coelho Ramos Rodrigues

Buckling resistance of high strength steel beams

PhD Thesis in Steel and Composite Construction supervised by Professor Luís Alberto Proença Simões da Silva and Professor Trayana Stoykova Tankova, and submitted to the Department of Civil Engineering, Faculty of Sciences and Technology of the University of Coimbra



UNIVERSIDADE DE
COIMBRA

Coimbra, April 2023

ABSTRACT

The use of high strength steel (HSS) has been successfully applied in several industries in the last few years and is becoming more common in structural engineering practice due to its improved qualities.

At present, in Europe, steel structures are designed according to Eurocode 3 Part 1-1 [1] (EN 1993-1-1), which gives structural guidance for columns, beams, and beam-columns for steel grades up to S460, while Eurocode 3 Part 1-12 [2] (EN 1993-1-12) provides additional rules for steel grades S500 to S700. The reason for these special rules is that there was insufficient test data on high strength steel structural members when these rules were made. Whereby, most of these rules lead to overly conservative results, or, in some situations, there are no design specifications for high strength steels, which is the case where the stability design falls. Currently, the buckling design rules presented in Eurocode 3 Part 1-1 [1] do not distinguish between conventional steel members and high strength steel members.

Nevertheless, recent studies on the buckling behaviour of welded H, I, and box columns in steel grades S460 to S960, even though limited, show that improved stability design rules can be used for high strength steel members. This enhanced behaviour is usually attributed to the improved material properties but is mainly due to the more favourable residual stress distribution.

In order to address the aforementioned shortcomings, the European Stability Design Rules (Eurocode 3 Part 1-1 [1] – EN 1993-1-1) for steel members, including columns, beams, and beam-columns, are evaluated in this thesis for high strength steel members through an extensive parametric study based on advanced numerical analyses validated against experimental tests.

The experimental programme includes twelve full-scale tests on the lateral-torsional buckling resistance of high strength steel beams, as well as measurements of residual stresses and geometrical imperfections and material characterization. The tested specimens cover different steel grades up to S690, welded and rolled sections, homogenous and hybrid (flanges in a higher steel grade than the web) sections, double and mono-symmetric sections, as well as variations in the cross-section class.

The advanced numerical models are calibrated against the experimental results, including the measured residual stress distributions and geometrical imperfections of the members, and assessed for various assumptions about the members' imperfections. A

simplified numerical model is further adopted to extend the scope of the buckling resistance of high strength steel members to columns, beams, and beam-columns with different cross-sections, normalized slenderness, steel grade, loading conditions, and residual stress distribution. These results are further compared with the Eurocode 3 design recommendations.

Finally, it was possible to justify more accurate design recommendations for the buckling resistance of high strength steel members.

Keywords:

High strength steel; Residual stresses; Lateral-torsional buckling; Eurocode 3.

RESUMO

Nos últimos anos os aços de alta resistência têm sido amplamente aplicados nos mais diversos tipos de indústrias. Apresentando propriedades superiores relativamente aos aços correntes, começa também a destacar-se a utilização de aços de alta resistência no dimensionamento de estruturas metálicas.

Atualmente, o dimensionamento de estruturas metálicas é realizado segundo o Eurocódigo 3 Parte 1-1 [1] (EN 1993-1-1), que fornece regras de dimensionamento para colunas, vigas e vigas-coluna para classes de aço até S460, enquanto o Eurocódigo 3 Parte 1-12 [2] (EN 1993-1-12) fornece regras adicionais para classes de aço S500 até S700. A necessidade de regras adicionais deve-se ao facto de não existirem dados experimentais suficientes realizados em aços de alta resistência aquando da criação destas regras. Como consequência, a maioria destas normas conduz a resultados excessivamente conservadores ou, em algumas situações, como o dimensionamento de estabilidade, não existem especificações para o dimensionamento utilizando aços de alta resistência. Em relação às regras de dimensionamento à encurvadura do Eurocódigo 3 Parte 1-1 [1], atualmente, não se verificam diferenças entre a utilização de elementos de aço de alta resistência ou aço de resistência normal (aços correntes). No entanto, estudos recentes sobre o comportamento à encurvadura de colunas em H, I e secções quadradas, ainda que limitados, mostram que as regras de dimensionamento de estabilidade para elementos constituídos por aços de alta resistência podem ser aperfeiçoadas, devido ao melhor comportamento à encurvadura evidenciado nos elementos de aço de alta resistência. Esta melhoria no comportamento à encurvadura é geralmente atribuída não só às melhores propriedades materiais dos aços de alta resistência, mas também devido a uma distribuição de tensões residuais mais favorável.

De modo a dar resposta às questões acima mencionadas, as regras europeias de dimensionamento de estabilidade (Eurocódigo 3 Parte 1-1 [1] – EN 1993-1-1) para elementos de aço, incluindo colunas, vigas e vigas-coluna, foram avaliadas nesta tese, aplicadas a elementos constituídos por aço de alta resistência. O trabalho incluiu um estudo paramétrico utilizando modelos numéricos avançados e validados com base em testes experimentais realizados. O programa experimental compreendeu 12 ensaios à escala real de resistência à encurvadura lateral de vigas constituídas por aços de alta resistência, incluindo medições de tensões residuais e imperfeições geométricas e caracterização do material. Os ensaios experimentais realizados abrangem diferentes classes de aço até S690, secções soldadas e

laminadas, secções homogéneas e híbridas (banzo com classe de aço superior em relação à alma), secções duplamente simétricas e mono simétricas, assim como variações na classe da secção transversal.

Os modelos numéricos avançados foram calibrados com base nos resultados experimentais, incluindo as distribuições de tensões residuais e imperfeições geométricas medidas, e posteriormente assumindo diferentes hipóteses para a consideração das imperfeições nos elementos. Um modelo numérico simplificado foi adotado para ampliar o âmbito do estudo da resistência à encurvadura de elementos constituídos por aços de alta resistência a colunas, vigas e vigas-coluna, utilizando diferentes secções transversais, níveis de esbelteza normalizada, classes de aço, carregamento e distribuição de tensões residuais. Os resultados foram posteriormente comparados com as recomendações de dimensionamento presentes no Eurocódigo 3.

Por fim, foi possível justificar recomendações de dimensionamento que se consideram mais adequadas para o cálculo da resistência à encurvadura de elementos metálicos constituídos por aços de alta resistência.

Palavras-chave:

Aço de alta resistência; Tensões residuais; Encurvadura lateral; Eurocódigo 3.

CONTENTS

| | |
|---|-------------|
| ABSTRACT | i |
| RESUMO..... | iii |
| LIST OF FIGURES..... | xi |
| LIST OF TABLES..... | xix |
| NOTATIONS | xxv |
| ABBREVIATIONS AND ACRONYMS | xxxi |
| 1. Introduction | 1 |
| 1.1. Motivation and scope | 1 |
| 1.2. Objectives and methodology..... | 2 |
| 1.3. Outline of the dissertation | 3 |
| 2. Stability design of steel members | 5 |
| 2.1. Introduction..... | 5 |
| 2.2. Member imperfections – residual stresses | 7 |
| 2.3. Stability of high strength steel members..... | 12 |
| 2.4. Buckling design of steel members according to Eurocode 3 | 16 |
| 2.4.1. Design of members in compression..... | 16 |
| 2.4.2. Design of members in bending..... | 18 |
| 2.4.2.1. General case..... | 19 |
| 2.4.2.2. Special case..... | 20 |
| 2.4.2.3. New EC3 method..... | 23 |
| 2.4.3. Design of members in bending and axial compression | 24 |
| 2.4.4. Design of semi-compact sections | 27 |
| 3. Experimental buckling behaviour of high strength steel beams..... | 29 |
| 3.1. Scope..... | 29 |

| | | |
|-----------|--|-----------|
| 3.2. | Tensile coupon tests on high strength steel..... | 30 |
| 3.3. | Residual stresses measurements on high strength steel beams..... | 31 |
| 3.4. | Geometrical imperfections measurements..... | 34 |
| 3.5. | Full-scale tests on lateral-torsional buckling..... | 35 |
| 3.6. | Experimental results..... | 41 |
| 3.6.1. | Tensile coupon tests..... | 41 |
| 3.6.2. | Residual stresses measurements..... | 43 |
| 3.6.3. | Geometrical imperfections measurements..... | 52 |
| 3.6.4. | Lateral-torsional buckling tests..... | 54 |
| 3.6.4.1. | Tests B1, B2 and B3..... | 55 |
| 3.6.4.2. | Tests B4, B5 and B6..... | 60 |
| 3.6.4.3. | Tests B7 and B8..... | 65 |
| 3.6.4.4. | Tests B11, B12, B13 and B14..... | 70 |
| 3.7. | Stability design of high strength steel members..... | 77 |
| 4. | Numerical studies..... | 81 |
| 4.1. | Numerical model..... | 81 |
| 4.1.1. | Geometry..... | 81 |
| 4.1.2. | Material properties..... | 82 |
| 4.1.3. | Boundary conditions..... | 83 |
| 4.1.4. | Loading..... | 85 |
| 4.1.5. | Imperfections – Residual stresses..... | 85 |
| 4.1.6. | Geometrical imperfections..... | 86 |
| 4.2. | Calibration to experimental results..... | 87 |
| 4.2.1. | Results for tests B1, B2, and B3..... | 87 |
| 4.2.2. | Results for tests B4, B5, and B6..... | 91 |
| 4.2.3. | Results for tests B7 and B8..... | 95 |
| 4.2.4. | Results for tests B11, B12, B13, and B14..... | 98 |
| 4.2.5. | Imperfection sensitivity..... | 103 |
| 4.3. | Simplified numerical model for parametric studies..... | 105 |
| 4.3.1. | Geometry..... | 105 |

| | |
|---|------------|
| 4.3.2. Material properties..... | 106 |
| 4.3.3. Boundary conditions..... | 107 |
| 4.3.4. Loading..... | 108 |
| 4.3.5. Geometrical imperfections | 108 |
| 4.3.6. Residual stresses pattern..... | 109 |
| 4.4. Parametric studies | 109 |
| 4.4.1. Columns..... | 110 |
| 4.4.2. Beams | 112 |
| 4.4.2.1. Hybrid beams | 113 |
| 4.4.3. Beam-Columns | 114 |
| 4.4.4. New residual stresses models | 116 |
| 4.4.4.1. Columns..... | 117 |
| 4.4.4.2. Beams | 117 |
| 4.5. Results..... | 118 |
| 4.5.1. Columns..... | 118 |
| 4.5.2. Beams | 121 |
| 4.5.2.1. Hybrid beams | 125 |
| 4.5.3. Beam-Columns | 130 |
| 4.5.4. New residual stresses models | 133 |
| 4.5.4.1. Columns..... | 133 |
| 4.5.4.2. Beams | 139 |
| 4.5.4.3. Discussion of results | 144 |
| 5. Development of stability design rules for high strength steel members | 149 |
| 5.1. Calibration of design guidance | 149 |
| 5.1.1. Design rules for members in compression | 149 |
| 5.1.2. Design rules for members in bending..... | 152 |
| 5.1.2.1. General case..... | 152 |
| 5.1.2.2. Special case..... | 154 |
| 5.1.2.3. New EC3 case..... | 155 |
| 5.2. Validation of the stability design rules for high strength steel members..... | 159 |
| 5.2.1. Columns..... | 159 |

| | |
|--|------------|
| 5.2.2. Beams | 162 |
| 5.2.2.1. Hybrid beams | 164 |
| 5.2.3. Beam-Columns | 166 |
| 5.2.4. New residual stresses models | 169 |
| 5.2.4.1. Columns | 169 |
| 5.2.4.2. Beams | 171 |
| 5.3. Recommendations | 173 |
| 5.3.1. Members in compression | 174 |
| 5.3.2. Members in bending | 174 |
| 5.3.2.1. General case | 175 |
| 5.3.2.2. New EC3 case | 175 |
| 5.3.3. Members in bending and axial compression | 176 |
| 6. Conclusions and further research | 177 |
| 6.1. Conclusions | 177 |
| 6.2. Future research | 180 |
| 6.3. Publications | 180 |
| REFERENCES | 183 |
| Annex A – Geometrical imperfections | A.1 |
| Annex B – Members in bending (beams) | B.1 |
| B.1 Constant bending moment – $\psi = 1$ | B.1 |
| B.2 Linear bending moment – $\psi = 0$ | B.5 |
| B.3 Linear bending moment – $\psi = -1$ | B.9 |
| B.4 Uniform distributed load – applied in the middle of the web | B.13 |
| B.5 Uniform distributed load – applied on the top flange and bottom flange | B.17 |
| B.6 Concentrated load at $L/2$ – applied in the middle of the web | B.21 |
| Annex C – Members in bending and axial compression (beam-columns) | C.1 |
| C.1 Constant bending moment – $\psi = 1$ | C.1 |
| C.2 Linear bending moment – $\psi = 0$ | C.4 |
| C.3 Linear bending moment – $\psi = -1$ | C.7 |
| C.4 Uniform distributed load | C.10 |

| | |
|---|------------|
| Annex D – New Residual stress models | D.1 |
| D.1 Constant bending moment – $\psi = 1$ | D.1 |
| D.2 Linear bending moment – $\psi = 0$ | D.3 |
| D.3 Linear bending moment – $\psi = -1$ | D.5 |

LIST OF FIGURES

Chapter 2:

| | |
|--|----|
| Figure 2.1 – European buckling curve representation as a function of slenderness..... | 6 |
| Figure 2.2 – Residual stresses patterns proposed by ECCS [24] | 8 |
| Figure 2.3 – Proposals for residual stress distributions for high strength steel members | 9 |
| Figure 2.4 – Residual stress distribution proposed by L. Schaper et al. [40] | 12 |
| Figure 2.5 – Representation of the elasto-plastic modulus W_{ep} | 28 |

Chapter 3:

| | |
|--|----|
| Figure 3.1 – Lateral-torsional buckling specimens after testing | 29 |
| Figure 3.2 – Coupons for 8mm thickness plate | 31 |
| Figure 3.3 – Coupons for 16mm thickness plate | 31 |
| Figure 3.4 – Residual stresses specimens after testing | 32 |
| Figure 3.5 – Residual stresses specimens | 32 |
| Figure 3.6 – Strain gauges instrumentation | 33 |
| Figure 3.7 – Geometrical imperfections measurements | 34 |
| Figure 3.8 – Representative scheme of the experimental layout | 35 |
| Figure 3.9 – Lateral-torsional buckling tests – experimental layout | 35 |
| Figure 3.10 – Experimental layout and instrumentation – tests B1, B2 and B3 | 37 |
| Figure 3.11 - Experimental layout and instrumentation – tests B4, B5 and B6 | 37 |
| Figure 3.12 – Experimental layout and instrumentation – tests B7 and B8 | 38 |
| Figure 3.13 – Experimental layout and instrumentation – tests B11, B12, B13 and B14..... | 38 |
| Figure 3.14 – Experimental layout - load application | 39 |
| Figure 3.15 – Measurement of strains | 40 |
| Figure 3.16 – Experimental layout – supports..... | 40 |
| Figure 3.17 – Experimental layout – lateral restraints | 40 |
| Figure 3.18 – Tensile coupon tests results – Plates 1, 2 and 3 | 42 |
| Figure 3.19 – Tensile coupon tests results – Plates 4, 5, 6 and 7 | 42 |
| Figure 3.20 – Tensile coupon tests results – Hot-rolled profiles..... | 42 |
| Figure 3.21 – Residual stresses distributions for welded sections B1 and B2 | 43 |
| Figure 3.22 – Residual stresses distributions for welded sections B4 and B5 | 44 |
| Figure 3.23 – Residual stresses distributions for welded sections B7 and B8 | 45 |
| Figure 3.24 – Residual stresses distributions for welded section B11 | 46 |

| | |
|--|----|
| Figure 3.25 – Residual stresses distributions for hot-rolled sections B3 and B6 | 47 |
| Figure 3.26 – Normalized residual stress distribution for welded sections | 49 |
| Figure 3.27 – Normalized residual stress distribution for rolled sections | 50 |
| Figure 3.28 – Residual stresses distribution histograms for welded sections | 51 |
| Figure 3.29 – Estimation of the geometrical imperfections | 52 |
| Figure 3.30 – Average geometrical imperfections | 54 |
| Figure 3.31 – Load displacement curves for tests B1, B2 and B3 | 56 |
| Figure 3.32 – Deformed shape – Tests B1, B2 and B3 | 56 |
| Figure 3.33 – Vertical displacements along the beams for tests B1, B2 and B3..... | 57 |
| Figure 3.34 – Horizontal displacements along the beams for tests B1, B2 and B3 | 57 |
| Figure 3.35 – Strain curves at section D (mid-span) for tests B1, B2 and B3..... | 58 |
| Figure 3.36 – Strain curves at sections H and I for tests B1, B2 and B3 | 59 |
| Figure 3.37 – Cross section deformation at maximum load and at the end of the tests | 59 |
| Figure 3.38 – Load displacement curves for tests B4, B5 and B6 | 61 |
| Figure 3.39 - Deformed shape – Tests B4, B5 and B6..... | 61 |
| Figure 3.40 – Vertical displacements along the beams for tests B4, B5 and B6..... | 62 |
| Figure 3.41 – Horizontal displacements along the beams for tests B4, B5 and B6 | 62 |
| Figure 3.42 – Strain curves at section D (mid-span) for tests B4, B5 and B6..... | 63 |
| Figure 3.43 – Strain curves at sections H and I for tests B4, B5 and B6 | 64 |
| Figure 3.44 – Cross section deformation at maximum load and at the end of the tests | 64 |
| Figure 3.45 – Load displacement curves for tests B7 and B8 | 66 |
| Figure 3.46 – Deformed shape – Tests B7 and B8..... | 66 |
| Figure 3.47 – Vertical displacements along the beams for tests B7 and B8 | 67 |
| Figure 3.48 – Horizontal displacements along the beams for tests B7 and B8 | 67 |
| Figure 3.49 – Strain curves at section D (mid-span) for tests B7 and B8 | 68 |
| Figure 3.50 – Strain curves at sections H and I for tests B7 and B8 | 69 |
| Figure 3.51 – Cross section deformation at maximum load and at the end of the tests | 69 |
| Figure 3.52 – Load displacement curves for tests B11, B12, B13 and B14..... | 71 |
| Figure 3.53 – Deformed shape – Tests B11, B12, B13 and B14 | 71 |
| Figure 3.54 – Vertical displacements along the beams for tests B11, B12, B13 and B14..... | 72 |
| Figure 3.55 – Horizontal displacements along the beams for tests B11, B12, B13 and B14... | 72 |
| Figure 3.56 – Strain curves at section D (mid-span) for tests B11, B12, B13 and B14..... | 73 |
| Figure 3.57 – Strain curves at sections H and I for tests B11, B12, B13 and B14..... | 74 |
| Figure 3.58 – Out-of-plane displacement evolution for test B11 | 75 |
| Figure 3.59 – Out-of-plane displacement evolution for test B12 | 75 |
| Figure 3.60 – Out-of-plane displacement evolution for test B13 | 76 |
| Figure 3.61 – Out-of-plane displacement evolution for test B14..... | 76 |
| Figure 3.62 – Comparison between experimental and Eurocode 3 buckling moment resistance | 77 |

| | |
|---|----|
| Figure 3.63 – Comparison between experimental values and current design specifications from Eurocode 3 – $h/b \leq 2$ | 79 |
| Figure 3.64 – Comparison between experimental values and current design specifications from Eurocode 3 – $h/b > 2$ | 80 |
| Chapter 4: | |
| Figure 4.1 – Model geometry | 82 |
| Figure 4.2 – Material properties | 83 |
| Figure 4.3 – Boundary conditions | 83 |
| Figure 4.4 – Lateral displacement prevented at load application point – models B1 to B6..... | 84 |
| Figure 4.5 – Lateral displacement prevented at load application point – models B7, B8 and B11 to B14..... | 84 |
| Figure 4.6 – Load application..... | 85 |
| Figure 4.7 – Residual stress input for numerical model..... | 86 |
| Figure 4.8 – Numerical model with geometrical imperfections..... | 87 |
| Figure 4.9 – Vertical displacements at load application point – experimental and numerical | 88 |
| Figure 4.10 – Vertical displacements at maximum load – experimental and numerical..... | 89 |
| Figure 4.11 – Horizontal displacements at maximum load – experimental and numerical | 89 |
| Figure 4.12 – Cross-section deformation at mid-span at maximum load and after maximum load – numerical model | 90 |
| Figure 4.13 – Example of the failure mode for test B2 | 91 |
| Figure 4.14 -Strains (top flange) at maximum load..... | 91 |
| Figure 4.15 – Vertical displacements at load application point – experimental and numerical | 92 |
| Figure 4.16 – Vertical displacements at maximum load – experimental and numerical..... | 93 |
| Figure 4.17 – Horizontal displacements at maximum load – experimental and numerical | 93 |
| Figure 4.18 – Cross-section deformation at mid-span at maximum load and after maximum load – numerical model | 94 |
| Figure 4.19 – Example of the failure mode for test B5 | 94 |
| Figure 4.20 – Strains (top flange) at maximum load..... | 95 |
| Figure 4.21 – Vertical displacements at load application point – experimental and numerical | 95 |
| Figure 4.22 – Vertical displacements at maximum load – experimental and numerical..... | 96 |
| Figure 4.23 – Horizontal displacements at maximum load – experimental and numerical | 96 |
| Figure 4.24 – Cross-section deformation at mid-span at maximum load and after maximum load – numerical model | 97 |
| Figure 4.25 – Example of the failure mode for test B8 | 98 |
| Figure 4.26 – Strains (top flange) at maximum load..... | 98 |

| | |
|--|-----|
| Figure 4.27 – Vertical displacements at load application point – experimental and numerical | 99 |
| Figure 4.28 – Vertical displacements at maximum load – experimental and numerical..... | 100 |
| Figure 4.29 – Horizontal displacements at maximum load – experimental and numerical ... | 100 |
| Figure 4.30 – Cross-section deformation at mid-span at maximum load and after maximum load – numerical model | 101 |
| Figure 4.31 – Example of the buckling modes observed | 102 |
| Figure 4.32 – Strains (top flange) at maximum load..... | 102 |
| Figure 4.33 – Modelling assumptions | 103 |
| Figure 4.34 – Cross-section geometry and mesh..... | 105 |
| Figure 4.35 – Elastic-plastic law without strain hardening | 106 |
| Figure 4.36 – Variation of the yield stress with nominal thickness | 106 |
| Figure 4.37 – Boundary conditions for the simplified numerical model | 107 |
| Figure 4.38 – Location of the intermediate lateral restraints in the cross-section..... | 107 |
| Figure 4.39 – Load applications in the simplified numerical model..... | 108 |
| Figure 4.40 – Critical buckling mode shape for flexural buckling..... | 108 |
| Figure 4.41 – Critical buckling mode shape for lateral-torsional buckling..... | 109 |
| Figure 4.42 – Residual stresses distributions for welded I sections | 109 |
| Figure 4.43 – Residual stresses patterns applied to a welded I-section..... | 116 |
| Figure 4.44 – Buckling curves for flexural buckling..... | 119 |
| Figure 4.45 – Scatter plots for flexural buckling..... | 119 |
| Figure 4.46 – Mean values of the safety factor using Eurocode 3 approach for flexural buckling | 121 |
| Figure 4.47 – Scatter plots for lateral-torsional buckling (all loading cases) – General case | 122 |
| Figure 4.48 – Scatter plots for lateral-torsional buckling (all loading cases) – Special case .. | 122 |
| Figure 4.49 – Scatter plots for lateral-torsional buckling (all loading cases) – New EC3 case | 123 |
| Figure 4.50 – Mean values of the safety factor for lateral-torsional buckling for all methods considered..... | 124 |
| Figure 4.51 - Scatter plots for lateral-torsional buckling of hybrid beams – General case and New EC3 case..... | 125 |
| Figure 4.52 – Scatter plots for special case for LTB of hybrid beams and mean values | 126 |
| Figure 4.53 – Assessment of the resistance for hybrid beams | 128 |
| Figure 4.54 – Mean values for the ratio $M_{b,Rd,Hybrid}/M_{b,Rd,Homogeneous}$ | 129 |
| Figure 4.55 – Interaction N+M – representation of the results for beam-columns | 130 |
| Figure 4.56 – Scatter plots for beam-columns without restraints (all loading cases)..... | 131 |
| Figure 4.57 – Scatter plots for beam-columns with minor axis restrained (all loading cases) | 131 |

| | |
|--|-----|
| Figure 4.58 – Mean values of the safety factor for combined bending and axial compression | 133 |
| Figure 4.59 – Buckling curves for flexural buckling with new residual stresses models | 134 |
| Figure 4.60 – Scatter plots for flexural buckling with new residual stresses models | 134 |
| Figure 4.61 – Mean values for flexural buckling with new residual stresses models | 136 |
| Figure 4.62 – Direct comparison between the reduction factors for flexural buckling with new residual stresses models | 137 |
| Figure 4.63 – Mean values for the ratio between the reduction factors for flexural buckling | 138 |
| Figure 4.64 – Scatter plots for lateral-torsional buckling with new residual stresses models (all cases) – General case | 139 |
| Figure 4.65 – Scatter plots for lateral-torsional buckling with new residual stresses models (all cases) – New EC3 case | 140 |
| Figure 4.66 – Scatter plots for lateral-torsional buckling with new residual stresses models (all cases) – Special case | 140 |
| Figure 4.67 – Mean values for lateral-torsional buckling with new residual stresses models | 142 |
| Figure 4.68 - Direct comparison between the reduction factors for lateral-torsional buckling with new residual stresses models | 143 |
| Figure 4.69 – Mean values for the ratio between the reductions factors for lateral-torsional buckling | 144 |
| Figure 4.70 – Flexural buckling | 146 |
| Figure 4.71 – Lateral-torsional buckling | 146 |
| Chapter 5: | |
| Figure 5.1 – Generalized imperfections for flexural buckling about major axis (y-y) | 151 |
| Figure 5.2 – Generalized imperfections for flexural buckling about minor axis (z-z) | 151 |
| Figure 5.3 – Generalized imperfections for lateral-torsional buckling – General case | 153 |
| Figure 5.4 – Generalized imperfections for lateral-torsional buckling – Special case | 155 |
| Figure 5.5 – Estimation for the imperfection factor α_{LT} – New EC3 case | 157 |
| Figure 5.6 – Estimation for the imperfection α_0 – New EC3 case | 158 |
| Figure 5.7 – Scatter plots for proposal for flexural buckling | 160 |
| Figure 5.8 – Comparison of the mean values between Eurocode 3 and proposal for flexural buckling | 161 |
| Figure 5.9 – Scatter plots for proposals for lateral-torsional buckling | 162 |
| Figure 5.10 – Comparison of the mean values between the current design and proposals | 163 |
| Figure 5.11 – Scatter plots for proposals for lateral-torsional buckling of hybrid beams | 164 |
| Figure 5.12 – Comparison of the mean values between the current design and proposals applied to hybrid beams | 165 |

| | |
|--|-----|
| Figure 5.13 – Scatter plots for proposals for beam-columns without restraints..... | 166 |
| Figure 5.14 – Mean values of the safety factor for combined bending and axial compression without restraints | 167 |
| Figure 5.15 – Scatter plots and mean values for proposal for beam-columns with minor axis restrained..... | 168 |
| Figure 5.16 – Scatter plots with new residual stresses models and proposals for flexural buckling | 170 |
| Figure 5.17 – Mean values with new residual stresses models and proposals for flexural buckling (major and minor axes)..... | 171 |
| Figure 5.18 – Scatter plots for lateral-torsional buckling with new residual stresses models and proposals (all cases) – General case and New EC3 case | 172 |
| Figure 5.19 – Mean values with new residual stresses models and proposals for lateral-torsional buckling | 173 |

Annex A:

| | |
|---|-----|
| Figure A.1 – Geometrical imperfections for specimen B1..... | A.1 |
| Figure A.2 – Geometrical imperfections for specimen B2..... | A.1 |
| Figure A.3 – Geometrical imperfections for specimen B3..... | A.1 |
| Figure A.4 – Geometrical imperfections for specimen B4..... | A.2 |
| Figure A.5 – Geometrical imperfections for specimen B5..... | A.2 |
| Figure A.6 – Geometrical imperfections for specimen B6..... | A.2 |
| Figure A.7 – Geometrical imperfections for specimen B7..... | A.3 |
| Figure A.8 – Geometrical imperfections for specimen B8..... | A.3 |
| Figure A.9 – Geometrical imperfections for specimen B11..... | A.3 |
| Figure A.10 – Geometrical imperfections for specimen B12..... | A.4 |
| Figure A.11 – Geometrical imperfections for specimen B13..... | A.4 |
| Figure A.12 – Geometrical imperfections for specimen B14..... | A.4 |

Annex B:

| | |
|--|-----|
| Figure B.1 – Mean values for ratio r_e/r_t for constant bending moment $\psi = 1$ – Class 1 or 2 | B.2 |
| Figure B.2 – Mean values for the ratio r_e/r_t for constant bending moment $\psi = 1$ – Class 3 .. | B.3 |
| Figure B.3 – Scatter plots for LTB with constant bending moment $\psi = 1$ – General case.. | B.3 |
| Figure B.4 – Scatter plots for LTB with constant bending moment $\psi = 1$ – Special case... | B.4 |
| Figure B.5 – Scatter plots for LTB with constant bending moment $\psi = 1$ – New EC3 case | B.4 |
| Figure B.6 – Mean values for the ratio r_e/r_t for linear bending moment $\psi = 0$ – Class 1 or 2 | B.6 |
| Figure B.7 – Mean values for the ratio r_e/r_t for linear bending moment $\psi = 0$ – Class 3 | B.7 |

| | |
|--|------|
| Figure B.8 – Scatter plots for LTB with linear bending moment $\psi = 0$ – General case..... | B.7 |
| Figure B.9 – Scatter plots for LTB with linear bending moment $\psi = 0$ – Special case..... | B.8 |
| Figure B.10 – Scatter plots for LTB with linear bending moment $\psi = 0$ – New EC3 case.. | B.8 |
| Figure B.11 – Mean values for ratio r_e/r_t for linear bending moment $\psi = -1$ – Class 1 or 2 | B.10 |
| Figure B.12 – Mean values for ratio r_e/r_t for linear bending moment $\psi = -1$ – Class 3 | B.11 |
| Figure B.13 – Scatter plots for LTB with linear bending moment $\psi = -1$ – General case | B.11 |
| Figure B.14 – Scatter plots for LTB with linear bending moment $\psi = -1$ – Special case | B.12 |
| Figure B.15 – Scatter plots for LTB with linear bending moment $\psi = -1$ – New EC3 case | B.12 |
| Figure B.16 – Mean values for ratio r_e/r_t for uniform distributed load (center) – Class 1 or 2 | B.14 |
| Figure B.17 – Mean values for ratio r_e/r_t for uniform distributed load (center) – Class 3 ... | B.15 |
| Figure B.18 – Scatter plots for LTB with uniform distributed load (center) – General case | B.15 |
| Figure B.19 – Scatter plots for LTB with uniform distributed load (center) – Special case | B.16 |
| Figure B.20 – Scatter plots for LTB with uniform distributed load (center) – New EC3 case | B.16 |
| Figure B.21 – Mean values for ratio r_e/r_t for uniform distributed load (top) – Class 1 or 2. | B.18 |
| Figure B.22 – Mean values for ratio r_e/r_t for uniform distributed load (bottom) – Class 1 or 2 | B.19 |
| Figure B.23 – Scatter plots for LTB with uniform distributed load (load applied at top and bottom flange) – General case | B.19 |
| Figure B.24 – Scatter plots for LTB with uniform distributed load (load applied at top and bottom flange) – Special case | B.20 |
| Figure B.25 – Scatter plots for LTB with uniform distributed load (load applied at top and bottom flange) – New EC3 case | B.20 |
| Figure B.26 – Mean values for ratio r_e/r_t for concentrated load (center) – Class 1 or 2..... | B.22 |
| Figure B.27 – Mean values for ratio r_e/r_t for concentrated load (center) – Class 3..... | B.23 |
| Figure B.28 – Scatter plots for LTB with concentrated load (center) – General case..... | B.23 |
| Figure B.29 – Scatter plots for LTB with concentrated load (center) – Special case | B.24 |
| Figure B.30 – Scatter plots for LTB with concentrated load (center) – New EC3 case..... | B.24 |

Annex C:

| | |
|---|-----|
| Figure C.1 – Mean values for ratio r_e/r_t for constant bending moment $\psi = 1$ | C.2 |
| Figure C.2 - Scatter plots – beam-columns: constant bending moment – $\psi = 1$ | C.2 |
| Figure C.3 – Scatter plots and mean values: constant bending moment – $\psi = 1$ | C.3 |
| Figure C.4 – Mean values for ratio r_e/r_t for linear bending moment $\psi = 0$ | C.5 |
| Figure C.5 - Scatter plots – beam-columns: linear bending moment – $\psi = 0$ | C.5 |
| Figure C.6 – Scatter plots and mean values: linear bending moment – $\psi = 0$ | C.6 |

Figure C.7 – Mean values for ratio r_e/r_t for linear bending moment $\psi = -1$ C.8
 Figure C.8 - Scatter plots – beam-columns: linear bending moment – $\psi = -1$ C.8
 Figure C.9 – Scatter plots and mean values: linear bending moment – $\psi = -1$ C.9
 Figure C.10 – Mean values for ratio r_e/r_t for uniform distributed load C.11
 Figure C.11 - Scatter plots – beam-columns: uniform distributed load C.11

Annex D:

Figure D.1 – Mean values for ratio r_e/r_t for constant bending moment $\psi = 1$ D.2
 Figure D.2 – Scatter plots for LTB with constant bending moment $\psi = 1$ – General case .D.2
 Figure D.3 – Scatter plots for LTB with constant bending moment $\psi = 1$ – New EC3 case
 D.3
 Figure D.4 – Mean values for ratio r_e/r_t for linear bending moment $\psi = 0$ D.4
 Figure D.5 – Scatter plots for LTB with linear bending moment $\psi = 0$ – General case D.4
 Figure D.6 – Scatter plots for LTB with linear bending moment $\psi = 0$ – New EC3 case... D.5
 Figure D.7 – Mean values for ratio r_e/r_t for linear bending moment $\psi = -1$ D.6
 Figure D.8 – Scatter plots for LTB with linear bending moment $\psi = -1$ – General case... D.6
 Figure D.9 – Scatter plots for LTB with linear bending moment $\psi = -1$ – New EC3 case
 D.7

LIST OF TABLES

Chapter 2:

| | |
|--|----|
| Table 2.1 – Residual stress measurements on welded sections in steel grades up to S460..... | 10 |
| Table 2.2 - Residual stress measurements on welded sections in steel grades higher than S460..... | 11 |
| Table 2.3 – Experimental tests on lateral-torsional buckling of high strength steel members | 15 |
| Table 2.4 – Imperfection factors for buckling curves (EN1993-1-1 – Table 6.2)..... | 17 |
| Table 2.5 – Selection of buckling curve for a cross-section (EN1993-1-1 – Table 6.2)..... | 18 |
| Table 2.6 – Recommended values for lateral-torsional buckling curves for cross-sections using the general case (EN1993-1-1 – Table 6.4) | 20 |
| Table 2.7 – Recommended values for imperfection factors for lateral-torsional buckling curves (EN1993-1-1 – Table 6.3)..... | 20 |
| Table 2.8 – Recommendation for the selection of lateral buckling curve for cross sections using special case (EN1993-1-1 – Table 6.5)..... | 21 |
| Table 2.9 – Correction factors k_c and f_M | 22 |
| Table 2.10 – Imperfection factor α_{LT} for lateral-torsional buckling of doubly symmetric I- and H-sections using the new EC3 method | 24 |
| Table 2.11 – Interaction factors k_{ij} for members not susceptible to lateral deformations (EN1993-1-1 – Table B.1)..... | 25 |
| Table 2.12 – Interaction factors k_{ij} for members susceptible to torsional deformations (EN1993-1-1 – Table B.2)..... | 26 |
| Table 2.13 – Equivalent uniform moment factors C_m (EN1993-1-1 – Table B.3)..... | 27 |

Chapter 3:

| | |
|--|----|
| Table 3.1 – Experimental programme | 30 |
| Table 3.2 – Residual stresses measurements – experimental programme..... | 34 |
| Table 3.3 – Tensile coupon tests: material properties | 41 |
| Table 3.4 – Statistical parameters for residual stresses measurements on welded sections | 48 |
| Table 3.5 - Measured dimensions of the tested specimens..... | 53 |
| Table 3.6 – Summary of the maximum loads and displacements obtained for experimental tests B1, B2 and B3 | 56 |

| | |
|---|----|
| Table 3.7 – Summary of the maximum loads and displacements obtained for experimental tests B4, B5 and B6 | 61 |
| Table 3.8 – Summary of the maximum loads and displacements obtained for experimental tests B7 and B8 | 66 |
| Table 3.9 – Summary of the maximum loads and displacements obtained for experimental tests B11, B12, B13 and B14..... | 70 |
| Table 3.10 – Comparison of critical moments and moment resistance..... | 79 |

Chapter 4:

| | |
|---|-----|
| Table 4.1 – Maximum applied load..... | 88 |
| Table 4.2 – Horizontal and vertical displacements at mid span – experimental and numerical | 90 |
| Table 4.3 – Maximum applied load..... | 92 |
| Table 4.4 – Vertical and horizontal displacements at mid span – experimental and numerical | 94 |
| Table 4.5 – Maximum applied load..... | 95 |
| Table 4.6 – Vertical and horizontal displacements at mid span – experimental and numerical | 97 |
| Table 4.7 – Maximum applied load..... | 99 |
| Table 4.8 – Vertical and horizontal displacements at mid span – experimental and numerical | 99 |
| Table 4.9 – Maximum applied load (kN) for different imperfections assumptions | 104 |
| Table 4.10 – Parametric study for columns | 110 |
| Table 4.11 – Sections for the columns parametric study..... | 111 |
| Table 4.12 – Parametric study for beams | 112 |
| Table 4.13 – Sections for the parametric study for beams | 113 |
| Table 4.14 – Parametric study for hybrid beams..... | 114 |
| Table 4.15 – Parametric study for beam-columns..... | 115 |
| Table 4.16 – Sections for the parametric study for beam-columns..... | 115 |
| Table 4.17 – Parametric study for columns with new residual stresses models..... | 117 |
| Table 4.18 – Parametric study for beams with new residual stresses models..... | 118 |
| Table 4.19 – Statistical parameters – flexural buckling | 120 |
| Table 4.20 – Statistical parameters for lateral-torsional buckling – General case | 123 |
| Table 4.21 – Statistical parameters for lateral-torsional buckling – Special case | 124 |
| Table 4.22 – Statistical parameters for lateral-torsional buckling – New EC3 case | 124 |
| Table 4.23 – Statistical parameters for lateral-torsional buckling of hybrid beams – General case | 126 |
| Table 4.24 – Statistical parameters for lateral-torsional buckling of hybrid beams – Special case | 127 |

| | |
|--|-----|
| Table 4.25 – Statistical parameters for lateral-torsional buckling of hybrid beams – New EC3 case | 127 |
| Table 4.26 – Statistical parameters for the ratio $M_{b,Rd,Hybrid}/M_{b,Rd,Homogeneous}$ | 129 |
| Table 4.27 – Statistical parameters for bending combined with axial compression without restrains..... | 132 |
| Table 4.28 – Statistical parameters for bending combined with axial compression with minor axis (z-z) restrained..... | 132 |
| Table 4.29 - Statistical parameters for flexural buckling with new residual stresses models | 135 |
| Table 4.30 – Statistical parameters for the ratio between the reduction factors (flexural buckling – major axis)..... | 137 |
| Table 4.31 – Statistical parameters for the ratio between the reduction factors (flexural buckling – minor axis)..... | 138 |
| Table 4.32 – Statistical parameters for new residual stresses models (lateral-torsional buckling – general case)..... | 141 |
| Table 4.33 – Statistical parameters for new residual stresses models (lateral-torsional buckling – new EC3 case) | 141 |
| Table 4.34 – Statistical parameters for new residual stresses models (lateral-torsional buckling – special case)..... | 141 |
| Table 4.35 – Statistical parameters for the ratio between the reduction factors (lateral-torsional buckling)..... | 144 |
| Table 4.36 – Additional numerical studies..... | 145 |
| Table 4.37 – Comparison of the reduction factors for flexural buckling | 147 |
| Table 4.38 – Comparison of the reduction factors for lateral-torsional buckling | 147 |

Chapter 5:

| | |
|---|-----|
| Table 5.1 – Proposed imperfections for flexural buckling applied to high strength steels | 152 |
| Table 5.2 – Proposed imperfections for the general case applied to high strength steels – lateral-torsional buckling..... | 154 |
| Table 5.3 – Proposed imperfections for the new EC3 case applied to high strength steels – lateral-torsional buckling..... | 159 |
| Table 5.4 – Statistical parameters for proposal for flexural buckling | 161 |
| Table 5.5 – Statistical parameters for proposal for general case – lateral-torsional buckling | 163 |
| Table 5.6 – Statistical parameters for proposal for new EC3 case – lateral-torsional buckling | 163 |
| Table 5.7 – Statistical parameters for lateral-torsional buckling of hybrid beams – Proposal for general case..... | 165 |

| | |
|--|-----|
| Table 5.8 – Statistical parameters for lateral-torsional buckling of hybrid beams – Proposal for new EC3 case | 165 |
| Table 5.9 – Statistical parameters for proposals for bending combined with axial compression without restrains | 167 |
| Table 5.10 – Statistical parameters for proposal for bending combined with axial compression with minor axis restrained | 169 |
| Table 5.11 - Statistical parameters for proposal for flexural buckling with new residual stresses models | 170 |
| Table 5.12 – Statistical parameters for new residual stresses models and proposal for general case (lateral-torsional buckling)..... | 172 |
| Table 5.13 – Statistical parameters for new residual stresses models and proposal for new EC3 case (lateral-torsional buckling) | 173 |
| Table 5.14 – Selection of a buckling curve for a cross-section for flexural buckling..... | 174 |
| Table 5.15 – Recommend values for lateral-torsional buckling curves for cross-sections using the general case | 175 |
| Table 5.16 – Imperfection factor α_{LT} for lateral-torsional buckling of doubly symmetric I- and H-sections using the new EC3 method | 176 |

Annex B:

| | |
|---|------|
| Table B.1 – Statistical parameters: constant bending moment $\psi = 1$ – Class 1 or 2 | B.1 |
| Table B.2 – Statistical parameters: constant bending moment $\psi = 1$ – Class 3..... | B.2 |
| Table B.3 – Statistical parameters: linear bending moment $\psi = 0$ – Class 1 or 2..... | B.5 |
| Table B.4 – Statistical parameters: linear bending moment $\psi = 0$ – Class 3..... | B.6 |
| Table B.5 – Statistical parameters: linear bending moment $\psi = -1$ – Class 1 or 2..... | B.9 |
| Table B.6 – Statistical parameters: linear bending moment $\psi = -1$ – Class 3..... | B.10 |
| Table B.7 – Statistical parameters: uniform distributed load (center) – Class 1 or 2..... | B.13 |
| Table B.8 – Statistical parameters: uniform distributed load (center) – Class 3..... | B.14 |
| Table B.9 – Statistical parameters: uniform distributed load (top) – Class 1 or 2 | B.17 |
| Table B.10 – Statistical parameters: uniform distributed load (bottom) – Class 1 or 2 | B.18 |
| Table B.11 – Statistical parameters: concentrated load (center) – Class 1 or 2 | B.21 |
| Table B.12 – Statistical parameters: concentrated load (center) – Class 3..... | B.22 |

Annex C:

| | |
|---|-----|
| Table C.1 – Statistical parameters – beam-columns: constant bending moment $\psi = 1$ – no restraints | C.1 |
| Table C.2 – Statistical parameters – beam-columns: constant bending moment $\psi = 1$ – minor axis restrained | C.3 |
| Table C.3 – Statistical parameters – beam-columns: linear bending moment $\psi = 0$ – no restraints | C.4 |

| | |
|--|------|
| Table C.4 – Statistical parameters – beam-columns: linear bending moment $\psi = 0$ – minor axis restrained | C.6 |
| Table C.5 – Statistical parameters – beam-columns: linear bending moment $\psi = -1$ – no restraints | C.7 |
| Table C.6 – Statistical parameters – beam-columns: linear bending moment $\psi = -1$ – minor axis restrained | C.9 |
| Table C.7 – Statistical parameters – beam-columns: uniform distributed load – no restraints | C.10 |

Annex D:

| | |
|--|-----|
| Table D.1 – Statistical parameters: constant bending moment $\psi = 1$ – Class 1, 2 and 3..... | D.1 |
| Table D.2 – Statistical parameters: linear bending moment $\psi = 0$ – Class 1, 2 and 3..... | D.3 |
| Table D.3 – Statistical parameters: linear bending moment $\psi = -1$ – Class 1, 2 and 3..... | D.5 |

NOTATIONS

Latin Upper-case Symbols

| | |
|---------------------------|--|
| A | Cross-sectional area |
| A_c | Area in compression |
| A_{eff} | Effective area of a cross-section |
| A_t | Area in tension |
| C_{my}, C_{mz}, C_{mLT} | Equivalent uniform moment factors |
| E | Modulus of elasticity |
| E_m | Modulus of elasticity mean value |
| E_{nom} | Modulus of elasticity nominal value |
| L | Length (member length, span length, etc) |
| M | Bending moment |
| M_0 | Sagging moment at mid-span of a member |
| $M_{b,Rd}$ | Design value of the buckling resistance of a member in bending |
| $M_{b,Rd(GC)}$ | Design value of the buckling resistance of a member in bending through the use of the general case |
| M_{cr} | Elastic critical moment for lateral-torsional buckling |
| $M_{cr,LBA}$ | Elastic critical moment for lateral-torsional buckling obtained through a linear buckling analysis |
| $M_{cr,LTBeam}$ | Elastic critical moment for lateral-torsional buckling obtained through LTBeam |
| M_{exp} | Moment resistance obtained experimentally |
| M_{Ed} | Design bending moment |
| $M_{ep,Rd}$ | Design value of the elasto-plastic bending moment resistance |
| M_h | Hogging moment at member ends |

| | |
|----------------------|---|
| M_{pl} | Plastic moment resistance |
| $M_{pl,Rd}$ | Design value of the plastic moment resistance |
| $M_{Rd,exp}$ | Cross-section bending moment resistance based on experimental values |
| $M_{Rd,nom}$ | Cross-section bending moment resistance based on nominal values |
| M_{Rk} | Characteristic value of the resistance to bending moment |
| M_s | Sagging moment at mid-span |
| $M_{y,Ed}$ | Design value of the bending moment about y-y axis |
| $M_{y,Rd}$ | Design value of the resistance to bending moment about y-y axis |
| $M_{z,Ed}$ | Design value of the bending moment about z-z axis |
| $M_{z,Rd}$ | Design value of the resistance to bending moment about z-z axis |
| N | Axial force |
| $N_{b,Rd}$ | Design buckling resistance of a compression member |
| N_{cr} | Elastic critical axial force for the relevant buckling mode based on gross cross-sectional properties |
| N_{Ed} | Design normal force |
| N_{pl} | Plastic resistance to axial force of the gross cross-section |
| N_{Rk} | Characteristic value of the resistance to axial force |
| P | Concentrated load |
| P_{max} | Maximum load |
| R_{eH} | Yield strength taken from the relevant product standard (tensile coupon test) |
| R_m | Ultimate strength taken from the relevant product standard (tensile coupon test) |
| W | Section modulus |
| W_{eff} | Effective section modulus |
| W_{el} | Elastic section modulus |
| $W_{el,y}, W_{el,z}$ | Elastic section modulus for bending about y-y axis and z-z axis, respectively |
| W_{ep} | Elasto-plastic section modulus for Class 3 section |
| $W_{ep,y}, W_{ep,z}$ | Elasto-plastic section modulus for bending about y-y axis and z-z axis, respectively |

| | |
|----------------------|---|
| W_{pl} | Plastic section modulus |
| $W_{pl,y}, W_{pl,z}$ | Plastic section modulus for bending about y-y axis and z-z axis, respectively |

Latin Lower-case Symbols

| | |
|----------------------------------|--|
| a_0, a, b, c, d | Class indexes for buckling curves according to Eurocode 3 Part 1-1 |
| a | Weld throat length |
| a_f | Tensile region in the flange |
| $a_{f,c}$ | Width of the flange compression zone |
| a_w | Tensile region in the web |
| $a_{w,c}$ | Width of the web compression zone |
| b | Width of a cross-section |
| b_c | Flange width in compression |
| b_f | Flange width |
| b_t | Flange width in tension |
| c | Width of depth of a part of a cross-section |
| e_0 | Amplitude of a member imperfection |
| f | Modification factor for χ_{LT} |
| f_M | Factor that accounts for the effect of the bending moment distribution between discrete lateral restraints |
| f_u | Ultimate strength |
| f_y | Yield strength |
| f_{ym} | Yield strength mean value |
| $f_{y,exp}$ | Yield strength measured in the tensile coupon test |
| $f_{y,nom}$ | Yield strength nominal value |
| h | Depth of a cross-section |
| h_w | Depth of a web |
| k_c | Correction factor for moment distribution |
| $k_{yy}, k_{yz}, k_{zy}, k_{zz}$ | Interaction factors for uniform members in bending and axial compression |

| | |
|-------|---|
| n | Number of cases |
| n_y | Ratio of design axial force to design value of the buckling resistance of a member in compression for buckling about y-y axis |
| n_z | Ratio of design axial force to design value of the buckling resistance of a member in compression for buckling about z-z axis |
| q | Distributed load |
| r_e | Experimental resistance (can be obtained from tests or numerical estimates from advanced simulations) |
| r_t | Theoretical resistance |
| t | Thickness |
| t_f | Flange thickness |
| t_w | Web thickness |
| u_x | Displacement along x-axis |
| u_y | Displacement along y-axis |
| u_z | Displacement along z-axis |
| w | Deflection |
| x-x | Axis along the member (longitudinal axis) |
| y-y | Cross-section axis parallel to the flanges (horizontal axis) |
| z-z | Cross-section axis perpendicular to the flanges (vertical axis) |

Greek Upper-case Symbols

| | |
|-------------------|--|
| $\Delta M_{y,Ed}$ | Moment about y-y axis due to the shift of the centroid |
| $\Delta M_{z,Ed}$ | Moment about z-z axis due to the shift of the centroid |
| ϕ | Value to determine the reduction factor χ for flexural buckling |
| ϕ_{LT} | Value to determine the reduction factor χ_{LT} for lateral-torsional buckling |

Greek Lower-case Symbols

| | |
|------------|---|
| α | Imperfection factor for flexural buckling |
| α_h | Factor describing the moment diagram; h = hogging |

| | |
|------------------------------|--|
| α_{LT} | Imperfection factor for lateral-torsional buckling |
| $\alpha_{LT,num}$ | Imperfection factor for lateral-torsional buckling obtained through numerical analysis |
| α_s | Factor describing the moment diagram; s= sagging |
| α_0 | Generalized imperfection amplitude factor |
| $\alpha_{0,num}$ | Generalized imperfection amplitude factor obtained through numerical analysis |
| β | Correction factor for the lateral-torsional buckling curves for rolled and welded sections |
| $\beta_{ep,y}, \beta_{ep,z}$ | Interpolation factor for bending about y-y axis and z-z axis, respectively |
| γ_M | Partial factor |
| γ_{M1} | Partial factor for resistance of members to instability assessed by member checks |
| ε | Material parameter depending on f_y |
| ε_{eng} | Engineering strain |
| ε_{pl} | Plastic strain |
| ε_u | Ultimate strain |
| ε_y | Yield strain |
| η | Generalized imperfection |
| η_{EC3} | Generalized imperfection according to Eurocode 3 Part 1-1 |
| η_{GC} | Generalized imperfection according to the general case of Eurocode 3 Part 1-1 |
| η_{LT} | Generalized imperfection for lateral-torsional buckling |
| η_{NewEC3} | Generalized imperfection according to the new version of Eurocode 3 Part 1-1 |
| η_{num} | Generalized imperfection obtained through numerical analysis |
| η_{SC} | Generalized imperfection according to the special case of Eurocode 3 Part 1-1 |
| η_y | Generalized imperfection for flexural buckling about y-y axis |
| η_z | Generalized imperfection for flexural buckling about z-z axis |
| θ | Rotation |
| θ_{xx} | Twist rotation |

| | |
|--------------------------|--|
| $\bar{\lambda}$ | Relative slenderness |
| $\bar{\lambda}_{LT,0}$ | Plateau length of the lateral-torsional buckling curves for rolled and welded sections |
| $\bar{\lambda}_{LT}$ | Relative slenderness for lateral-torsional buckling |
| $\bar{\lambda}_{LT,exp}$ | Relative slenderness for lateral torsional-buckling based on experimental values |
| $\bar{\lambda}_{LT,nom}$ | Relative slenderness for lateral torsional buckling based on nominal values |
| $\bar{\lambda}_y$ | Relative slenderness for flexural buckling about y-y axis |
| $\bar{\lambda}_z$ | Relative slenderness for flexural buckling about z-z axis |
| σ_c | Compressive stress |
| σ_{cf} | Compressive residual stress in the flange |
| σ_{cw} | Compressive residual stress in the web |
| σ_{eng} | Engineering stress |
| $\sigma_{f,c}$ | Compression stress value in the flange |
| σ_{tf} | Tensile residual stress in the flange |
| σ_{true} | True stress |
| σ_{tw} | Tensile residual stress in the web |
| $\sigma_{w,c}$ | Compression stress value in the web |
| χ | Reduction factor for relevant buckling mode |
| χ_{LT} | Reduction factor for lateral-torsional buckling |
| $\chi_{LT,exp}$ | Reduction factor for lateral-torsional buckling based on experimental values |
| $\chi_{LT,mod}$ | Modified reduction factor for lateral-torsional buckling |
| χ_{num} | Reduction factor for the relevant buckling mode obtained through numerical analysis |
| χ_y | Reduction factor due to flexural buckling about y-y axis |
| χ_z | Reduction factor due to flexural buckling about z-z axis |
| ψ | Ratio of end moments in a segment of beam, or stress ratio |

ABBREVIATIONS AND ACRONYMS

| | |
|---------------|---|
| COV | Coefficient of variation |
| EC3 | Eurocode 3 |
| EC3-1-1 | Eurocode 3 Part 1-1 |
| ECCS | European Convention for Constructional Steelwork |
| FB | Flexural buckling |
| FB y-y | Flexural buckling about major axis |
| FB z-z | Flexural buckling about minor axis |
| FEM | Finite element method |
| GC | General case |
| GMNIA | Geometric and material non-linear analysis with imperfections |
| HSS | High strength steel |
| LBA | Linear buckling analysis |
| LTB | Lateral-torsional buckling |
| LVDT | Linear variable differential transformer |
| NEC3 | New EC3 case |
| Non-TC or NTC | Non-Thermal cut residual stress model |
| NSS | Normal strength steel |
| RS | Residual stress |
| SC | Special case |
| SG | Strain gauge |
| STROBE | Stronger Steels in the Built Environment |
| TC | Thermal cut residual stress model |

1. Introduction

1.1. Motivation and scope

High strength steel (HSS) has been available for several decades, and it has been successfully applied in some areas, such as the automotive and oil-gas industries [3]. However, in the construction sector, its applications in buildings are not very common, being restricted to special buildings.

This restricted use in the construction sector can be explained partly because of fabrication and standardisation issues, as the design procedures available in different standards limit the steel grades. Furthermore, there are no specific rules for high strength steels, or, in some cases, the design specifications are incomplete or too conservative. Also, other difficulties regarding welding and ductile behaviour at low temperatures of quenched and tempered materials have been identified.

Concerning structural design procedures, in Europe, steel structures are designed according to EN 1993-1-1 [1], which gives structural design guidance for steels up to S460, while EN 1993-1-12 [2] provides additional rules for steels up to S700. The reason for these special rules and the upper strength limit of S700 is that there was insufficient test data on high strength steel structural members to justify less conservative rules when they were formulated. Whereby, in most cases, these rules are overly conservative, and in some cases, there are no specific rules for the design when using high strength steel, such as the lateral-torsional buckling of beams. The current design standard, EN 1993-1-1 [1], usually referred to as Eurocode 3, Part 1-1, does not distinguish between normal strength steel and high strength steel when designing steel members subjected to lateral-torsional buckling. In the case of flexural buckling, it already has some improvements in the selection of the buckling curve, although these improvements are limited to hot-rolled sections and only cover the steel grade S460, leaving the other cases with the same rules as for normal strength steel.

However, due to continuous improvements in steel production technology, it is possible to manufacture high strength steels with a nominal yield stress higher than 460 MPa with excellent weldability and toughness properties [4]. The European steel product standard EN 10025 [5]

covers steels up to S960, and the fabrication standard EN 1090 [6] is being extended to accommodate steels up to S960 as well.

Following this trend, the revised version of FprEN 1993-1-1 [7] will include steels up to S700 in its main part, whereas rules for steels up to S960 will be given in prEN 1993-1-12 – High strength steels [8], with a focus on ultra-high strength steels. These advances were only possible due to the development of intense research activities with a focus on high strength steels, such as the European research projects OPTIBRI, HILONG, and RUOSTE, among others.

The present dissertation was performed in line with the most recent European research project with an emphasis on high strength steels, the European research project STROBE RFSR-CT-2016-743504 – Stronger Steels in the Built Environment. The main objective of this project was to assess the design rules for steel members and materials up to S700. Since the use of high strength steel potentially leads to decreased member sizes, which are more susceptible to instabilities (local and global buckling), it is essential to assess the net benefit, by considering the improved material properties. These rules are expected to be less severe for high strength steel members.

As part of the European project STROBE, this research is focused on the study of the buckling behaviour of high strength steel beams and how the current buckling design rules apply to high strength steel members, based on experimental and numerical evidence, in order to increase the use of high strength steel and provide evidence on the benefits of using HSS in steel structures. Further stress is placed on how these benefits can be maximised by exploiting the actual limits of HSS in terms of stability design.

1.2. Objectives and methodology

The goal of this research work is to contribute towards the increase of the use of high strength steel in steel construction, extend the knowledge in the structural buckling behaviour of high strength steel members, and provide insight on its benefits compared to normal strength steel.

The goal was achieved through the assessment of the current design rules available in Eurocode 3 [1] for the buckling resistance of high strength steel members and proposing new buckling design rules applicable to high strength steels, through the use of the following methodology:

Experimental buckling behaviour of high strength steel beams: the buckling behaviour of high strength steel beams was characterized through an experimental campaign in the

framework of the European research project STROBE RFSR-CT-2016-743504 – Stronger Steels in the Built Environment, which aims to investigate the structural response of high strength steels ranging from S460 to S700, considering both welded and rolled I-shaped sections, homogenous and hybrid, and including supplementary tests for the material characterization and residual stresses and geometrical imperfections measurements. It was possible to: (1) Evaluate the influence of the material, through the use of different steel grades, S355, S460 and S690; (2) Evaluate the influence of the fabrication procedure on the lateral-torsional buckling resistance, thus testing S460 rolled sections and equivalent HSS welded beams; (3) Evaluate the lateral-torsional buckling resistance of hybrid beams, and (4) Evaluate the influence of the residual stresses and geometrical imperfections on the structural behaviour of high strength steels.

Numerical studies: through the use of advanced numerical models, it was possible to accurately represent the lateral-torsional buckling tests, in order to extend the scope of the study of the buckling resistance of high strength steel members to assess the current buckling design rules through an extensive parametric study which included the assessment of the following members/conditions: (1) columns; (2) beams; (3) hybrid beams; (4) beam-columns, and (5) considering different residual stresses patterns for columns and beams. The advanced numerical models also contributed to the evaluation of the members' imperfections, through an imperfection sensitivity test, considering different approaches for the numerical modelling of the residual stresses pattern and geometrical imperfections.

Development of stability design rules for high strength steel members: the assessment of the buckling design rules, allowed to propose and validate new buckling design rules applicable to high strength steel members, based on the calibration of the imperfection factors and buckling curves currently present in the Eurocode. The development of stability design rules for high strength steel members was performed for the following: (1) members in compression; (2) members in bending, and (3) members in bending and axial compression.

1.3. Outline of the dissertation

The research topics/objectives presented above, are developed throughout the six chapters of this dissertation.

Chapter 1 provides a general introduction, scope and main objectives of the research. The following chapter, Chapter 2, presents a general state of the art for the stability design of steel members, as well as the current Eurocode 3 recommendations and design procedures for the buckling resistance of steel members (flexural buckling of columns, lateral-torsional buckling of beams and combined flexural and lateral-torsional buckling of beam-columns).

In Chapter 3, the experimental programme carried out in the scope of the research project STROBE – Stronger Steels in the Built Environment is presented. It includes the execution of tensile coupon tests, residual stresses and geometrical imperfections measurements, and full-scale tests on lateral-torsional buckling of high strength steel beams. The experimental layouts for the buckling tests and for the supplementary tests (residual stress and geometrical imperfections measurements and material characterization) are described, followed by the presentation and discussion of the experimental results and the comparison of the experimental results with the current design recommendations for members subjected to lateral-torsional buckling.

In Chapter 4, the numerical studies are defined and described. It begins with the numerical modelling using finite element modelling, in order to reproduce the lateral-torsional buckling tests. The development of the advanced numerical models is presented, and the calibration of the numerical models is done against the experimental results. Then, in order to extend the scope of the buckling behaviour of high strength steel members, a simplified numerical model using standard conditions based on the previously calibrated models is presented. This simplified numerical model further sets the groundwork for an extensive parametric study, presented and performed for different members (columns, beams, and beam-columns), including the assumption of different residual stress patterns. Finally, the results obtained in the parametric study are presented and compared with the current Eurocode 3 recommendations for the buckling design of steel members.

Based on the results obtained in the parametric study performed previously, in Chapter 5 it is intended to develop stability design rules suitable for high strength steel members. The development of new design rules derives on the calibration of the imperfection factors/buckling curves available in the buckling design of steel members according to Eurocode 3. Lastly, the proposed design rules are applied to the cases carried out in the parametric study in order to validate the proposed design rules. The chapter ends with the recommendations for the buckling design of steel members made of high strength steel (columns, beams, and beam-columns).

Finally, in Chapter 6 the general/main conclusions of this research are summarized and highlighted.

2. Stability design of steel members

2.1. Introduction

The stability design of steel members in Europe is carried out according to Eurocode 3 – Part 1-1 [1], through clause 6.3, “buckling resistance of members”. The buckling resistance of uniform steel members is determined according to the loading type (compression or bending), through the multiplication of the cross-section resistance by a buckling reduction factor to account for the stability phenomenon. The reduction factor is dependent on the selection of the imperfection factor.

An imperfection factor is introduced to account for the members imperfections, such as geometrical imperfections and residual stresses since they highly influence the stability behaviour of steel members. The selection of the imperfection factor is associated with the selection of a buckling curve, also known as the buckling curve approach.

According to Simões da Silva et al. [9], buckling curves were first introduced for the column buckling (flexural buckling) in the 1970s. Their development was based on an extensive experimental programme carried out by the European Convention for Constructional Steelwork (ECCS) in several European countries.

The extensive experimental programme carried out by Sfantesco [10] comprised 1067 column tests, covering a wide variety of cross-sections (hollow, I-, H-, and T-shaped sections) and different fabrication procedures (rolled and welded sections), including the assessment of the material and geometrical (cross-section dimensions and imperfections) properties of each column.

Based on the ECCS experimental campaign, Beer and Schulz [11] assessed several parameters which could affect the resistance of the compressed members, with a focus on: (i) initial out-of-straightness; (ii) load eccentricity; and (iii) residual stresses.

The geometrical imperfections measured in the experimental programme allowed for an estimation of the initial geometrical imperfection, showing that an initial imperfection of $L/1000$ could cover loads with eccentricities up to 5 mm [11].

Regarding the residual stresses, due to the lack of available measurements and the high variability of the measurements available, it was difficult to determine their magnitude.

Whereby, to assess the influence of the residual stresses and geometrical imperfections, several comparisons were performed, through the consideration of different levels of geometrical imperfections ($L/500$, $L/1000$, and $L/2000$), with or without the consideration of the residual stresses. It was noted that the influence of the geometrical imperfections decreased with the increase of the residual stresses.

Later, Strating and Vos [12], through Monte Carlo simulation, assessed the safety of one of the curves, considering the variability of several parameters, such as residual stresses, out-of-straightness, load eccentricity, geometrical properties, and material properties.

Maquoi and Rondal [13] derived the analytical Ayrton-Perry format of the design verification, as it is presented today in Eurocode 3 [1], and the curves were put into the equation.

Based on the experimental programme carried out by ECCS, four buckling curves ranging from a to d were initially calibrated and proposed based on the extensive experimental programme. A more favourable curve, a_0 , was later added to account for the most favourable properties of high strength steels (Figure 2.1).

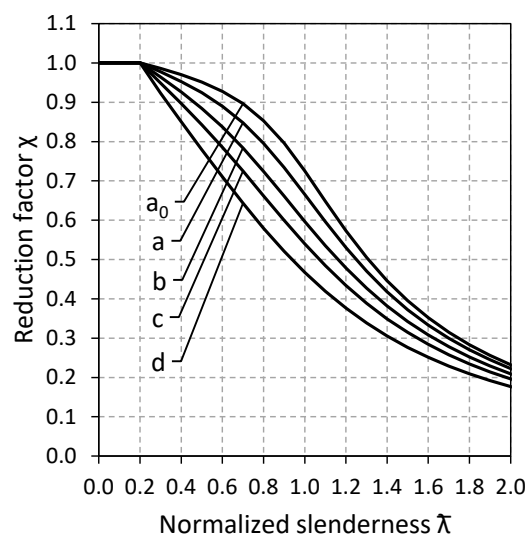


Figure 2.1 – European buckling curve representation as a function of slenderness

For the lateral-torsional buckling case and upon the approach proposed for flexural buckling (the buckling curve approach), Eurocode 3 currently proposes two methods for the buckling resistance of members subjected to lateral-torsional buckling.

The first method, the general case, assumes that the compression flange of the beam behaves like an equivalent column, adopting the same imperfection factors as the flexural buckling case. Nonetheless, this method has been criticized for being too conservative, as it does not

distinguish between members with variable bending moment, assuming the same reduction factor for different conditions [14].

The alternative approach for the lateral-torsional buckling resistance of rolled and welded sections is denoted as special case. The method was calibrated based on extensive experimental and numerical studies [15], [16], [17], and [18]. Nonetheless, the method was shown to be unsafe when compared to numerical results [14] and [20].

More recently, a research carried out by Taras and Greiner [21] resulted in a new Ayrton-Perry design rule based on a mechanically consistent analytical derivation and imperfection factors calibrated through extensive numerical study. The method was approved and validated through the SAFEBRICKTILE assessment procedure [22] and [23] with consistent results and is included in the new version of Eurocode 3 [7].

Nonetheless, the mentioned methods were developed and validated in the basis of normal strength steels (NSS) or limited to steel grades up to S460, particularly in the case of lateral-torsional buckling, where the code provides no distinction between normal strength steel and high strength steel. This lack of design guidance for high strength steel members can be attributed to the insufficient test data available at the time for high strength steel members.

Furthermore, due to the improvements in steel production and consequently in the steels' quality improving the high strength steel properties (toughness and ductility) compared to older steels, the interest in the field of the research of high strength steels has increased.

The following sections are intended to provide information on recent advances in the research of high strength steel stability behaviour.

2.2. Member imperfections – residual stresses

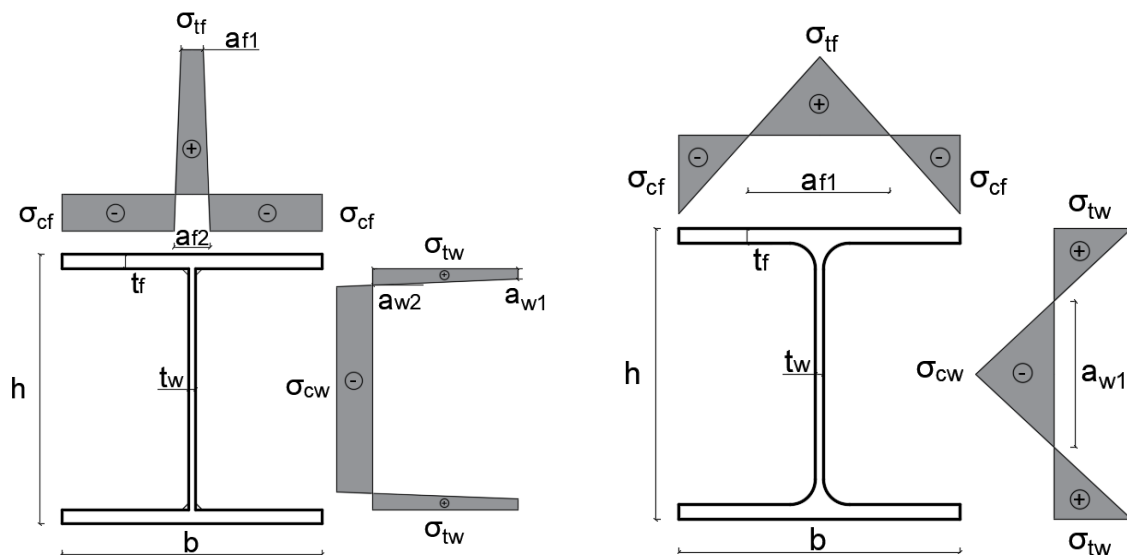
Residual stresses play an important role in determining the stability behaviour of steel members, since their superposition with the stresses coming from the loading can cause the premature yielding of the steel member and loss of stiffness [24].

The presence of residual stresses in steel members are unavoidable since they result from the non-uniform cooling and heating during the manufacture process of the steel plate. Nonetheless, due to the manufacturing process, the residual stress distribution in welded and rolled sections is quite different.

Residual stress results from the differential cooling from a more or less homogeneous temperature field in rolled sections. For welded sections, the residual stresses are induced due to the local heating during the welding of the flanges to the web plates.

Hence, knowledge of the magnitude and distribution of the residual stresses in the steel cross-section is essential when studying the stability behaviour of steel members.

The most commonly adopted residual stress patterns in Europe were proposed by ECCS [24], split according to the manufacturing process of the steel cross-section (rolled or welded sections), as shown in Figure 2.2, where σ_{tf} and σ_{tw} represent the tensile residual stress and σ_{cf} and σ_{cw} the compressive residual stress, in the flanges and web, respectively. The maximum tensile residual stress is 235 MPa , and the compressive residual stress is $0.25 \cdot 235 \text{ MPa}$ (58.75 MPa), not depending on the steel grade. Another commonly used residual stress pattern included in prEN 1993-1-14 [25] adopts the same distribution as the ECCS model for welded sections (Figure 2.2), however, it considers the maximum tensile residual stress equal to the yield strength of the steel plate (f_y) and the compressive residual stress equal to $0.25 \cdot f_y$. Nonetheless, these models were proposed on the basis of measurements performed in normal strength steels.



σ_{tf} – tensile residual stress in the flange;

σ_{tw} – tensile residual stress in the web;

a_f – tensile region in the flange;

σ_{cf} – compressive residual stress in the flange;

σ_{cw} – compressive residual stress in the web;

a_w – tensile region in the web;

a) Welded I-sections

b) Rolled I-sections

Figure 2.2 – Residual stresses patterns according to ECCS [24]

Regarding the scope of research on steel grades higher than or equal to S460, Tankova et al. [26], summarised the residual stress measurements performed so far. Table 2.1 and Table 2.2 summarise residual stress measurements performed for steel grades up to S460 (Table 2.1) and higher than S460 (Table 2.2), respectively, supplemented by more recent work.

Some of the measurements performed resulted in proposals for residual stress patterns for welded I or H-shaped sections, these residual stress distributions are presented in Figure 2.3. Liu and Chung [27] pointed out that the welding energy has a negative impact on the residual stresses and should be kept ideally above 2 kJ/mm. According to Rasmussen and Hancock [28], residual stress has a greater impact in normal strength steel columns than in high strength steel columns. Furthermore, Liu [29] and Wang [30] performed experimental tests and welding simulations in order to measure the residual stress distributions in steel grades S355 and S690, concluding that when the residual stresses are expressed as a function of the yield stress (f_y), for higher steel grades, the magnitude of the residual stresses is lower.

The research work presented in Table 2.1 and Table 2.2 in the scope of residual stress measurements performed for welded sections is recent, where the last work is related to 2013, and the majority of them were developed after 2015. Given that these measurements were performed considering the current manufacturing processes, they are considered representative of the actual magnitude of the residual stresses.

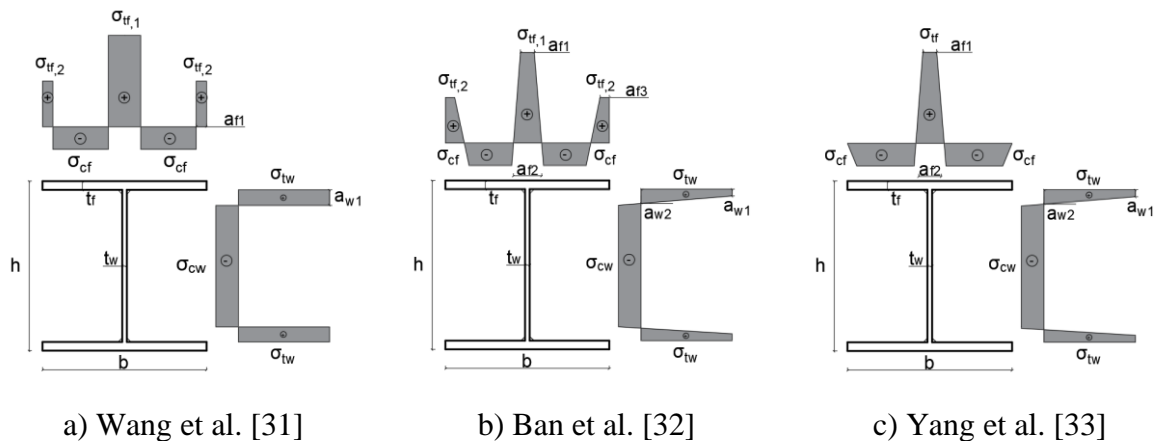


Figure 2.3 – Proposals for residual stress distributions for high strength steel members

Table 2.1 – Residual stress measurements on welded sections in steel grades up to S460

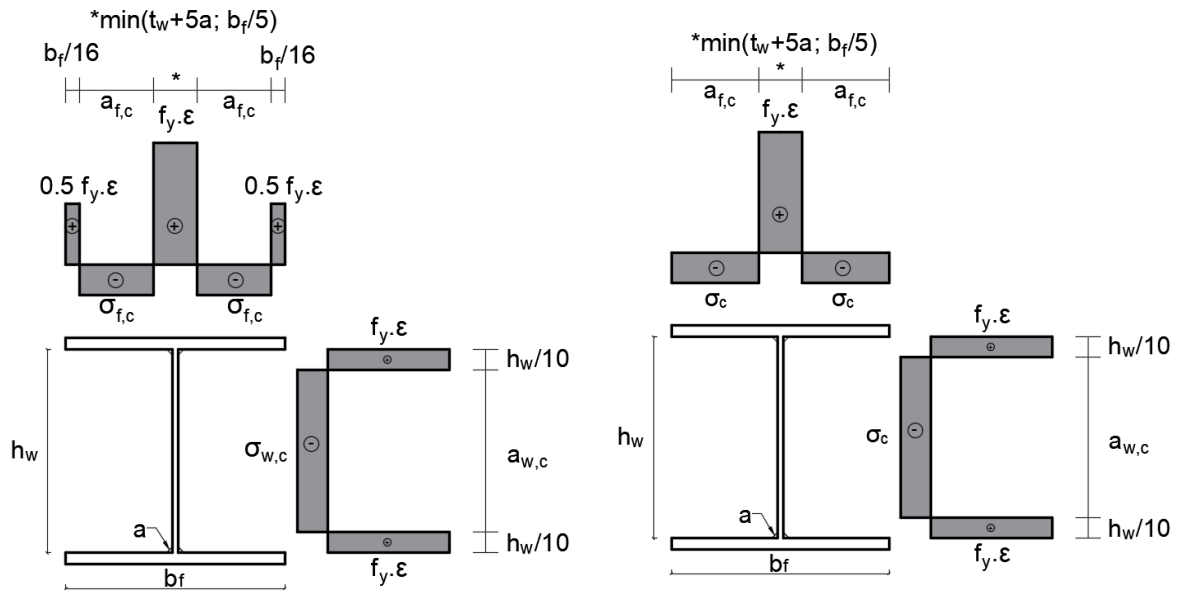
| Reference | Number of tests | Type of cross-section | Range of cross-section dimensions [mm] | | | Yield stress f_y [MPa] |
|----------------------------|-----------------|-----------------------|--|---------|-------|--------------------------|
| | | | h | b | t | |
| Unsworth et al. [34], [35] | 4 | I-sections | 600-800 | 300-430 | 12-31 | 355 |
| Tankova et al. [26] | 4 | I-sections | 143-317 | 100-110 | 6-16 | 355 |
| Schaper et al. [36], [37] | 15 | I-sections | 370-840 | 200-350 | 12-40 | 355 and 460 |
| Ban et al. [32], [38] | 6 | Box sections | 100-380 | 100-380 | 10-14 | 460 |
| | 8 | I-sections | 110-360 | 130-348 | 10-14 | 460 |
| Wang et al. [31] | 3 | H-sections | 168-320 | 156-314 | 11-21 | 460 |
| Yang et al. [33], [39] | 16 | I-sections | 170-450 | 162-312 | 8-42 | 460 |

More recently, the experimental measurements of residual stresses in high strength steel members carried out at the University of Coimbra - in the scope of the STROBE project and included in the present research work - and at the Universität Bochum resulted in a new model proposed by Schaper et al. [40] to predict the residual stresses for welded I-sections. The model was proposed on the premises that the commonly adopted models, ECCS [24] and prEN 1993-1-14 [25], do not reflect the recent residual stress measurements since they do not consider the tensile stresses at the flange tips, which can have a direct impact on the stability behaviour, and also the non-proportionality of the yield strength in the magnitude of the residual stresses.

Schaper et al. [40] proposed a model applicable to steel grades ranging from S235 to S890 to account for the thermal cut of the plates, taking tensile stresses at the flange tips into account. Alternatively, the model also accounts for the non-thermal cut of the plates, as shown in Figure 2.4.

Table 2.2 - Residual stress measurements on welded sections in steel grades higher than S460

| Reference | Number of tests | Type of cross-section | Range of cross-section dimensions [mm] | | | Yield stress f_y [MPa] |
|---------------------------|-----------------|-----------------------|--|---------|-------|--------------------------|
| | | | h | b | t | |
| Somodi and Kovesdi [41] | 21 | Box-sections | 80-250 | 80-250 | 4-8 | 235 to 960 |
| Launert et al. [42], [43] | 4 | T-sections | 220 | 150 | 10-25 | 355 and 690 |
| Li et al. [44] | 3 | Box sections | 108-203 | 141-235 | 16 | 690 |
| | 3 | H-sections | 206-258 | 209-261 | 16 | 690 |
| Liu [29] and Chung [27] | 4 | H-sections | 140-280 | 120-250 | 6-16 | 690 |
| Wang [30] | 3 | I-sections | 300-306 | 126-190 | 6-16 | 690 |
| Yang et al. [45] | 1 | Box-sections | 300 | 300 | 14 | 690 |
| | 1 | H-sections | 300 | 300 | 14 | 690 |
| Le et al. [46] | 3 | I-sections | 354-184 | 160 | 7-11 | 690 and 890 |
| Li et al. [47] | 2 | Box sections | 150-250 | 150-250 | 5 | 960 |
| | 2 | I-sections | 150-250 | 75-125 | 5 | 960 |
| Su et al. [48] | 2 | I-sections | 150-200 | 150 | 6 | 960 |
| Wang and Lui [49] | 3 | I-sections | 192 | 144-192 | 12 | 690 |
| Cao et al. [50] | 4 | T-sections | 78-120 | 54-139 | 7 | 800 |



$a_{f,c}$ and $a_{w,c}$ are determined as the remaining flange/web length

$\sigma_{f,c}$ and $\sigma_{w,c}$ are determined by equilibrium conditions at each plate

$$\varepsilon = \sqrt{235/f_y}$$

a) Thermal cut plates

b) Non-thermal cut plates

Figure 2.4 – Residual stress distribution proposed by L. Schaper et al. [40]

2.3. Stability of high strength steel members

The study of the buckling behaviour of high strength steel members was initially carried out mainly for columns, where the flexural buckling behaviour of welded box, H- and I-sections about major and minor axes in steel grades S460 to S960 was studied experimentally and numerically by several authors [28], [51], [52], and [53]. These studies already reported improved stability behaviour of the high strength steel members, verifying significant differences between the experimental buckling resistance and the buckling resistance provided by the design codes. Nevertheless, they were carried out for a limited range of cross-section dimensions, covering only sections with a depth-to-width ratio less than 1.2 ($h/b \leq 1.2$).

Liu [29] determined a complete residual stress distribution in a welded cross-section in steel grade S690 using thermo-mechanical coupled simulations calibrated with measure data for four welded high strength steel sections, then studied the behaviour of the HSS beams and columns through experimental and advanced numerical analyses.

Regarding the study of the lateral-torsional buckling behaviour of high strength steel beams, experimental tests of fully restrained and partially restrained welded I-section beams made of

S690 were carried out by Wang [30], who reported significant differences between the measured buckling resistance and the design buckling resistance and attributed this difference to the reduced residual stress ratios in S690 welded I-sections when compared to the normal strength steel welded I-sections.

Schaper et al. [36] carried out lateral-torsional buckling tests of double and mono-symmetric welded I-sections of steel S355 and S460 with residual stress measurements of the same cross-section of the tested specimens in order to study the influence of the residual stresses on the lateral-torsional buckling resistance. The experimental results were compared with the European design methods (general case and simplified method of Eurocode 3), showing that these methods lead to conservative results and should be revised in order to consider the effects of the residual stresses more thoroughly.

Feng et al. [54], [55] performed experimental tests on the flexural behaviour of H-shaped high strength steel beams with perforated web, studying the influence of the web depth to flange width ratio (h/b), flange width to thickness ratio (b/t_f), web depth to thickness ratio (h/t_w), hole diameter to web depth (d/h), and number of holes in the web on the flexural resistance of the high strength steel members. Based on advanced numerical analyses validated against the experimental results, compared the flexural resistance with existing design codes, showing that the design rules in most cases give conservative results, and proposing design equations to predict the flexural capacities of H-section high strength steel beams with web openings.

Yang et al. [56] used advanced numerical analyses, including geometrical imperfections and residual stresses, to perform a parametric study in order to investigate the effects of span length, cross-section dimensions, and steel grade on the buckling strength of high strength steel I-section beams in steel grades S460 to S960. The models were validated through the comparison with experimental results available in the literature. The parametric study indicated that the buckling resistance of I-section beams depended mainly on the normalized slenderness and section slenderness. It was also noted that the buckling resistance of high strength steel beams was higher than that of normal strength steel beams with the same normalized slenderness and section slenderness, proposing a new formulation to predict the buckling strength of HSS beams considering coupled local and lateral-torsional buckling.

Hybrid beams, beams with flange plates made of a higher steel grade than the web, can also benefit from the use of high strength steel, as they are often more cost-effective than homogeneous beam sections, since the web of a beam only contributes a modest amount to the total bending resistance, whereby it is more economical to use a less expensive (lower-strength) steel in the web than the flanges. The lateral-torsional buckling behaviour of hybrid beams was previously numerically studied by Nethercot [57], who concluded that the early yielding of the hybrid beam web had little influence on the lateral stability.

The lateral-torsional buckling of hybrid beams was further studied by Veljkovic and Johansson [58], who concluded that the design of hybrid beams can be done with the Eurocode 3 design rules with some minor modifications. Nonetheless, a limitation that the strength of the flanges should not exceed twice that of the web for serviceability reasons was suggested.

Shokouhian et al. [59] performed experimental tests on homogenous and hybrid I-section beams made of Q345 and Q460 steel grades. Based on the experimental tests, a numerical model was developed to carry out a parametric study in order to study the interactive effects of flange local buckling, web local buckling, and lateral-torsional buckling modes on the flexural strength and propose design equations to determine the flexural resistance of hybrid and homogenous section beams based on their overall slenderness.

Table 2.3 presents some experimental tests recently performed in the study of the lateral-torsional buckling resistance of beams made of high strength steel, in which the authors compared the obtained experimental results with the design code specifications provided by the Eurocode 3 (EN 1993-1-1) [1], for the plastic moment resistance ($M_{pl,Rd}$) and buckling moment resistance ($M_{b,Rd}$). These studies already report some significant conservative results provided by the design code. When comparing the buckling resistance obtained through the Eurocode 3 to the buckling resistance obtained experimentally, differences ranging from 15% to 80% were found.

Nevertheless, a thorough experimental, analytical, and statistical investigation into the stability design of high strength steel members with hybrid and homogeneous solutions in accordance with the Eurocode methodology is still required, since the current design rules for the lateral-torsional buckling of steel members are not dependent on the steel grade, meaning that the code does not distinguish between the stability behaviour of normal strength steel and high strength steel members.

Validated design rules for high strength steel members are still required for the practitioners, since the designers will only specify high strength steel solutions if simple design procedures and design tools are available and recommended in the codes.

Table 2.3 – Experimental tests on lateral-torsional buckling of high strength steel members

| Reference | No. of tests | f_y [MPa] | Cross-section dimensions [mm] | | | | M_{exp} [kN.m] | $\frac{M_{exp}}{M_{pl,Rd}}$ | $\frac{M_{exp}}{M_{b,Rd}}$ |
|--------------------|--------------|----------------|-------------------------------|-------|-------------|-------|---------------------|-----------------------------|----------------------------|
| | | | h | b | t_f | t_w | | | |
| Le et al. [60] | 7 | 690 | 354.0 | 159.5 | 11.77 | 7.70 | 478 | 0.67 | - |
| | | 690 | 353.5 | 159.3 | 11.77 | 7.70 | 659 | 0.92 | - |
| | | 690 | 354.3 | 160.0 | 11.77 | 7.70 | 509 | 0.71 | - |
| | | 890 | 353.5 | 159.9 | 11.80 | 7.95 | 572 | 0.66 | - |
| | | 890 | 352.9 | 159.5 | 11.80 | 7.95 | 844 | 0.98 | - |
| | | 890 | 354.0 | 160.2 | 11.80 | 7.95 | 634 | 0.74 | - |
| | | 890 | 353.8 | 120.3 | 11.80 | 7.95 | 330 | 0.47 | - |
| | | 890 | 254.5 | 120.2 | 11.80 | 7.95 | 259 | 0.58 | - |
| Yan et al. [61] | 4 | 460 | 202.0 | 101.9 | 10.08 | 10.9 | 68.5 | - | 1.17 |
| | | 460 | 200.0 | 100.0 | 10.08 | 10.0 | 73.6 | - | 1.18 |
| | | 460 | 350.5 | 179.5 | 10.08 | 10.6 | 303.5 | - | 1.20 |
| | | 460 | 350.0 | 180.2 | 10.08 | 10.2 | 285.8 | - | 1.19 |
| Wang et al. [62] | 12 | 690 | 262 | 112.2 | 10.1 | 6.0 | 319.7 | 1.11 | 1.16 |
| | | 690 | 300 | 126.3 | 10.0 | 6.0 | 383.6 | 1.03 | 1.20 |
| | | 690 | 430 | 170.1 | 10.1 | 6.0 | 710.0 | 1.05 | 1.19 |
| | | 690 | 300 | 190.1 | 16.0 | 6.0 | 831.5 | 1.15 | 1.21 |
| | | 690 | 268 | 111.9 | T9.9/B16.0 | 6.0 | 296.4 | 0.98 | 1.18 |
| | | 690 | 306 | 125.9 | T10.0/B16.0 | 6.0 | 383.5 | 1.01 | 1.15 |
| | | 690 | 262 | 112.2 | 9.9 | 6.0 | 282.8 | 1.00 | 1.22 |
| | | 690 | 300 | 126.1 | 10.0 | 6.0 | 303.8 | 0.82 | 1.18 |
| | | 690 | 430 | 170.1 | 10.0 | 6.0 | 444.8 | 0.66 | 1.51 |
| | | 690 | 300 | 190.1 | 16.0 | 6.0 | 748.4 | 1.04 | 1.51 |
| | | 690 | 268 | 111.9 | T10.0/B16.0 | 6.0 | 268.9 | 0.88 | 1.29 |
| | | 690 | 306 | 126.1 | T10.0/B16.0 | 6.0 | 355.4 | 0.93 | 1.44 |
| Xiong et al. [63] | 8 | 690 | 270 | 180 | 12 | 10 | 365.7 | 0.68 | 1.52 |
| | | 690 | 270 | 180 | 12 | 10 | 328.1 | 0.60 | 1.59 |
| | | 690 | 270 | 180 | 12 | 10 | 281.7 | 0.52 | 1.61 |
| | | 690 | 270 | 180 | 12 | 10 | 256.4 | 0.47 | 1.65 |
| | | 690 | 450 | 180 | 12 | 10 | 507.9 | 0.48 | 1.77 |
| | | 690 | 450 | 180 | 12 | 10 | 407.3 | 0.38 | 1.73 |
| | | 690 | 450 | 180 | 12 | 10 | 318.9 | 0.30 | 1.59 |
| | | 690 | 450 | 180 | 12 | 10 | 274.5 | 0.26 | 1.59 |
| Xiong et al. [64] | 12 | 690 | 350 | 200 | 10 | 14 | 878 | 0.99 | 1.25 |
| | | 690 | 350 | 200 | 10 | 14 | 860 | 1.01 | 1.29 |
| | | 690 | 350 | 200 | 10 | 14 | 818 | 1.00 | 1.29 |
| | | 690 | 350 | 200 | 10 | 14 | 849 | 0.97 | 1.62 |
| | | 690 | 350 | 200 | 10 | 14 | 811 | 0.95 | 1.66 |
| | | 690 | 350 | 200 | 10 | 14 | 759 | 0.93 | 1.66 |
| | | 690 | 450 | 200 | 10 | 14 | 1171 | 0.97 | 1.39 |
| | | 690 | 450 | 200 | 10 | 14 | 1070 | 0.91 | 1.32 |
| | | 690 | 450 | 200 | 10 | 14 | 1091 | 0.97 | 1.42 |
| | | 690 | 450 | 200 | 10 | 14 | 864 | 0.72 | 1.57 |
| | | 690 | 450 | 200 | 10 | 14 | 990 | 0.85 | 1.78 |
| | | 690 | 450 | 200 | 10 | 14 | 939 | 0.83 | 1.80 |

T – top flange; B – bottom flange.

2.4. Buckling design of steel members according to Eurocode 3

The current design rules and recommendations available in the EN1993-1-1 [1] (Eurocode 3), and in the new version of the Eurocode 3, prEN1993-1-1 [7], for the buckling design of steel members are presented in this section.

2.4.1. Design of members in compression

The buckling resistance of uniform members subjected to compression is given in the clause 6.3.1 of Eurocode 3 [1]. According to the code, the buckling resistance of members is verified through:

$$\frac{N_{Ed}}{N_{b,Rd}} \leq 1.0 \quad (2.1)$$

where N_{Ed} is the design value of the compression force, and $N_{b,Rd}$ is the design buckling resistance of the compression member and should be taken as:

$$N_{b,Rd} = \frac{\chi A f_y}{\gamma_{M1}} \quad \text{For class 1, 2 and 3 cross-sections} \quad (2.2)$$

$$N_{b,Rd} = \frac{\chi A_{eff} f_y}{\gamma_{M1}} \quad \text{For class 4 cross-sections} \quad (2.3)$$

where χ is the reduction factor for the relevant buckling mode.

$$\chi = \frac{1}{\phi + \sqrt{\phi^2 - \bar{\lambda}^2}} \leq 1.0 \quad (2.4)$$

$$\phi = 0.5[1 + \alpha(\bar{\lambda} - 0.2) + \bar{\lambda}^2] \quad (2.5)$$

$\bar{\lambda}$ is the normalized slenderness and α is the imperfection factor (Table 2.4), corresponding to the appropriate buckling curve. The correspondent buckling curves for I-sections are chosen according to Table 2.5.

Table 2.4 – Imperfection factors for buckling curves (EN1993-1-1 – Table 6.2)

| Buckling curve | a_0 | a | b | c | d |
|------------------------------|-------|------|------|------|------|
| Imperfection factor α | 0.13 | 0.21 | 0.34 | 0.49 | 0.76 |

$$\bar{\lambda} = \sqrt{\frac{Af_y}{N_{cr}}} \quad \text{For class 1, 2 and 3 cross-sections} \quad (2.6)$$

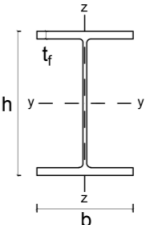
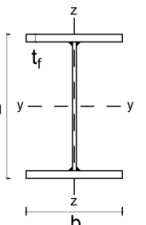
$$\bar{\lambda} = \sqrt{\frac{A_{eff}f_y}{N_{cr}}} \quad \text{For class 4 cross-sections} \quad (2.7)$$

N_{cr} is the elastic critical force for the relevant buckling mode based on the gross cross-sectional properties.

It should be noted that there is an inconsistency regarding the selection of the buckling curve for rolled sections with steel grades higher than S460 in the current Eurocode 3 [1], “Current EC3 version”, in Table 2.5.

The buckling curve selection for different buckling axes is always more favourable for in-plane buckling than out-of-plane buckling for steel grades up to S420. This is explained by the more unfavourable residual stress distribution for minor axis flexural buckling. Nonetheless, for steel grades higher than S460, this fact is not reflected in the buckling curve selection for rolled sections, which uses the same buckling curve for major and minor axes flexural buckling (Current EC3 version - Table 2.5). This was further investigated [9], and the buckling curve selection for rolled sections was revised and will be included in the new version of Eurocode 3 [7] (New EC3 version - Table 2.5).

Table 2.5 – Selection of buckling curve for a cross-section (EN1993-1-1 – Table 6.2)

| Cross section | Limits | Buckling about axis | Buckling curve | | | |
|--|--------------------------------|---------------------------|-----------------------------|---------------------|-----------------------|----------|
| | | | Current and New EC3 version | Current EC3 version | New EC3 version | |
| | | | S235; S275; S355; S420 | S460 | S460 up to S700 | |
| Rolled sections  | $h/b > 1.2$ | $t_f \leq 40 \text{ mm}$ | y – y | <i>a</i> | <i>a</i> ₀ | |
| | | | z – z | <i>b</i> | <i>a</i> ₀ | <i>a</i> |
| | $40 \text{ mm} < t_f \leq 100$ | y – y | <i>b</i> | <i>a</i> | <i>a</i> | |
| | | z – z | <i>c</i> | <i>a</i> | <i>b</i> | |
| | $h/b \leq 1.2$ | $t_f \leq 100 \text{ mm}$ | y – y | <i>b</i> | <i>a</i> | <i>a</i> |
| | | z – z | <i>c</i> | <i>a</i> | <i>b</i> | |
| $t_f > 100 \text{ mm}$ | y – y | <i>d</i> | <i>c</i> | <i>c</i> | | |
| | z – z | <i>d</i> | <i>c</i> | <i>c</i> | | |
| Welded I-sections  | $t_f \leq 40 \text{ mm}$ | y – y | <i>b</i> | <i>b</i> | <i>b</i> | |
| | | z – z | <i>c</i> | <i>c</i> | <i>c</i> | |
| | $t_f > 40 \text{ mm}$ | y – y | <i>c</i> | <i>c</i> | <i>c</i> | |
| | | z – z | <i>d</i> | <i>d</i> | <i>d</i> | |

2.4.2. Design of members in bending

The buckling resistance of members subjected to major axis bending is verified against lateral-torsional buckling in the clause 6.3.2 of Eurocode 3 [1], using:

$$\frac{M_{Ed}}{M_{b,Rd}} \leq 1.0 \quad (2.8)$$

where M_{Ed} is the design value of the moment, and $M_{b,Rd}$ is the design buckling resistance moment and should be taken as:

$$M_{b,Rd} = \chi_{LT} W_y \frac{f_y}{\gamma_{M1}} \quad (2.9)$$

W_y is the appropriate section modulus, according to:

- $W_y = W_{pl,y}$ for class 1 or 2 cross-sections
- $W_y = W_{el,y}$ for class 3 cross-sections
- $W_y = W_{eff,y}$ for class 4 cross-sections

χ_{LT} is the reduction factor for lateral-torsional buckling.

For the determination of the reduction factor for lateral-torsional buckling, χ_{LT} , there are currently two approaches available in Eurocode 3 [1]: the general case and the special case. Furthermore, the new version of Eurocode 3 [7], will include the method proposed by Taras and Greiner [21], which will be addressed in this section, since it will be an Eurocode design method. Henceforth, it will be referred to as “new EC3 case” or “nEC3”.

2.4.2.1. General case

The reduction factor for lateral-torsional buckling (χ_{LT}), when using the general case, is taken as:

$$\chi_{LT} = \frac{1}{\phi_{LT} + \sqrt{\phi_{LT}^2 - \bar{\lambda}_{LT}^2}} \leq 1.0 \quad (2.10)$$

$$\phi_{LT} = 0.5[1 + \alpha_{LT}(\bar{\lambda}_{LT} - 0.2) + \bar{\lambda}_{LT}^2] \quad (2.11)$$

Where $\bar{\lambda}_{LT}$ is the normalized slenderness for lateral-torsional buckling and α_{LT} is the imperfection factor depending on the buckling curve. The buckling curves are chosen according to the cross-section geometry in Table 2.6, with the imperfection factors given in Table 2.7.

$$\bar{\lambda}_{LT} = \sqrt{\frac{W_y f_y}{M_{cr}}} \quad (2.12)$$

M_{cr} is the elastic critical moment for lateral-torsional buckling.

Table 2.6 – Recommended values for lateral-torsional buckling curves for cross-sections using the general case (EN1993-1-1 – Table 6.4)

| Cross-section | Limits | Buckling curve |
|----------------------|--------------|----------------|
| Rolled I-sections | $h/b \leq 2$ | <i>a</i> |
| | $h/b > 2$ | <i>b</i> |
| Welded I-sections | $h/b \leq 2$ | <i>c</i> |
| | $h/b > 2$ | <i>d</i> |
| Other cross-sections | - | <i>d</i> |

Table 2.7 – Recommended values for imperfection factors for lateral-torsional buckling curves (EN1993-1-1 – Table 6.3)

| Buckling curve | <i>a</i> | <i>b</i> | <i>c</i> | <i>d</i> |
|-----------------------------------|----------|----------|----------|----------|
| Imperfection factor α_{LT} | 0.21 | 0.34 | 0.49 | 0.76 |

2.4.2.2. Special case

The special case is intended for the verification of lateral-torsional buckling of rolled sections or equivalent welded sections. The reduction factor (χ_{LT}) is determined from:

$$\chi_{LT} = \frac{1}{\phi_{LT} + \sqrt{\phi_{LT}^2 - \beta \bar{\lambda}_{LT}^2}} \leq \begin{cases} 1.0 \\ \frac{1}{\bar{\lambda}_{LT}^2} \end{cases} \quad (2.13)$$

$$\phi_{LT} = 0.5[1 + \alpha_{LT}(\bar{\lambda}_{LT} - \bar{\lambda}_{LT,0}) + \beta\bar{\lambda}_{LT}^2] \quad (2.14)$$

The additional parameters $\bar{\lambda}_{LT,0}$ and β are given in the National Annex, the recommended values are: $\bar{\lambda}_{LT,0} = 0.4$ and $\beta = 0.75$. The method is applied with the imperfections factors from Table 2.7 (same factors as the general case), with the buckling curves according to Table 2.8.

Table 2.8 – Recommendation for the selection of lateral buckling curve for cross sections using special case (EN1993-1-1 – Table 6.5)

| Cross-section | Limits | Buckling curve |
|-------------------|--------------|----------------|
| Rolled I-sections | $h/b \leq 2$ | <i>b</i> |
| | $h/b > 2$ | <i>c</i> |
| Welded I-sections | $h/b \leq 2$ | <i>c</i> |
| | $h/b > 2$ | <i>d</i> |

For taking into account different bending moment distributions, the method allows a modification in the reduction factor (χ_{LT}), as follows:







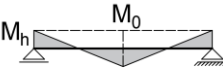

$$\chi_{LT,mod} = \frac{\chi_{LT}}{f} \leq \begin{cases} 1.0 \\ 1 \\ \frac{1}{\bar{\lambda}_{LT}^2} \end{cases} \quad (2.15)$$

where the f values may be defined in the National Annex, the recommended values are:

$$f = 1 - 0.5(1 - k_c) [1 - 2(\bar{\lambda}_{LT} - 0.8)^2] \leq 1.0 \quad (2.16)$$

k_c is a correction factor depending on the bending moment distribution and is chosen according to Table 2.9.

Table 2.9 – Correction factors k_c and f_M

| Moment distribution | k_c | f_M |
|---|-----------------------------|--|
|  | 1.0 | 1.0 |
|  | $\frac{1}{1.33 - 0.33\psi}$ | $1.25 - 0.1\psi - 0.15\psi^2$ |
|  | 0.94 | 1.05 |
|  | 0.90 | $0 \leq \frac{M_0}{M_h} < 2: 1.0 + 1.35 \frac{M_0}{M_h} - 0.33 \left(\frac{M_0}{M_h}\right)^3$ $\frac{M_0}{M_h} \geq 2: 1.05$ |
|  | 0.91 | $0 \leq \frac{M_0}{M_h} < 1.47: 1.25 + 0.5 \left(\frac{M_0}{M_h}\right)^2 - 0.275 \left(\frac{M_0}{M_h}\right)^4$ $\frac{M_0}{M_h} \geq 1.47: 1.05$ |
|  | 0.86 | 1.10 |
|  | 0.77 | $0 \leq \frac{M_0}{M_h} < 2: 1.0 + 1.25 \frac{M_0}{M_h} - 0.30 \left(\frac{M_0}{M_h}\right)^3$ $\frac{M_0}{M_h} \geq 2: 1.10$ |
|  | 0.82 | $0 \leq \frac{M_0}{M_h} < 1.5: 1.25 + 0.325 \left(\frac{M_0}{M_h}\right)^2 - 0.175 \left(\frac{M_0}{M_h}\right)^4$ $\frac{M_0}{M_h} \geq 1.5: 1.10$ |

2.4.2.3. New EC3 method

The new version of Eurocode 3 [7] has a new method for the calculation of the buckling reduction factor (χ_{LT}) for H- and I- sections and fork boundary conditions at both ends. The buckling reduction factor is calculated from the following:

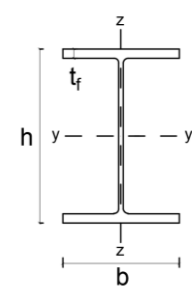
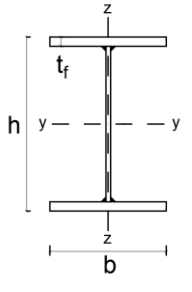
$$\chi_{LT} = \frac{f_M}{\phi_{LT} + \sqrt{\phi_{LT}^2 - f_M \bar{\lambda}_{LT}^2}} \leq 1.0 \quad (2.17)$$

$$\phi_{LT} = 0.5 \left[1 + f_M \left(\left(\frac{\bar{\lambda}_{LT}}{\bar{\lambda}_z} \right)^2 \alpha_{LT} (\bar{\lambda}_z - 0.2) + \bar{\lambda}_{LT}^2 \right) \right] \quad (2.18)$$

where α_{LT} is the imperfection factor taken from Table 2.10, $\bar{\lambda}_{LT}$ is the relative slenderness for lateral-torsional buckling, as defined in (2.12) and $\bar{\lambda}_z$ is the corresponding slenderness for weak axis flexural buckling, defined in (2.6) and (2.7) with the buckling length taken as the distance between the discrete lateral restraints.

The factor f_M takes into account the effect of the bending moment distribution between discrete lateral restraints, chosen according to Table 2.9 (it may be conservatively taken as 1.0 in cases not covered in Table 2.9).

Table 2.10 – Imperfection factor α_{LT} for lateral-torsional buckling of doubly symmetric I- and H-sections using the new EC3 method

| Cross-section | Limits | α_{LT} |
|--|--------------------------|---|
| Rolled I-sections  | $h/b > 1.2$ | $t_f \leq 40 \text{ mm}$ $0.12 \sqrt{\frac{W_{el,y}}{W_{el,z}}} \leq 0.34$ |
| | $h/b > 1.2$ | $t_f > 40 \text{ mm}$ $0.16 \sqrt{\frac{W_{el,y}}{W_{el,z}}} \leq 0.49$ |
| | $h/b \leq 1.2$ | - $0.16 \sqrt{\frac{W_{el,y}}{W_{el,z}}} \leq 0.49$ |
| Welded I-sections  | $t_f \leq 40 \text{ mm}$ | $0.21 \sqrt{\frac{W_{el,y}}{W_{el,z}}} \leq 0.64$ |
| | $t_f > 40 \text{ mm}$ | $0.25 \sqrt{\frac{W_{el,y}}{W_{el,z}}} \leq 0.76$ |

2.4.3. Design of members in bending and axial compression

The stability of members subjected to bending and axial compression is verified according to clause 6.3.3 of Eurocode 3 [1]. The design should satisfy the following interaction formulas:

$$\frac{N_{Ed}}{\chi_y N_{Rd}} + k_{yy} \frac{M_{y,Ed} + \Delta M_{y,Ed}}{\chi_{LT} M_{y,Rd}} + k_{yz} \frac{M_{z,Ed} + \Delta M_{z,Ed}}{M_{z,Rd}} \leq 1.0 \quad (2.19)$$

$$\frac{N_{Ed}}{\chi_z N_{Rd}} + k_{zy} \frac{M_{y,Ed} + \Delta M_{y,Ed}}{\chi_{LT} M_{y,Rd}} + k_{zz} \frac{M_{z,Ed} + \Delta M_{z,Ed}}{M_{z,Rd}} \leq 1.0 \quad (2.20)$$

where N_{Ed} , $M_{y,Ed}$, and $M_{z,Ed}$ are the design values of the compression force and the maximum bending moments about the y-y and z-z axis along the member, respectively. N_{Rd} , $M_{y,Rd}$, and $M_{z,Rd}$ are the design resistances and $\Delta M_{y,Ed}$ and $\Delta M_{z,Ed}$ are the moments due to shift of the centroidal axis (in case of class 4 sections).

χ_y and χ_z are the reduction factors due to flexural buckling, defined in (2.4) and χ_{LT} the reduction factor due to lateral-torsional buckling also defined in (2.10).

k_{ii} and k_{ij} are the interaction factors. Currently, there are 2 methods available in Eurocode 3 [1] to obtain the interaction factors, method 1 in Annex A and method 2 in Annex B. Nonetheless, only method 2 will be addressed (Annex B) in this document, since only this method will be adopted in the next version of the Eurocode 3 [1]. The interaction factors, according to method 2, are given in Table 2.11 for members not susceptible to lateral-torsional buckling, and Table 2.12 for members susceptible to lateral-torsional buckling.

Table 2.11 – Interaction factors k_{ij} for members not susceptible to lateral deformations (EN1993-1-1 – Table B.1)

| Interaction factors | Type of sections | Design assumptions | |
|---------------------|------------------|--|--|
| | | Elastic cross-sectional properties – class 3 and class 4 | Plastic cross-sectional properties – class 1 and class 2 |
| k_{yy} | I-sections | $C_{my}(1 + 0.6\bar{\lambda}_y n_y)$ | $C_{my}(1 + (\bar{\lambda}_y - 0.2)n_y)$ |
| | RHS-sections | $\leq C_{my}(1 + 0.6n_y)$ | $\leq C_{my}(1 + 0.8n_y)$ |
| k_{yz} | I-sections | k_{zz} | $0.6 k_{zz}$ |
| | RHS-sections | | |
| k_{zy} | I-sections | $0.8 k_{yy}$ | $0.6 k_{yy}$ |
| | RHS-sections | | |
| k_{zz} | I-sections | $C_{mz}(1 + 0.6\bar{\lambda}_z n_z)$ | $C_{mz}(1 + (2\bar{\lambda}_z - 0.6)n_z)$ |
| | RHS-sections | $\leq C_{mz}(1 + 0.6n_z)$ | $\leq C_{mz}(1 + 1.4n_z)$ |
| | | | $C_{mz}(1 + (\bar{\lambda}_z - 0.2)n_z)$ |
| | | | $\leq C_{mz}(1 + 0.8n_z)$ |

In order to simplify the equations to obtain the interaction factors, the factors n_y and n_z are introduced as follows:

$$n_y = \frac{N_{Ed}}{\chi_y N_{Rk} / \gamma_{M1}} \quad (2.21)$$



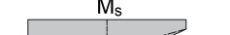
$$n_z = \frac{N_{Ed}}{\chi_z N_{Rk} / \gamma_{M1}} \quad (2.22)$$

Table 2.12 – Interaction factors k_{ij} for members susceptible to torsional deformations (EN1993-1-1 – Table B.2)

| Interaction factors | Design assumptions | |
|---------------------|--|---|
| | Elastic cross-sectional properties – class 3 and class 4 | Plastic cross-sectional properties – class 1 and class 2 |
| k_{yy} | k_{yy} from Table 2.11 | k_{yy} from Table 2.11 |
| k_{yz} | k_{yz} from Table 2.11 | k_{yz} from Table 2.11 |
| k_{zy} | $\left[1 - \frac{0.05 \bar{\lambda}_z}{(C_{mLT} - 0.25)} n_z \right]$ $\geq \left[1 - \frac{0.05}{(C_{mLT} - 0.25)} n_z \right]$ | $\left[1 - \frac{0.1 \bar{\lambda}_z}{(C_{mLT} - 0.25)} n_z \right]$ $\geq \left[1 - \frac{0.1}{(C_{mLT} - 0.25)} n_z \right]$ <p>For $\bar{\lambda}_z < 0.4$:</p> $k_{zy} = 0.6 + \bar{\lambda}_z \leq 1 - \frac{0.1 \bar{\lambda}_z}{(C_{mLT} - 0.25)} n_z$ |
| k_{zz} | k_{zz} from Table 2.11 | k_{zz} from Table 2.11 |

The equivalent uniform moment factors C_m , are selected according to Table 2.13.

Table 2.13 – Equivalent uniform moment factors C_m (EN1993-1-1 – Table B.3)

| Moment diagram | Range | C_{my} and C_{mz} and C_{mLT} | |
|---|--|--|-------------------------------------|
| | | Uniform loading | Concentrated load |
|  | $-1 \leq \psi \leq 1$ | $0.6 + 0.4\psi \geq 0.4$ | |
|  $\alpha_s = M_s/M_h$ | $0 \leq \alpha_s \leq 1$ $-1 \leq \psi \leq 1$ | $0.2 + 0.8\alpha_s \geq 0.4$ | $0.2 + 0.8\alpha_s \geq 0.4$ |
| | $-1 \leq \alpha_s < 0$ $0 \leq \psi \leq 1$ | $0.1 - 0.8\alpha_s \geq 0.4$ | $-0.8\alpha_s \geq 0.4$ |
| | $-1 \leq \alpha_s < 0$ $-1 \leq \psi < 0$ | $0.1(1 - \psi) - 0.8\alpha_s \geq 0.4$ | $0.2(-\psi) - 0.8\alpha_s \geq 0.4$ |
|  $\alpha_h = M_h/M_s$ | $0 \leq \alpha_h \leq 1$ $-1 \leq \psi \leq 1$ | $0.95 + 0.05\alpha_h$ | $0.90 + 0.10\alpha_h$ |
| | $-1 \leq \alpha_h < 0$ $0 \leq \psi \leq 1$ | $0.95 + 0.05\alpha_h$ | $0.90 + 0.10\alpha_h$ |
| | $-1 \leq \alpha_h < 0$ $-1 \leq \psi < 0$ | $0.95 + 0.05\alpha_h(1 + 2\psi)$ | $0.90 + 0.10\alpha_h(1 + 2\psi)$ |

For members with sway buckling mode the equivalent uniform moment factor should be taken $C_{my} = 0.9$ or $C_{mz} = 0.9$, respectively.

C_{my} , C_{mz} and C_{mLT} should be obtained according to the bending moment diagram between the relevant braced points.

2.4.4. Design of semi-compact sections

According to the new version of Eurocode 3 [7], the stability of members in bending or bending and axial force of semi-compact (class 3 cross-sections) doubly symmetric I- or H sections, can be done using the elasto-plastic section modulus W_{ep} , alternatively to the elastic section modulus W_{el} .

The elasto-plastic section modulus W_{ep} , is obtained using the Annex B of new version of Eurocode 3 [7], through an interpolation between the plastic section modulus and the elastic section modulus (Figure 2.5) about one principal axis of a cross-section as follows:

$$W_{ep,y} = W_{pl,y} - (W_{pl,y} - W_{el,y})\beta_{ep,y} \quad (2.23)$$

$$W_{ep,z} = W_{pl,z} - (W_{pl,z} - W_{el,z})\beta_{ep,z} \quad (2.24)$$

where the values of $\beta_{ep,y}$ and $\beta_{ep,z}$ are dependent on the material parameter ε , and the width-to-thickness ratio used for the cross-section classification.

- For I- or H sections, rolled or welded:

$$\beta_{ep,y} = \text{Max} \left(\frac{\frac{c}{t_f} - 10\varepsilon}{4\varepsilon}; \frac{\frac{c}{t_w} - 83\varepsilon}{38\varepsilon}; 0 \right) \leq 1.0 \quad (2.25)$$

$$\beta_{ep,z} = \text{Max} \left(\frac{\frac{c}{t_f} - 10\varepsilon}{6\varepsilon}; 0 \right) \leq 1.0 \quad (2.26)$$

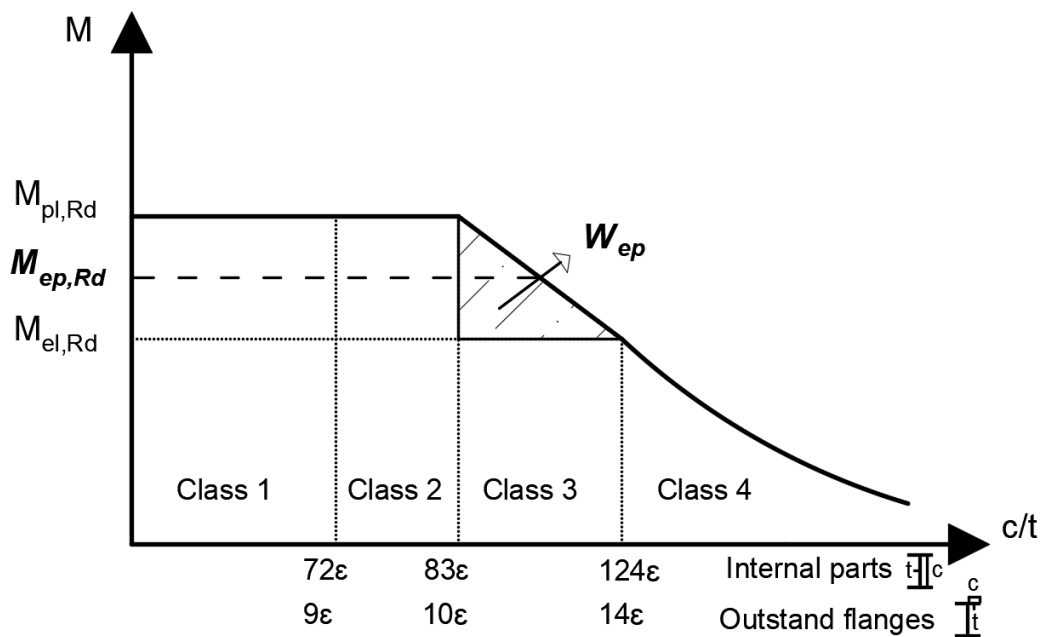


Figure 2.5 – Representation of the elasto-plastic modulus W_{ep}

3. Experimental buckling behaviour of high strength steel beams

3.1. Scope

The experimental programme was focused on the study of the lateral-torsional buckling of HSS beams. The nominal dimensions of the tested specimens are summarized in Table 3.1.

The experimental campaign comprises 12 lateral-torsional buckling tests, under constant bending moment. It includes 12 beams specimens (Figure 3.1), with different height-to-width ratios, different steel grades (S460 and S690), welded I-sections and equivalent rolled I-sections, including monosymmetric and hybrid beams (where the flanges are made of a higher steel grade than the web).

In order to acquire a complete characterization (geometrical imperfections and material properties) of the specimens, all the beams' dimensions were measured prior to the tests, through advanced laser measurements. In addition to the lateral-torsional buckling tests, tensile coupon tests for each steel plate were performed for material characterization, and residual stresses measurements for 9 specimens using the sectioning method.



Figure 3.1 – Lateral-torsional buckling specimens after testing

Table 3.1 – Experimental programme

| Type | Dimensions (mm) $h \times b_c(b_t) \times t_w \times t_f$ | Fabrication | Steel grade (Plate) | | Section Class | | |
|--------|--|-------------|---------------------|----------------|---------------|-----|---------|
| | | | Flanges | Web | Flange | Web | Overall |
| B1 | $500 \times 200(200) \times 8 \times 16$ | Welded | S460 (PL-7) | S460 (PL-6) | 1 | 2 | 2 |
| B2 | $500 \times 200(200) \times 8 \times 16$ | Welded | S690 (PL-4) | S690 (PL-3) | 2 | 3 | 3 |
| B3 | IPE 500 | Rolled | S460 | S460 | 1 | 1 | 1 |
| B4 | $310 \times 300(300) \times 8 \times 16$ | Welded | S460 (PL-7) | S460 (PL-6) | 3 | 1 | 3 |
| B5 | $310 \times 300(300) \times 8 \times 16$ | Welded | S690 (PL-4) | S690 (PL-3) | 4 | 1 | 4 |
| B6 | HE 320A | Rolled | S460 | S460 | 3 | 1 | 3 |
| B7 | $750 \times 200(200) \times 8 \times 16$ | Welded | S690 (PL-5) | S690 (PL-2) | 2 | 4 | 4 |
| B8_h | $750 \times 200(200) \times 8 \times 16$ | Welded | S690 (PL-5) | S355 (PL-1) | 2 | 4 | 4 |
| B11_m | $750 \times 200(400) \times 8 \times 16$ | Welded | S690 (PL-5) | S690 (PL-2) | 2 | 4 | 4 |
| B12_mh | $750 \times 200(400) \times 8 \times 16$ | Welded | S690 (PL-5) | S355 (PL-1) | 2 | 4 | 4 |
| B13_m | $750 \times 200(400) \times 8 \times 16$ | Welded | S460 (PL-7) | S460 (PL-6) | 1 | 4 | 4 |
| B14_mh | $750 \times 200(400) \times 8 \times 16$ | Welded | S460 (PL-7) | S355 (PL-1) | 1 | 4 | 4 |

m – monosymmetric beam; h – hybrid beam (flange with higher steel grade than web)

All the above specimens have a total length of 6.0 m

3.2. Tensile coupon tests on high strength steel

The characterisation of the material properties of the high strength steel plates were carried out through tensile coupon tests. The tests were performed according to ISO-6892-1: Metallic materials – Tensile testing – Part 1: Method of test at room temperature [65], where three specimens were taken parallel to the rolling direction from each plate. The tests were carried out at room temperature.

The specimen geometry for 8 mm and 16 mm plates is presented in Figure 3.2 and Figure 3.3, respectively.

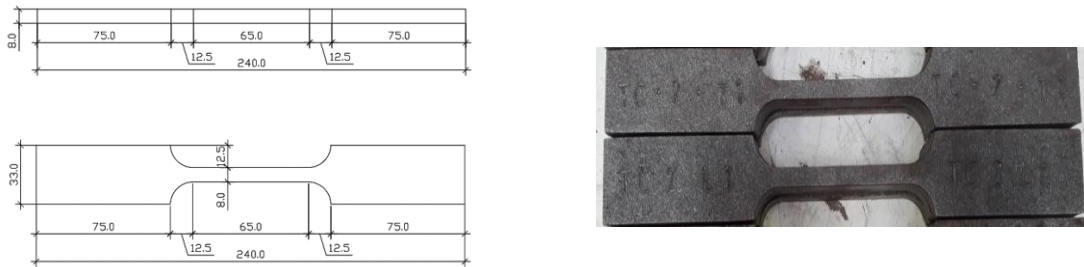


Figure 3.2 – Coupons for 8mm thickness plate

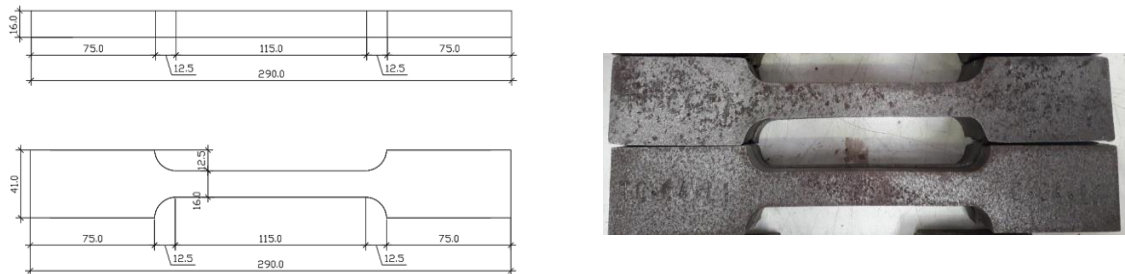


Figure 3.3 – Coupons for 16mm thickness plate

3.3. Residual stresses measurements on high strength steel beams

In order to understand the magnitude and distribution of the residual stresses in high strength steel members, 9 residual stresses measurements were performed on rolled and welded HSS sections, including different steel grades (S355, S460 and S690), homogenous and hybrid beams (Figure 3.4).

So as to avoid differences between the buckling test specimen and the residual stress specimen, the specimens were fabricated with an initial length of $L1+L2$ (Figure 3.5), where $L1$ is the length of the buckling tests specimen and $L2$ is the length of the residual stress test specimen, thus allowing for the estimation of the residual stress distribution in the buckling test specimen.



Figure 3.4 – Residual stresses specimens after testing

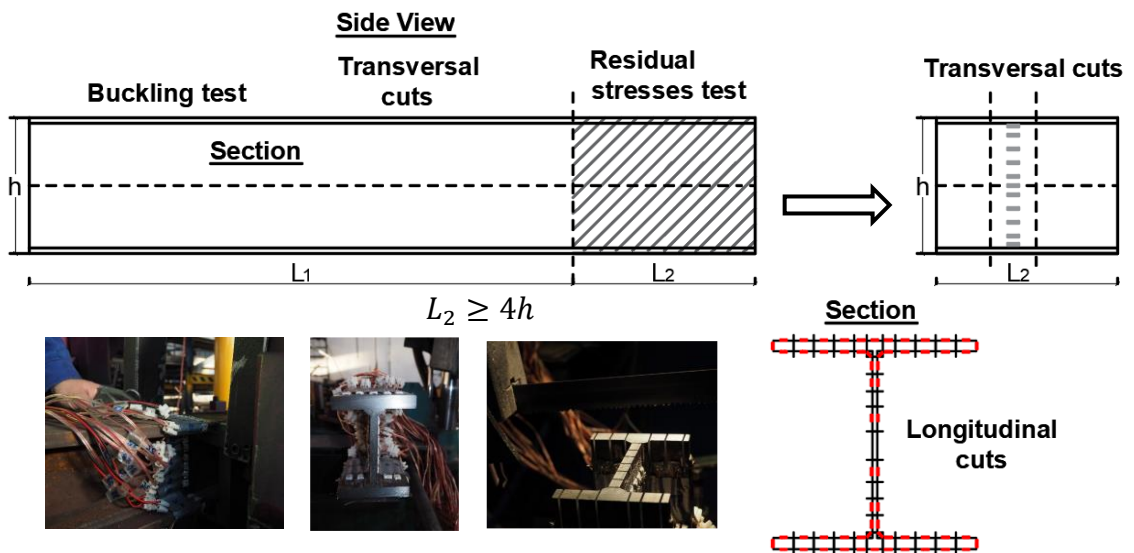


Figure 3.5 – Residual stresses specimens

The residual stresses were measured using the sectioning method [66], which consists in longitudinal and transversal cuts that provoke the release of the stresses locked in the specimens. The stress releases cause deformations recorded by the strain gauges during the experiment. The measurements are then converted into stresses using Hooke's law. For reasons of simplification, it is assumed that the transverse stresses in the specimen are negligible.

The tested specimens, as well as the number of strain gauges used, number of cuts performed and also the length of the specimens (L2 in Figure 3.5), are presented in Table 3.2. The geometry of the tested specimens corresponds to the buckling tests from Table 3.1.

The strain gauges used in the specimen's instrumentation are electrical strain gauges (2 x 6mm) manufactured by Tokyo Sokki Kenkyujo Co. Ltd. The strain gauges were glued on both sides of the flanges and web for each specimen in order to obtain the average membrane stress. The instrumentation used, and the cuts performed for each test specimen are presented in Figure 3.6.

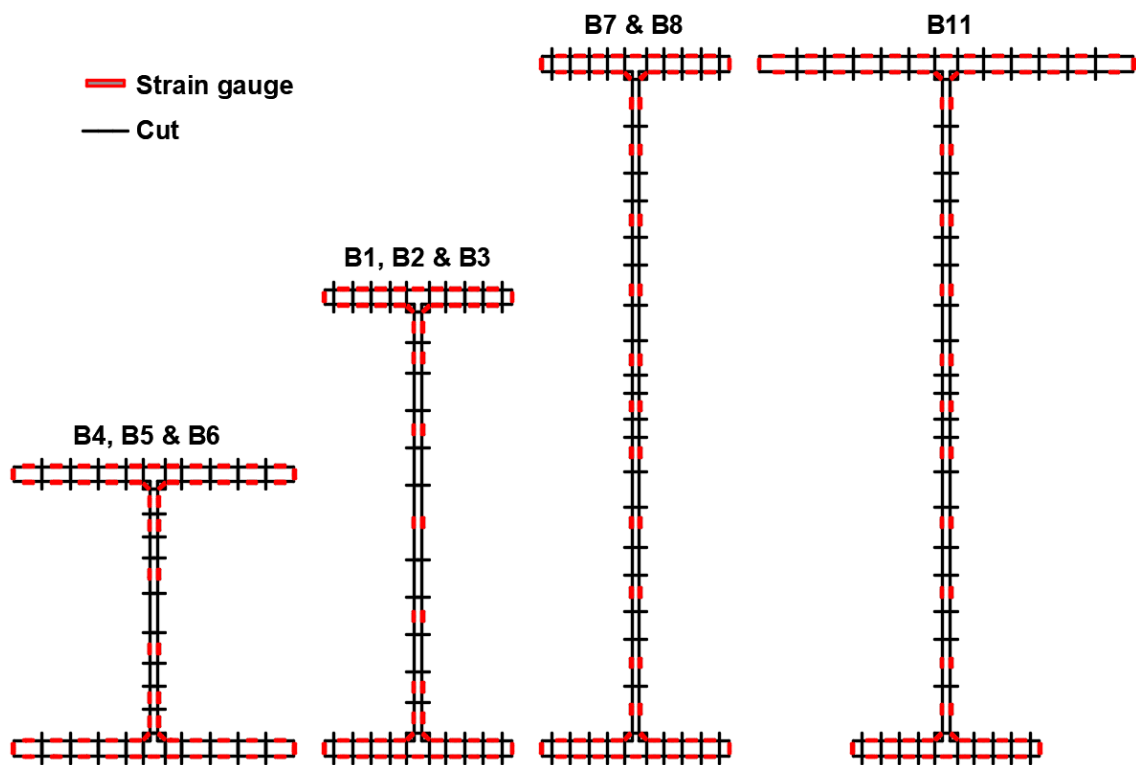


Figure 3.6 – Strain gauges instrumentation

Table 3.2 – Residual stresses measurements – experimental programme

| Type | Member $h \times b \times t_w \times t_f$ | Fabri- cation | Length (m) | Steel grade | | No. of strain gauges | No. of cuts* |
|-------|--|------------------|---------------|-------------|-------|----------------------------|-----------------|
| | | | | Flanges | Web | | |
| B1 | 500 x 200 x 8 x 16 | Welded | 3.0 | S 460 | S 460 | 56 | 24 |
| B2 | 500 x 200 x 8 x 16 | Welded | 3.0 | S 690 | S 690 | 56 | 24 |
| B3 | IPE 500 | Rolled | 3.0 | S 460 | S 460 | 56 | 24 |
| B4 | 310 x 300 x 8 x 16 | Welded | 2.0 | S 460 | S 460 | 62 | 22 |
| B5 | 310 x 300 x 8 x 16 | Welded | 2.0 | S 690 | S 690 | 62 | 22 |
| B6 | HE 320 A | Rolled | 2.0 | S 460 | S 460 | 62 | 22 |
| B7 | 750 x 200 x 8 x 16 | Welded | 3.0 | S 690 | S 690 | 64 | 32 |
| B8_h | 750 x 200 x 8 x 16 | Welded | 3.0 | S 690 | S 355 | 64 | 32 |
| B11_m | 750 x 200(400) x 8 x 16 | Welded | 3.0 | S 690 | S 690 | 72 | 35 |

*No. of cuts: The first 2 cuts are always transversal cuts, and the remaining are longitudinal cuts.

3.4. Geometrical imperfections measurements

The geometrical dimensions of the test specimens were measured prior to the lateral-torsional buckling tests for each member. The imperfections were measured using the advanced system “MetraSCAN 3D™”, as represented in Figure 3.7. This measurement procedure results in a cloud of points that describes the real geometry of the element (specimen).

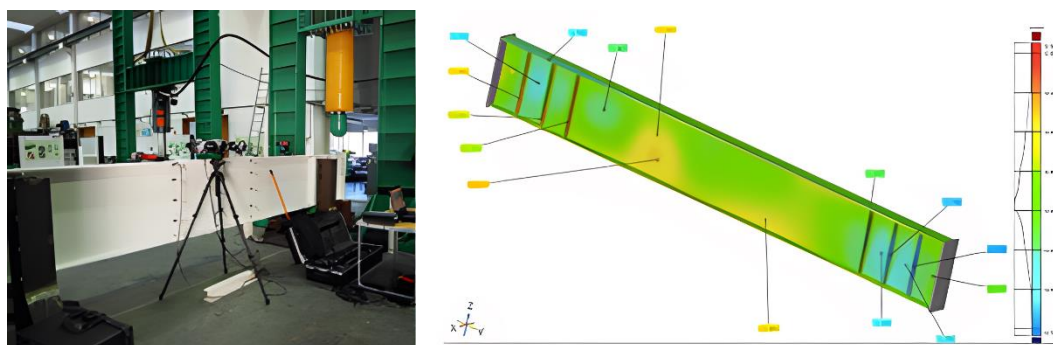


Figure 3.7 – Geometrical imperfections measurements

3.5. Full-scale tests on lateral-torsional buckling

The lateral-torsional buckling tests were performed using the same test configuration, as represented in Figure 3.8, and according to the test set-up presented in Figure 3.9. A four-point bending moment test was carried out with simply supported conditions at the extremities, under constant bending moment in the central four meters of the beam.

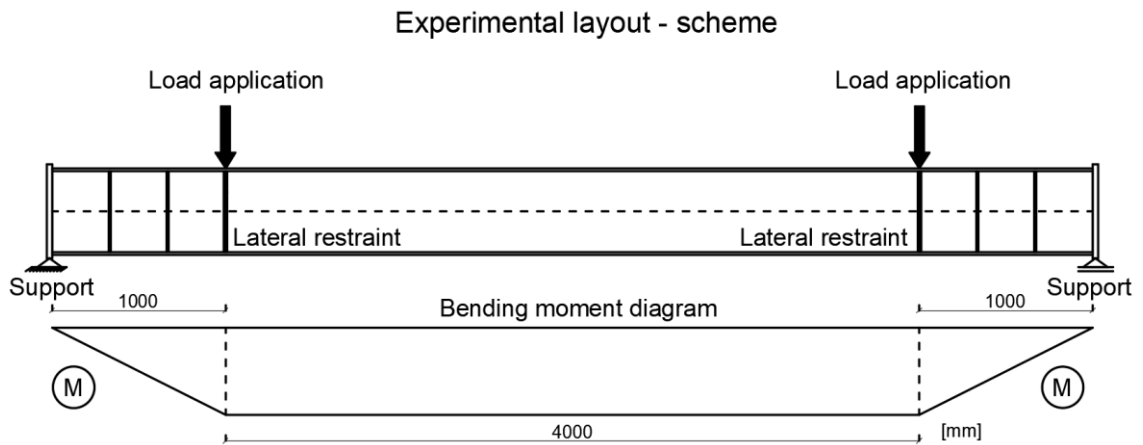


Figure 3.8 – Representative scheme of the experimental layout

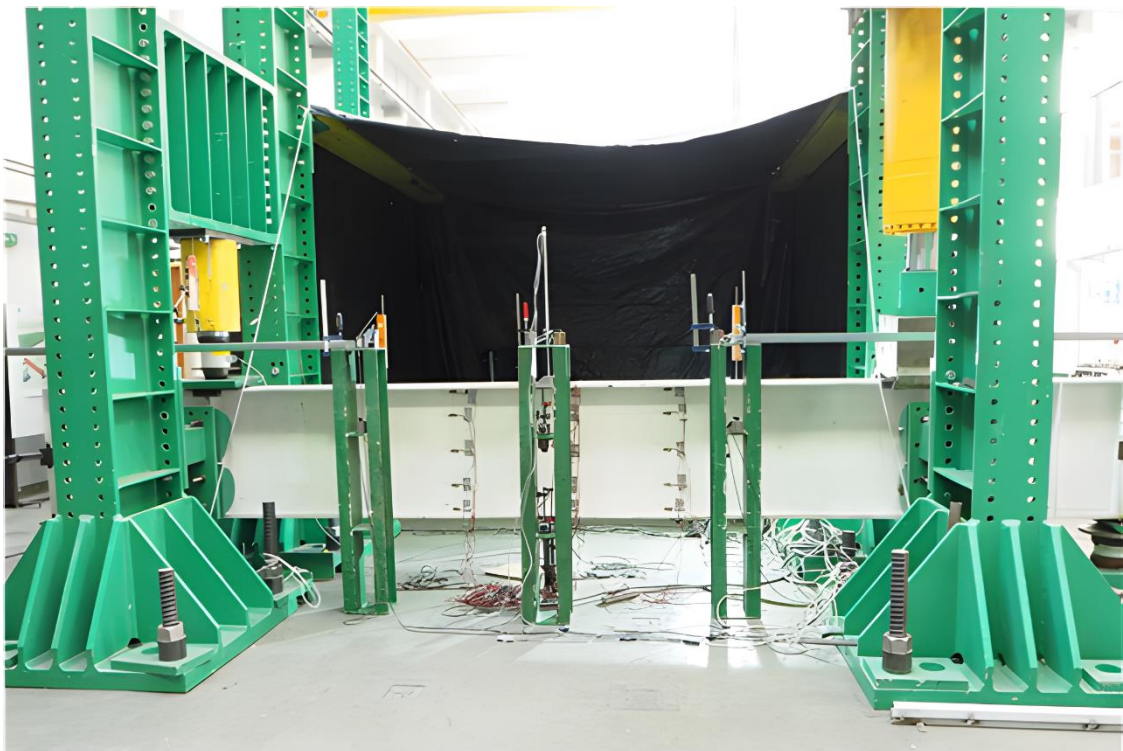


Figure 3.9 – Lateral-torsional buckling tests – experimental layout

The specimens (beams) had an overall length of 6m with the cross-section dimensions presented in Table 3.1.

Even though the experimental layout model is the same for all the 12 lateral-torsional buckling tests, some slight changes in the instrumentation and position of the lateral restrains need to be made according to the geometry of the beams. Then, the experimental tests were performed divided into groups according to the cross-section geometry of the specimens:

- Specimens B1, B2 and B3 – experimental layout and instrumentation according to Figure 3.10;
- Specimens B4, B5 and B6 – experimental layout and instrumentation according to Figure 3.11;
- Specimens B7 and B8 – experimental layout and instrumentation according to Figure 3.12;
- Specimens B11, B12, B13 and B14 – experimental layout and instrumentation according to Figure 3.13.

The beams were supported at the extremities, in axes A and G, as shown in the experimental layouts, Figure 3.10 to Figure 3.13.

The load was applied using a hydraulic jack with 3000 kN capacity on one side, and a hydraulic jack with 6000 kN capacity on the other side, at axes B and F, 1m apart from the supports (Figure 3.14). The loading was applied through displacement control at a low displacement speed of 0.01mm/s.

At the points of load application, the beams were laterally restrained and thus, in the middle region, between axes B and F, the beams were subjected to constant bending moment. For specimens B1 to B6, a steel member was welded to the stiffeners plates, allowing for a complete lateral restraint, as represented in sections B and F in Figure 3.10 and Figure 3.11. For specimens B7, B8, and B11 to B14, the lateral restrains were directly in touch with the stiffeners plates, as shown in sections B and F from Figure 3.12 and Figure 3.13.

The vertical and horizontal displacements were measured during the experiments using LVDTs (linear variable differential transformer), installed at several locations along the beams.

The vertical displacements were monitored at each point of load application, LVDT's V1 and V6 (axes B and F). At mid-span (axis D), the vertical displacements were measured at the extremities of each flange, V2 and V3 at the bottom flange, and V4 and V5 at the top flange (as represented in section D - Figure 3.10 to Figure 3.13). Two additional LVDT's, V9 and V10 were used to measure the vertical displacements at the top flange in axes C and E (1m apart from the mid-span).

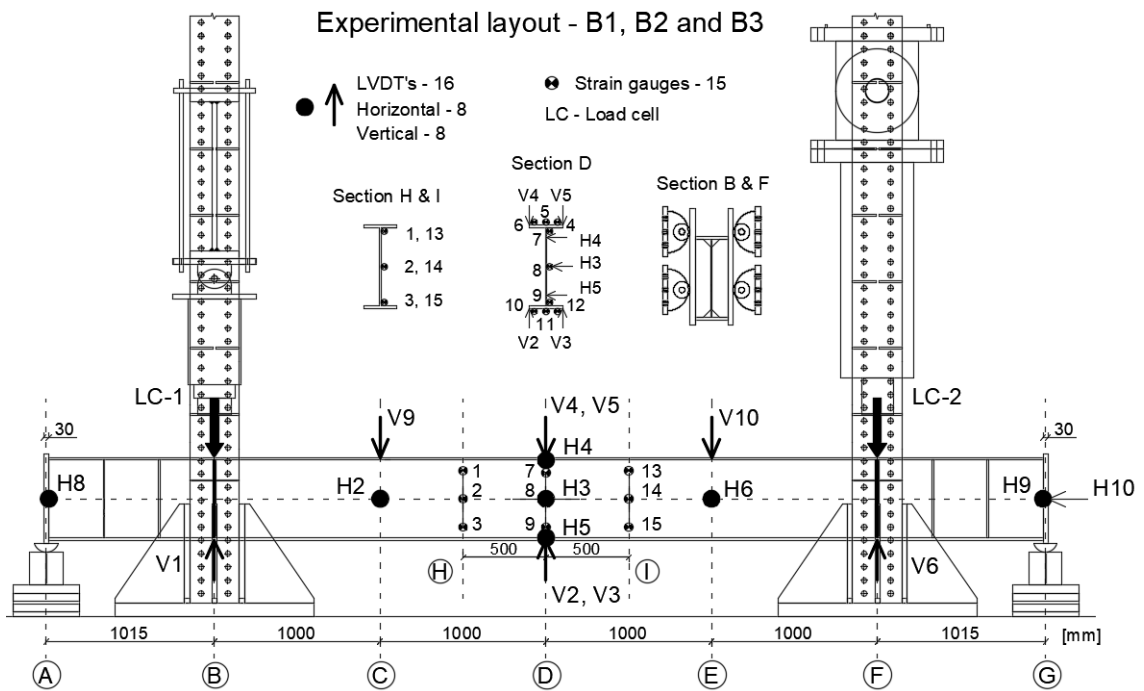


Figure 3.10 – Experimental layout and instrumentation – tests B1, B2 and B3

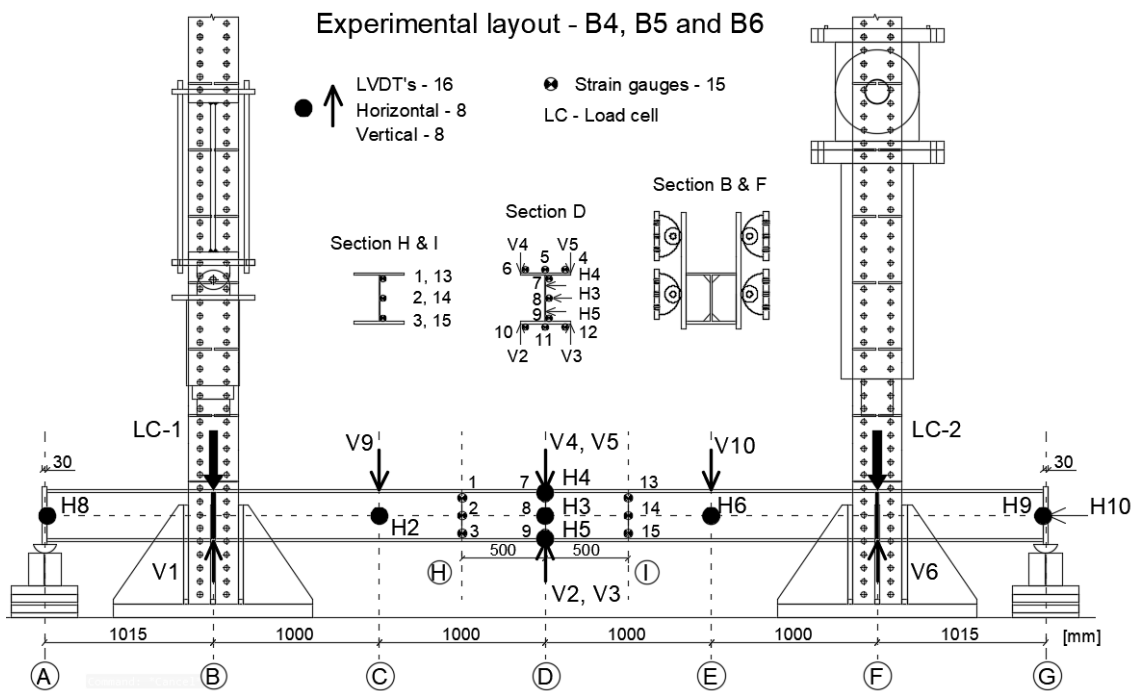


Figure 3.11 - Experimental layout and instrumentation – tests B4, B5 and B6

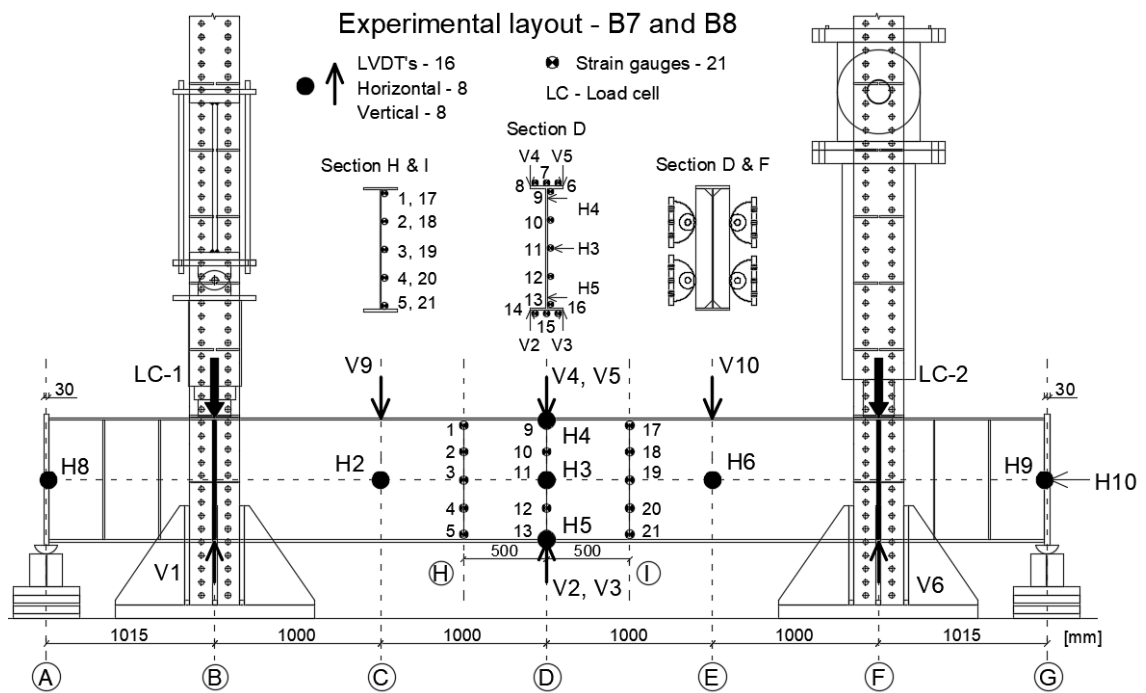


Figure 3.12 – Experimental layout and instrumentation – tests B7 and B8

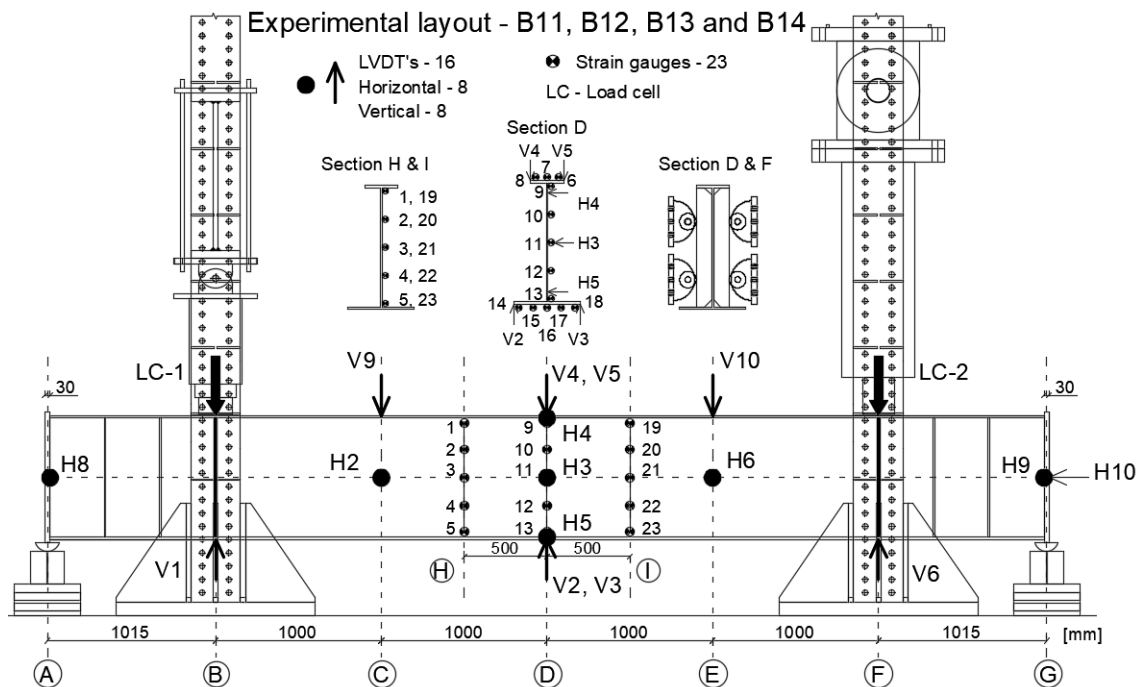


Figure 3.13 – Experimental layout and instrumentation – tests B11, B12, B13 and B14

The horizontal (out-of-plane) displacements were recorded at mid span, axis D, in three different locations, at top of the web (H4), in the middle of the web (H3), and at the bottom of the web (H5). Additionally, the horizontal displacements were also measured 1m apart from the mid-span at axes C and E (H2 and H6) and also at the supports, H8 and H9 (axes A and G). The longitudinal displacement was measured in axis G through LVDT H10.

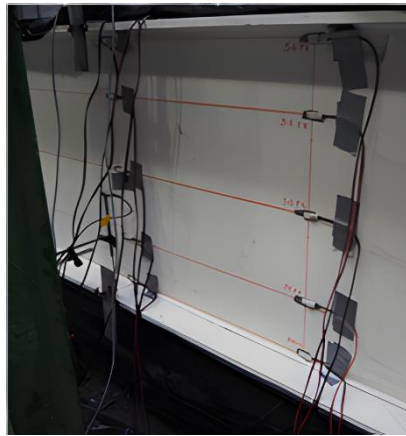
The strains were measured using electrical strain gauges (same as for residual stress measurements), glued to the web and flanges at mid-span (axis D), and to the web at axis H and I (0.5m apart from mid-section). For specimens B1 to B6, 3 strain gauges were glued to the web and 3 to the flange, SG1 to SG3 in section H and SG13 to SG15 in section I and SG4 to SG12 in section D, as shown in Figure 3.10 and Figure 3.11. For specimens B7 and B8, 3 strain gauges were glued to the flange and 5 to the web, SG1 to SG5 in section H and SG17 to SG21 in section I and SG6 to SG16 in section D (Figure 3.12). Finally, for specimens B11 to B14, 5 strain gauges were glued to the web, 3 at the top flange and 5 at the bottom flange, SG1 to SG5 in section H and SG19 to SG23 in section I and SG6 to SG18 in section D (Figure 3.13). The strain gauges were glued only on one side of the web, since on the other side, a Digital Image Correlation system was used for the middle 2m of the beams, in order to acquire full strain distribution map for this region, during the test (Figure 3.15).

The supports at the extremities consist in a half-cylinder welded to the beam end plate, allowing for free in-plane rotation, as shown in Figure 3.16. Below the half-cylinder, a load cell was placed to measure the vertical reaction (in order to confirm the applied load).

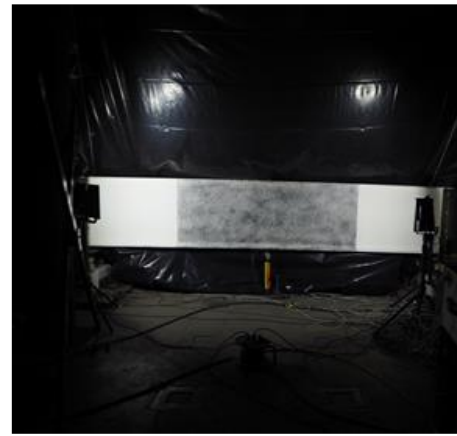
The lateral restraints at the point of load application consisted in two sets of rollers applied at each side of the beam, allowing for free vertical displacements and restraining lateral movements (Figure 3.17).



Figure 3.14 – Experimental layout - load application



a) Strain gauges



b) Digital image correlation

Figure 3.15 – Measurement of strains



Figure 3.16 – Experimental layout – supports



Figure 3.17 – Experimental layout – lateral restraints

3.6. Experimental results

3.6.1. Tensile coupon tests

The stress-strain curves recorded during the tensile coupon tests, where for each plate 3 testes were made (except for plate PL-6, where 3 more additional tests were made), are presented in Figure 3.18 to Figure 3.20.

The values of the yield stress (f_y) and ultimate strength (f_u), are taken as the upper yield strength (R_{eH}), and ultimate tensile strength (R_m), respectively.

The material properties, modulus of elasticity (E), upper yield strength (R_{eH}), ultimate tensile strength (R_m), and ultimate strain (ϵ_u), are based on the average values from all the tests performed for each plate. The results are summarized in Table 3.3.

Additionally, the ratios between the nominal and measured values of the yield stress for the plate material specimens are also presented (Table 3.3). It is noted that the material overstrength of approximately 12% is present in all the steel plates considered.

Table 3.3 – Tensile coupon tests: material properties

| Plate name / Thickness | Steel Grade | Modulus of elasticity E [GPa] | Upper yield strength R_{eH} [MPa] | Ultimate tensile strength R_m [MPa] | Ultimate strain ϵ_u [%] | Ratio $\frac{R_{eH}}{f_{y,nom}}$ |
|------------------------|-------------|------------------------------------|--|--|-------------------------------------|-------------------------------------|
| PL-1 / 8mm | S355J2+N | 202.6 | 425.5 | 634.7 | 12.2 | 1.20 |
| PL-2 / 8mm | S690QL | 200.4 | 755.3 | 813.0 | 6.2 | 1.09 |
| PL-3 / 8mm | S690QL | 203.8 | 792.2 | 818.0 | 6.0 | 1.15 |
| PL-4 / 8mm | S690QL | 205.6 | 781.7 | 846.7 | 5.6 | 1.13 |
| PL-5 / 16mm | S690QL | 204.0 | 798.4 | 854.8 | 5.9 | 1.16 |
| PL-6 / 8mm | S460NL | 212.5 | 528.8 | 639.2 | 11.0 | 1.15 |
| PL-7 / 16mm | S460NL | 201.1 | 498.9 | 656.2 | 9.4 | 1.08 |
| B3-W / 10.2mm | S460 | 210.5 | 519.8 | 581.9 | 12.8 | 1.13 |
| B3-F / 16mm | S460 | 197.5 | 508.3 | 592.5 | 13.4 | 1.11 |
| B6-W / 9mm | S460 | 218.7 | 521.6 | 622.9 | 10.6 | 1.13 |
| B6-F / 15.5mm | S460 | 215.2 | 508.2 | 569.2 | 13.7 | 1.10 |

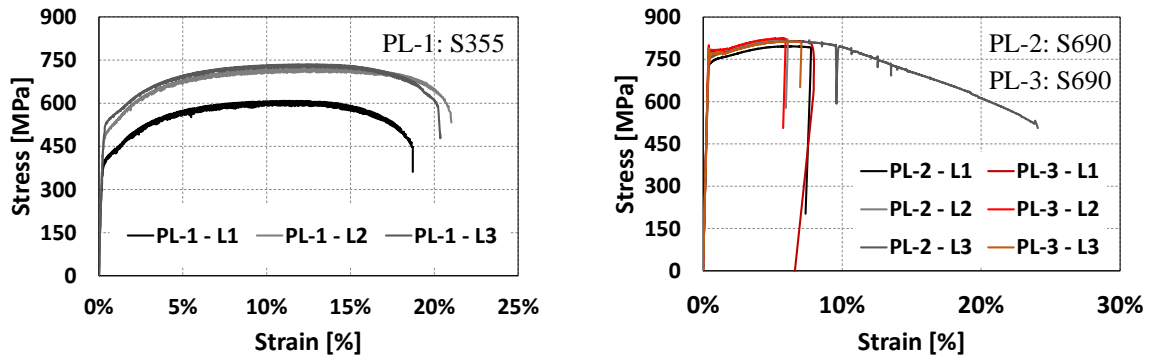


Figure 3.18 – Tensile coupon tests results – Plates 1, 2 and 3

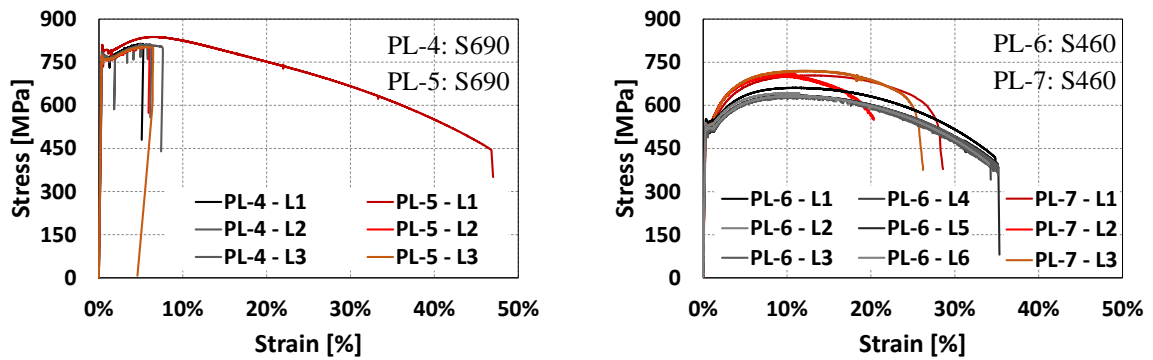


Figure 3.19 – Tensile coupon tests results – Plates 4, 5, 6 and 7

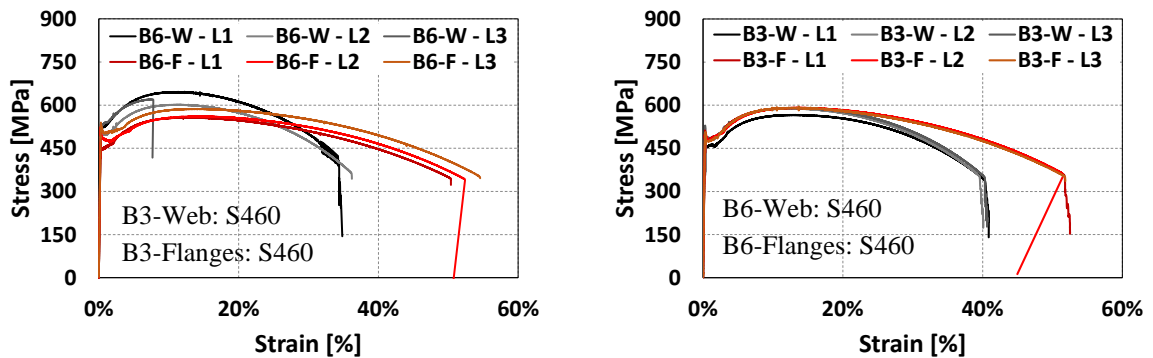


Figure 3.20 – Tensile coupon tests results – Hot-rolled profiles

It is important to note that, for plate PL-7, additional tensile coupon tests were performed, in which the exact data of the stress-strain curves were not provided, nonetheless, to obtain the average values for the material properties, these tests were considered. Due to this fact, there is a noticeable difference in the values presented in Table 3.3 for plate PL-7, and the plotted stress-strain curves in Figure 3.19.

3.6.2. Residual stresses measurements

The obtained residual stresses measurements at both sides of the specimens (distributions represented as in and out), are presented according to the cross-section geometry for the welded sections, (i) Figure 3.21 for specimens B1 and B2, (ii) Figure 3.22 for specimens B4 and B5, (iii) Figure 3.23 for specimens B7 and B8, and (iv) Figure 3.24 for specimen B11. The distributions for the rolled sections, B3 and B6 are given in Figure 3.25. The distributions referred to as “mid” are based on the average from the in and out values; the plotted values (in bold) refer to the values from the mid distribution, since it is the distribution of main interest.

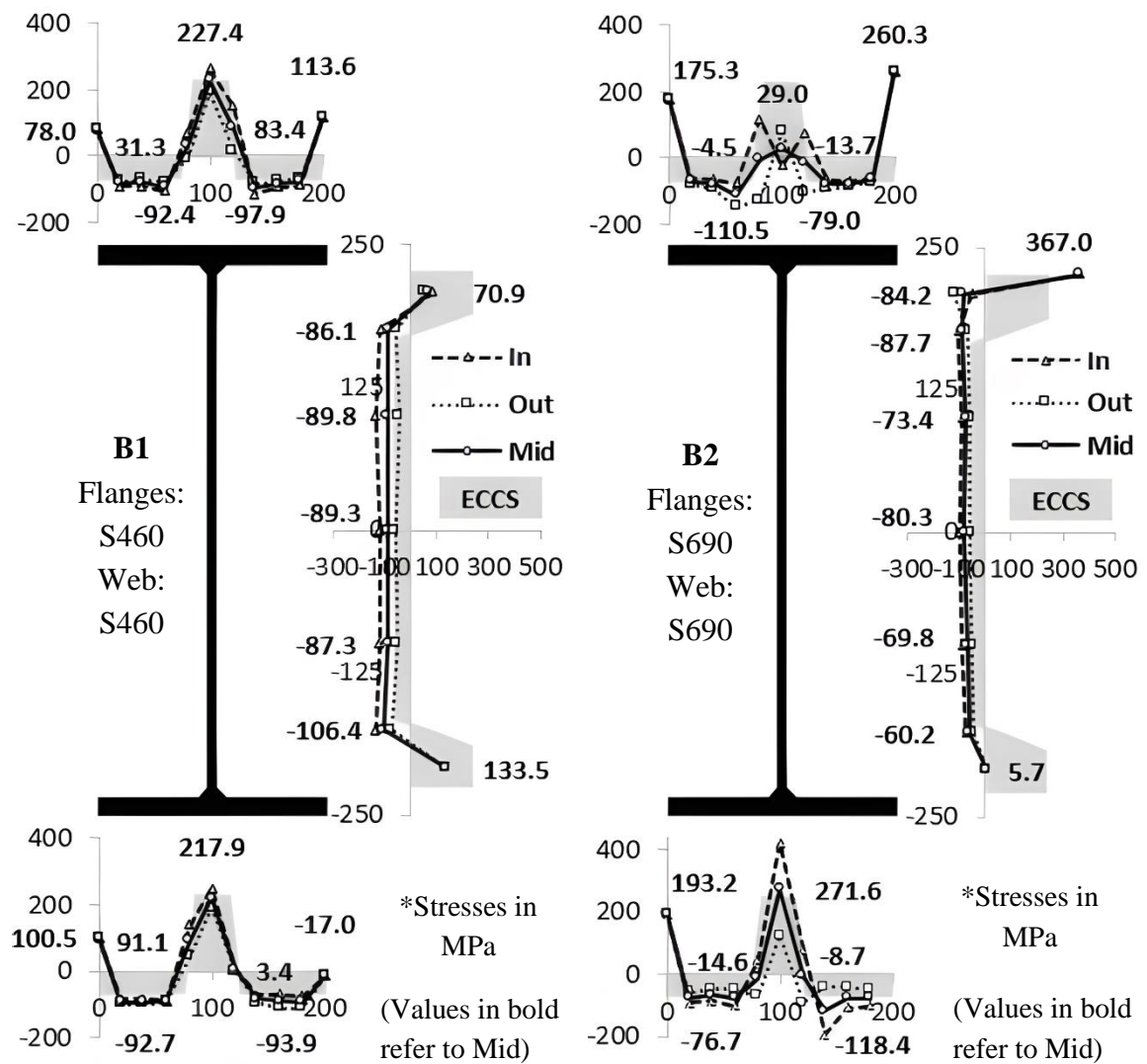


Figure 3.21 – Residual stresses distributions for welded sections B1 and B2

The stresses values refer to the recorded values at the end of the experiments, approximately 15/20 minutes after the last cut, as long as no further variations in the readings were observed.

Since the data were recorded during the entire experiment, it was also noted that the transverse cuts (first two cuts) were the main contribution to the final residual stress value. After the first two (transversal) cuts, the variations in the recordings are slight.

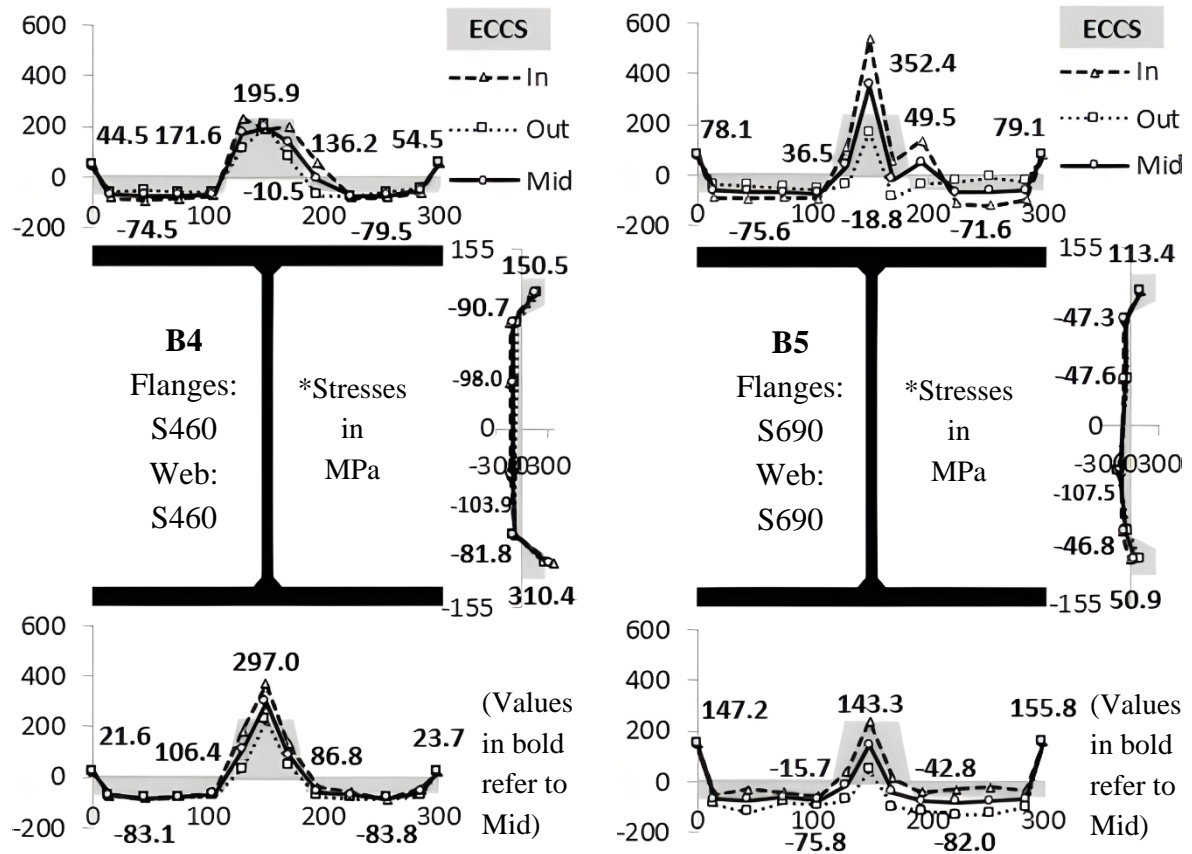


Figure 3.22 – Residual stresses distributions for welded sections B4 and B5

Furthermore, together with the residual stresses measurements, the residual stresses distributions recommended by ECCS [24] (presented in Section 2.2) are plotted (grey shading). It is noted that the ECCS recommended patterns closely follow the experimental patterns, both for the welded and rolled sections, with the main difference, in the case of the welded sections, being the presence of tensile residual stresses at the tips of the flanges due to the flame cutting procedure of the plates' specimens, which is not accounted for in the ECCS pattern. Moreover, there are also some differences in the extreme values, since the ECCS distribution is limited to the value $f_y = 235 \text{ MPa}$.

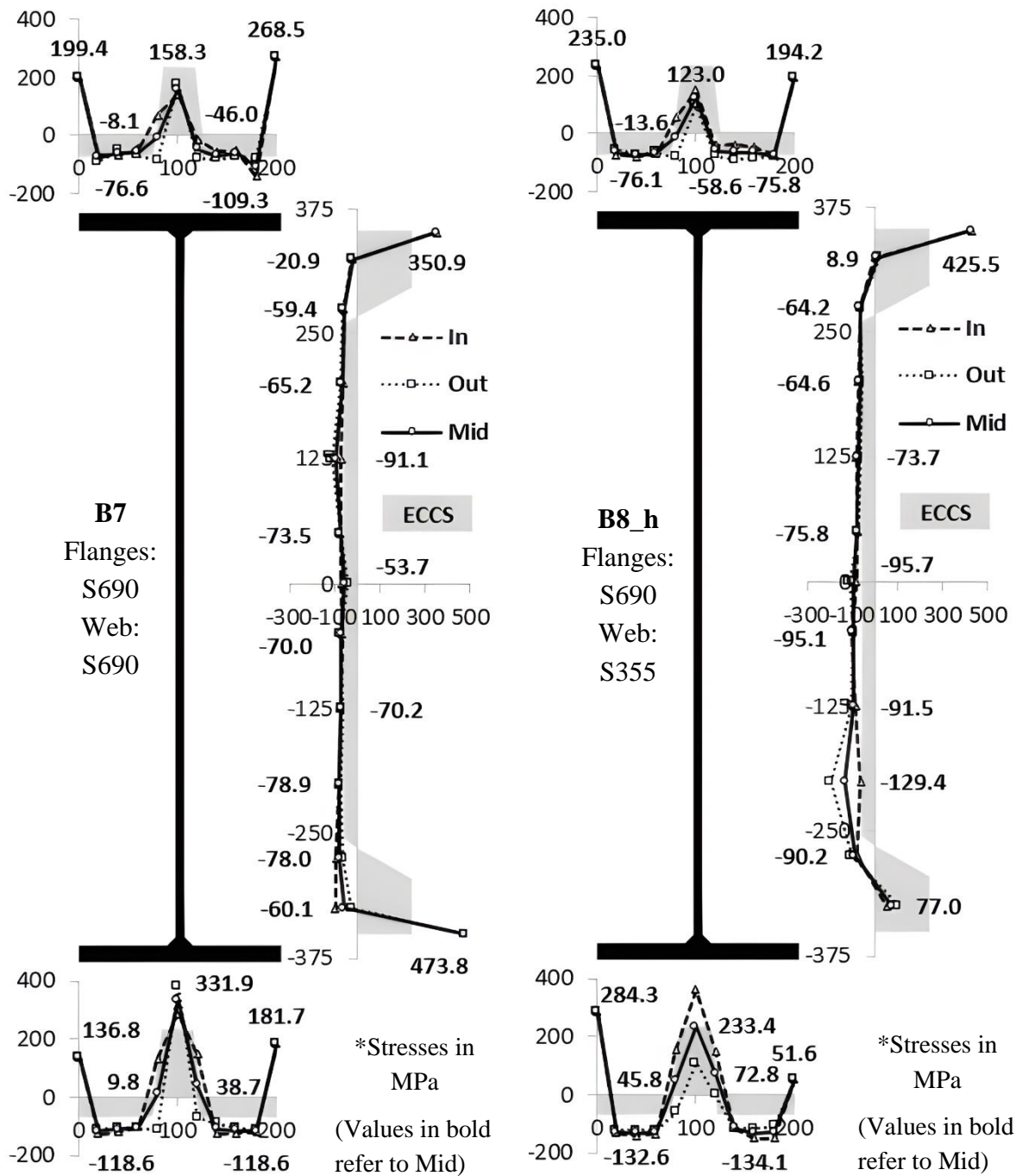


Figure 3.23 – Residual stresses distributions for welded sections B7 and B8

Analysing the residual stresses distributions of the specimens with the same welded cross-section, B1 and B2 in Figure 3.21, B4 and B5 in Figure 3.22, and B7 and B8 in Figure 3.23, it is observed that the distributions and magnitudes of the residual stresses are very similar between the sections with the same dimensions, even though they are built with different steel grades. Furthermore, comparing the residual stresses distributions in the flanges from B1 and

B2 with B4 and B5, it is observed that the average compression in the flanges is lower in specimens B4 and B5 (average 78.2 MPa) than B1 and B2 (average 95.2), due to the higher width of the flange cross-section (higher compression width). Therefore, it is observed that the effect of the geometry on the distributions/magnitude of the residual stresses has a higher impact than the steel grade.

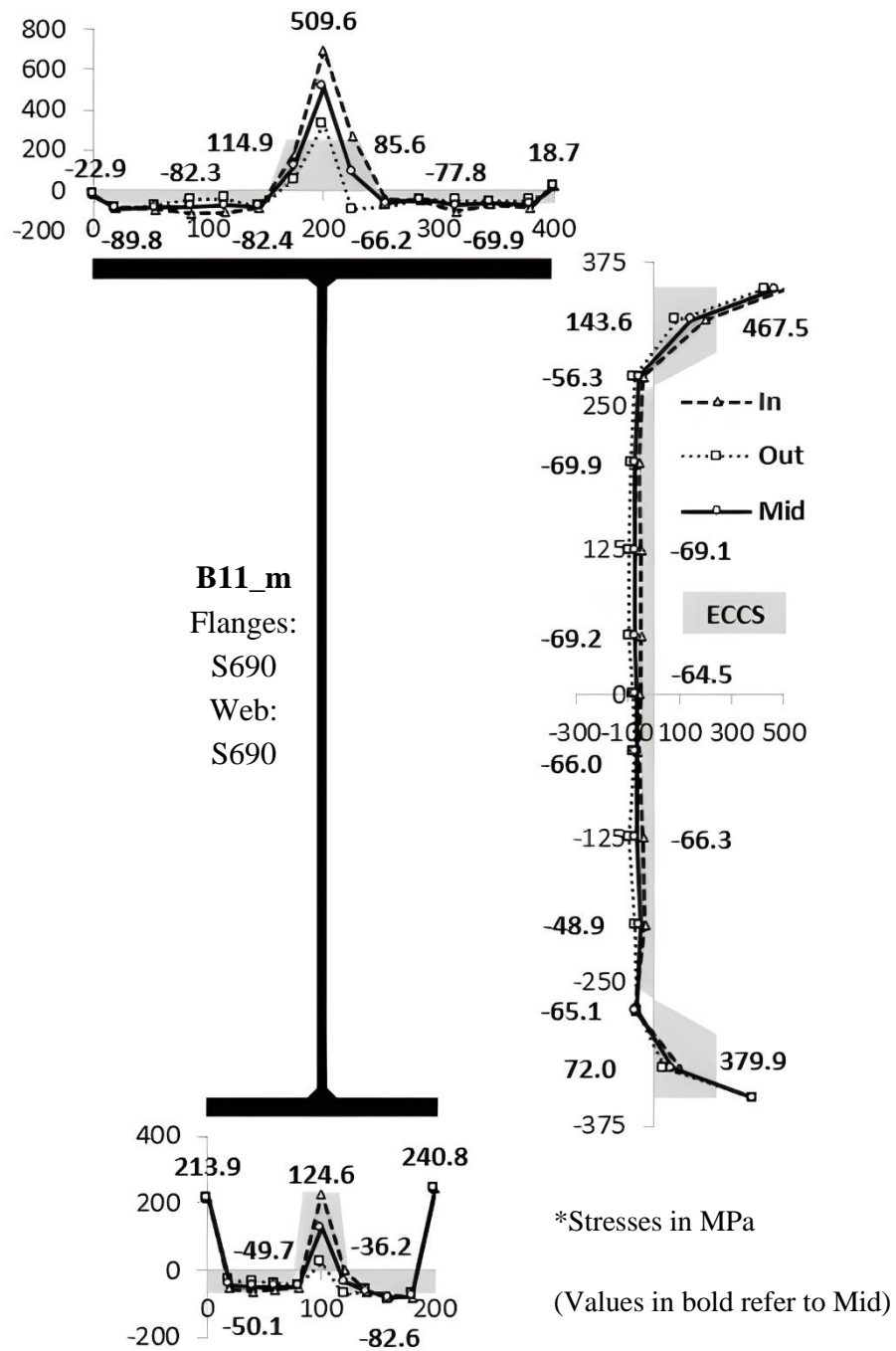


Figure 3.24 – Residual stresses distributions for welded section B11

Further analysing the main data of interest, such as the flange tip tension, flange tension, flange compression, web compression and web tension, the statistical parameters for those specific parts of the cross-section were evaluated. The results are summarized in Table 3.4.

The compressive residual stresses, both for the web and flanges, were obtained as an average for the unit length per outstand flange or total web (an equivalent rectangle with the same compression or tension area obtained in the experimental measurements), whereas, the tensile stresses (web and flanges) were always considered as the maximum values of the mid distribution.

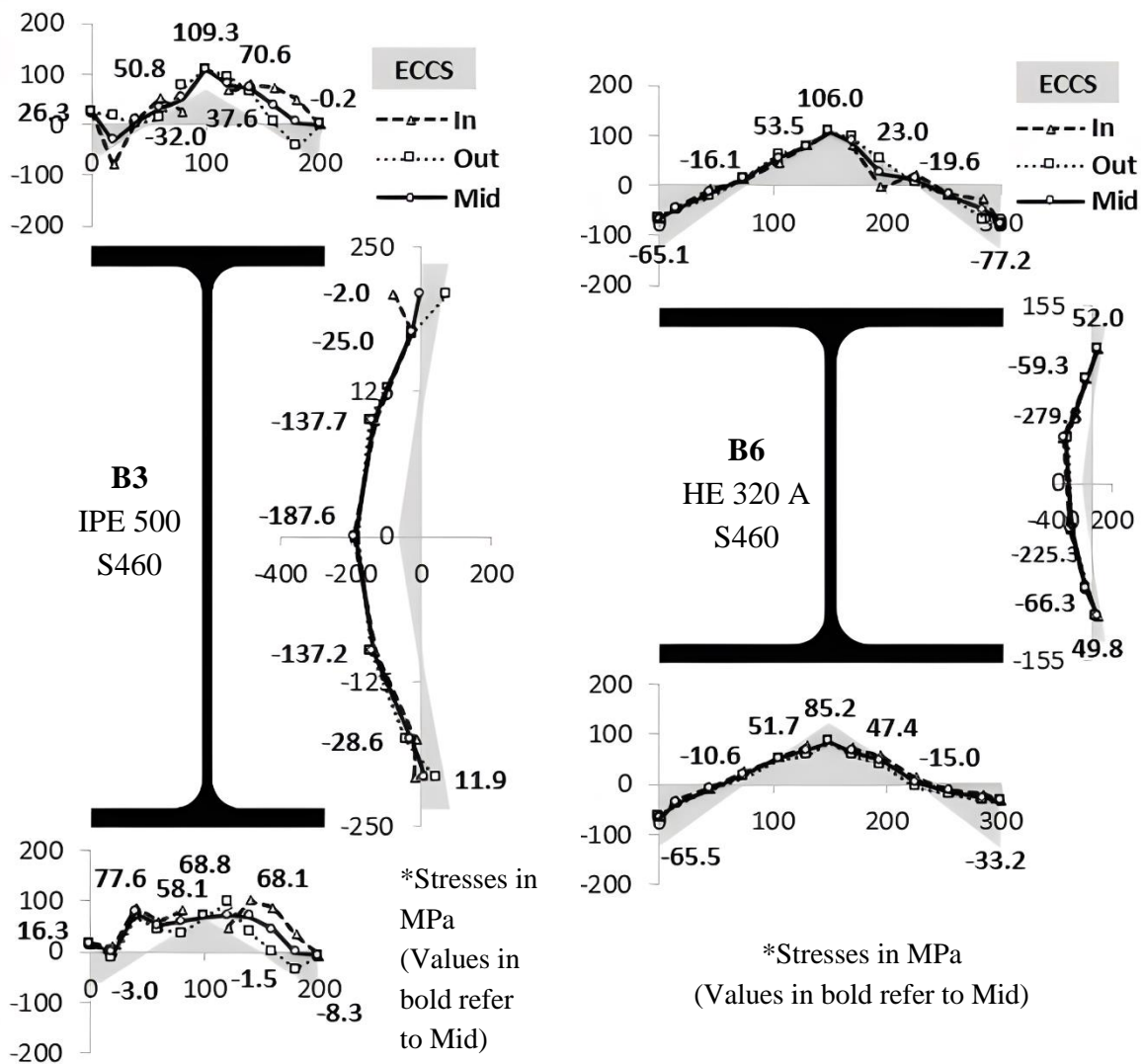


Figure 3.25 – Residual stresses distributions for hot-rolled sections B3 and B6

The mean values obtained for the tensile residual stresses measured at the flanges (flange tension – 229.68 MPa) are close to the ECCS recommendation for maximum tension at the flanges (235 MPa). The average compressive residual stresses in the flanges (-68.79 MPa) were found to be higher than the ECCS recommended values (-58.75 MPa). However, this is accounted to the presence of tensile residual stresses at the tips of the flanges and thus leading to the need for higher compressive residual stresses to achieve equilibrium. In the case of the average values for the web compression, the average value (-75.62 MPa) is also slightly higher than the ECCS recommendation (-58.75 MPa), which makes the average web tension values (410.76 MPa) higher than the ECCS, since the equilibrium condition remains. Nonetheless, the number of samples of the web tension is reduced, as during the experiments it was hard for some specimens not to damage the strain gauge in the weld zone, as a cut near the weld zone was also performed.

Table 3.4 – Statistical parameters for residual stresses measurements on welded sections

| | [MPa] | Flange tip tension | Flange Compression | Flange Tension | Web Compression | Web Tension |
|-------------|----------|-----------------------|-----------------------|-------------------|--------------------|----------------|
| All | Mean | 130.01 | -68.79 | 229.68 | -75.62 | 410.76 |
| | St. Dev. | 91.51 | 14.56 | 119.84 | 11.71 | 52.66 |
| | c.o.v | 70% | 21% | 52% | 15% | 13% |
| | Min | -22.88 | -108.13 | 29.02 | -92.90 | 350.88 |
| | Max | 284.26 | -45.66 | 509.57 | -62.03 | 473.79 |
| | n | 27 | 28 | 14 | 7 | 6 |
| S690 | Mean | 162.68 | -69.08 | 227.73 | -66.96 | 407.81 |
| | St. Dev. | 86.88 | 17.00 | 141.75 | 4.49 | 58.31 |
| | c.o.v | 53% | 25% | 62% | 7% | 14% |
| | Min | -22.88 | -108.13 | 29.02 | -72.03 | 350.88 |
| | Max | 284.26 | -45.66 | 509.57 | -62.03 | 473.79 |
| | n | 19 | 20 | 10 | 4 | 5 |
| S460 | Mean | 52.40 | -68.08 | 234.55 | -89.83 | - |
| | St. Dev. | 43.69 | 5.65 | 43.69 | 4.34 | - |
| | c.o.v | 83% | 8% | 19% | 5% | - |
| | Min | -16.99 | -77.09 | 195.87 | -92.90 | - |
| | Max | 113.56 | -57.99 | 297.01 | -86.76 | - |
| | n | 8 | 8 | 4 | 2 | 0 |

Finally, the measurements were converted into non-dimensional values, where the stress distribution for each section was normalized to the yield stress obtained from the tensile coupon tests (presented in Table 3.3). The normalized residual stress distributions are presented in Figure 3.26 for the welded sections divided by steel grade and in Figure 3.27 for the rolled sections.

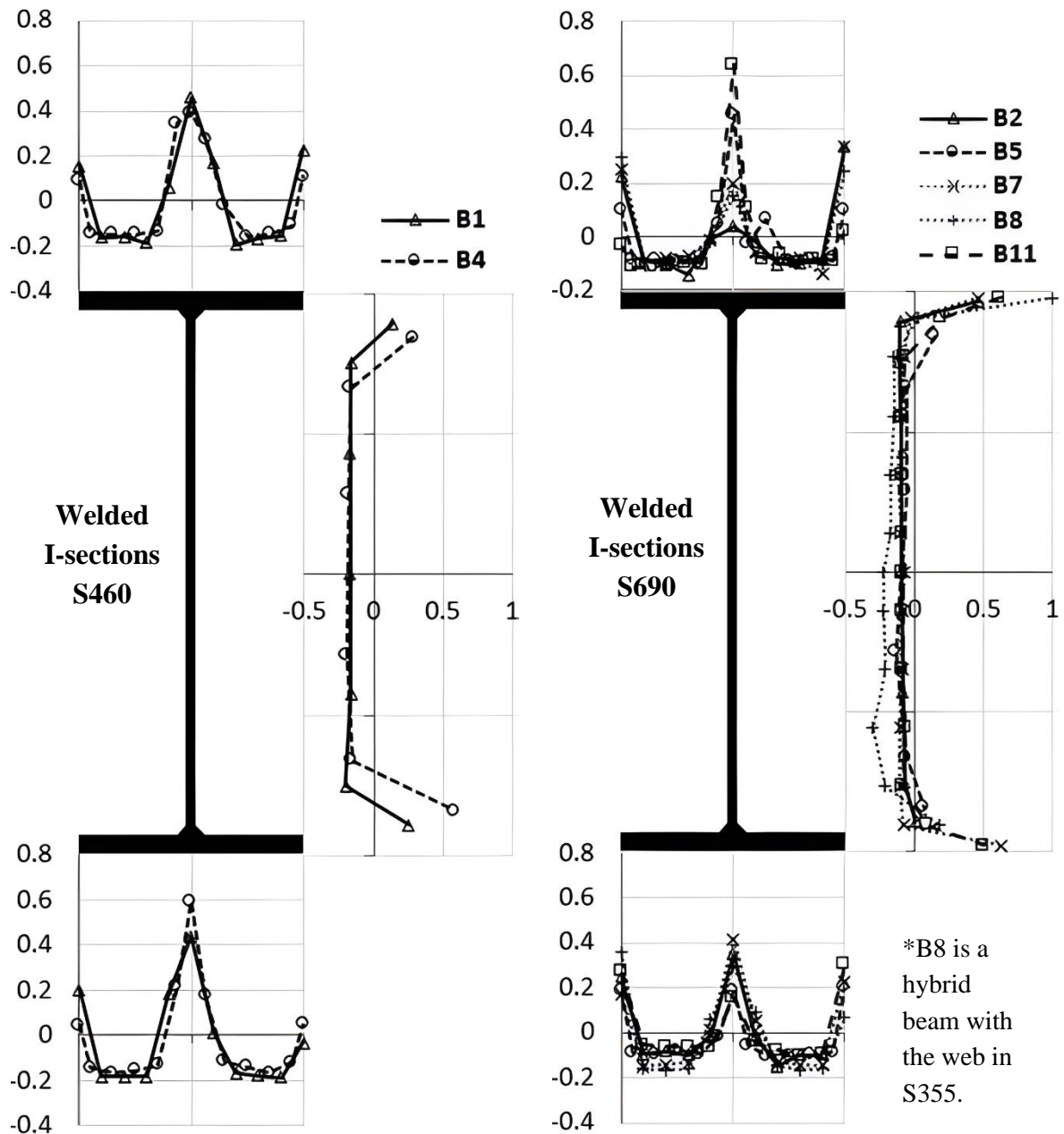


Figure 3.26 – Normalized residual stress distribution for welded sections

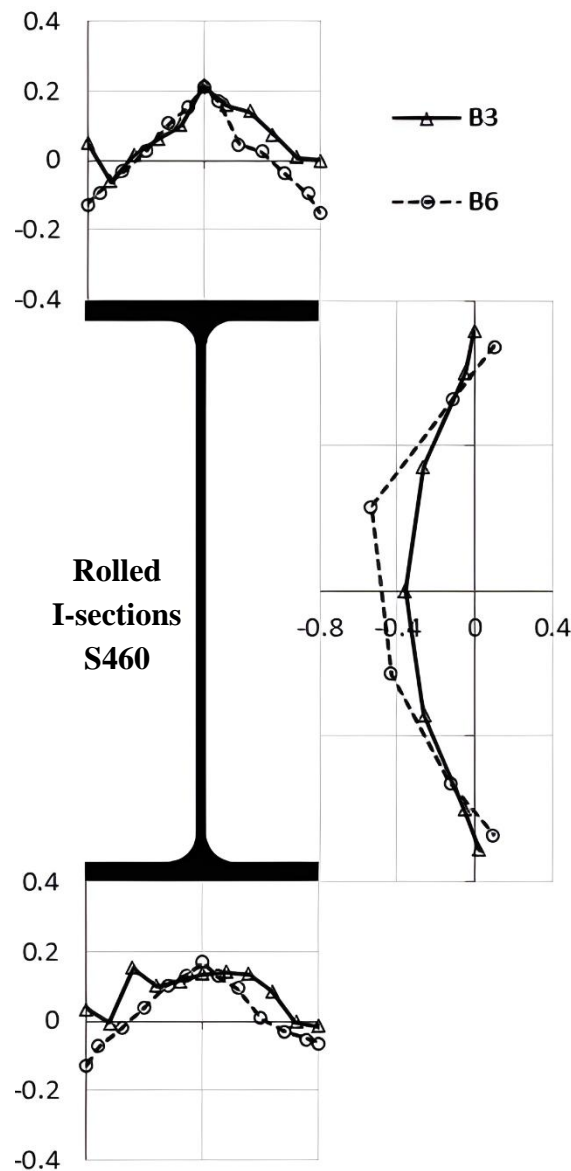


Figure 3.27 – Normalized residual stress distribution for rolled sections

A histogram based on the frequency of the values observed in the normalized residual stresses distributions for welded sections is given in Figure 3.28 for the flange compression (Figure 3.28a), flange tensions (Figure 3.28b), web compression (Figure 3.28c), and flange tip tension (Figure 3.28c).

From Figure 3.26, it is observed that the maximum tensile stress in the flanges was about $0.6f_y$ and the compression in the flanges exhibits a maximum of about $-0.2f_y$. The flange tip tension shows a maximum value of $0.4f_y$. Nonetheless, assessing the variability of the residual stresses for the welded sections through the histograms in Figure 3.28, the flange compression shows the lowest variability, where all the cases were found in the range of $-0.1f_y$ to $-0.2f_y$.

The flange tip tension varies from 0 to $0.4f_y$, where 40% of the cases are in the $0.2f_y$ range. The flange tension exhibits the highest variability, from 0 to $0.6f_y$, where $0.2f_y$ is the value with the highest frequency (29% of cases).

The residual stresses distribution in the web, varies from $-0.1f_y$ to $-0.2f_y$ for the web compression and $0.5f_y$ to $1.0f_y$ for the web tension, where the value of $1.0f_y$ was obtained for the lowest steel grade (S355), and the remaining values were found in the range of $0.5f_y$ to $0.6f_y$, as it can be seen in Figure 3.26.

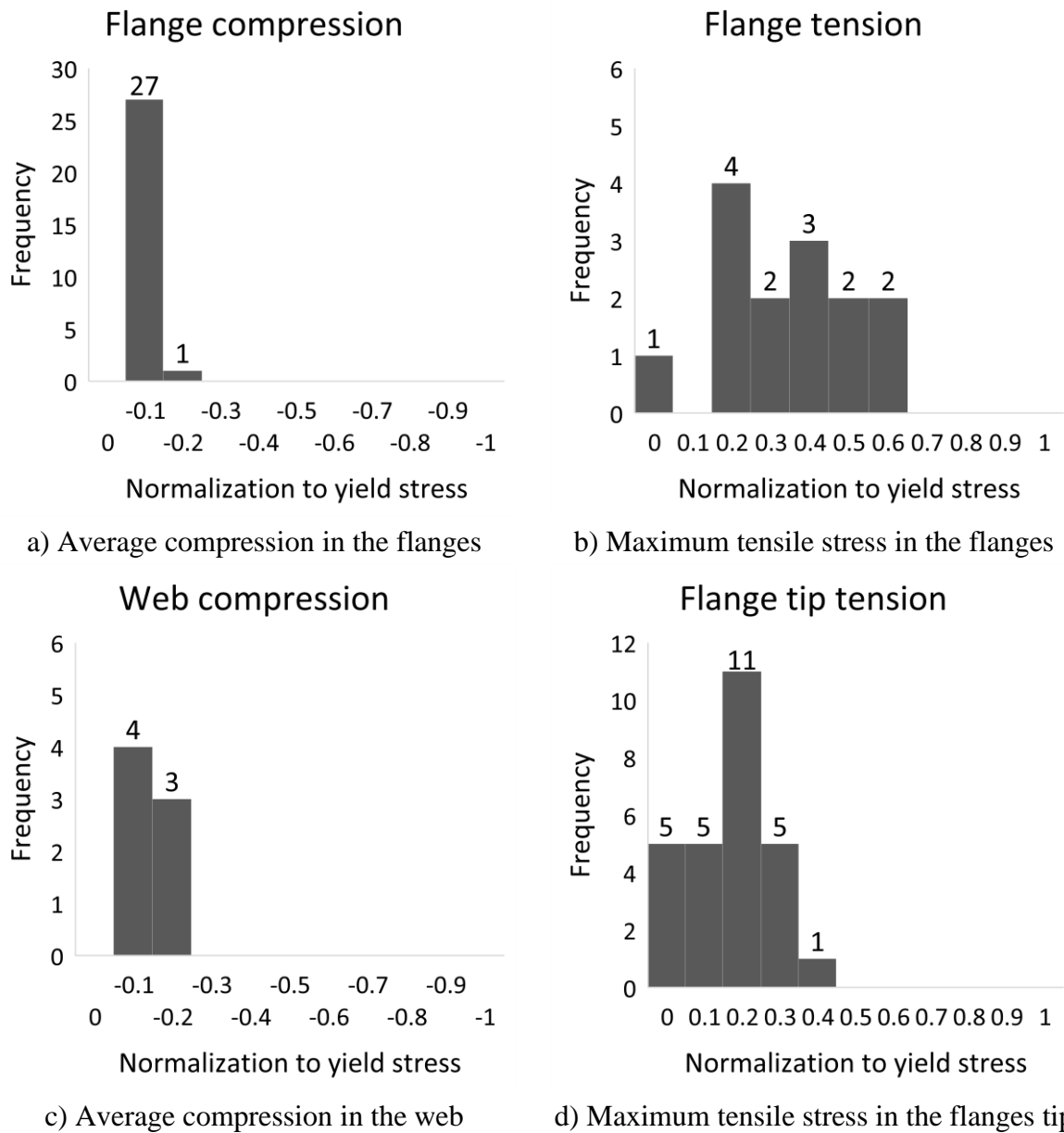


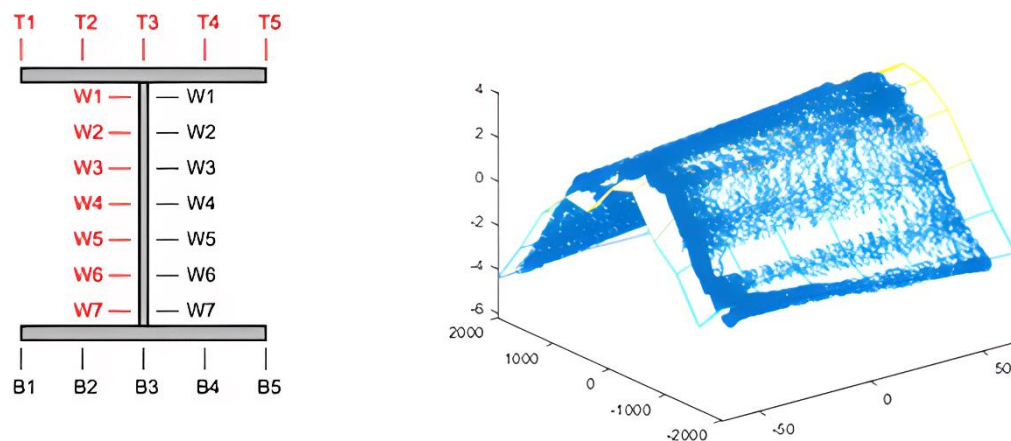
Figure 3.28 – Residual stresses distribution histograms for welded sections

The rolled sections were not assessed in terms of variability (histograms and statistics), since only two measurements were performed on rolled sections. However, in terms of normalized distributions (Figure 3.27), the maximum value observed for the tensile stress in the flanges was about $0.20f_y$ and $-0.15f_y$ for the flange compression. For the web tension, the maximum value was $0.10f_y$, and for the web compression, $-0.50f_y$.

3.6.3. Geometrical imperfections measurements

As described in Section 3.4, the geometrical properties of all the specimens were measured prior to the buckling tests, and the resulting measurements are provided as a cloud of points.

In order to interpret the measurements (and the imperfections), the measured data is plotted along the flanges and web of each member. The flanges were divided into four parts and the webs in six parts. Whereby, the points are plotted into five lines for both flanges (T1 to T5 and B1 to B5), and seven lines for each side of the web (W1 to W7), as shown in Figure 3.29.



a) Alignments considered

b) Set of points

Figure 3.29 – Estimation of the geometrical imperfections

The centre of the coordinate system was assumed to be in the middle of the specimen, so in order to obtain the value of the imperfection, half of the section height for the flanges has to be subtracted to the value of the coordinate obtained, and half of the web thickness for the web.

The results obtained for each line (web and flanges) according to Figure 3.29 for the geometric imperfections of each specimen are presented in detail in Annex A. The values of the imperfections were assessed in the middle 4m (between the points of load application, where the beam is under constant bending moment). It can generally be observed that the average imperfections obtained for each specimen are lower than the nominal imperfection magnitude

of $L/1000$ (4mm), except for the specimens B5 and B12, where this value is exceeded for the imperfections in the flanges for B5 and in the web and flanges for B12.

Furthermore, these measurements were used to estimate the geometrical dimensions of each beam cross-section, based on the average values of the measurements, where the thickness of the flanges and webs were averaged according to the plate from which the beam was fabricated (see Table 3.1). The cross-section dimensions are presented in Table 3.5.

Finally, in order to have a general overview of the initial member imperfections, the results obtained for each line (presented in Annex A), were averaged to obtain a general in-plane (vertical direction – lines T1 to T5 and B1 to B5, top and bottom flanges) and out-of-plane (lateral/horizontal – lines W1 to W7 for both sides of the web) imperfection for each specimen along the middle 4m. The results are presented in Figure 3.30.

Table 3.5 - Measured dimensions of the tested specimens

| Specimen | h [mm] | b_{f1} [mm] | b_{f2} [mm] | t_w [mm] | t_f [mm] |
|----------|----------|---------------|---------------|------------|------------|
| B1 | 498.94 | 200.64 | 201.03 | 16.19 | 8.58 |
| B2 | 498.02 | 200.4 | 200.26 | 15.72 | 8.29 |
| B3 | 496.54 | 201.70 | 201.44 | 14.97 | 10.24 |
| B4 | 308.06 | 299.68 | 297.91 | 16.19 | 8.58 |
| B5 | 309.08 | 299.74 | 300.90 | 15.72 | 8.29 |
| B6 | 308.48 | 296.41 | 296.5 | 14.93 | 8.47 |
| B7 | 745.40 | 201.79 | 201.58 | 15.81 | 8.31 |
| B8 | 746.18 | 201.62 | 200.95 | 15.81 | 8.07 |
| B11 | 743.9 | 200.67 | 398.02 | 15.81 | 8.31 |
| B12 | 743.38 | 197.08 | 400.62 | 15.81 | 8.07 |
| B13 | 747.94 | 200.16 | 398.93 | 16.19 | 8.58 |
| B14 | 748.04 | 199.75 | 399.79 | 16.19 | 8.07 |

Through the average geometrical imperfections (Figure 3.30), it is confirmed that the maximum amplitude is not within the limits of the usual assumption of $L/1000$ only for the specimens B5 and B12.

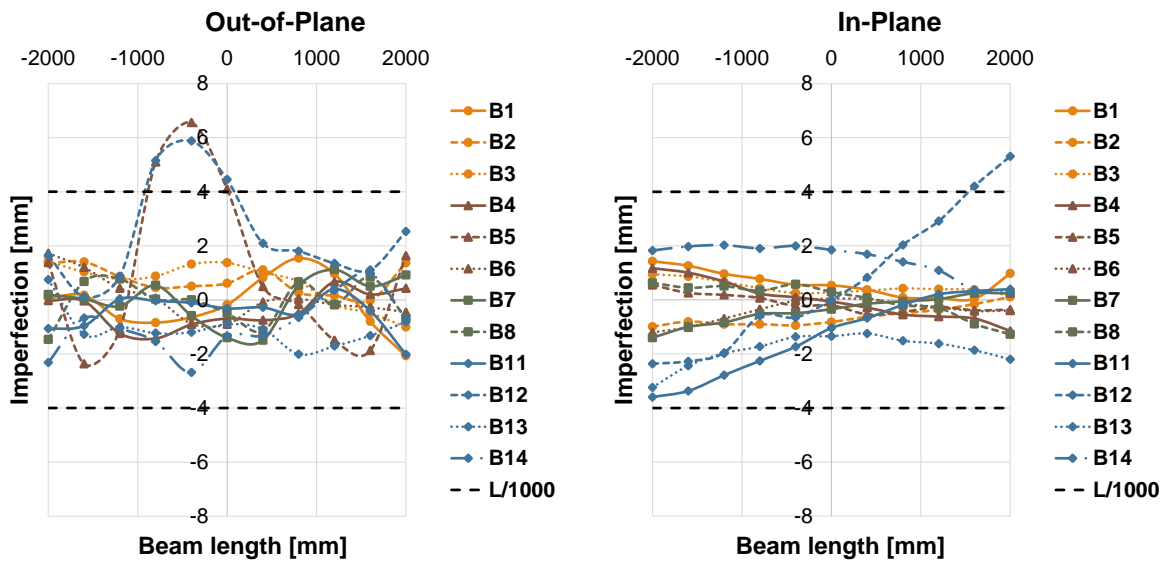


Figure 3.30 – Average geometrical imperfections

For the remaining specimens, the maximum amplitude is lower than $L/1000$ (4mm), where in most of the cases is even lower than $L/2000$ (2mm). This confirms that the usual assumption of $L/1000$ is a safe estimation for the initial member imperfection.

3.6.4. Lateral-torsional buckling tests

In this section, the results recorded during the lateral-torsional buckling tests are presented, according to the instrumentation presented in 3.5. In order to allow for an easier comparison of the results for the different tests, the results are presented into 4 groups, according to the cross-sections dimensions presented in Table 3.1:

- Tests B1, B2, and B3: B1 (S460) and B2 (S690) welded cross-sections with equivalent dimensions to a hot-rolled section IPE 500 as beam B3 (S460);
- Tests B4, B5, and B6: B4 (S460) and B5 (S690) welded cross-sections with equivalent dimensions to a hot-rolled section HE 320A as beam B6 (S460);
- Tests B7 and B8: B7 and B8 with the same welded cross-section, B7 is a homogeneous beam in S690 and B8 is a hybrid beam (flanges in S690 and web in S355);
- Tests B11, B12, B13, and B14: all four beams have the same welded monosymmetric cross-section, B11 and B13 are homogenous beams in S690 and S460, respectively, B12 and B14 are hybrid beams, B12 has the flanges in S690 and B14 in S460, and both have the web in S355.

3.6.4.1. Tests B1, B2 and B3

The first set of tests, B1, B2, and B3 with similar geometry, where B3 is a rolled section IPE 500 in steel grade S460 and B1 and B2 are equivalent welded cross-section in steel grades S460 and S690, respectively.

Table 3.6 summarizes the maximum recorded loads and displacements during the experimental test, for each specimen. The displacements correspond to the maximum vertical displacement observed at load application (V1 and V6) and mid-span at bottom flange (V2, V3) and the maximum horizontal displacement at mid-span (H3).

The resistance obtained (maximum load) for B2 (1041.93 kN) is higher than the resistance obtained for B1 and B3, at about 34% and 25%, whereas the difference of the nominal yield strength of the two steel grades is 50%, showing that the beam resistance is conditioned by stability. The difference between B1 and B3 (same steel grade) is about 7% and is explained by the slightly higher cross-section area of the rolled IPE profile, compared to the equivalent welded one.

Figure 3.31 shows the load-displacement curves for the vertical displacement at load application point (V1 and V6), for the three specimens (Figure 3.31a) and the horizontal displacements at mid-span (H3, H4 and H5 - Figure 3.31b). It is observed that all three beams have the same initial stiffness and where the maximum load is reached, the horizontal displacements start to increase significantly when the lateral-torsional buckling is achieved. The lateral-torsional buckling deformed shape observed was similar for the three beams, according to Figure 3.32.

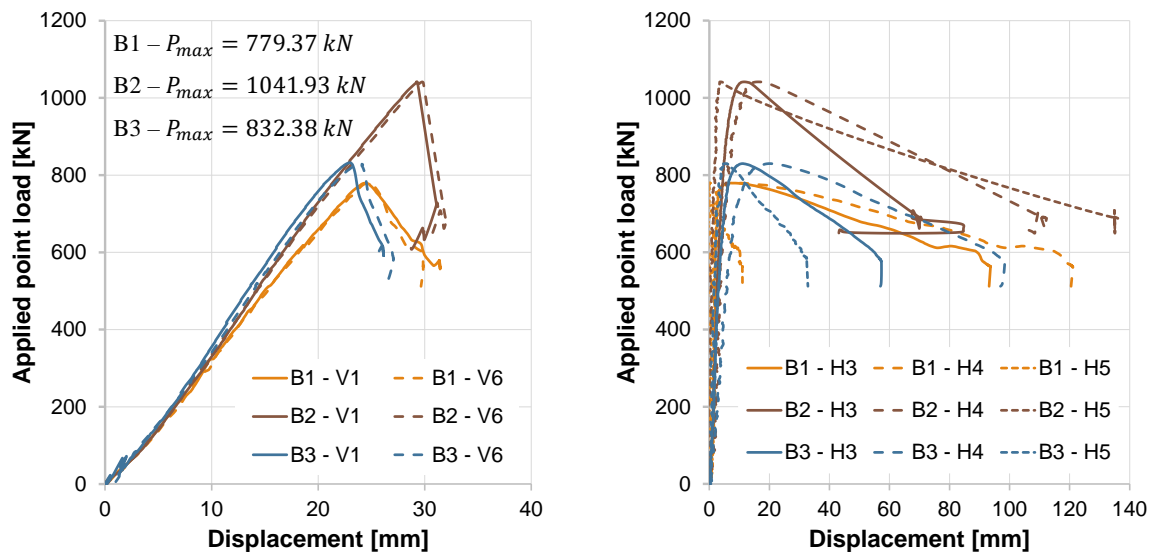
Additional measurements of displacements were performed at various locations along the beams. Figure 3.33 and Figure 3.34 show the evolution of the vertical and horizontal displacements along the beam at four different stages of the experiment (two before the maximum load, one at the maximum load, and one after reaching the maximum load).

From Figure 3.33 and Figure 3.34 it is possible to observe that the evolution of the vertical displacements is more or less gradual for the different stages represented. In contrast, the horizontal displacements show a low amplitude until the last stage (after the maximum load), where the displacements increase significantly due to the lateral-torsional buckling.

Due to the high deformations recorded, as can be shown by the measurements, in some cases, these high displacements led to the impossibility of measuring some displacements, as some LVDTs lost their contact to the specimen and/or changed their location and/or the LVDT became unresponsive to the movement. Hence, the readings of the LVDT V10 in the last two stages of the test B3 should be disregarded so as not to compromise the consistency of the results.

Table 3.6 – Summary of the maximum loads and displacements obtained for experimental tests B1, B2 and B3

| Test | Load [kN] | Vertical displacement (load application) [mm] | Vertical displacement (mid-span) [mm] | Horizontal displacement (mid-span) [mm] |
|------|-----------|---|---------------------------------------|---|
| B1 | 779.37 | 32.08 | 57.84 | 93.67 |
| B2 | 1041.93 | 33.34 | 63.78 | 84.80 |
| B3 | 832.38 | 27.89 | 54.72 | 57.34 |



a) Vertical displacement – Load application b) Horizontal displacements – Mid-span
 Figure 3.31 – Load displacement curves for tests B1, B2 and B3



Figure 3.32 – Deformed shape – Tests B1, B2 and B3

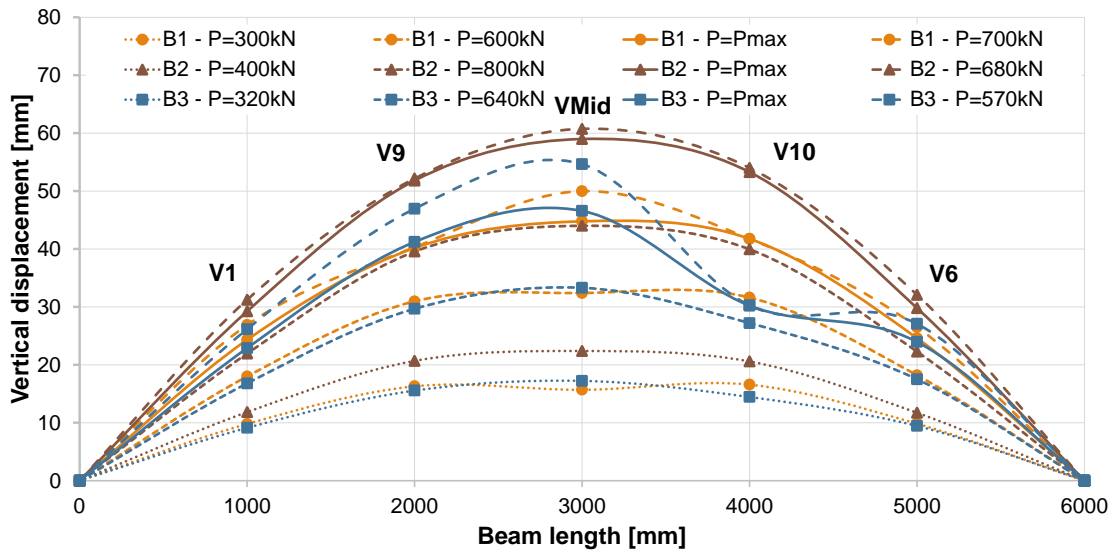


Figure 3.33 – Vertical displacements along the beams for tests B1, B2 and B3

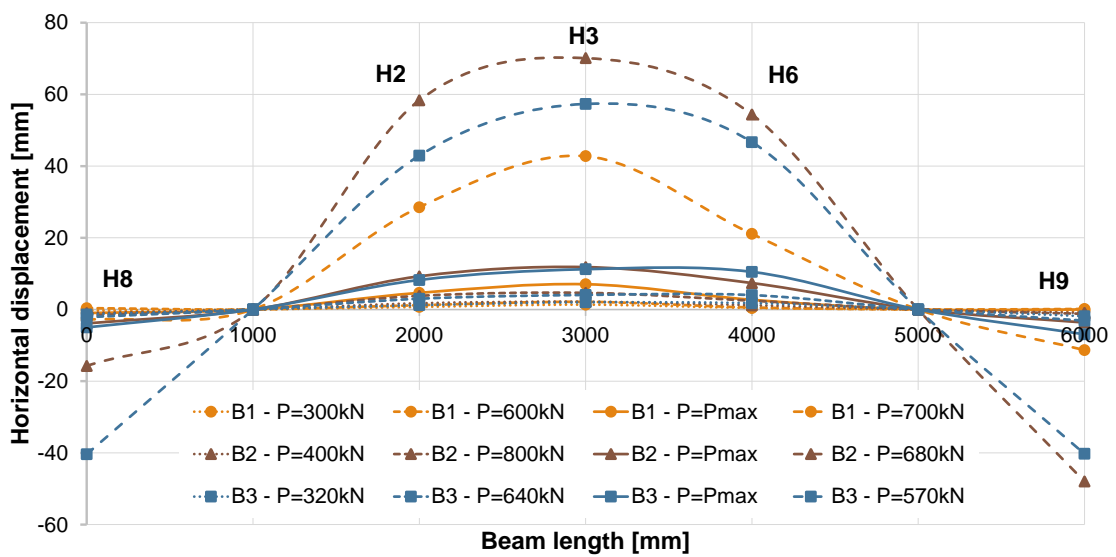
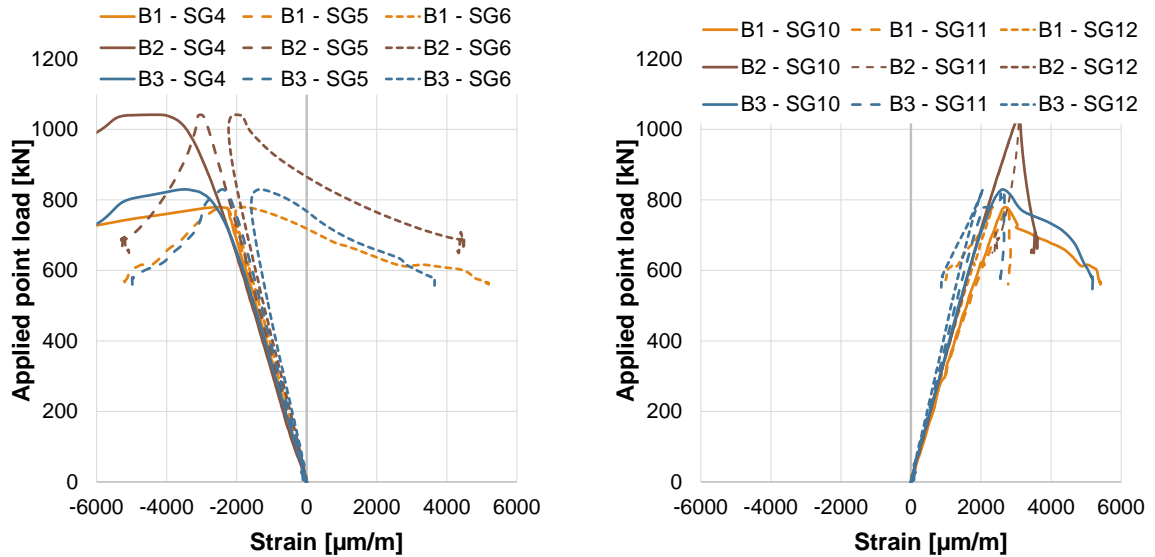


Figure 3.34 – Horizontal displacements along the beams for tests B1, B2 and B3

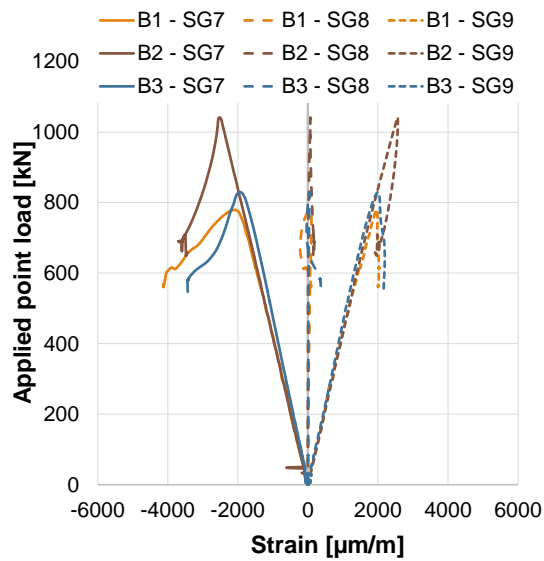
The strains at mid-section (section D) are presented in Figure 3.35, for the top flange (Figure 3.35a), bottom flange (Figure 3.35b), and web (Figure 3.35c). In all cases, the presence of lateral-torsional buckling due to a sudden change can be seen in the recordings, mainly in the top flange (Figure 3.35a), where the stress variation due to LTB can be seen, with compressive strains on one side and tensile strains on the other.

The strain recordings in the web at section H and I (0.5m apart from the middle section for each side) are presented in Figure 3.36. The results show consistency, as they present similar strain development in sections H and I, equally spaced from the mid-section.



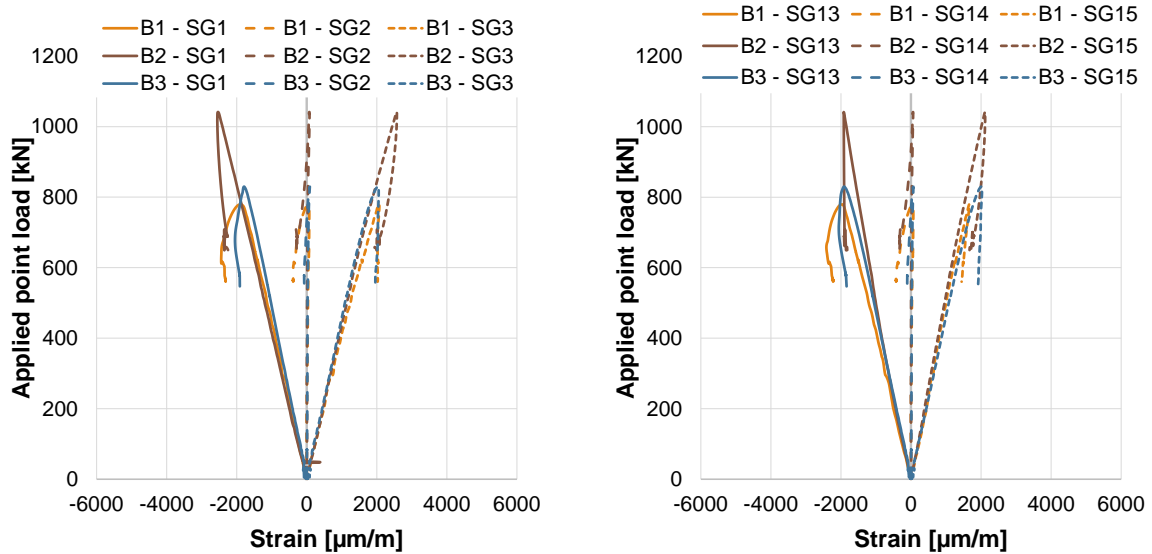
a) Top flange – Section D (mid-span)

b) Bottom flange – Section D (mid-span)



c) Web – Section D (mid-span)

Figure 3.35 – Strain curves at section D (mid-span) for tests B1, B2 and B3



a) Web – Section H
 b) Web – Section I
 Figure 3.36 – Strain curves at sections H and I for tests B1, B2 and B3

Finally, Figure 3.37 represents the cross-section deformation at mid-span at point of maximum load and at the end of the experimental tests, where it is possible to confirm what as previously mentioned: The gradual increase of the in-plane (vertical) displacements during the tests, and the significant increase of the out-of-plane (horizontal) displacements after reaching the maximum load, due to lateral-torsional buckling.

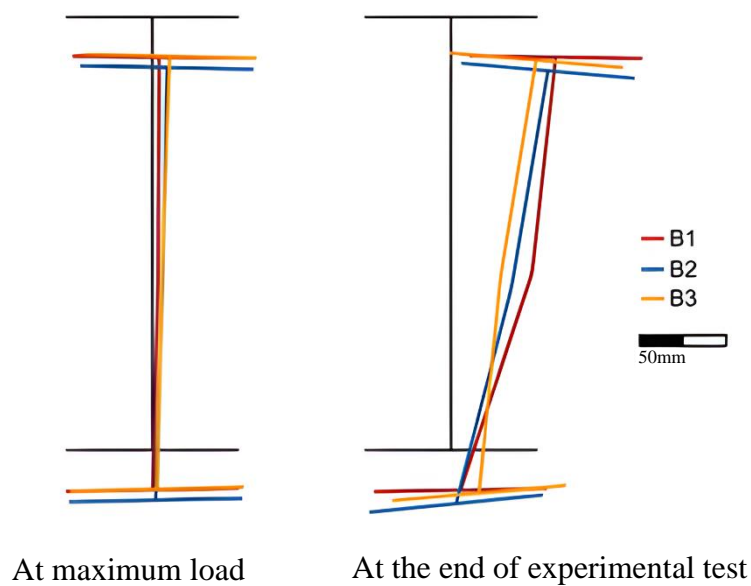


Figure 3.37 – Cross section deformation at maximum load and at the end of the tests

3.6.4.2. Tests B4, B5 and B6

The second group of tests, B4, B5, and B6, comprises a rolled section HE 320 A in steel grade S460, specimen B6, and equivalent welded cross-sections in steel grade S460 and S690, specimens B4 and B5, respectively.

Similar to the previous group, Table 3.7 summarizes the maximum recorded loads and displacements during the experimental test, for each specimen. The displacements correspond to the maximum vertical displacement observed at load application (V1 and V6) and mid-span at bottom flange (V2, V3) and the maximum horizontal displacement at mid-span (H3).

The maximum resistance (load applied) was obtained for test B5 made in steel grade S690, higher than the maximum loads applied in B4 and B6, by 51% and 41%, respectively. The difference between the nominal yield strength of the steel grades (S460 and S690) is 50%. This improvement in the results for the test with higher steel grade (S690), compared to the previous group (increase of 34% and 25% compared to 51% and 41%), results from the lower cross-section slenderness and therefore has a higher lateral-torsional buckling reduction factor. The difference between the tests with the same steel grade (S460), B4 and B6, of about 7%, is explained by the slightly higher cross-section area of the rolled profile, when compared to the welded section.

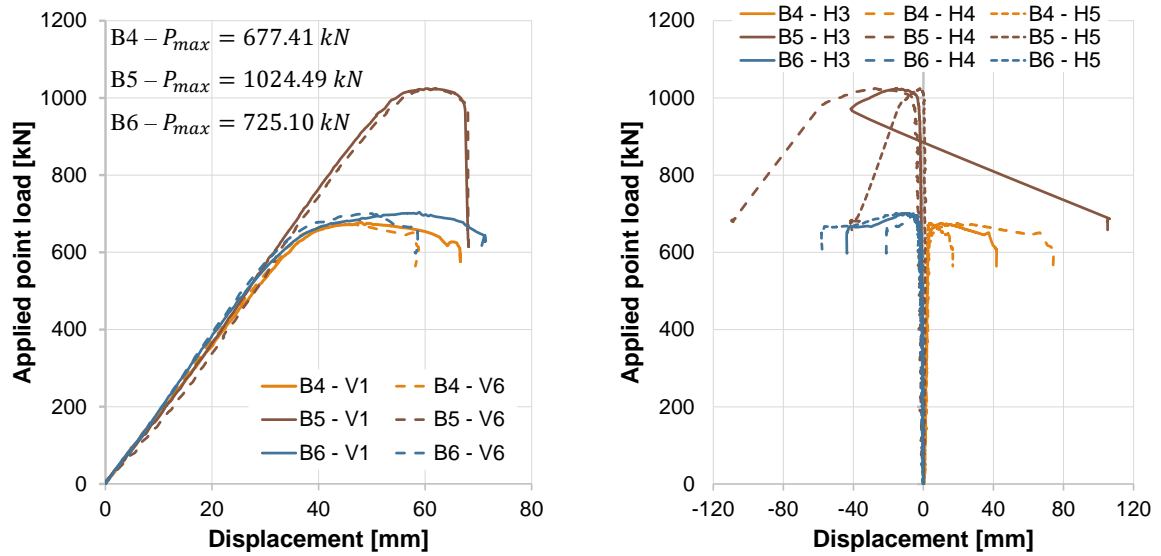
The load-displacement curves are shown in Figure 3.38 for the vertical displacement at load application point (V1 and V6), for the three specimens (Figure 3.31a) and for the horizontal displacements at mid-span (H3, H4, and H5 - Figure 3.31b). All three beams have the same initial stiffness and after the maximum load is reached, the horizontal displacements start to increase significantly, when the lateral-torsional buckling is achieved. The lateral-torsional buckling deformed shape observed was similar for the three beams, according to Figure 3.39.

Figure 3.40 and Figure 3.41 show the development of the vertical (Figure 3.40) and horizontal (Figure 3.41) displacements along the beam at four different stages during the experimental tests (two before the maximum load, one at the maximum load, and one after reaching the maximum load). The evolution of the vertical displacements is regular during all the tests, whereas the horizontal displacements are residual until the maximum load is reached. After the maximum load, large horizontal displacements are recorded due to the lateral-torsional buckling.

Figure 3.42 shows the strain measurements at mid-section (section D), for the top flange (Figure 3.42a), bottom flange (Figure 3.42b), and web (Figure 3.42c). The sudden change in the strains is noticeable due to the presence of lateral-torsional buckling in all three tests, and also at the top flange (Figure 3.42a) the presence of compressive strains (SG 4 and SG5) and tensile strains (SG 6), due to the LTB.

Table 3.7 – Summary of the maximum loads and displacements obtained for experimental tests B4, B5 and B6

| Test | Load [kN] | Vertical displacement (load application) [mm] | Vertical displacement (mid-span) [mm] | Horizontal displacement (mid-span) [mm] |
|------|-----------|---|---------------------------------------|---|
| B4 | 677.41 | 68.21 | 140.33 | 41.81 |
| B5 | 1024.49 | 68.64 | 154.25 | 106.38 |
| B6 | 725.10 | 73.03 | 146.55 | 43.83 |



a) Vertical displacement – Load application b) Horizontal displacements – Mid-span
 Figure 3.38 – Load displacement curves for tests B4, B5 and B6



Figure 3.39 - Deformed shape – Tests B4, B5 and B6

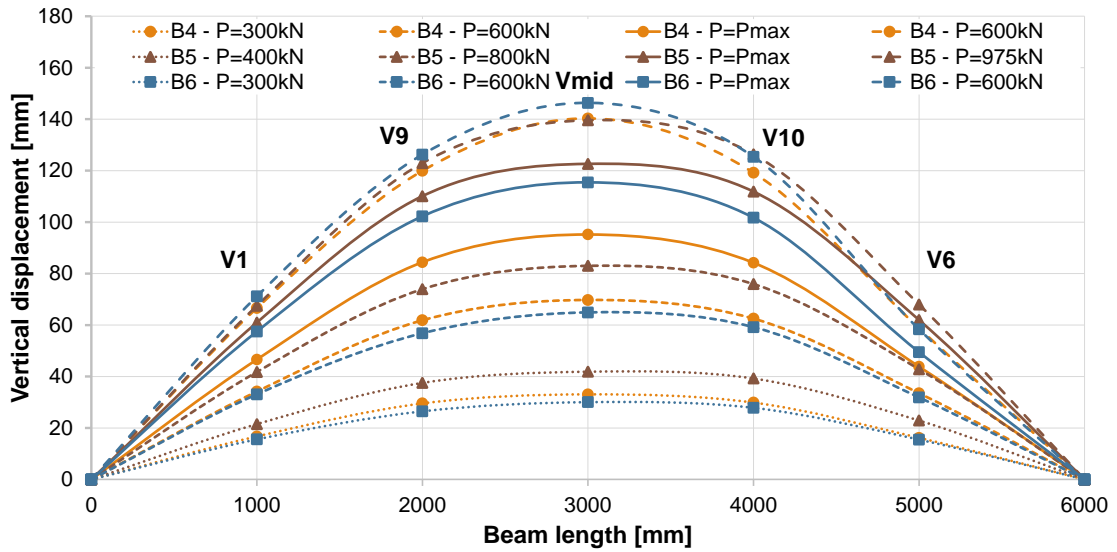


Figure 3.40 – Vertical displacements along the beams for tests B4, B5 and B6

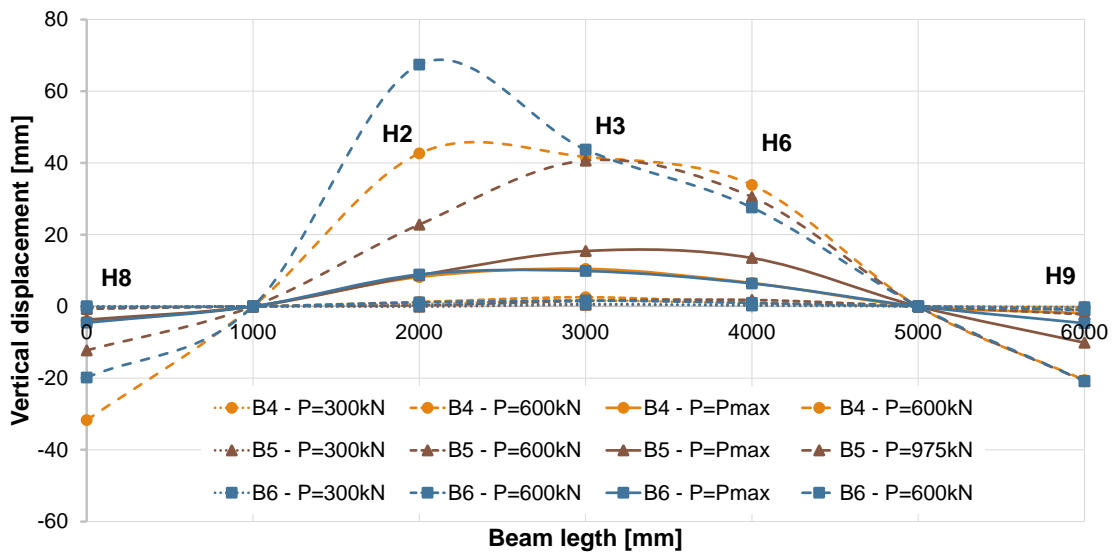
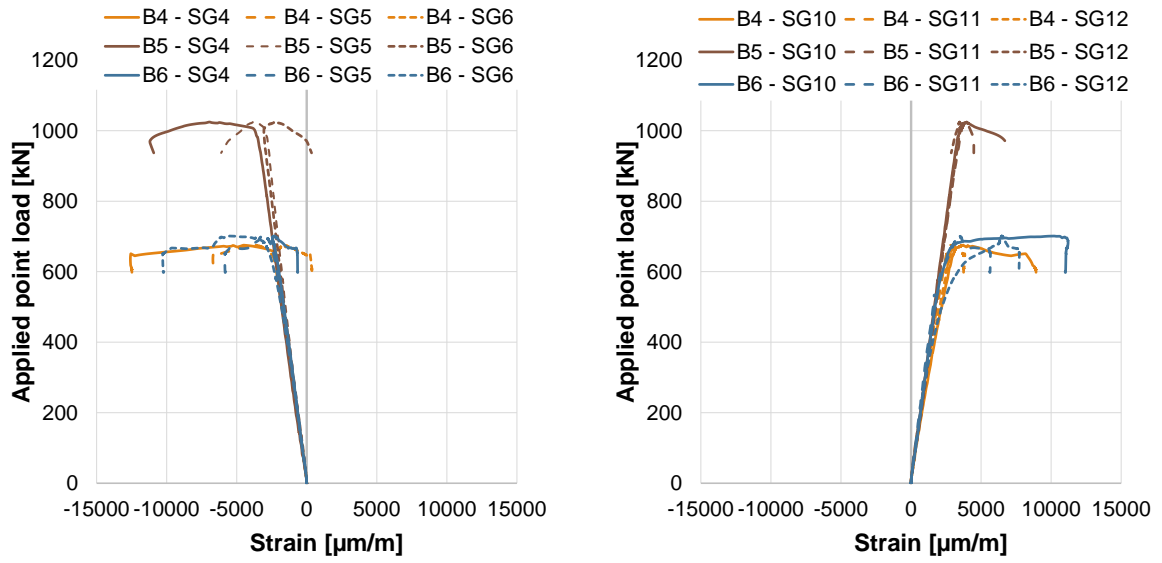


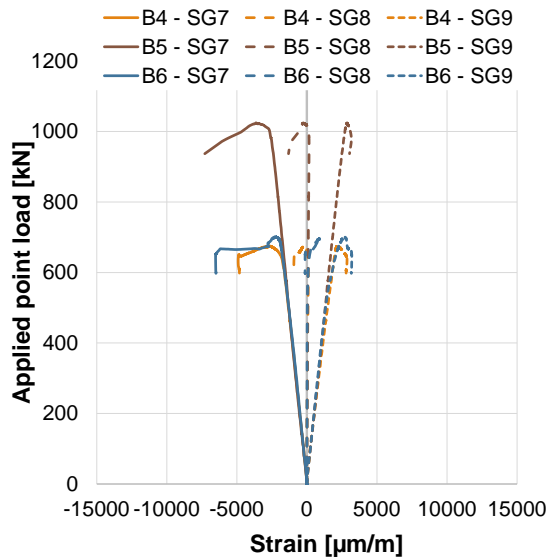
Figure 3.41 – Horizontal displacements along the beams for tests B4, B5 and B6

The strains at sections H and I in the web (0.5 m apart from the middle section for each side) are presented in Figure 3.43. The strain measurements show similar developments and are consistent with what was measured at the web in the middle section, indicating that the results are consistent.



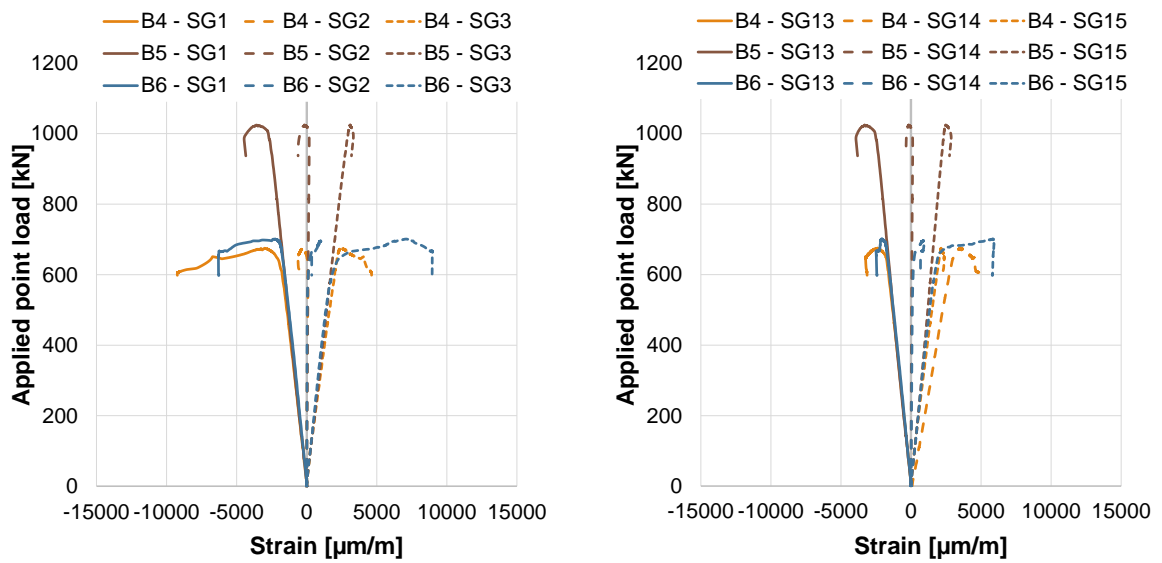
a) Top flange – Section D (mid-span)

b) Bottom flange – Section D (mid-span)



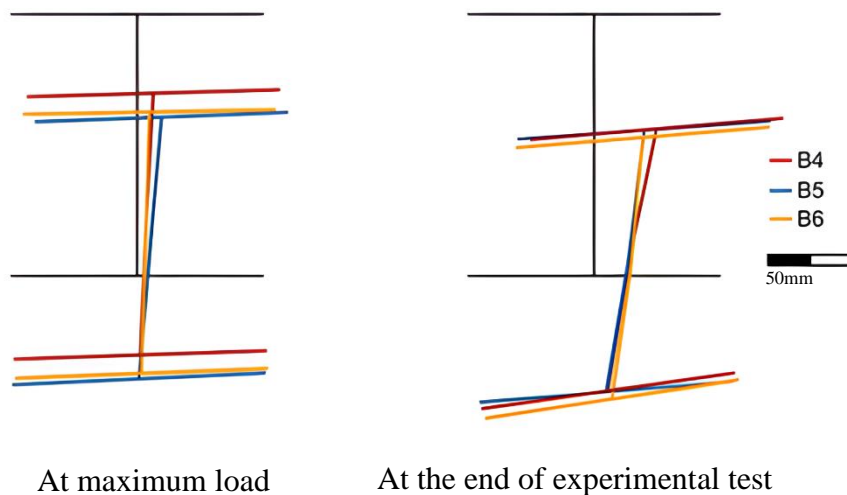
c) Web – Section D (mid-span)

Figure 3.42 – Strain curves at section D (mid-span) for tests B4, B5 and B6



a) Web – Section H
 b) Web – Section I
 Figure 3.43 – Strain curves at sections H and I for tests B4, B5 and B6

Figure 3.44 shows the cross-section deformation at mid-span, at maximum load and before the end of the experimental tests. The results confirm what was mentioned before, the gradually increasing of the in-plane (vertical) displacements, and significant out-of-plane (horizontal) displacements, after reaching the maximum load (and before the end of the experimental tests).



At maximum load At the end of experimental test
 Figure 3.44 – Cross section deformation at maximum load and at the end of the tests

3.6.4.3. Tests B7 and B8

The third group of tests is composed of beams B7 and B8. B7 is entirely made in steel grade S690 (homogeneous beam) and B8 is a hybrid beam, in which the web is made in steel grade S355 and the flanges in S690.

Table 3.8 summarizes the maximum recorded loads and displacements during the experimental test, for each specimen. The displacements correspond to the maximum vertical displacement observed at load application (V1 and V6) and mid-span at bottom flange (V2, V3) and the maximum horizontal displacement at mid-span (H3).

As expected, the highest resistance (maximum applied load) was found for test B7 (1404.90 kN), nonetheless, the resistance between both beams only differs by 5% (1336.34 kN for B8), showing that the hybrid beams can be competitive compared to the homogeneous solution.

The load-displacement curves are shown in Figure 3.45 for the vertical displacement at load application point (V1 and V6), for both beams (Figure 3.45a), and for the horizontal displacements at mid-span (H3, H4 and H5 - Figure 3.45b).

The noticeable difference between the measurements of LVDT V1 and V6 for test B7 was due to a mistake in positioning the LVDT V6, as it was placed approximately 700mm from the beam end, instead of 1000mm from the beam end (as presented in Figure 3.12). This resulted in lower vertical displacements in V6 compared to V1 (as can be seen from Figure 3.45a). Despite this fact, both beams (B7 and B8) showed a similar behaviour, where for both tests, lateral-torsional buckling was observed with similar deformed shape (Figure 3.46).

Figure 3.47 and Figure 3.48 show the evolution of the vertical and horizontal displacements along the beam at four different stages of the experimental tests, two before the maximum load, one at the maximum load, and one after reaching the maximum load.

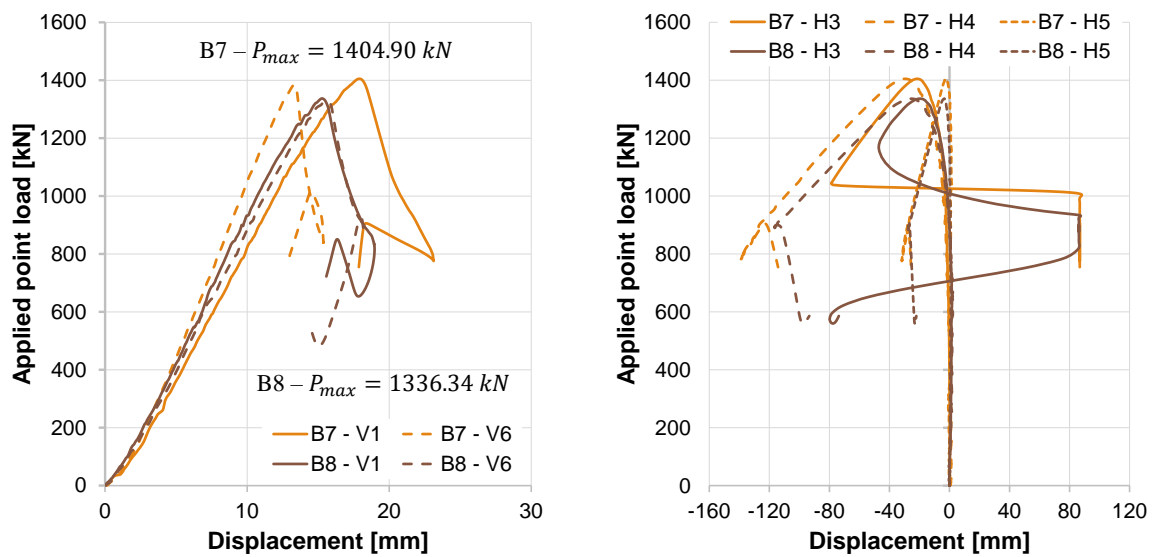
As observed in the previous groups of tests, the development of the displacements for tests B7 and B8 follows the same trend, horizontal displacements increasing gradually during the tests, whereas there is a significant horizontal deformation due to the lateral-torsional buckling of the beam, after reaching the maximum load.

Figure 3.49 shows the strain measurements at mid-section (section D) for the top flange (Figure 3.49a), bottom flange (Figure 3.49b), and web (Figure 3.49c). As in the previous groups, the significant increase of the strains is quite noticeable, mainly in the top flange (Figure 3.49a), due to the presence of lateral-torsional buckling in both beams.

The strain measurements at sections H and I in the web (0.5 m apart from the middle section for each side) are presented in Figure 3.50, showing similar strain developments at the web for the same levels along the web (SG 1 and 17, 2 and 18, 3 and 19, 4 and 20, and 5 and 21).

Table 3.8 – Summary of the maximum loads and displacements obtained for experimental tests B7 and B8

| Test | Load [kN] | Vertical displacement (load application) [mm] | Vertical displacement (mid-span) [mm] | Horizontal displacement (mid-span) [mm] |
|------|-----------|---|---------------------------------------|---|
| B7 | 1404.90 | 24.18 | 40.08 | 88.16 |
| B8 | 1336.34 | 18.98 | 36.57 | 87.53 |



a) Vertical displacement – Load application b) Horizontal displacements – Mid-span

Figure 3.45 – Load displacement curves for tests B7 and B8

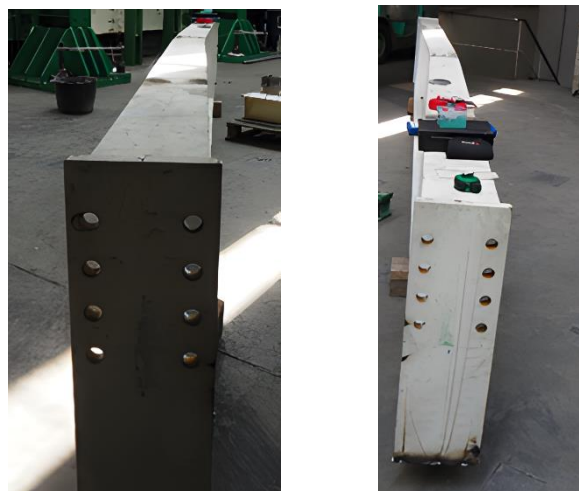


Figure 3.46 – Deformed shape – Tests B7 and B8

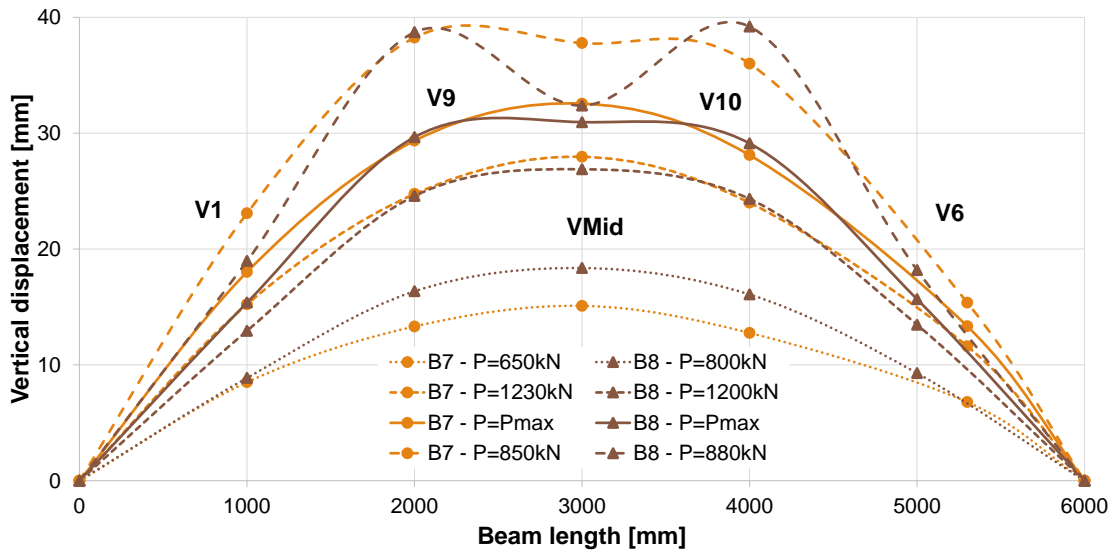


Figure 3.47 – Vertical displacements along the beams for tests B7 and B8

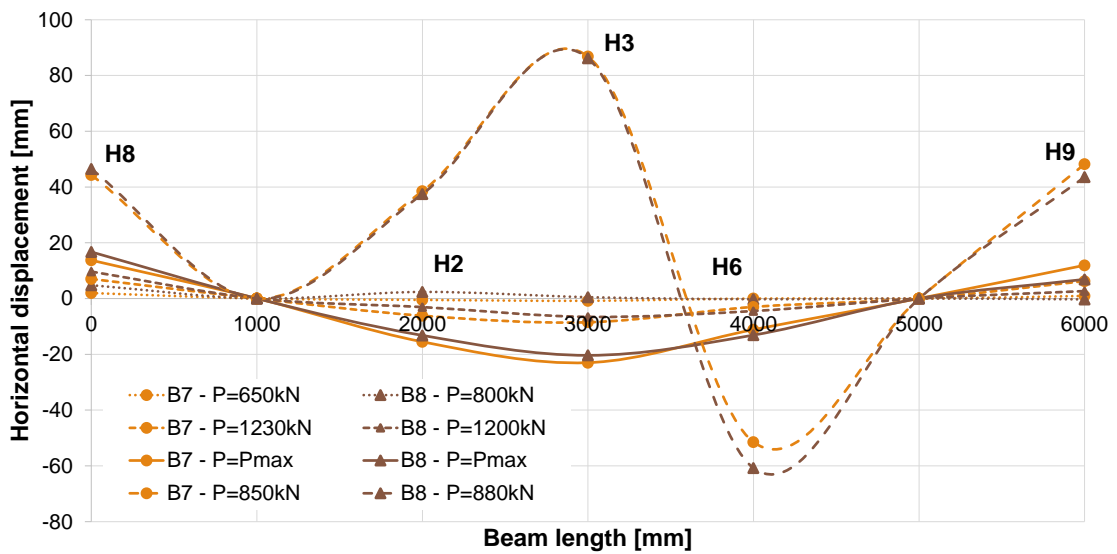


Figure 3.48 – Horizontal displacements along the beams for tests B7 and B8

Figure 3.51 shows the deformed shape for the middle cross-section, at the point of maximum load and at the end of the experimental tests. The results are in line with the previous ones, large out-of-plane (horizontal) displacements after reaching the maximum load, and gradually increasing of the in-plane (vertical) displacements.

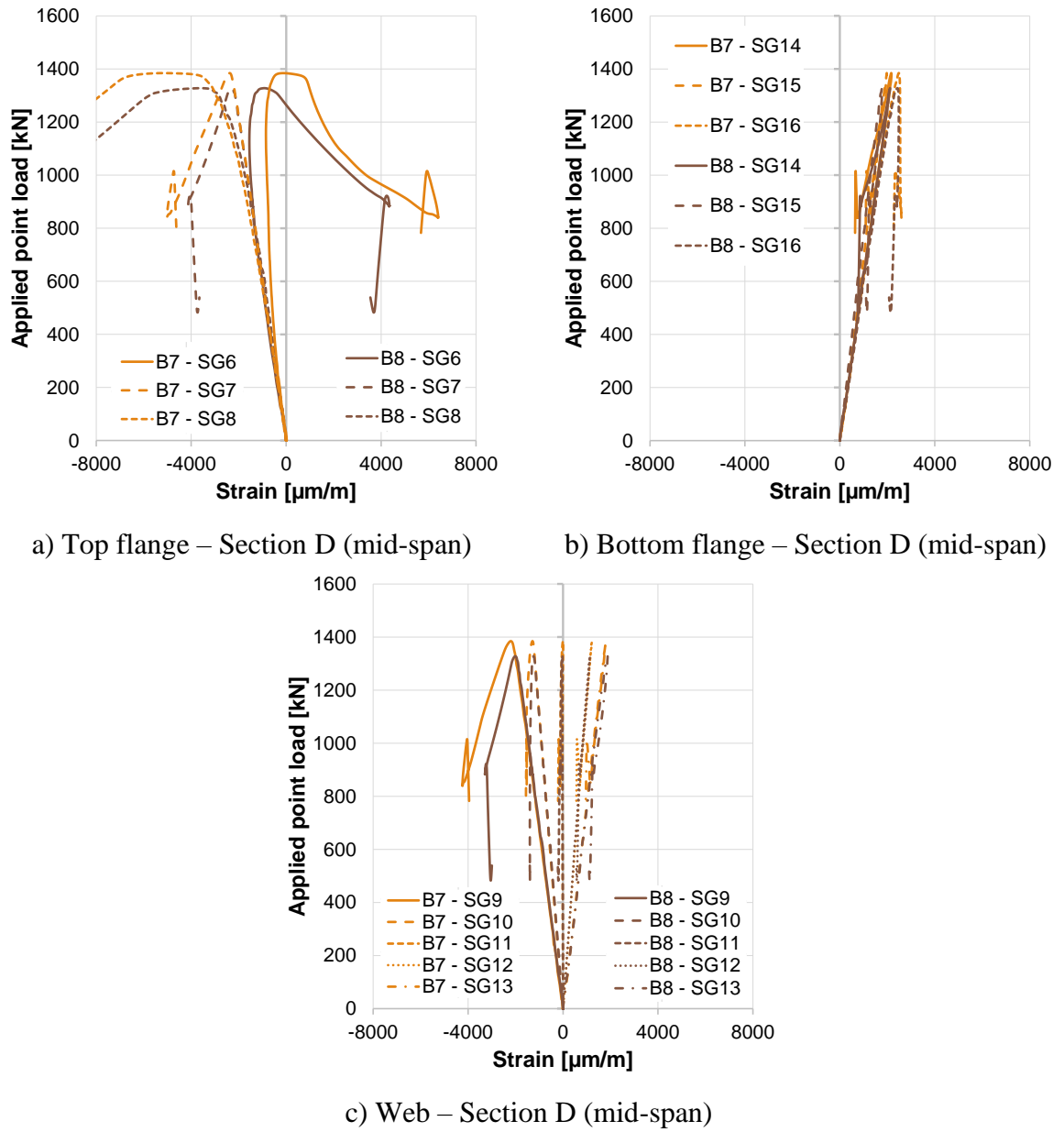
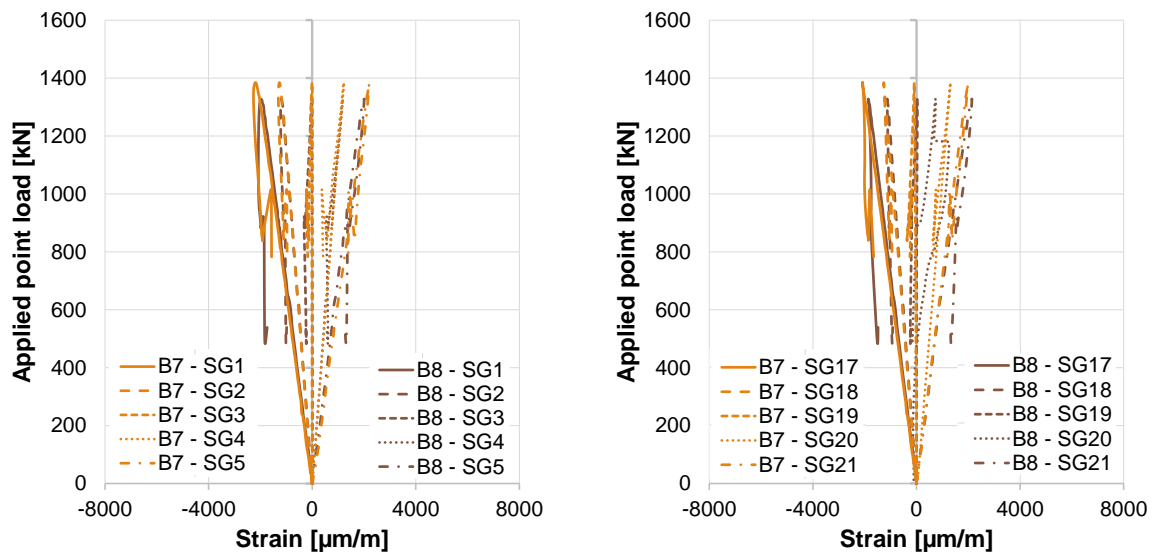


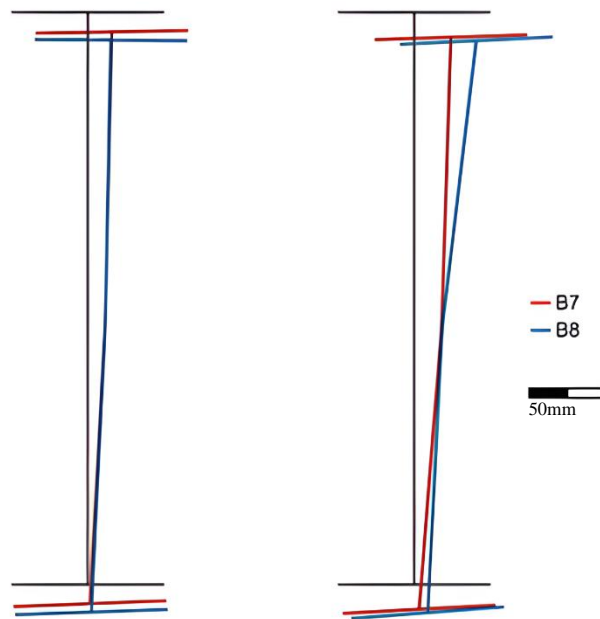
Figure 3.49 – Strain curves at section D (mid-span) for tests B7 and B8



a) Web – Section H

b) Web – Section I

Figure 3.50 – Strain curves at sections H and I for tests B7 and B8



At maximum load

At the end of experimental test

Figure 3.51 – Cross section deformation at maximum load and at the end of the tests

3.6.4.4. Tests B11, B12, B13 and B14

The last group of tests, B11 to B14, is composed of monosymmetric beams, whereby the bottom flange (400mm) has twice the width of the top flange (200mm), having a larger part of the web in compression. B11 is entirely made in steel grade S690 and B12 is a hybrid beam, with the flanges in S690 and the web in S355. B13 is entirely made in steel grade S460 and B14 is a hybrid beam, with the flanges in S460 and the web in S355.

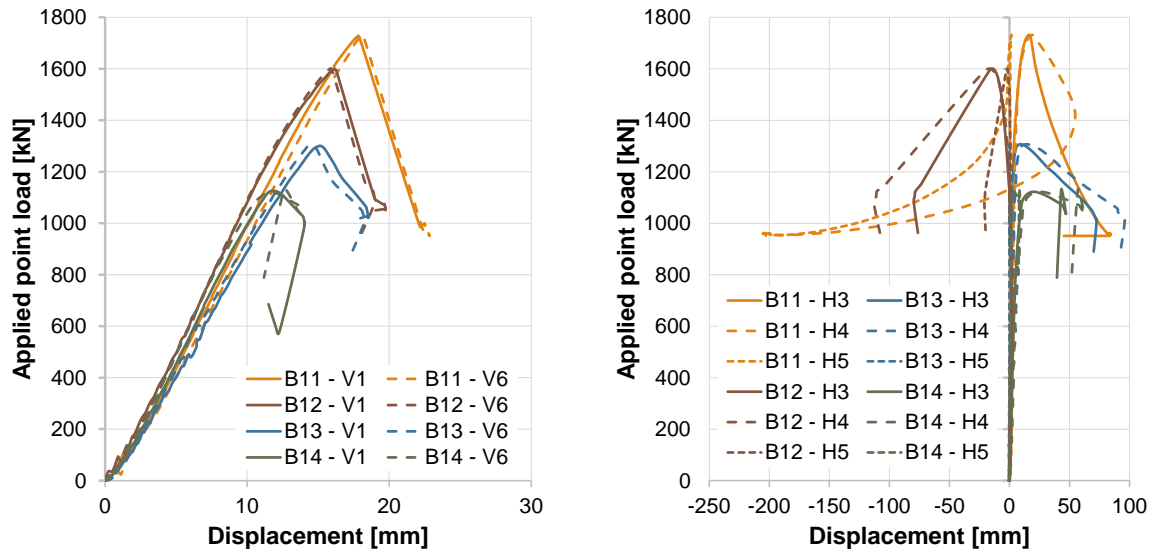
Table 3.9 summarizes the maximum recorded loads and displacements during the experimental test, for each specimen. The displacements correspond to the maximum vertical displacement observed at load application (V1 and V6) and mid-span at bottom flange (V2, V3) and the maximum horizontal displacement at mid-span (H3).

The maximum applied load was obtained for test B11 as it is entirely S690. Comparing the maximum load between B11 (1731.80 kN) and B13 (1307.18 kN), both homogenous beams in S690 and S460, respectively, there is a gain in the resistance at about 32% for using a higher strength steel. The use of the hybrid solutions, B12 and B14, results in a loss of resistance at about 8% and 15%, respectively, compared to the equivalent homogeneous beam. For the hybrid beams, there is a gain of about 41% in the resistance for using a higher strength steel in the flanges.

Figure 3.52 shows the load-displacement curves, for the vertical displacement at load application point (V1 and V6), for the four specimens (Figure 3.52a) and the horizontal displacements at mid-span (H3, H4 and H5 -Figure 3.52b). All four beams show a similar initial stiffness. The horizontal displacements are residual until the maximum load is reached, observing large deformations after this stage, when the lateral-torsional buckling is achieved. The lateral-torsional buckling deformed shape observed was similar for all the specimens (Figure 3.53).

Table 3.9 – Summary of the maximum loads and displacements obtained for experimental tests B11, B12, B13 and B14

| Test | Load [kN] | Vertical displacement (load application) [mm] | Vertical displacement (mid-span) [mm] | Horizontal displacement (mid-span) [mm] |
|------|-----------|---|---------------------------------------|---|
| B11 | 1731.80 | 22.83 | 46.94 | 84.07 |
| B12 | 1601.03 | 19.74 | 40.71 | 79.66 |
| B13 | 1307.18 | 18.52 | 31.82 | 72.61 |
| B14 | 1133.28 | 14.05 | 27.01 | 47.08 |



a) Vertical displacement – Load application b) Horizontal displacements – Mid-span
 Figure 3.52 – Load displacement curves for tests B11, B12, B13 and B14



Figure 3.53 – Deformed shape – Tests B11, B12, B13 and B14

The development of the vertical and horizontal displacements along the beam is shown in Figure 3.54 and Figure 3.55, respectively. The displacements are plotted at four different stages of the experimental tests (two before the maximum load, one at the maximum load, and one after reaching the maximum load). The results show what was previously pointed out, namely, the large out-of-plane (horizontal) deformations after the maximum load, due to the lateral-torsional buckling. While the evolution of the in-plane (vertical) displacements remains constant during all the experimental test.

Regarding the vertical displacements (Figure 3.54), the measurement of LVDT V9 in the last stage (after maximum load) of the test B11 should be disregarded, as it was previously mentioned that in some cases, due to the sudden deformations, the LVDTs went out of position. The difference in the vertical displacements at the last stage, mainly between B11 and B12 and B13 and B14 is due to the fact that as they reach a higher load, and the load chosen for the last stage is approximately the same for all the specimens, for specimens B11 and B12, more time has passed between the stage of maximum load and the last stage.

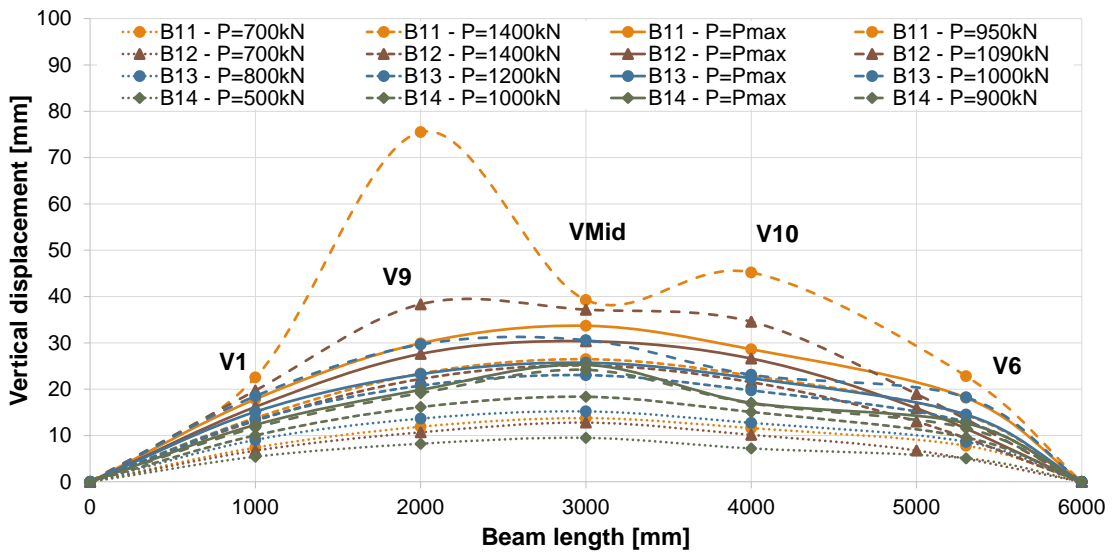


Figure 3.54 – Vertical displacements along the beams for tests B11, B12, B13 and B14

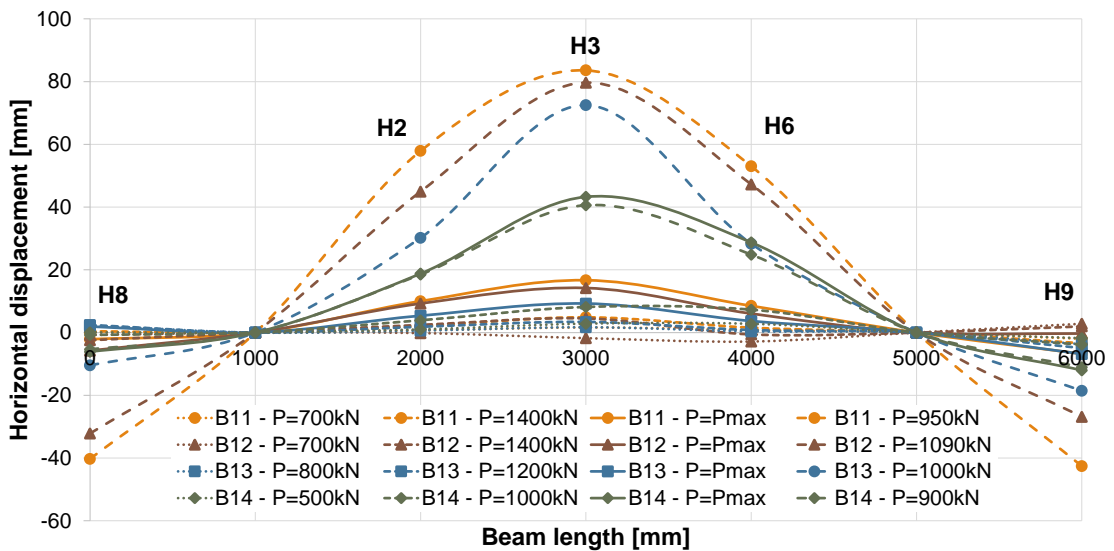


Figure 3.55 – Horizontal displacements along the beams for tests B11, B12, B13 and B14

The horizontal displacements for specimen B14 in the last stage (Figure 3.55) are slightly lower than the moment of maximum load. This is explained by the fact that when the load reached its maximum, the horizontal displacements started to increase, and then there was a sudden movement and the LVDTs went backward, as can also be seen in Figure 3.52b) from H3 and H4.

The strain measurements at mid-section (section D) are presented in Figure 3.56, and at section H and I in the web (0.5m apart from the middle section for each side) in Figure 3.57.

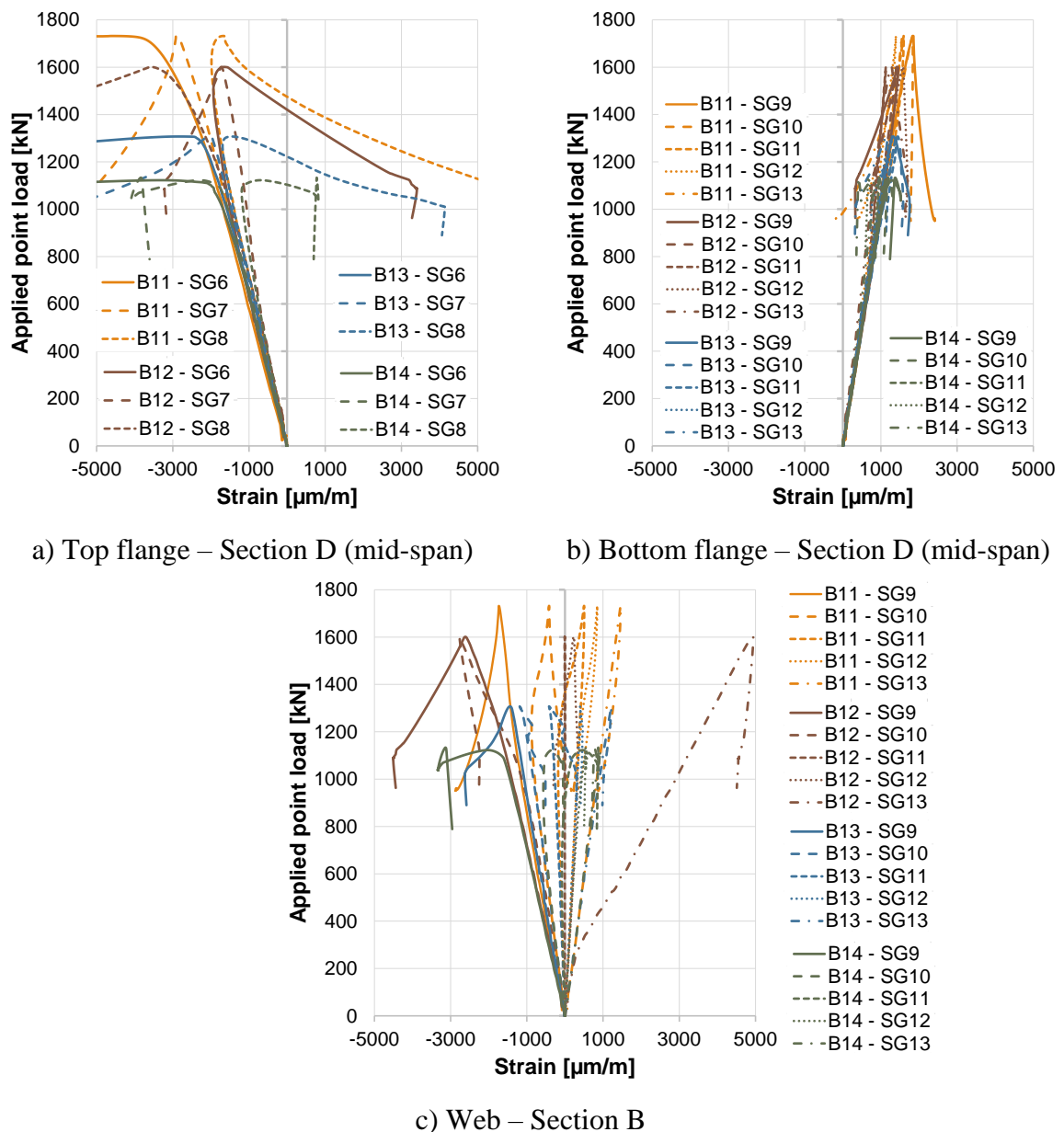


Figure 3.56 – Strain curves at section D (mid-span) for tests B11, B12, B13 and B14

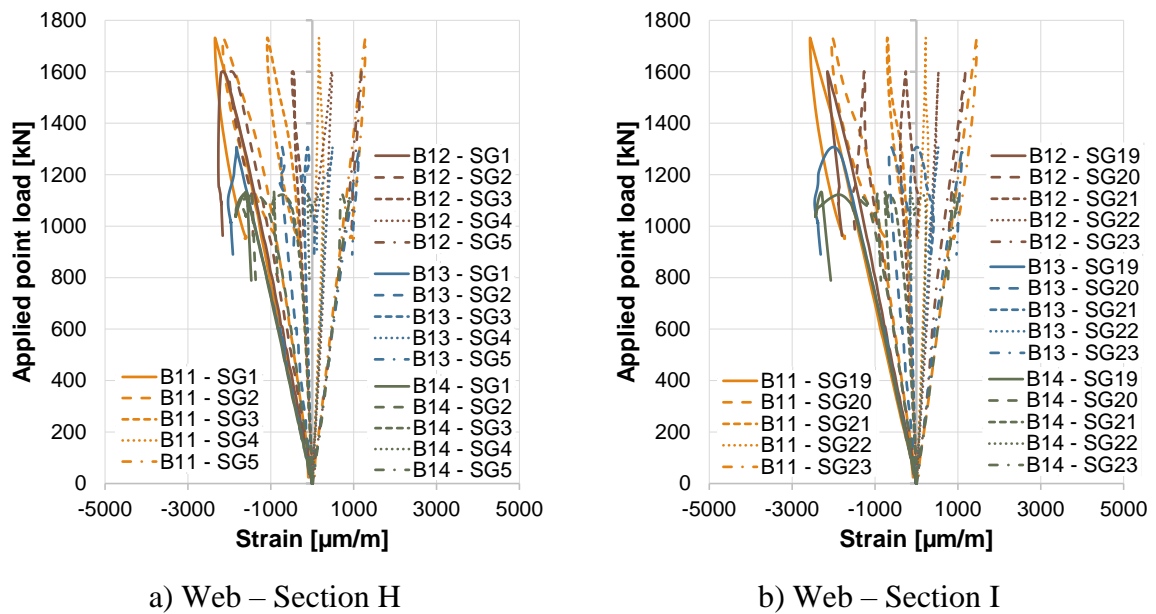


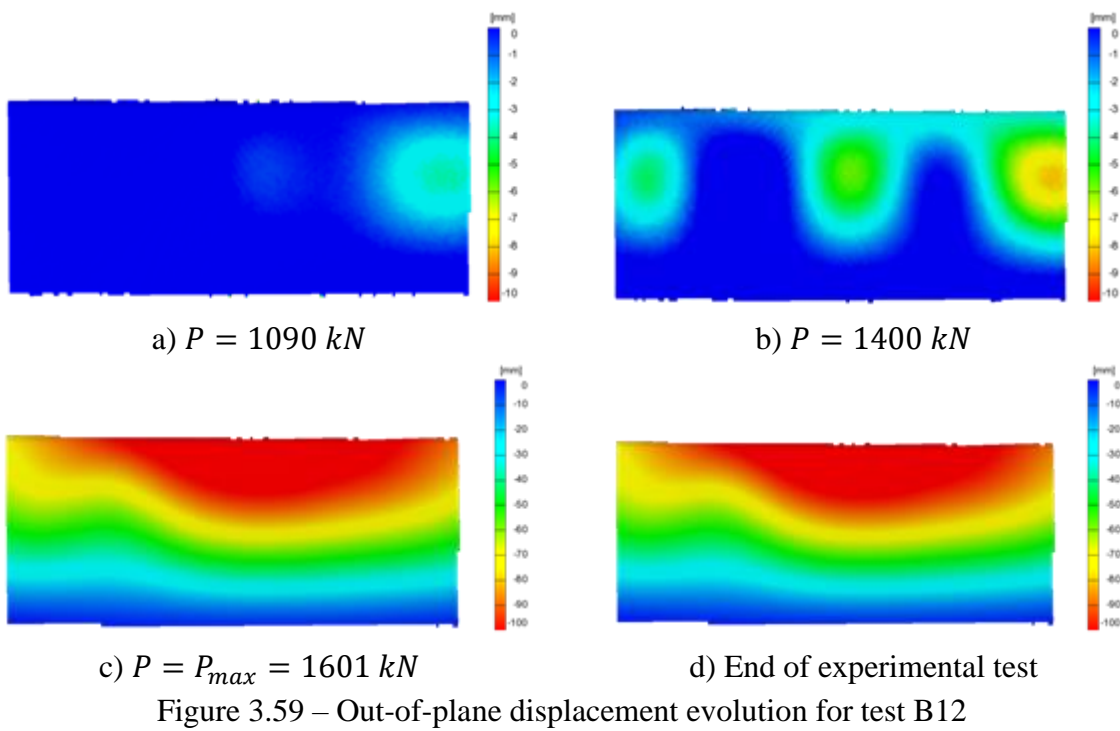
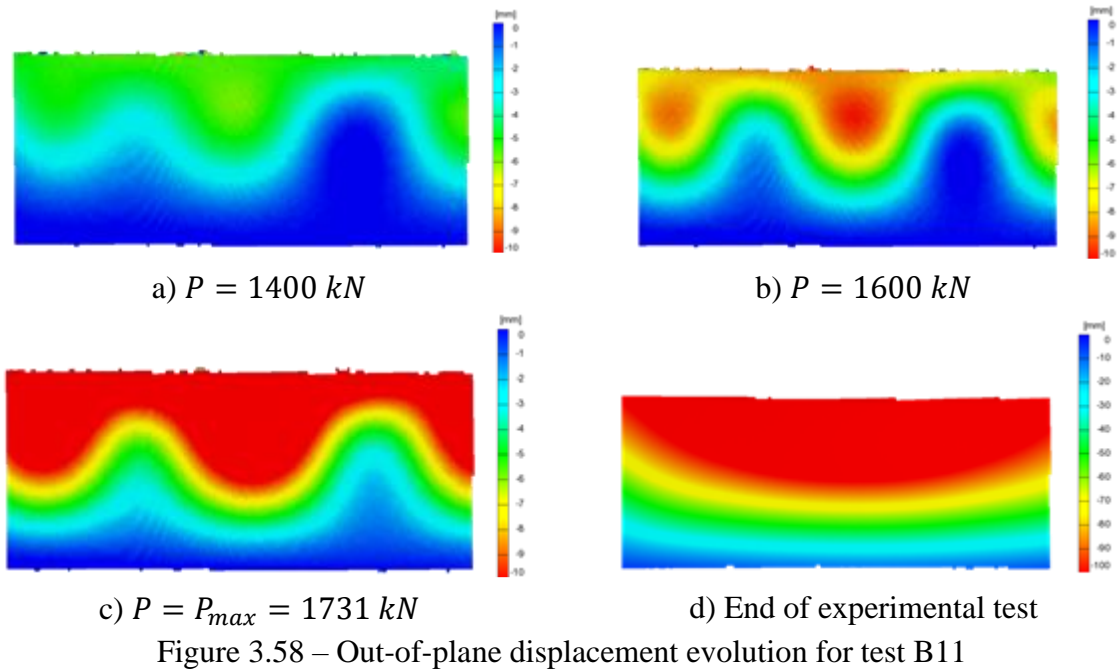
Figure 3.57 – Strain curves at sections H and I for tests B11, B12, B13 and B14

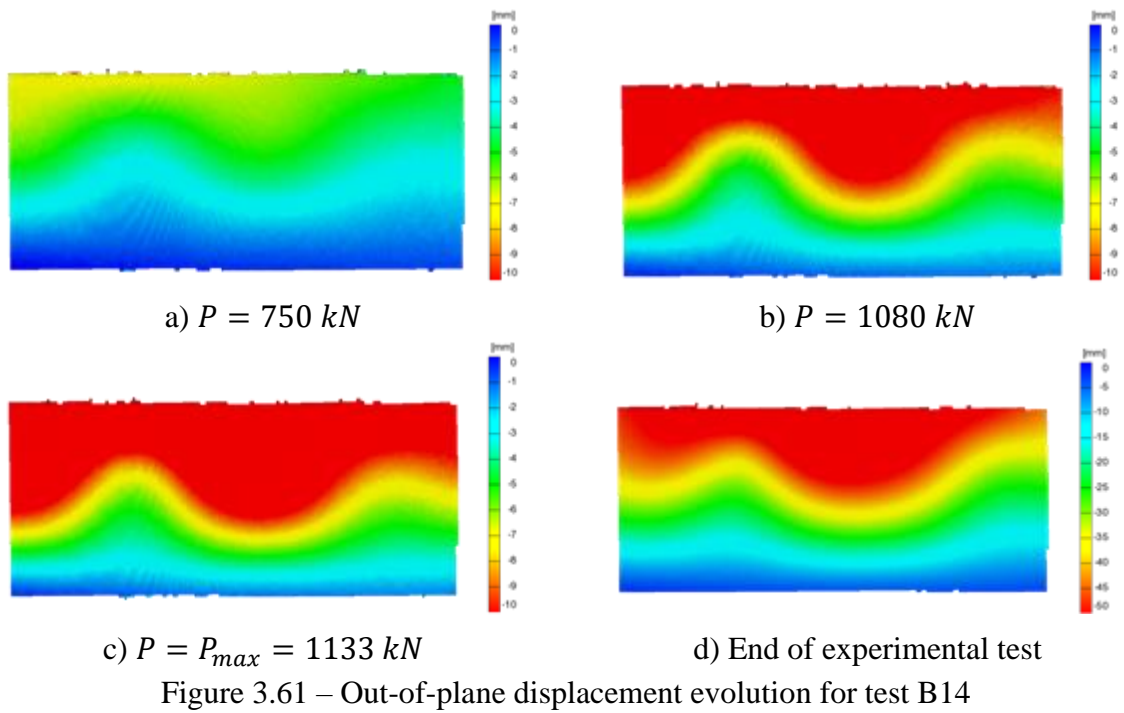
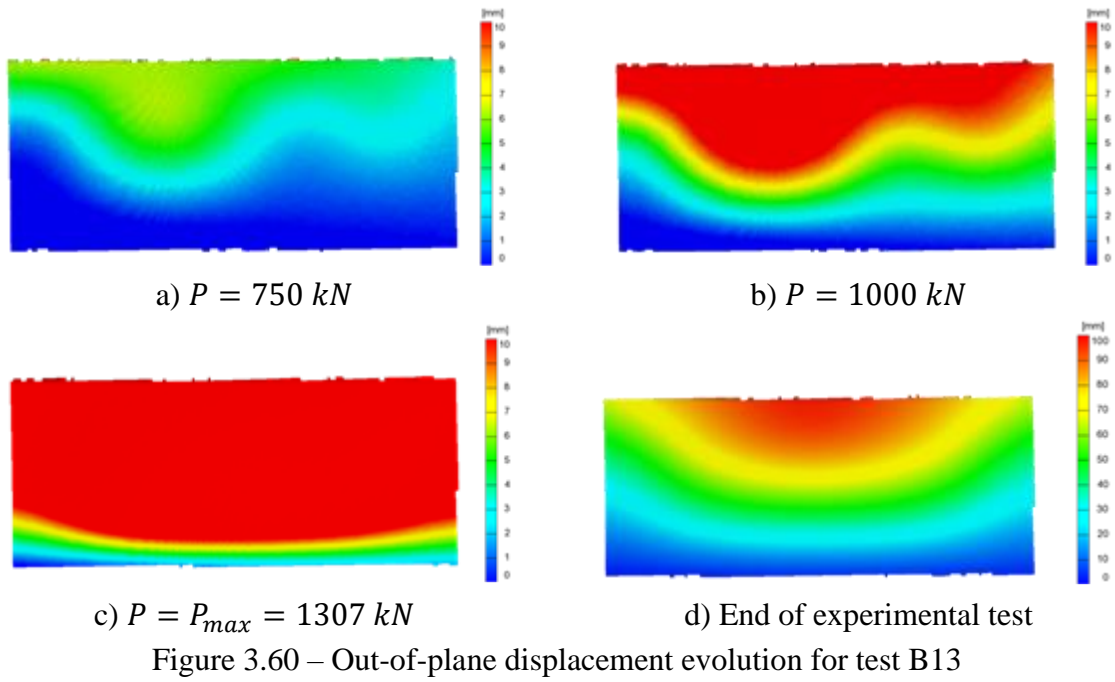
The strain measurements are in line with the previous results, showing the presence of lateral-torsional buckling, mainly through the strain variation at the top flange (Figure 3.56a), with compressive strains on one side and tensile strains on the other. On the web (Figure 3.57 and Figure 3.56c), the strain measurements show similar development in all sections, H, I, and D, with slightly higher magnitudes in the middle section (section D).

The DIC (digital image correlation) system, used during the experiments for the central web panel of the beam, especially for this last group of tests, B11-B14, allowed for a better understanding of the results since the monosymmetric sections were loaded with the smaller flange in compression and a larger part of the web was in compression.

Figure 3.58 to Figure 3.61 present some of the results obtained through the DIC system for specimens B11 to B14 for four load increments (two below the maximum load, one at the maximum load, and one at the end of the test). It was possible to observe local deformations of the webs during the tests since a mix of global and local behaviour was observed.

Through the performed measurements (Figure 3.58 to Figure 3.61), it can be seen that B11 and B13 (homogeneous beams) failed in a pure LTB mode even though local buckles were observed at lower load increments; whereas for B12 and B14 (hybrid beams), a mixed-mode was observed, even though the local buckles remained even after the maximum load was reached.





3.7. Stability design of high strength steel members

The experimental results of the lateral-torsional buckling tests, presented in Section 3.6.4, were further compared with the current Eurocode 3 [1] design rules for members in bending subjected to lateral-torsional buckling, namely, the general case and the special case, which were also presented in Section 2.4.2.

Figure 3.62 shows the comparison of the obtained buckling moment resistance using the methods provided by the code (general case and special case) and obtained experimentally (maximum bending moment applied during the experimental tests). The results clearly show the difference in buckling resistance between the actual rules provided by the code and the ones obtained experimentally, especially in the general case, where in the majority of the represented cases the code underestimates the resistance by 30% or more, pointing out the need for appropriate stability design rules for high strength steel members.

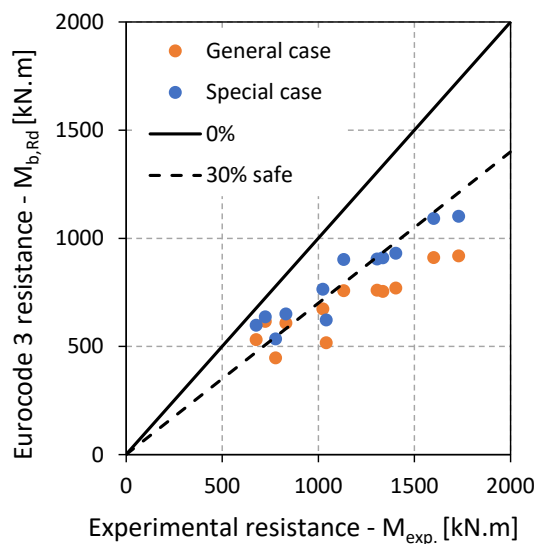


Figure 3.62 – Comparison between experimental and Eurocode 3 buckling moment resistance

The results were further assessed in terms of the buckling curve representation, whereas the experimental reduction factor was obtained according to Equation (3.1) as the ratio between the experimental resistance, denominated M_{exp} , and cross-section resistance. The cross-section resistance was obtained based on the measured yield strength ($f_{y,exp}$) in the tensile coupon tests performed (Section 3.6.1), and W is the appropriate section modulus, according to the cross-section class: (i) plastic section modulus (W_{pl}) for cross-sections class 1 or 2, (ii) elastic section

modulus (W_{el}) for cross-sections class 3, and (iii) effective section modulus (W_{eff}) for cross-sections class 4.

The experimental normalized slenderness, $\bar{\lambda}_{LT,exp}$, is calculated according to Equation (3.2), where the critical moment was obtained from a linear buckling analysis ($M_{cr,LBA}$).

$$\chi_{LT,exp} = \frac{M_{exp}}{W \cdot f_{y,exp}} \quad (3.1)$$

$$\bar{\lambda}_{LT,exp} = \sqrt{\frac{W \cdot f_{y,exp}}{M_{cr,LBA}}} \quad (3.2)$$

Table 3.10 shows the partial values used to calculate the lateral-torsional buckling reduction factor (χ_{LT}), both experimentally and using Eurocode 3 [1], in order to perform a buckling curve representation ($\bar{\lambda}_{LT}, \chi_{LT}$). The cross-section bending moment resistance ($M_{Rd,nom}$), buckling resistance moment ($M_{b,Rd(GC)}$) according to general case (Eurocode 3), and the normalized slenderness ($\bar{\lambda}_{LT,nom}$) were all obtained using nominal properties. Whereas the experimental values, $M_{Rd,exp}$ ($W \cdot f_{y,exp}$) and $\bar{\lambda}_{LT,exp}$ (Equation (3.2)), were based on the plate's material properties from the tensile coupon tests.

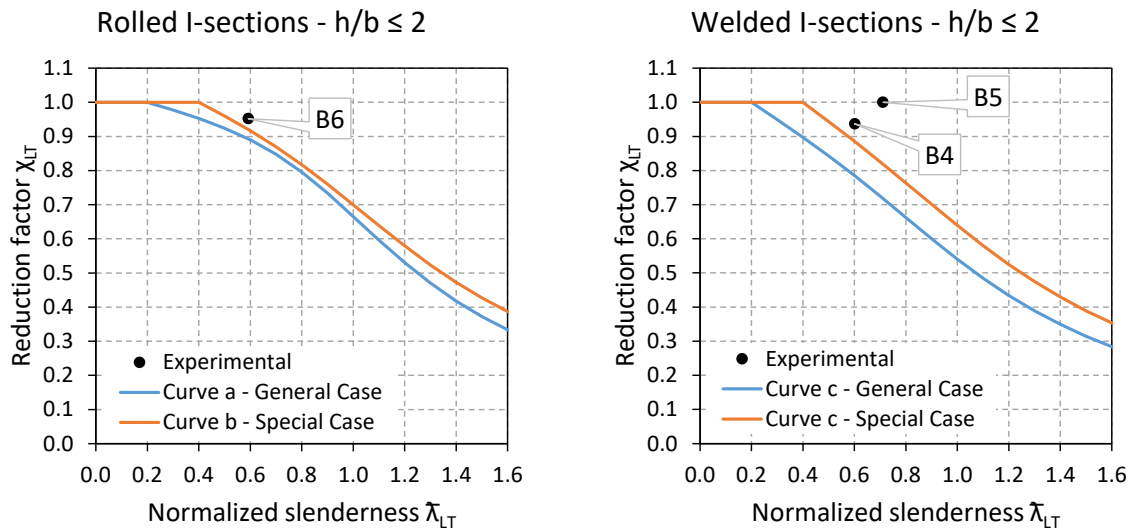
The nominal normalized slenderness ($\bar{\lambda}_{LT,nom}$) was calculated using the critical moment from the software LTBeam [67]. The differences in the critical moment obtained from the linear buckling analysis (LBA) and from the LTBeam are due to minor differences in geometrical properties and modulus of elasticity, where measured properties were used in the LBA and nominal properties were used in the LTBeam.

The buckling curves for the general case and special case (Eurocode 3) are represented in Figure 3.63 and Figure 3.64, together with the experimental results, split according to the Eurocode 3 provisions for rolled and welded sections with a ratio h/b less than or equal to two (Figure 3.63) or higher than two (Figure 3.64).

As can be seen from Figure 3.63 and Figure 3.64, in all cases, the experimental results are above the corresponding buckling curve, meaning that Eurocode 3 underestimates the member resistance, not taking full advantage of the use of high strength steel.

Table 3.10 – Comparison of critical moments and moment resistance

| Test | $M_{cr,LBA}$ [kN.m] | $M_{cr,LTBeam}$ [kN.m] | $M_{Rd,nom}$ [kN.m] | $\bar{\lambda}_{LT,nom}$ ($M_{cr,LTBeam}$) | $M_{b,Rd(GC)}$ [kN.m] | $M_{Rd,exp}$ [kN.m] | $\bar{\lambda}_{TL,exp}$ ($M_{cr,LBA}$) | M_{exp} [kN.m] |
|------|------------------------|---------------------------|------------------------|---|--------------------------|------------------------|--|---------------------|
| B1 | 996.20 | 1061.30 | 913.95 | 0.93 | 461.74 | 1004.31 | 1.00 | 779.37 |
| B2 | 1016.90 | 1061.30 | 1236.35 | 1.08 | 529.68 | 1403.66 | 1.17 | 1041.93 |
| B3 | 1023.30 | 1099.30 | 1009.24 | 0.96 | 629.52 | 1127.83 | 1.05 | 832.38 |
| B4 | 1995.60 | 2193.10 | 663.66 | 0.58 | 530.34 | 722.82 | 0.60 | 677.41 |
| B5 | 2027.40 | 2193.10 | 903.45 | 0.67 | 672.77 | 1024.41 | 0.71 | 1024.49 |
| B6 | 2175.40 | 2180.70 | 680.34 | 0.56 | 615.57 | 761.54 | 0.59 | 725.10 |
| B7 | 1457.00 | 1548.30 | 1944.99 | 1.16 | 767.47 | 2241.44 | 1.24 | 1404.90 |
| B8 | 1470.70 | 1548.30 | 1752.07 | 1.09 | 740.79 | 2128.05 | 1.20 | 1336.34 |
| B11 | 1925.30 | 1975.50 | 2006.95 | 1.02 | 916.22 | 2309.78 | 1.09 | 1731.80 |
| B12 | 1938.30 | 1975.50 | 1853.54 | 0.98 | 886.90 | 2276.71 | 1.05 | 1601.03 |
| B13 | 1887.20 | 1975.50 | 1391.85 | 0.86 | 757.82 | 1530.61 | 0.90 | 1307.18 |
| B14 | 1912.70 | 1975.50 | 1336.96 | 0.84 | 745.90 | 1515.07 | 0.88 | 1133.28 |


 Figure 3.63 – Comparison between experimental values and current design specifications from Eurocode 3 – $h/b \leq 2$

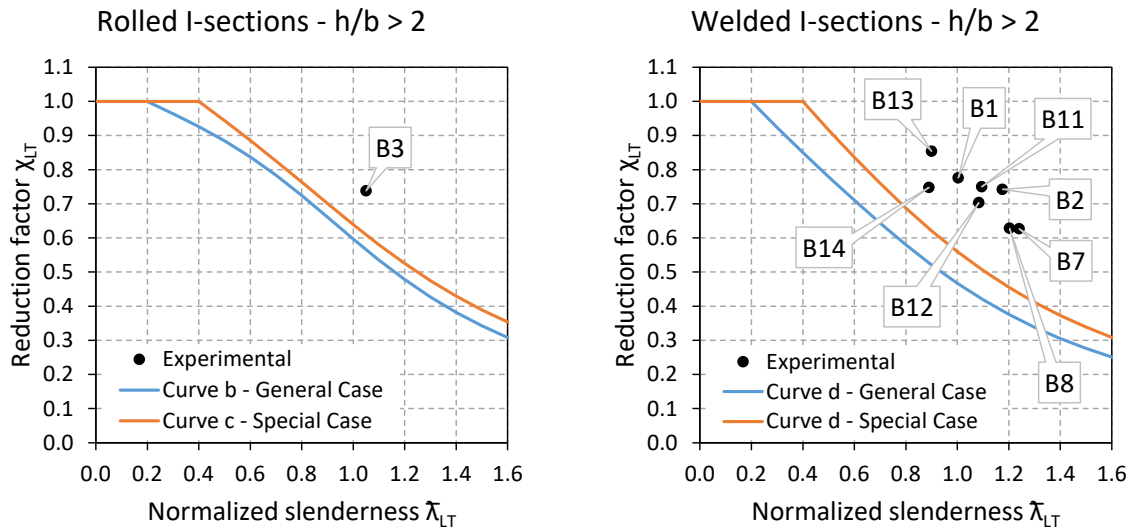


Figure 3.64 – Comparison between experimental values and current design specifications from Eurocode 3 – $h/b > 2$

This underestimation of the resistance can be due to the member imperfections, as the current design provisions in Eurocode 3 do not distinguish between the different steel grades, meaning that there is no difference in the stability design when using normal strength steel and high strength steel, and so assuming that the residual stresses have the same impact with the increase in the yield strength. As it was shown in Section 3.6.2, the magnitude of the residual stresses is not directly linked with the yield strength of the material, and the geometry of the cross-section also plays an important role in the magnitude and distribution of the residual stresses.

Nevertheless, the trends observed through the experimental campaign need to be exploited and extended for further assessment in order to provide adequate stability design rules for high strength steel members.

4. Numerical studies

4.1. Numerical model

Although the experimental tests were performed by varying several parameters, such as steel grade and cross-section geometry, the number of results is still insufficient if it is intended to assess design rules or to calibrate new design rules. Nowadays, the computational resources allow to carry out a large number of simulations in a relatively short amount of time, which can be used to extend the scope of the experimental studies.

Hence, the adopted approach was to use advanced numerical models to reproduce the experimental tests.

This section illustrates how the advanced numerical models were implemented by describing the choice of the key parameters in order to properly represent the experimental tests. The models were developed using the software ABAQUS [68] with shell elements.

The stability of members is highly influenced by the members' imperfections, such as geometrical imperfections and residual stresses. Thus, in order to ensure the highest accuracy, the numerical analyses were performed using a geometrical and material non-linear analysis with imperfections included. To perform this type of analysis, also known as GMNIA, firstly, the geometrical imperfections must be introduced/considered in the numerical model. In this work, the geometrical imperfections are introduced into the numerical model through two different approaches: i) by using the measured imperfections; ii) by previously performing a linear buckling analysis (LBA) as to obtain the imperfection shape for the relevant buckling mode.

4.1.1. Geometry

The geometry of the numerical model consists in modelling the beams cross-section with the dimensions presented in Table 3.1, where the shell reference lines for the flanges thickness were considered to be such that there is no intersection with the web, to avoid material overlap. The cross-section geometry was extruded to 6m length, and the stiffeners were linked to the web using a tie constraint. The stiffeners at both ends of the beam were modelled using the coupling constraint available in ABAQUS [68] software, with the aim of coupling all the beam cross-section points at both ends of the beam to the cross-section mid-point.

The model was created with shell elements, using the type of element S4R, a four-node element with reduced integration and six degrees of freedom per node.

The adopted mesh was kept constant along the member size and the same for all types of beams, with a 10mm mesh size.

Figure 4.1 represents the geometry of the model.

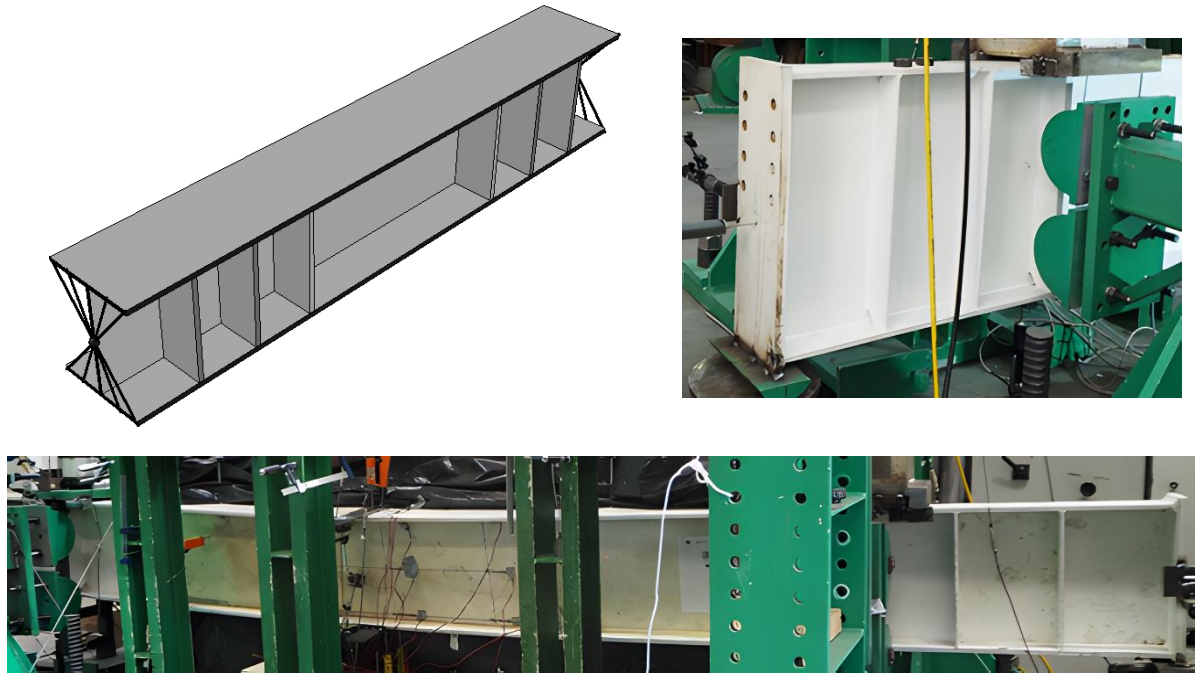
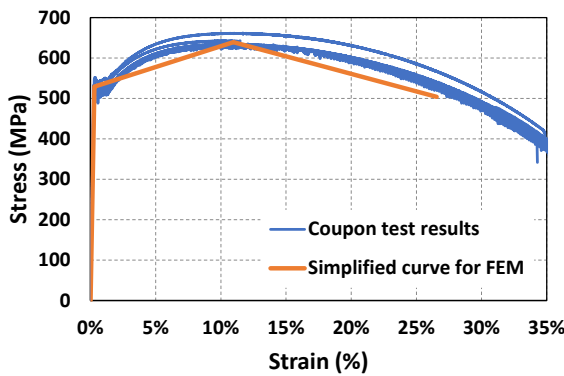


Figure 4.1 – Model geometry

4.1.2. Material properties

The material properties used in the numerical model are based on the coupon tests performed for each plate, whose results were previously presented in Section 3.6.1. As a simplification of the whole set of points that defines the stress-strain curve obtained for each plate, for the numerical model, the experimental curve is simplified using three points: i) upper yield strength, R_{eH} ; ii) ultimate tensile strength, R_m ; and iii) ultimate strain, ϵ_u .

Then, the values are converted in true-stress and true-strain, to introduce in the model as input values (Figure 4.2).



$$(1) \sigma_{true} = \sigma_{eng}(1 + \varepsilon_{eng})$$

$$(2) \varepsilon_{pl} = \ln(1 + \varepsilon_{eng}) - \frac{\sigma_{true}}{E}$$

| Young's Modulus | Poisson's Ratio |
|-----------------|-----------------|
| 210 GPa | 0.3 |
| Yield Stress | Plastic Strain |
| 530.414 MPa | 0 |
| 709.264 MPa | 0.101 |
| 637.655 MPa | 0.232 |

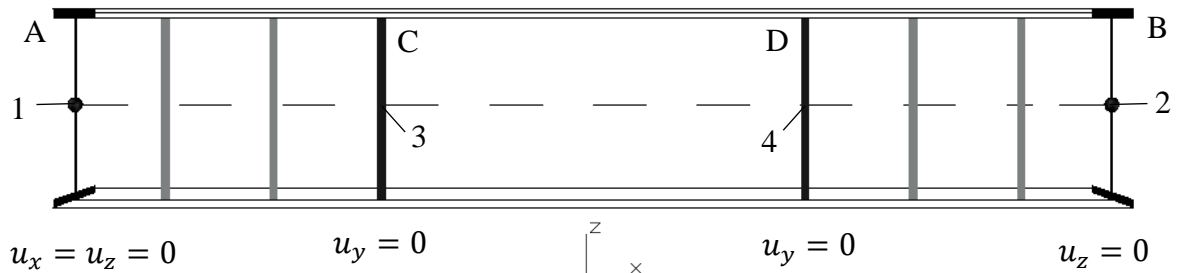
Convert into true-stress and true plastic strain - (1)
and (2) → Input values for FEM

Input values

Figure 4.2 – Material properties

4.1.3. Boundary conditions

The boundary conditions adopted for the numerical model and represented in Figure 4.3 are based on a simply supported beam. Whereby, at the end sections (sections A and B), the vertical displacements were prevented and, at the end of a section (section A), the longitudinal displacement was also prevented. At the load application points (sections C and D), the lateral displacement was prevented at the stiffeners.



(1) – Horizontal and vertical displacements prevented.

(3) and (4) – Lateral displacement prevented.

(2) – Vertical displacement prevented.

Figure 4.3 – Boundary conditions

It is worth mentioning that, for the experimental tests B1 to B6, the rollers were acting on the whole length of the stiffener, whereas for the numerical models for beams B1 to B6, the lateral displacement is blocked along the whole stiffener length, as represented in Figure 4.4.

For tests B7, B8 and B11 to B14, the rollers were not acting on the whole stiffeners' length, only touching them in some areas. For this reason, in the numerical models (for beams B7, B8 and B11 to B14), the lateral displacements were prevented at a certain area, according to what was observed during the experimental tests, as shown in Figure 4.5.

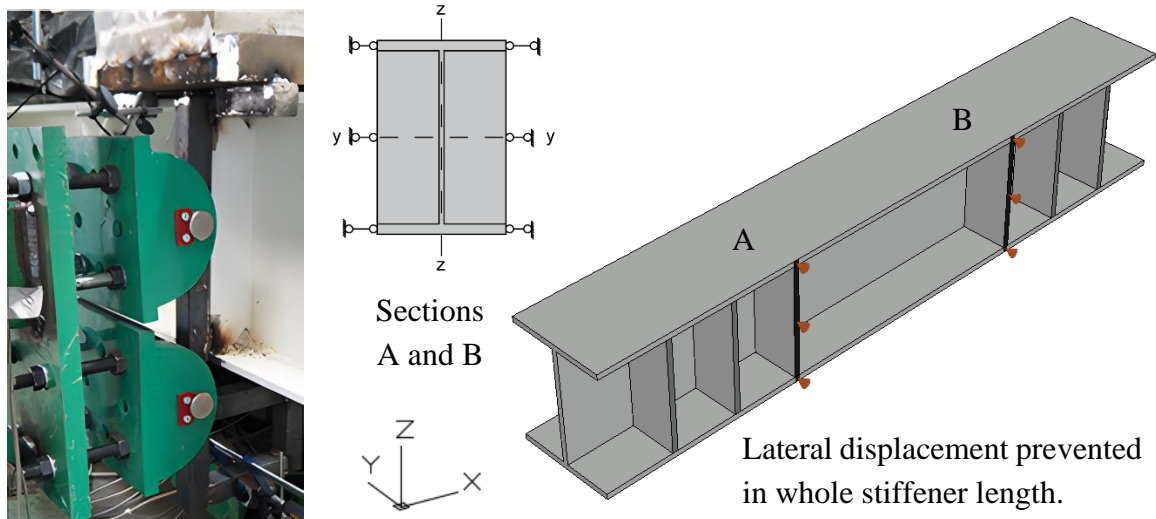


Figure 4.4 – Lateral displacement prevented at load application point – models B1 to B6

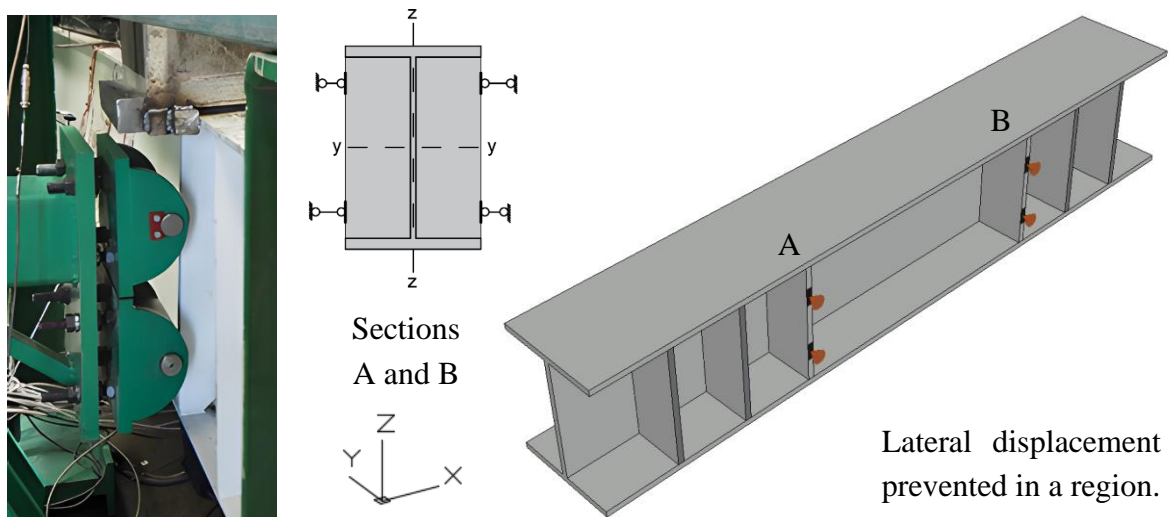


Figure 4.5 – Lateral displacement prevented at load application point – models B7, B8 and B11 to B14

4.1.4. Loading

The loads are applied 1m apart from the end sections at the top of the flange, as shown in Figure 4.6. The load is introduced in the numerical model through the application of a vertical displacement with a displacement amplitude similar to that observed in the experimental test.

The GMNIA analysis is carried out through a Static-Riks solver analysis.

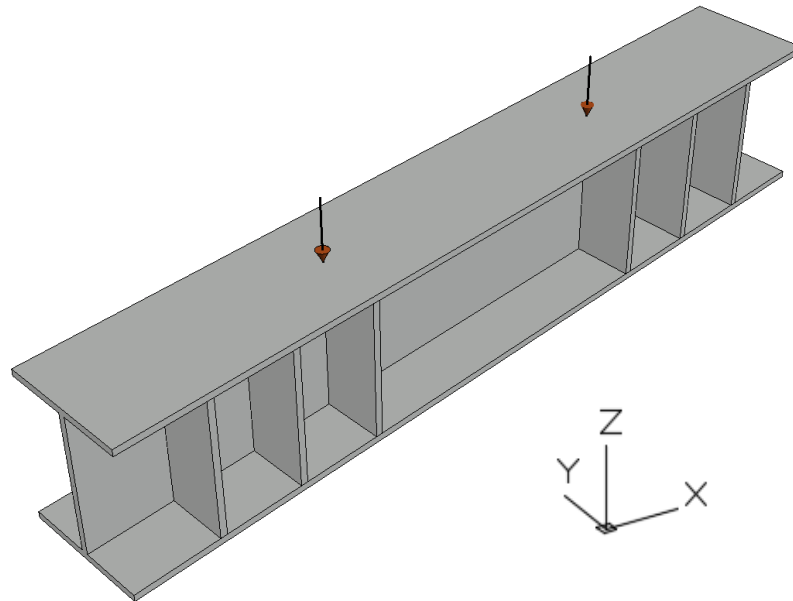


Figure 4.6 – Load application

4.1.5. Imperfections – Residual stresses

The residual stresses are introduced in the numerical model using the predefined fields tool, where a constant stress value is introduced along the members, in the intended direction, into the numerical model before applying any type of loading.

The residual stresses patterns adopted for models B1 to B8 and B11 were based on the average values obtained in the residual stresses measurements performed for these specimens (see Section 3.6.2).

Since for the beams B12, B13, and B14, no residual stresses measurements were specifically performed, whereby the strategy adopted for the residual stresses pattern to introduce in the numerical model was the following: for the tension flange and web, the residual stresses were assumed to be equal to those of test B11, and for the compression flange, the residual stresses were taken as the average values of the measurements from B7, B8, and B11, since they have the same geometry.

The residual stresses measurements collected from the tests are then converted into a constant equivalent value in order to introduce the residual stresses in the numerical model in different partitions along the member, as represented in Figure 4.7.

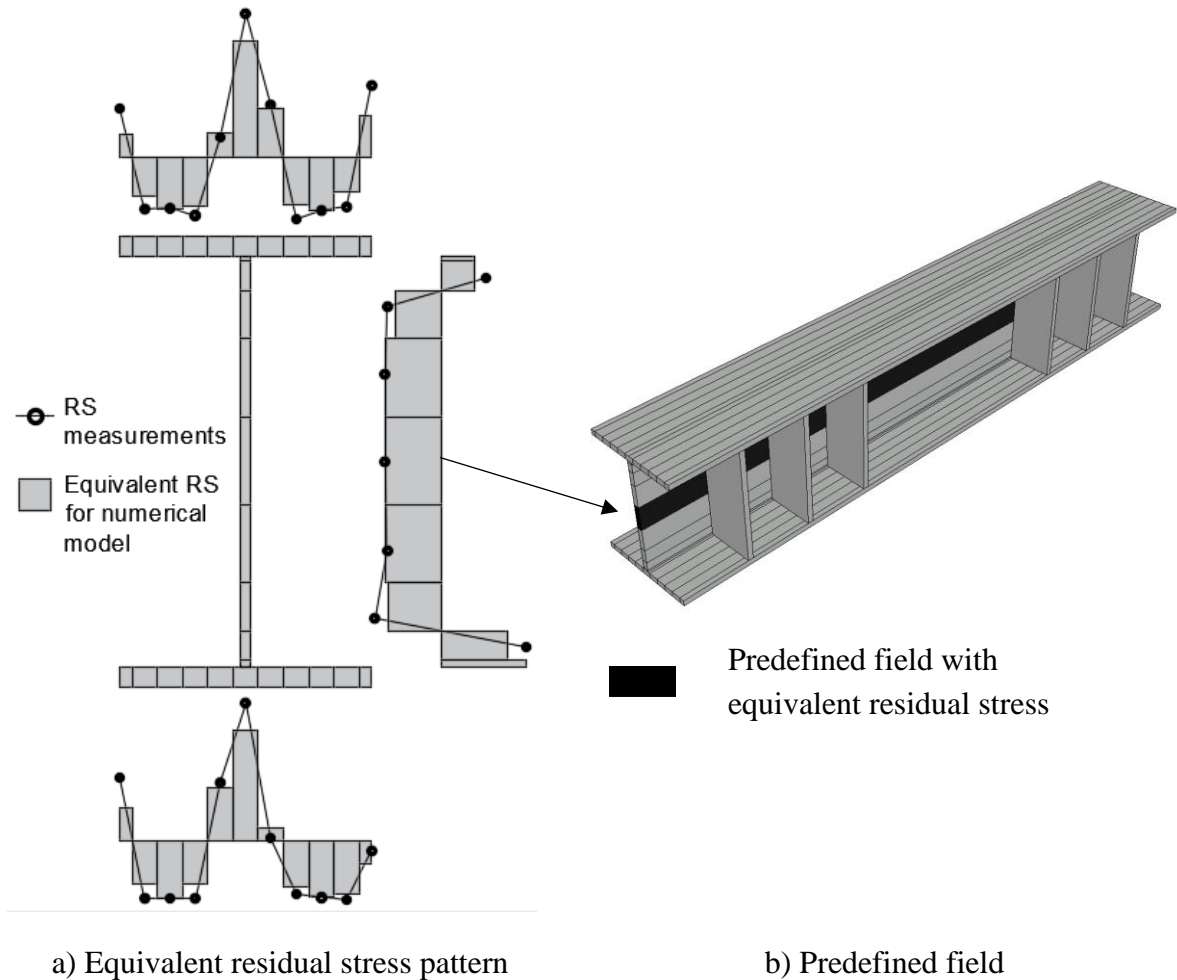
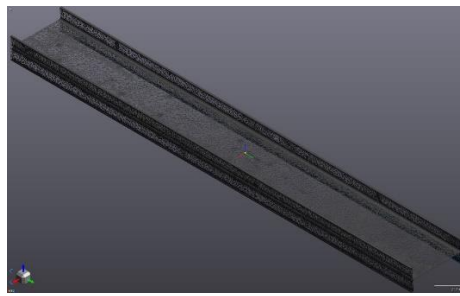


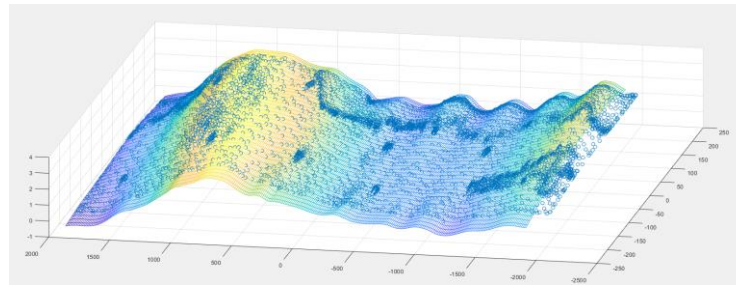
Figure 4.7 – Residual stress input for numerical model

4.1.6. Geometrical imperfections

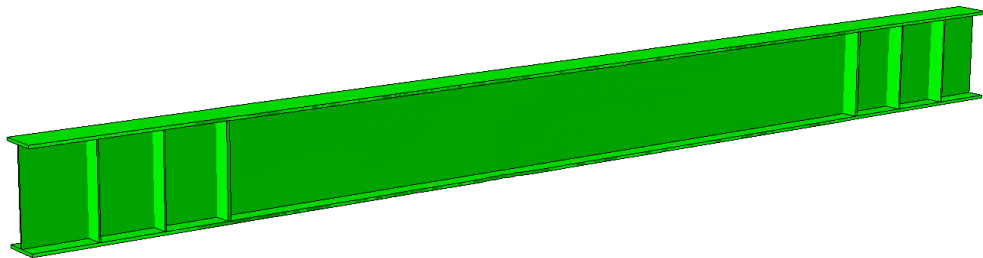
The geometrical imperfections measured through the digital scanning system (results presented in Annex A) were introduced in the numerical model using a MATLAB [69] subroutine which interpolates the geometrical imperfections measured into the finite element mesh chosen for the respective numerical model. Hence, the geometry of the numerical model has the real dimensions of the measured beam (Figure 4.8).



a) Measured dimensions



b) Interpolation between measured imperfections and finite element mesh



c) Numerical model with real imperfections

Figure 4.8 – Numerical model with geometrical imperfections

4.2. Calibration to experimental results

In this section, the numerical results are compared with the experimental results. The main objective of this comparison is to validate the modelling strategy and further apply it in order to extend the scope of the buckling resistance of high strength steel members with numerical experiments.

As it was previously done when presenting the experimental results (Section 3.6.4), the comparison between the numerical and experimental results is performed separated into four groups according to cross-section dimensions: i) Tests B1, B2, and B3; ii) Tests B4, B5, and B6; iii) Tests B7 and B8; and iv) Tests B11, B12, B13, and B14.

4.2.1. Results for tests B1, B2, and B3

The first set of results is composed of the beams with 500mm depth, where beams B1 and B2 are welded sections made of steel grade S460 and S690, respectively, and beam B3 is the equivalent rolled section (IPE 500) made of steel grade S460.

The calibration is firstly performed through the comparison of the numerical and experimental load-displacement curve presented in Figure 4.9 for beams B1, B2, and B3. The load applied and the vertical displacement at the load application point are plotted for one point of load application (referred to as V1 in the experimental tests – see Section 3.5), since the obtained results were equivalent with the other point of load application and therefore it was chosen not to present them. It is observed that the numerical curve closely follows the experimental behaviour at the load application point for both tests (B1, B2, and B3) and that the numerical initial stiffness is almost the same as the experimental one.

The predicted maximum loads by the numerical model are given in Table 4.1 in comparison with the maximum load obtained in the experimental test. A good agreement is found for the three beams, with a maximum error smaller than 4%, obtained for beam B2 and errors of approximately 2% and 1% for beams B2 and B3, respectively.

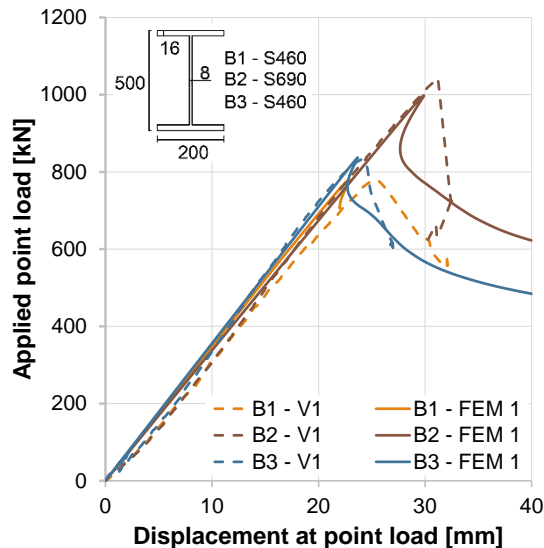


Table 4.1 – Maximum applied load

| Test | P_{max} [kN] Experimental | P_{max} [kN] Numerical | Error |
|------|--------------------------------|-----------------------------|--------|
| B1 | 779.37 | 797.32 | 2.30% |
| B2 | 1041.42 | 1002.32 | -3.75% |
| B3 | 829.75 | 837.09 | 0.89% |

Figure 4.9 – Vertical displacements at load application point – experimental and numerical

Further comparisons between experimental and numerical were performed in terms of vertical and horizontal displacements. Figure 4.10 and Figure 4.11 present the comparison of the vertical and horizontal displacements along the beams, numerical (solid lines) and experimental (dashed lines), at the moment of maximum load applied. A good agreement is also found for horizontal and vertical displacements for the three beams, where the difference between the numerical and experimental values for the vertical displacement at mid-span is of approximately 10% for the three tests, and of less than 10% for tests B1 and B2, and of 35% for test B3 for the horizontal displacements at mid-span, as it can be seen in Table 4.2.

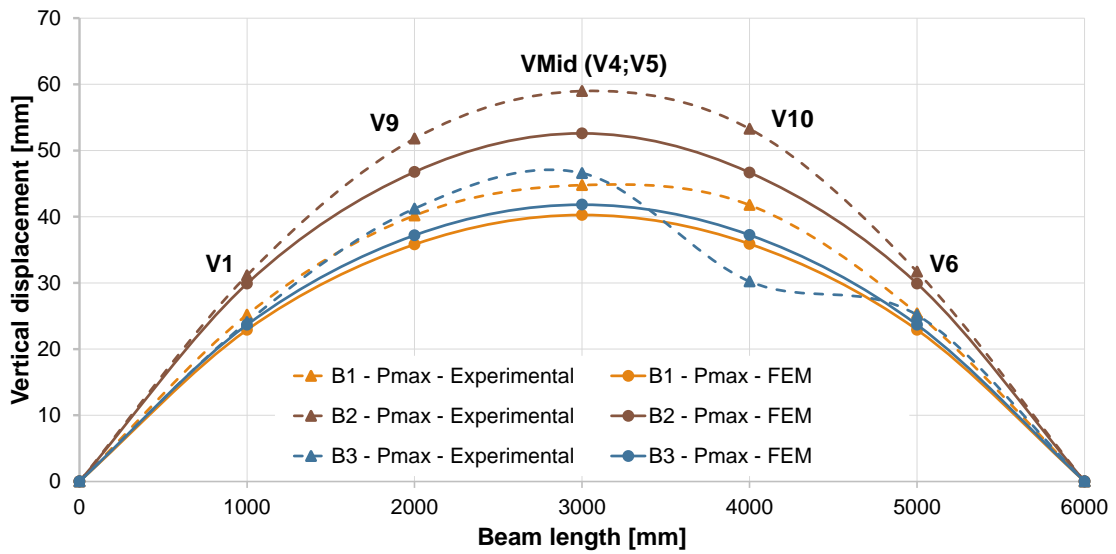


Figure 4.10 – Vertical displacements at maximum load – experimental and numerical

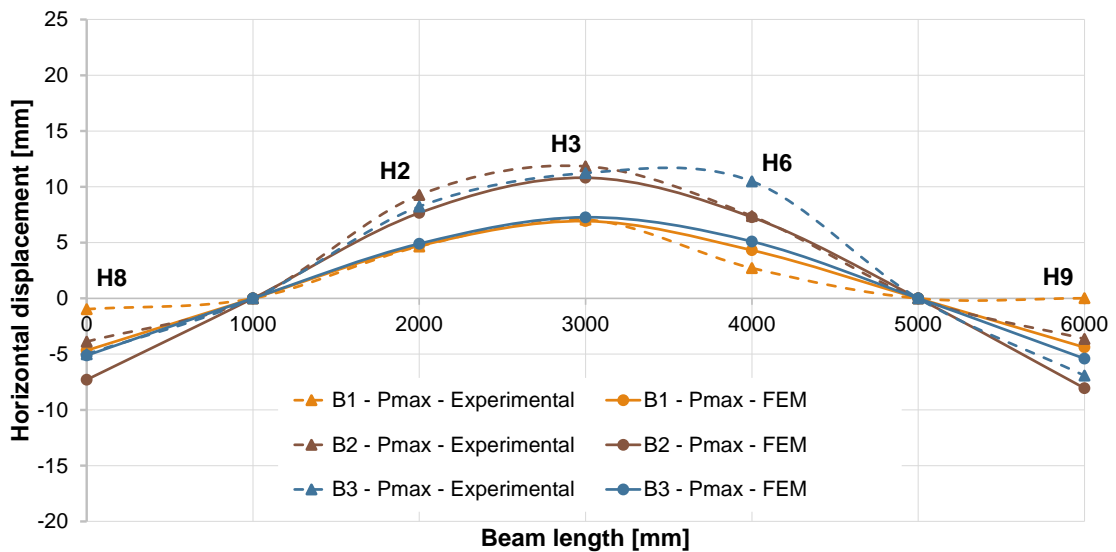


Figure 4.11 – Horizontal displacements at maximum load – experimental and numerical

The comparison between the experimental and numerical failure modes was also assessed, where Figure 4.12 represents the cross-section deformation at mid-span at maximum load and after reaching the maximum load, for the three beams. Lateral-torsional buckling was observed for the three beams, as it was obtained in the experimental tests (see Figure 3.37). After reaching the maximum load, the horizontal displacements start to increase significantly. An example of the lateral-torsional buckling shape obtained in the numerical model (similar for tests B1, B2, and B3) for test B2 is presented in Figure 4.13.

Table 4.2 – Horizontal and vertical displacements at mid span – experimental and numerical

| Test | Vertical displacement at mid span (VMid) – Maximum applied load | | | Horizontal displacement at mid span (H3) – Maximum applied load | | |
|------|--|-------------------|------------------|--|-------------------|------------------|
| | Experimental [mm] | Numerical [mm] | Deviation [%] | Experimental [mm] | Numerical [mm] | Deviation [%] |
| B1 | 44.78 | 40.25 | -10.12 | 7.06 | 6.93 | -1.89 |
| B2 | 58.99 | 52.58 | -10.87 | 11.83 | 10.81 | -8.62 |
| B3 | 46.58 | 41.81 | -10.24 | 11.23 | 7.26 | -35.35 |

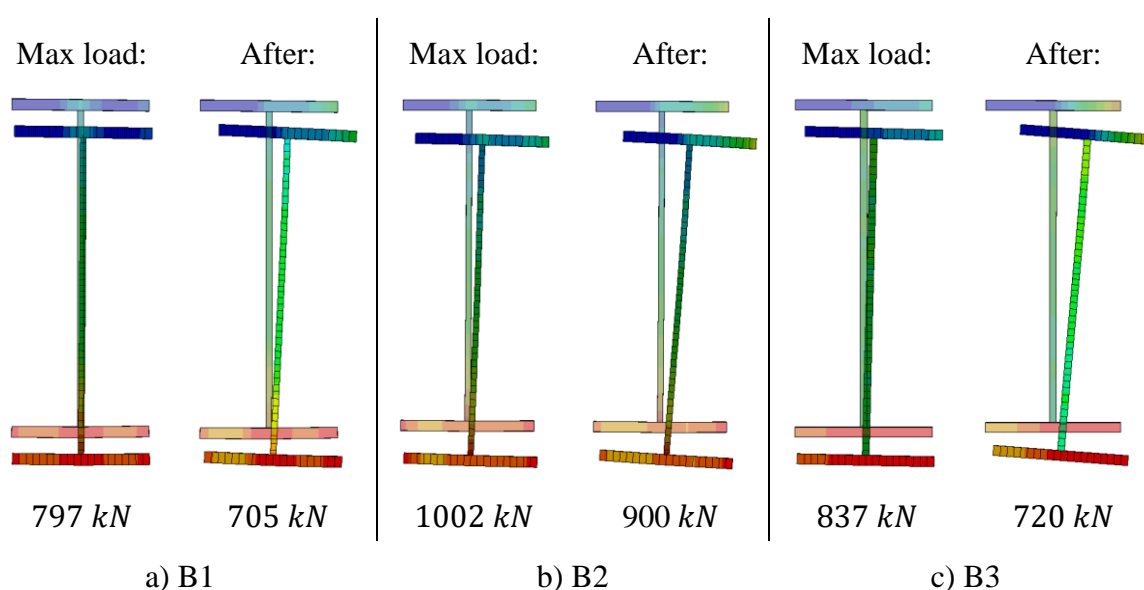


Figure 4.12 – Cross-section deformation at mid-span at maximum load and after maximum load – numerical model

In order to assess if the assumed simplified curves (described in Section 4.1.2) for the material properties in the numerical models are in line with the tensile coupon tests performed for each plate (Section 3.6.1), for each test (B1, B2, and B3), the stress and strain of the point with maximum strain in the middle region of the top flange at maximum load in the numerical model were extracted, converted into engineering stress and strain, and plotted into the curves obtained from the tensile coupon tests. The obtained results are presented in Figure 4.14, split according to the flange steel grade, where the black dots represent the stress and strain extracted from the numerical models. As it can be seen, the strains in the numerical models for all the tests (B1, B2, and B3) are very close to the measured yield strain from the tensile coupon tests, whereby the simplified curves for the material properties are accurate for this type of failure.

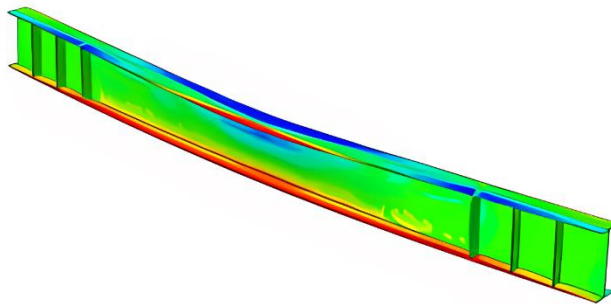
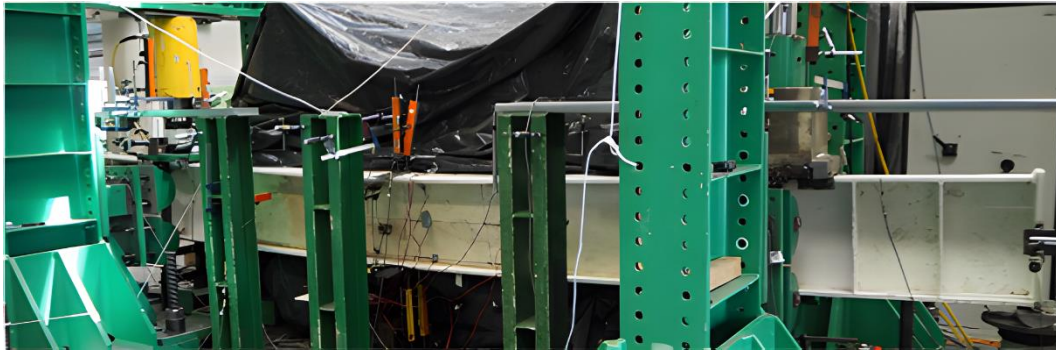
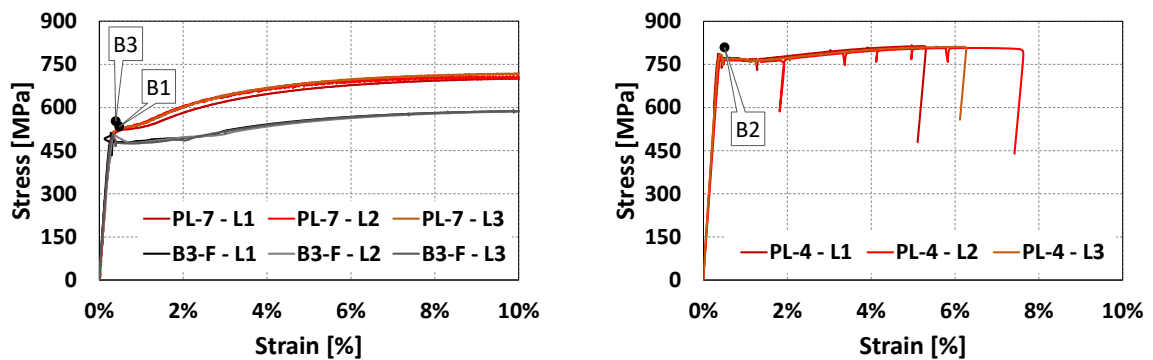


Figure 4.13 – Example of the failure mode for test B2



a) Flange steel grade: S460

b) Flange steel grade: S690

Figure 4.14 -Strains (top flange) at maximum load

4.2.2. Results for tests B4, B5, and B6

The second group of beams is composed of the beams with 310mm depth, where beams B4 and B5 are welded sections made of steel grade S460 and S690 respectively, and beam B3 is the equivalent rolled section (HE 320A) made of steel grade S460.

The assessment of the results/calibration of the numerical model is carried out in the same way as in the previous group of tests.

Figure 4.15 depicts the load-displacement (vertical) curve at one point of load application (referred to as V1 – see Section 3.5) and Table 4.3 shows the difference between the maximum load obtained experimentally and numerically for the three tests performed.

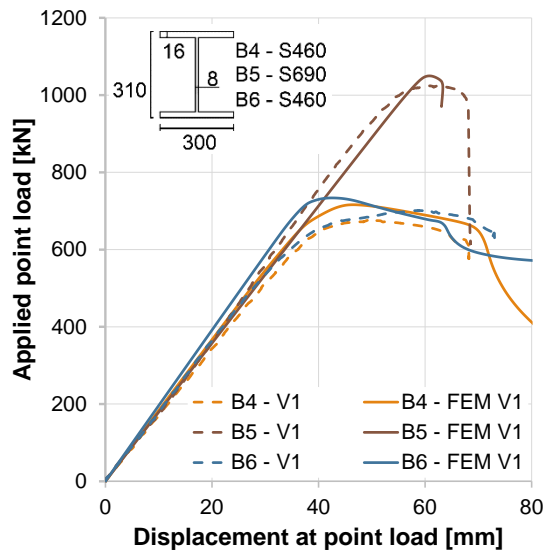


Table 4.3 – Maximum applied load

| Test | P_{max} [kN] Experimental | P_{max} [kN] Numerical | Error |
|------|--------------------------------|-----------------------------|-------|
| B4 | 675.21 | 716.14 | 6.06% |
| B5 | 1024.49 | 1052.90 | 2.77% |
| B6 | 725.10 | 733.79 | 1.20% |

Figure 4.15 – Vertical displacements at load application point – experimental and numerical

For all the beams of this group (B4, B5, and B6), the numerical model represents the behaviour observed in the experimental tests with good accuracy. In terms of the maximum loads applied, the differences obtained are of less than 3% for tests B5 and B6, and of less than 6% for test B4, which is still not a significant difference.

Figure 4.16 and Figure 4.17 represent the vertical and horizontal displacements along the beams at maximum load, obtained experimentally and numerically. The differences in the displacements (both vertical and horizontal) are on average smaller than 10%, as it can be seen from Table 4.4, where the maximum difference is found for the vertical displacement at mid span for beam B6 (22% difference) and the remaining displacements with differences of less than 10%.

For all the three numerical models, lateral-torsional buckling was observed with large lateral displacements after reaching the maximum load, as depicted in Figure 4.18, which is in agreement with the observation registered during the experimental tests (see Figure 3.44). An example of the buckling mode obtained in the numerical model for test B5 (and similar for the three beams) is presented in Figure 4.19.

As previously done for the first group of tests, the accuracy of the simplified curves for the material properties was assessed for this group of tests. The results are represented in Figure 4.20, where the extracted stress and strain (from the numerical models) match the coupon test results for the yield strain for B4 and B6. For B5, it is slightly above, yet still quite close to the yield strain from the tensile coupon test, confirming the accuracy of the simplified approach.

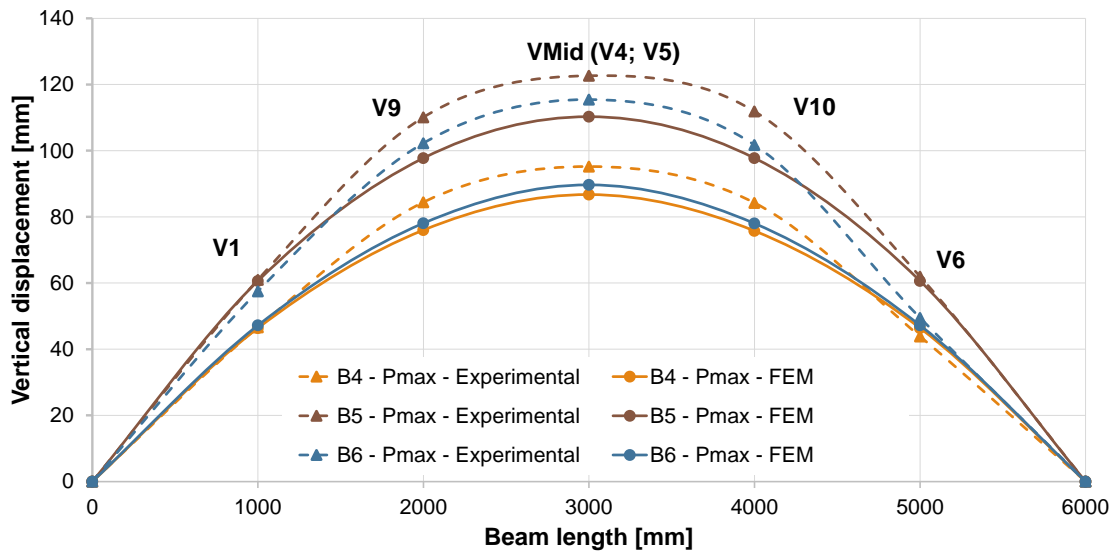


Figure 4.16 – Vertical displacements at maximum load – experimental and numerical

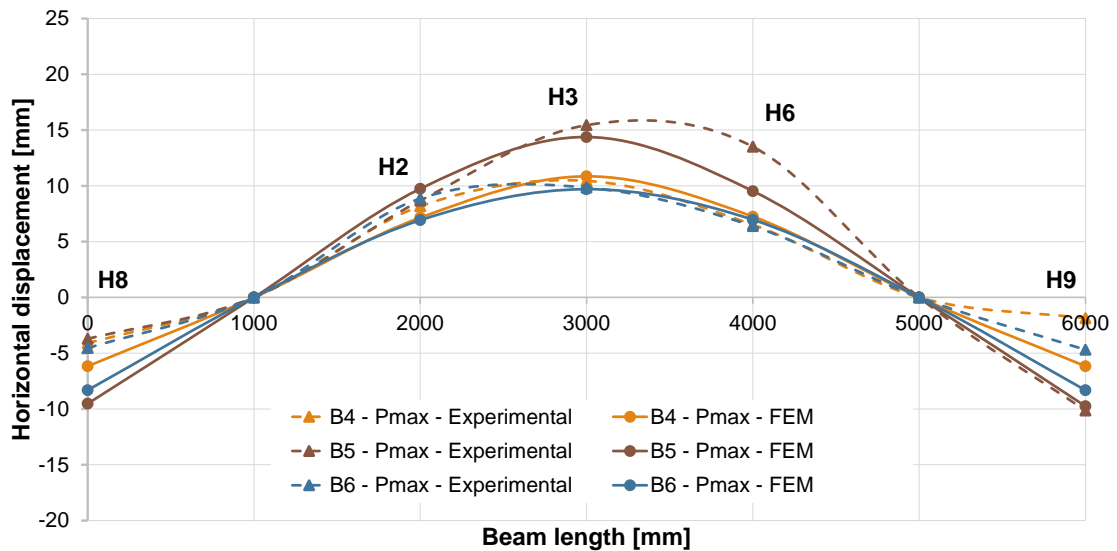


Figure 4.17 – Horizontal displacements at maximum load – experimental and numerical

Table 4.4 – Vertical and horizontal displacements at mid span – experimental and numerical

| Test | Vertical displacement at mid span (VMid) – Maximum applied load | | | Horizontal displacement at mid span (H3) – Maximum applied load | | |
|------|---|----------------|---------------|---|----------------|---------------|
| | Experimental [mm] | Numerical [mm] | Deviation [%] | Experimental [mm] | Numerical [mm] | Deviation [%] |
| B4 | 95.20 | 86.75 | -8.80 | 10.45 | 10.85 | 3.82 |
| B5 | 122.63 | 110.28 | -10.07 | 15.44 | 14.37 | -6.93 |
| B6 | 115.45 | 89.68 | -22.31 | 9.85 | 9.70 | -1.61 |

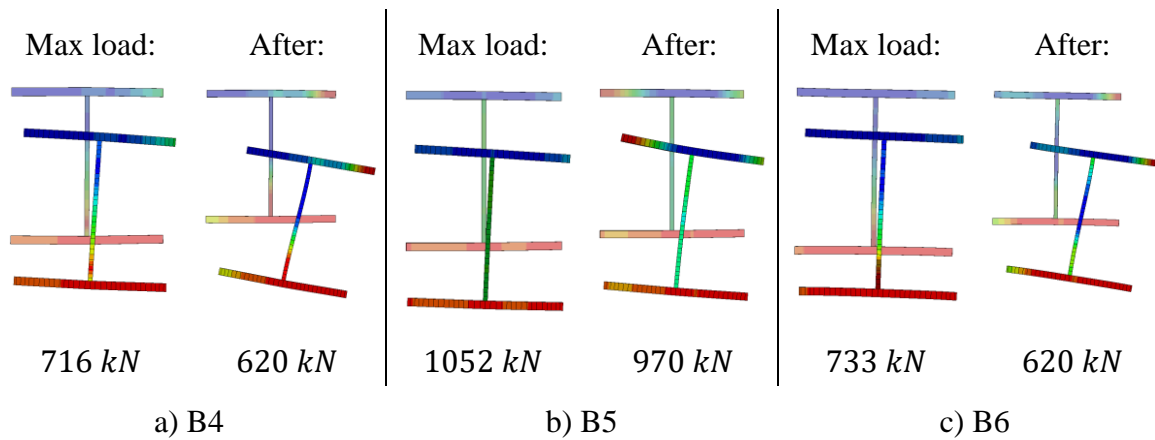


Figure 4.18 – Cross-section deformation at mid-span at maximum load and after maximum load – numerical model

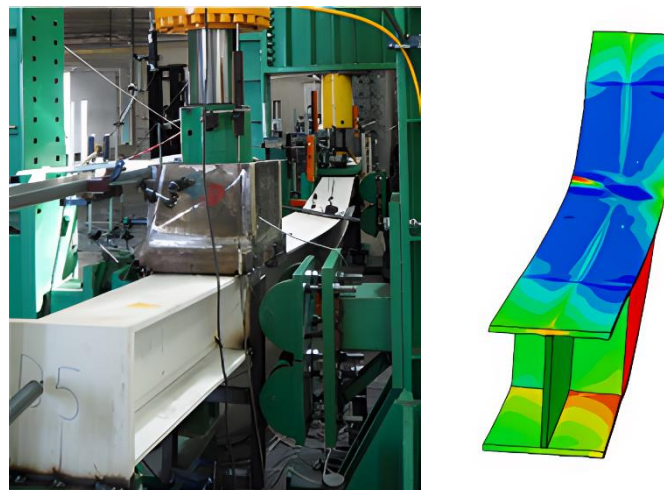


Figure 4.19 – Example of the failure mode for test B5

The vertical and horizontal displacements obtained at maximum load experimentally and numerically are plotted in Figure 4.22 (vertical displacements) and Figure 4.23 (horizontal displacements), along the beams. The difference between the experimental and numerical displacements at mid-span (vertical and horizontal) is presented in Table 4.7. In terms of the vertical displacements, the difference is of less than 5% for both beams and for the horizontal displacements is of approximately 14% for beam B7 and of 10% for beam B8.

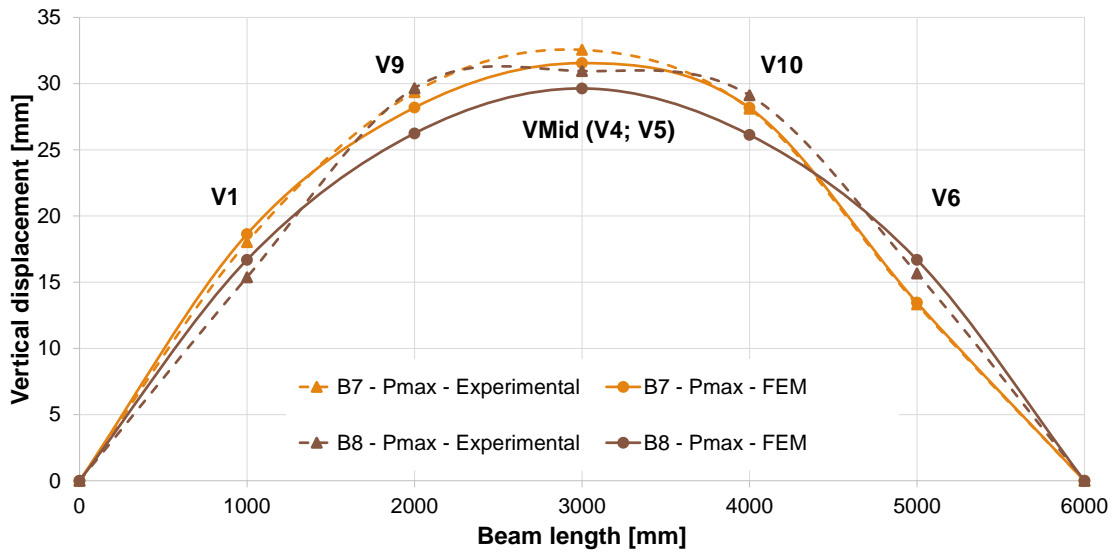


Figure 4.22 – Vertical displacements at maximum load – experimental and numerical

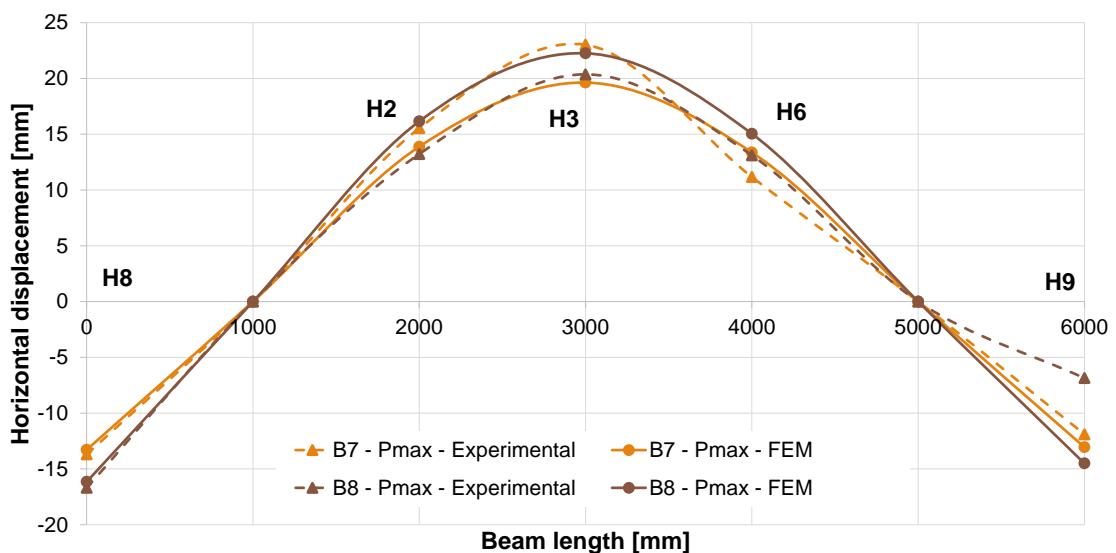


Figure 4.23 – Horizontal displacements at maximum load – experimental and numerical

The buckling mode observed in the experimental tests is similar to that observed in the numerical model, as represented in Figure 4.25, where the horizontal displacements at mid-span increased significantly in both cases after reaching the maximum load. These horizontal displacements are presented in Figure 4.24 (similar to the experimental displacements previously presented in Figure 3.51) for the moment of maximum load and after the maximum load.

Regarding the stress and strain at maximum load in the numerical model for the third group of tests (B7 and B8), in both cases, the black dots match the yield stress points obtained from the tensile coupon tests, as depicted in Figure 4.26.

Table 4.6 – Vertical and horizontal displacements at mid span – experimental and numerical

| Test | Vertical displacement at mid span (VMid) – Maximum applied load | | | Horizontal displacement at mid span (H3) – Maximum applied load | | |
|------|--|-----------|-----------|--|-----------|-----------|
| | Experimental | Numerical | Deviation | Experimental | Numerical | Deviation |
| | [mm] | [mm] | [%] | [mm] | [mm] | [%] |
| B7 | 32.55 | 31.55 | -3.08 | 23.02 | 19.63 | -14.75 |
| B8 | 30.95 | 29.63 | -4.26 | 20.36 | 22.25 | 9.26 |

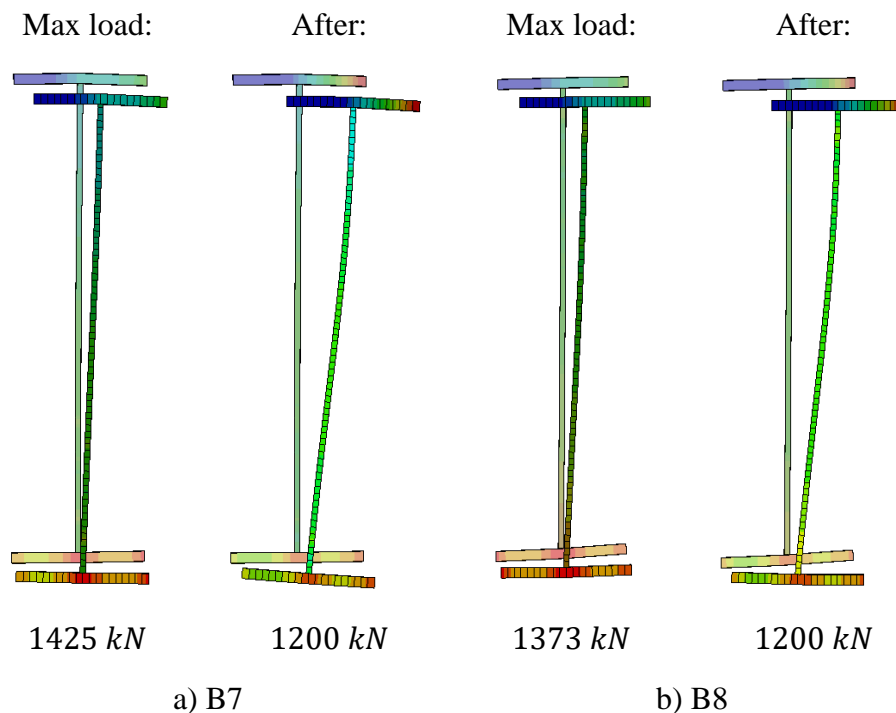


Figure 4.24 – Cross-section deformation at mid-span at maximum load and after maximum load – numerical model

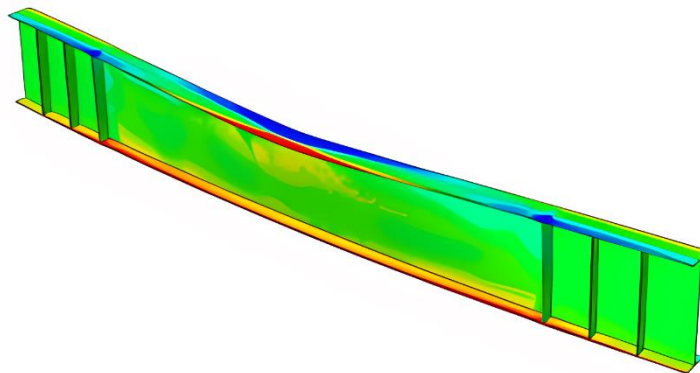
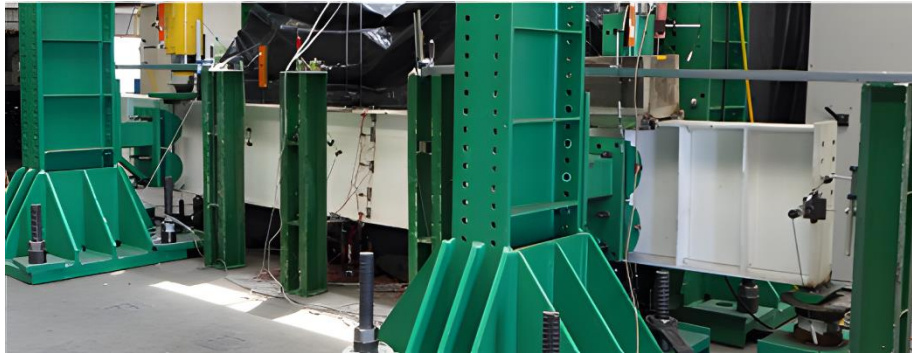
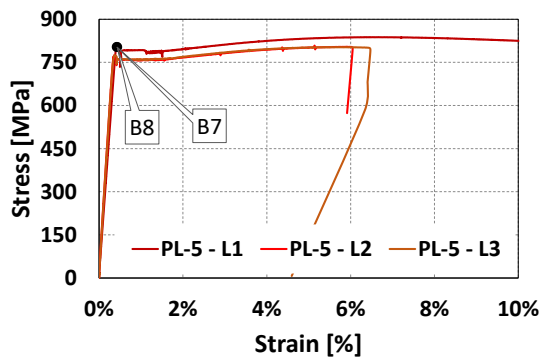


Figure 4.25 – Example of the failure mode for test B8



a) Flange steel grade: S690

Figure 4.26 – Strains (top flange) at maximum load

4.2.4. Results for tests B11, B12, B13, and B14

The last group of tests, B11 to B14, are monosymmetric beams with the same cross-section, 750mm depth, where the bottom flange in tension has 400mm width and the top flange in compression 200mm. B11 is entirely made of steel grade S690, B12 is hybrid with S690 flanges and S355 web, B13 is entirely in S460 and B14 is hybrid with S460 flanges and S355 web.

The experimental and numerical load-displacement curves for all tests are shown in Figure 4.27 and the maximum applied loads in Table 4.7. The maximum error is smaller than 4%, except from beam B14, where a higher difference was found, of approximately 11%. This higher difference could be explained by a variation in the residual stresses for this specimen since they were specified in the numerical model as the average of the measurements for B7, B8, and B11 as the measurement of the residual stresses was not carried out for this specimen.

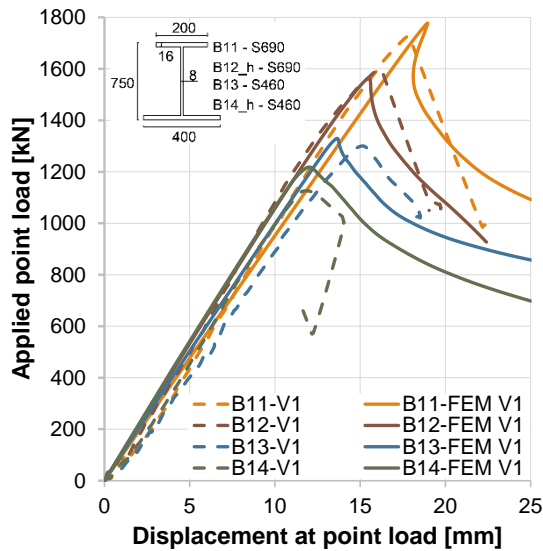


Table 4.7 – Maximum applied load

| Test | P_{max} [kN] Experimental | P_{max} [kN] Numerical | Error |
|-------|--------------------------------|-----------------------------|--------|
| B11 | 1731.80 | 1794.97 | 3.65% |
| B12_h | 1601.03 | 1587.63 | -0.84% |
| B13 | 1307.18 | 1329.57 | 1.71% |
| B14_h | 1133.28 | 1258.34 | 11.04% |

*h – hybrid beam with web S355

Figure 4.27 – Vertical displacements at load application point – experimental and numerical

The vertical and horizontal displacements along the beams at maximum load are presented in Figure 4.28 and Figure 4.29, respectively. The average error is of less than 8%, as it can be seen in Table 4.8, where a difference higher than 8% (14% and 21%, respectively) was only observed for the vertical displacement at mid-span for beam B13 and for the horizontal displacement at mid-span for beam B14.

Table 4.8 – Vertical and horizontal displacements at mid span – experimental and numerical

| Test | Vertical displacement at mid span (VMid) – Maximum applied load | | | Horizontal displacement at mid span (H3) – Maximum applied load | | |
|------|--|-------------------|------------------|--|-------------------|------------------|
| | Experimental [mm] | Numerical [mm] | Deviation [%] | Experimental [mm] | Numerical [mm] | Deviation [%] |
| B11 | 32.76 | 31.13 | -4.98 | 12.55 | 12.59 | 0.34 |
| B12 | 30.34 | 27.75 | -8.54 | 14.21 | 15.31 | 7.79 |
| B13 | 26.57 | 22.62 | -14.88 | 9.04 | 8.49 | -6.02 |
| B14 | 20.48 | 21.41 | 4.53 | 11.17 | 13.53 | 21.10 |

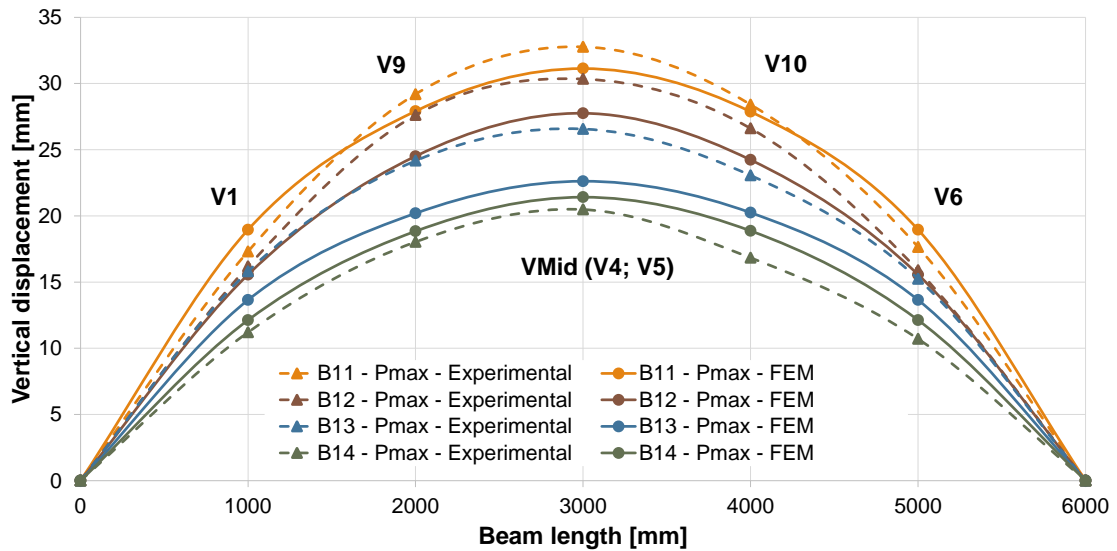


Figure 4.28 – Vertical displacements at maximum load – experimental and numerical

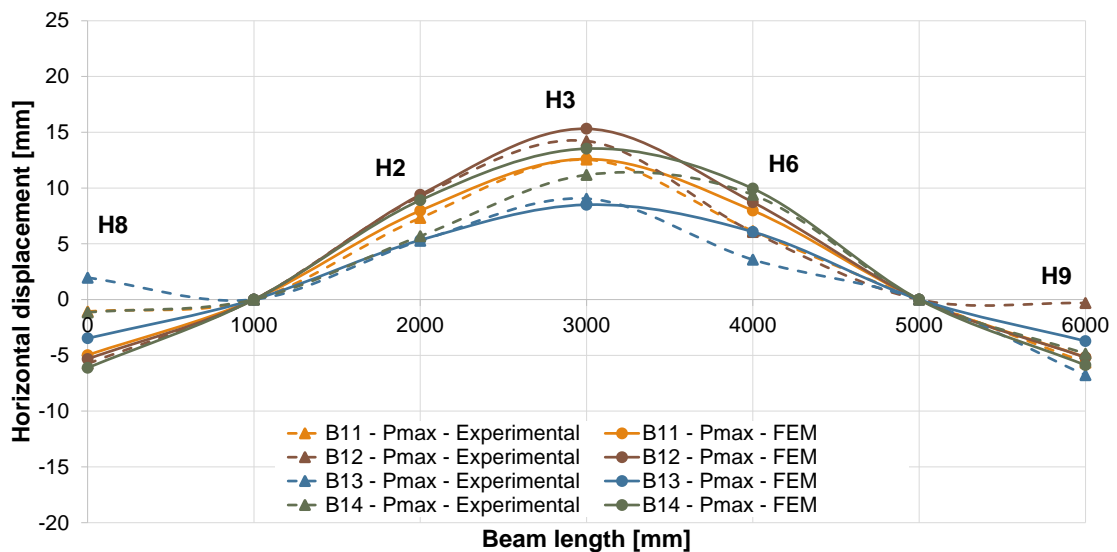


Figure 4.29 – Horizontal displacements at maximum load – experimental and numerical

The observed behaviour at maximum load and after reaching the maximum load for the cross-section at mid span is presented in Figure 4.30. These results are in line with the measurements performed during the experimental tests using the DIC system, as previously presented in Section 3.6.4 (see Figure 3.58 to Figure 3.61).

Figure 4.31 depicts the lateral-torsional buckling mode observed after maximum load for beam B11 and similar to beam B13 (Figure 4.31a) – pure mode), and the observed mixed mode

for beam B14 and similar to beam B12 (Figure 4.31b) – mixed mode), where the local buckles remain after reaching the maximum load.

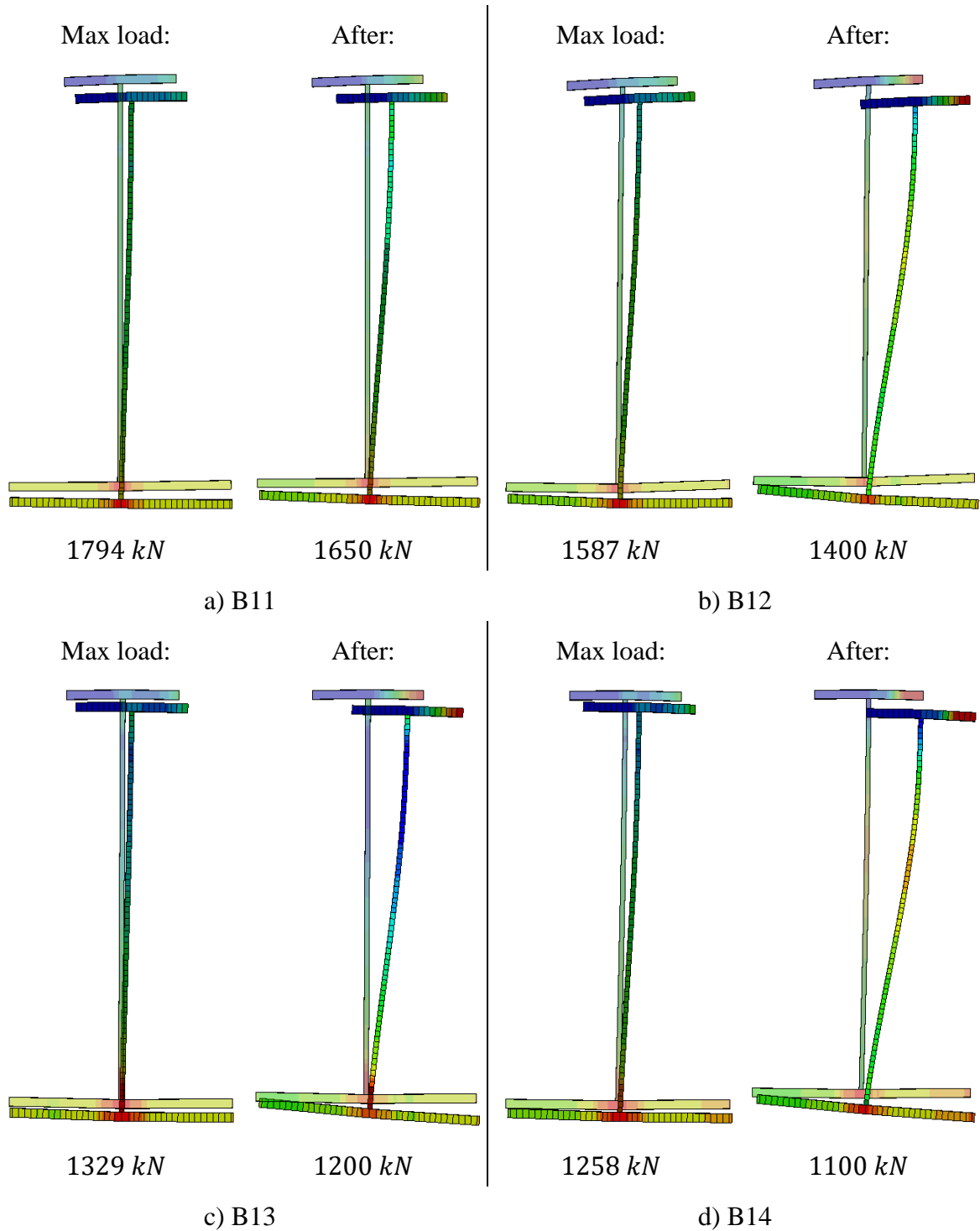
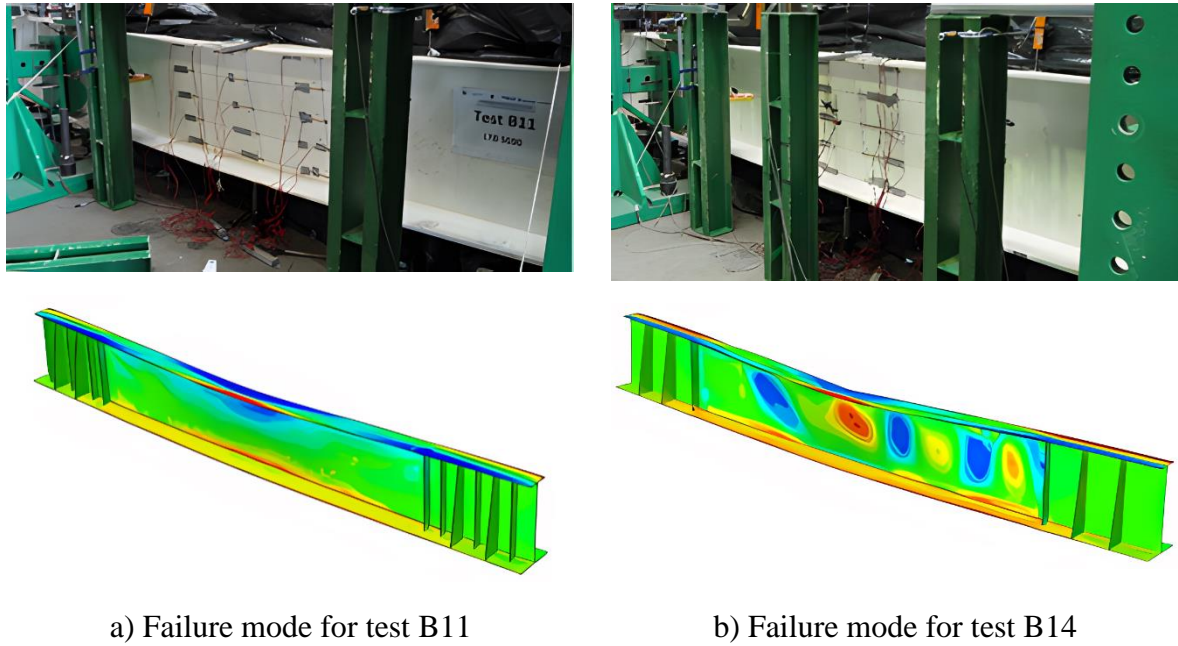
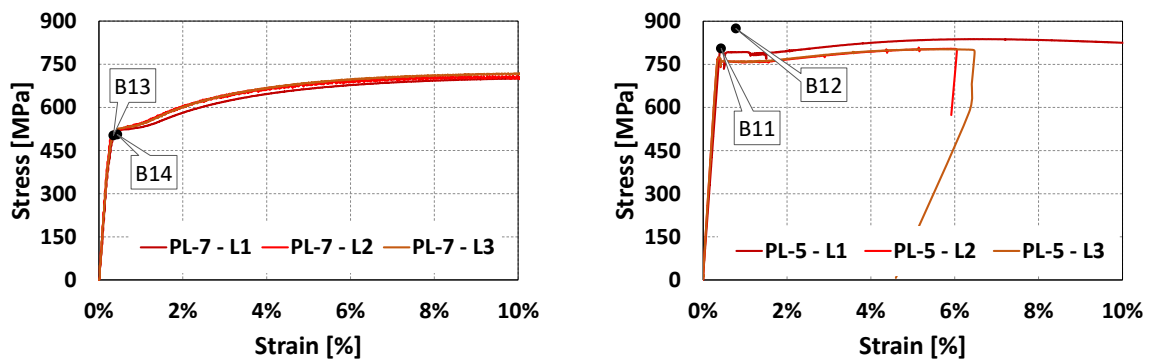


Figure 4.30 – Cross-section deformation at mid-span at maximum load and after maximum load – numerical model



a) Failure mode for test B11 b) Failure mode for test B14
 Figure 4.31 – Example of the buckling modes observed

For the last group of tests (B11 to B14), the extracted stress and strain are plotted in Figure 4.32, where B11, B13, and B14 match the experimental curve at the yield stress point from the tensile coupon tests. Even though B12 is slightly above the experimental curve, it is nevertheless close to the yield strain of the tensile coupon tests. All the results show that the simplified material properties used in the numerical model have no effect on this type of failure.

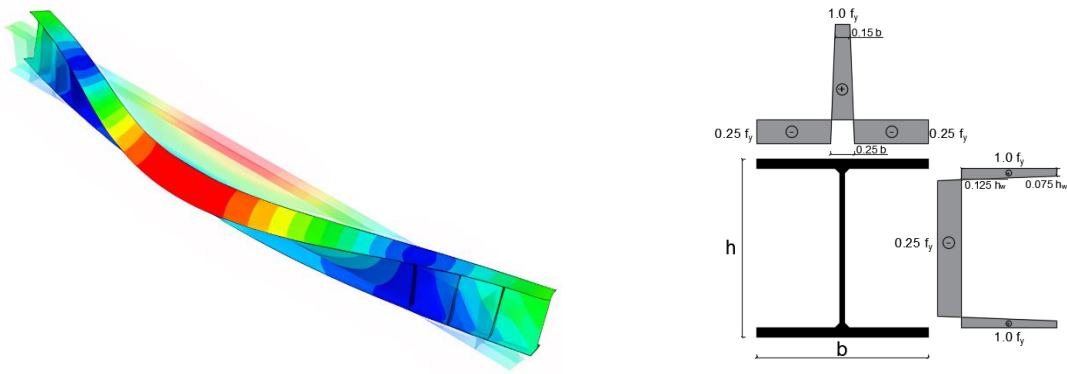


a) Flange steel grade: S460 b) Flange steel grade: S690
 Figure 4.32 – Strains (top flange) at maximum load

4.2.5. Imperfection sensitivity

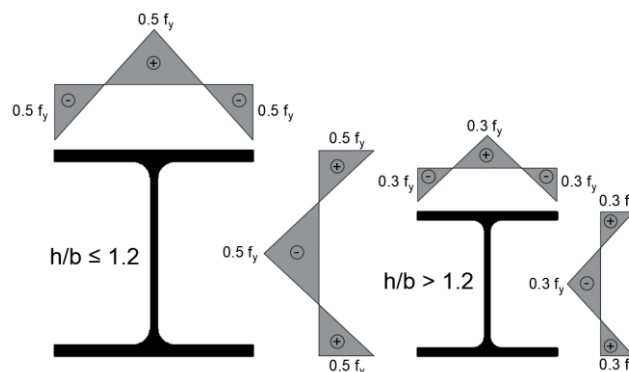
In order to assess the influence of adopting different assumptions about the members' imperfections, four different combinations between measured and standard assumptions (Figure 4.33) were considered according to the following assumptions:

- Geometrical imperfections and residual stresses according to the measurements performed (previously performed);
- Geometrical imperfections according to the relevant buckling mode (through a linear buckling analysis) with an amplitude of $L/1000$ and residual stresses according to the measurements performed;
- Geometrical imperfections according to the measurements performed and residual stresses pattern provided by ECCS [24] for welded and hot-rolled sections;
- Geometrical imperfections according to the relevant buckling mode with an amplitude of $L/1000$ and residual stresses pattern provided by ECCS [24] for welded and hot-rolled sections (standard conditions).



a) Initial geometrical imperfection – amplitude $L/100$

b) ECCS residual stresses distribution for welded sections – $f_y = 235 \text{ MPa}$



c) ECCS residual stresses distribution for hot-rolled sections – $f_y = 235 \text{ MPa}$

Figure 4.33 – Modelling assumptions

The maximum load applied and the error obtained for each approach in comparison to the experimental value are summarised in Table 4.9.

Table 4.9 – Maximum applied load (kN) for different imperfections assumptions

| Test | Experi- mental | Imp. and RS measured | Error (%) | Imp. L/1000 and RS measured * | Error (%) | Imp. measured and RS from ECCS* | Error (%) | Imp. L/1000 and RS from ECCS* | Error (%) |
|----------------------------|-------------------|----------------------------|--------------|---|--------------|---|--------------|---|--------------|
| B1 | 779.37 | 797.32 | 2.30 | 684.56 | -12.16 | 771.57 | -1.00 | 667.28 | -14.38 |
| B2 | 1041.42 | 1002.32 | -3.75 | 904.82 | -13.12 | 987.08 | -5.22 | 879.57 | -15.54 |
| B3 | 829.75 | 837.09 | 0.88 | 799.93 | -3.59 | 824.61 | -0.62 | 750.13 | -9.60 |
| B4 | 675.21 | 716.14 | 6.06 | 716.17 | 6.07 | 707.35 | 4.76 | 746.41 | 10.54 |
| B5 | 1024.49 | 1052.90 | 2.77 | 1123.22 | 9.64 | 1050.59 | 2.55 | 1100.67 | 7.44 |
| B6 | 725.1 | 733.79 | 1.20 | 776.48 | 7.09 | 765.78 | 5.61 | 777 | 7.16 |
| B7 | 1384.59 | 1425.74 | 2.97 | 1311.89 | -5.25 | 1381.08 | -0.25 | 1277.4 | -7.74 |
| B8 | 1327.9 | 1373.10 | 3.40 | 1295.85 | -2.41 | 1354.89 | 2.03 | 1272.59 | -4.17 |
| B11 | 1731.8 | 1794.97 | 3.65 | 1684.07 | -2.76 | 1828.14 | 5.56 | 1608.58 | -7.12 |
| B12 | 1601.03 | 1587.63 | -0.84 | 1690.86 | 5.61 | 1535.13 | -4.12 | 1606.95 | 0.37 |
| B13 | 1307.18 | 1329.57 | 1.71 | 1389.32 | 6.28 | 1291.70 | -1.18 | 1215.54 | -7.01 |
| B14 | 1133.28 | 1258.34 | 11.04 | 1398.11 | 23.37 | 1190.82 | 5.08 | 1215.26 | 7.23 |
| Absolute average error (%) | | | 3.38 | | 8.11 | | 3.17 | | 8.19 |

*with nominal cross-section geometrical dimensions.

RS – residual stresses pattern.

Imp. – geometrical imperfections.

The results show that, in general, the assumption of an amplitude of L/1000 is a safe-sided estimate for the global imperfection, leading to values which are, on average, approximately 10% on the safe-side. In contrast, the assumption of the residual stresses patterns according to ECCS combined with the real geometrical imperfection follows quite closely the experimental

results, with an absolute average difference smaller than 4%. The most significant difference between the measured residual stresses and the ECCS distribution is the tensile stress at the flange tips for the measured ones. Although the compression residual stresses of the ECCS recommendation are generally lower in comparison with the measurements, the tensile stress at the flange tips has a beneficial effect, leading to higher loads, as seen, for example for beam B14.

4.3. Simplified numerical model for parametric studies

The numerical model presented in Section 4.1 and calibrated against the experimental results (Section 4.2) is adopted for the parametric studies. However, in order to be applicable to several conditions, such as different cross-section dimensions, type of loading, material properties, some changes in the numerical model to standard conditions were necessary.

In this section, the changes applied in the previously calibrated numerical model to obtain the simplified numerical model for parametric studies are described.

4.3.1. Geometry

The simplified numerical model is also made using shell elements, with element type S4R (4 nodes shell element) which was accurately calibrated to experimental results. Nonetheless, the mesh density is considered as constant with 16 elements for each flange and web plates and 300 elements along the member axis.

The cross-section geometry is introduced based on the nominal cross-section dimensions, cross-section depth (h), width of the flanges (b), web thickness (t_w) and flanges thickness (t_f), as represented in Figure 4.34.

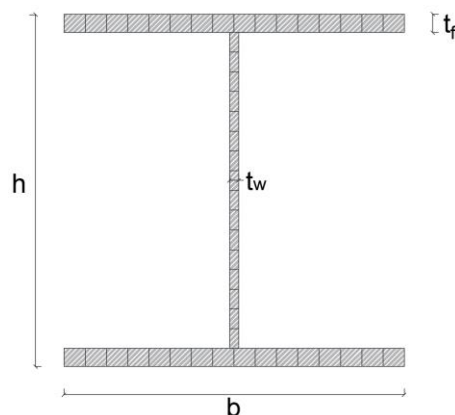


Figure 4.34 – Cross-section geometry and mesh

4.3.2. Material properties

The material behaviour is introduced by the material model using an elastic-plastic law without strain hardening (perfect plasticity), as shown in Figure 4.35, with a modulus of elasticity (Young's modulus) $E = 210 \text{ GPa}$, and a Poisson ratio $\nu = 0.3$.

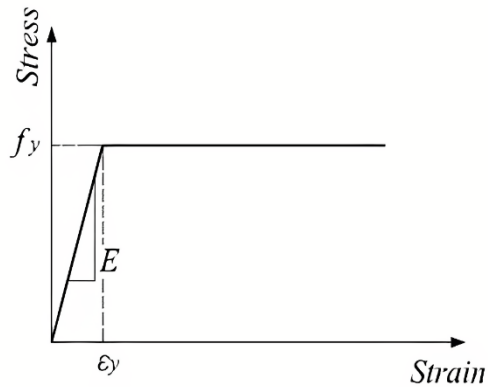


Figure 4.35 – Elastic-plastic law without strain hardening

The yield stress f_y is considered according to the product standard EN10025 [5], varying according to the thickness of the plates (flanges and web). Figure 4.36 depicts the yield strength of the plate depending on the nominal thickness according to EN10025 [5] and EN1993-1-1 [1], for the steel grades to be used in the parametric study.

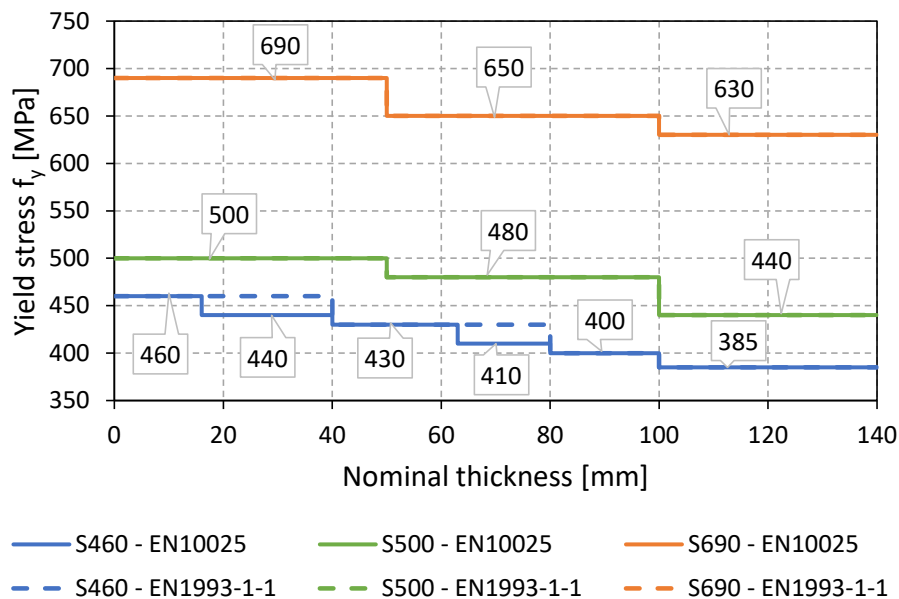


Figure 4.36 – Variation of the yield stress with nominal thickness

4.3.3. Boundary conditions

For the implementation of the boundary conditions, simple-supported conditions with end fork conditions were adopted in the simplified numerical model, as shown in Figure 4.37.

The vertical (u_z) and transverse (u_y) displacements and the rotation about the x-axis (θ_{xx}) are restrained at the end supports (represented as nodes 1 and 2) of the member. In addition, the longitudinal (u_x) displacement is prevented at one end (node 1).

The end cross-sections are constrained to remain straight but allowing the flanges to move from the web. Furthermore, for major axis flexural buckling behaviour, minor axis displacements (u_y) are restrained at both flange tips and at the centre of the web along the length of the member, as represented in Figure 4.38.

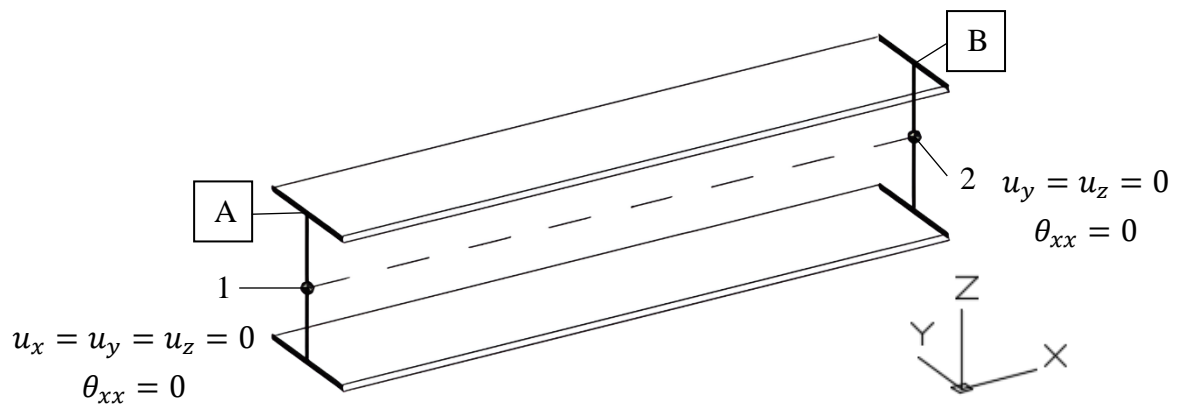


Figure 4.37 – Boundary conditions for the simplified numerical model

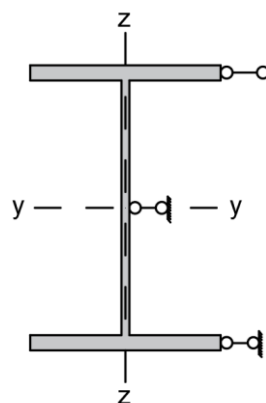


Figure 4.38 – Location of the intermediate lateral restraints in the cross-section

4.3.4. Loading

The loads are applied at the middle point of the end supports, in case of concentrated moment (M) or axial force (N). The concentrated load is applied in the middle point of the cross-section (middle of the web) at mid-span. For the distributed load, 3 different cases are considered: the distributed load applied at (1) the top flange, (2) the bottom flange, and (3) the cross-section centre (middle of the web). For all the cases, the distributed load is applied along the member span.

Figure 4.39 represents the load applications cases in the simplified numerical model. For all the cases, the load is applied using load increment method with appropriate increment size in order to meet convergence criteria.

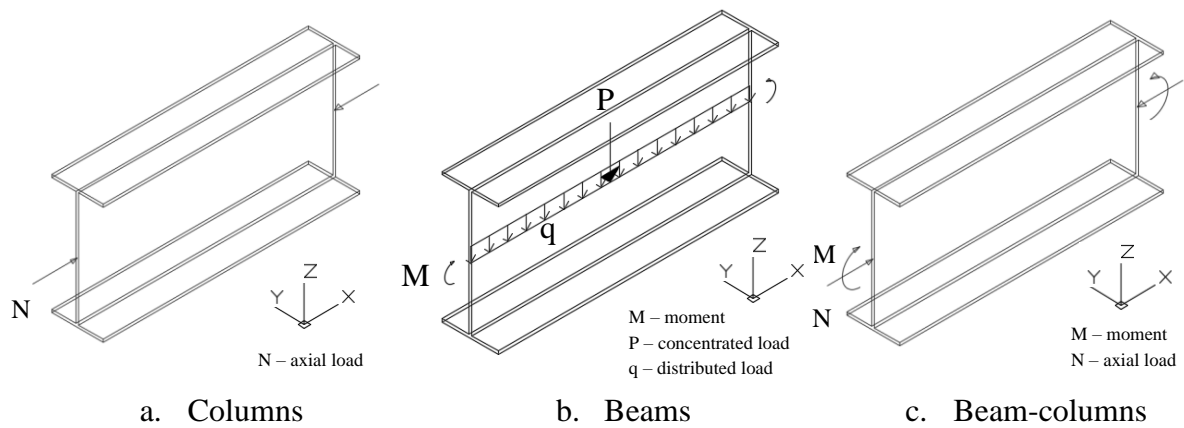


Figure 4.39 – Load applications in the simplified numerical model

4.3.5. Geometrical imperfections

Geometrical imperfections are modelled using the critical buckling mode shape according to the buckling mode considered (Figure 4.40 and Figure 4.41), obtained from a linear buckling analysis, with an amplitude $e_0 = L/1000$.

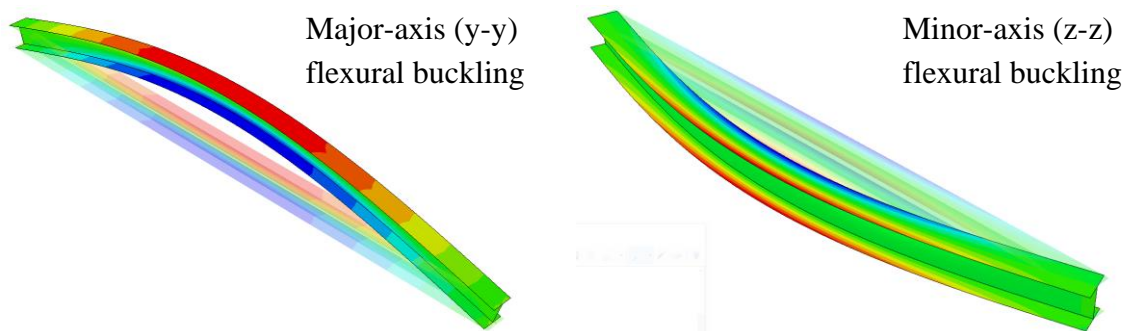


Figure 4.40 – Critical buckling mode shape for flexural buckling

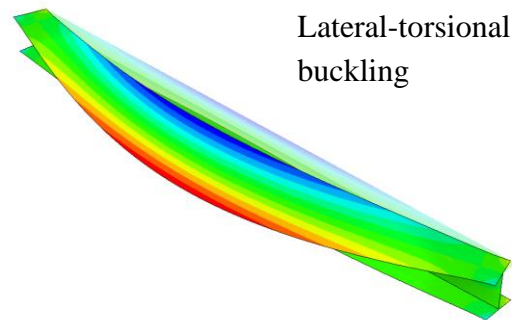


Figure 4.41 – Critical buckling mode shape for lateral-torsional buckling

4.3.6. Residual stresses pattern

Residual stresses are considered according to ECCS [24] residual stresses patterns for welded I sections, as shown in Figure 4.42. f_y is considered equal to 235 MPa according to the ECCS [24] publication.

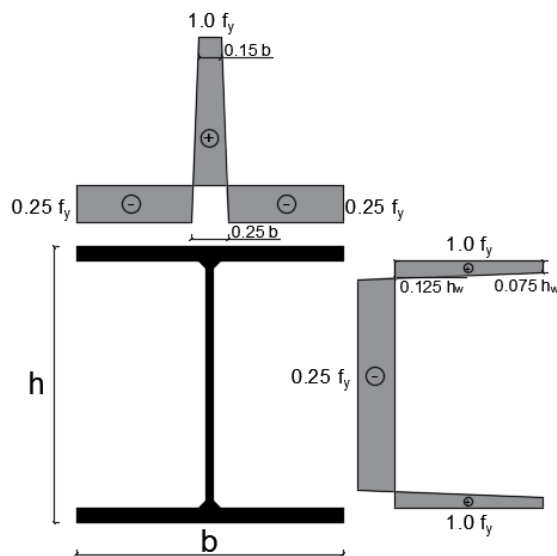


Figure 4.42 – Residual stresses distributions for welded I sections

4.4. Parametric studies



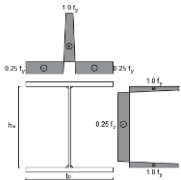
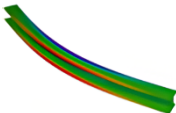
In order to extend the study on the buckling behaviour of high strength steel and based on the previously described model (Section 4.3), an extensive parametric study was performed.

4.4.1. Columns

The parametric study for columns comprises 3198 numerical models for flexural buckling about minor and major axes (1599 models for each buckling mode), including 45 different welded cross-sections with various h/b ratios. Table 4.10 summarises the different levels of slenderness ($\bar{\lambda}$) and steel grades (f_y) according to EN10025 [5], in the parametric study.

Table 4.11 presents the welded sections dimensions selected for the parametric study, where all the cross sections are classified as class 3 or lower under pure compression.

Table 4.10 – Parametric study for columns

| Fabrication | Imperfections | Normalized slenderness $\bar{\lambda}_{y z}$ | Material Properties f_y | Buckling mode | Number of sections (simulations) |
|-------------|--|--|----------------------------------|---|----------------------------------|
| Welded | Geometrical imperfections  | $L/1000$ 0.5; 0.6; 0.7; 0.8; 0.9; 1.0; 1.2; 1.4; 1.5; 1.6; 1.8; 2.0; 2.5; | EN10025: S460 S500 S690 |  In plane (y-y) | 45 (1599) |
| | Residual stresses  ECCS | | |  Out plane (z-z) | 45 (1599) |

Even though the selection of the buckling curve according to Eurocode 3 Part 1-1 [1] for welded sections is only determined by the flange thicknesses, $t_f \leq 40 \text{ mm}$ and $t_f > 40 \text{ mm}$, the limits presented in Table 4.12 are according to the limits for rolled sections since they were all covered in the parametric study.


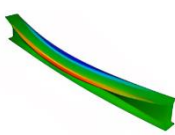


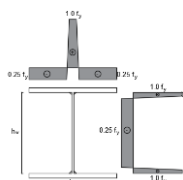




Table 4.11 – Sections for the columns parametric study

| Fabrication | Limits: EC3-1-1 Columns | Sections | | | | |
|-----------------------------|----------------------------|---|-----------------------------|------------------|---------------|------|
| | | Profile ($h \times b \times t_w \times t_f$) | h/b | t_f (mm) | | |
| Welded | $t_f \leq 40$ mm | 377x309x21x40 | 1.22 | 40 | | |
| | | 524x306x21x40 | 1.71 | 40 | | |
| | | 140x73x5x7 | 1.92 | 7 | | |
| | | 668x305x21x40 | 2.19 | 40 | | |
| | | 80x46x4x5 | 1.74 | 5 | | |
| | | 100x55x4x6 | 1.82 | 6 | | |
| | | 400x300x14x24 | 1.33 | 24 | | |
| | | 500x300x15x28 | 1.67 | 28 | | |
| | | 160x82x5x7 | 1.95 | 7 | | |
| | | 432x307x21x40 | 1.41 | 40 | | |
| | | 450x300x14x26 | 1.50 | 26 | | |
| | | 395x308x21x40 | 1.28 | 40 | | |
| | | $h/b > 1.2$ | 40 mm $< t_f \leq 100$ mm | 975x427x31x56 | 2.28 | 56 |
| | | | | 987x431x35x62 | 2.29 | 62 |
| | 1061x451x55x99 | | | 2.35 | 99 | |
| | 1056x314x36x64 | | | 3.36 | 64 | |
| | 1011x437x41x74 | | | 2.31 | 74 | |
| | 999x434x38x68 | | | 2.30 | 68 | |
| | 993x322x36x65 | | | 3.08 | 65 | |
| | 1068x417x39x70 | | | 2.56 | 70 | |
| | 711x347x39x69 | | | 2.05 | 69 | |
| | 648x315x30x54 | | | 2.06 | 54 | |
| | $t_f > 100$ mm | | 728x308x25x46 | 2.36 | 46 | |
| | | | 842x313x30x54 | 2.69 | 54 | |
| | | | 938x312x30x54 | 3.01 | 54 | |
| | | | 580x471x95x130 | 1.23 | 130 | |
| | | | 1081x457x61x109 | 2.37 | 109 | |
| | | | 531x442x66x106 | 1.201 | 106 | |
| | | | 550x448x72x115 | 1.23 | 115 | |
| | | | 1093x461x64x115 | 2.37 | 115 | |
| | | | 1093x473x77x115 | 2.31 | 115 | |
| | | | 569x454x78x125 | 1.25 | 125 | |
| | | | 600x476x100x140 | 1.26 | 140 | |
| | | | $h/b \leq 1.2$ | $t_f \leq 40$ mm | 360x300x13x23 | 1.20 |
| | 96x100x5x8 | 0.96 | | | 8 | |
| | 300x300x11x19 | 1.00 | | | 19 | |
| 340x310x21x39 | 1.10 | 39 | | | | |
| 100x100x6x10 | 1.00 | 10 | | | | |
| 200x200x9x15 | 1.00 | 15 | | | | |
| 240x240x10x17 | 1.00 | 17 | | | | |
| 40 mm $< t_f \leq 100$ mm | | 514x437x61x97 | | 1.18 | 97 | |
| | | 455x418x42x68 | | 1.09 | 68 | |
| | | 474x424x48x77 | | 1.12 | 77 | |
| | | 425x409x33x53 | 1.04 | 53 | | |
| | | 465x421x45x72 | 1.10 | 72 | | |

4.4.2. Beams

For the parametric study for beams, a total of 4595 simulations were made, with variations in the normalized slenderness ($\bar{\lambda}_{LT}$), steel grade (f_y) according to EN10025 [5], bending moment distributions, and loading, as shown in Table 4.12.

Table 4.12 – Parametric study for beams

| Fabrication | Imperfections | Normalized slenderness $\bar{\lambda}_{LT}$ | Material Properties f_y | Bending moment distribution | Load application | Number of sections (simulations) | |
|-------------|--|---|---|--|--|----------------------------------|----------|
| Welded | Geometrical imperfections | | |  | - | 30 (1175) | |
| |  | $L/1000$ | 0.4; 0.6; 0.8; 1.0; | EN10025: |  | - | 30 (769) |
| | | | | |  | - | 30 (634) |
| | Residual stresses |  | 1.1; 1.2; 1.3; 1.4; 1.5; 1.6; 1.7; 1.8; 2.0; 2.1; | S460 S500 S690 |  | Center | 30 (837) |
| | | | | |  | Top flange | 10 (238) |
| | | | | |  | Bottom flange | 10 (245) |
| | ECCS | | | |  | Center | 30 (697) |

To avoid unrealistic beam lengths, the beams parametric study was limited to beams with ratios $L/h < 40$, where L is the beam length and h the cross-section depth.

Table 4.13 shows the welded cross-sections of the beams used in the parametric study, organized according to the Eurocode 3 [1] limits for the selection of the buckling curve for lateral-torsional buckling.

Table 4.13 – Sections for the parametric study for beams

| Fabrication | Limits: EC3-1-1 Beams | Sections | | | Class (pure bending) | | |
|----------------|-----------------------------|---|-------|------------|----------------------|------|------|
| | | Profile ($h \times b \times t_w \times t_f$) | h/b | t_f (mm) | S460 | S500 | S690 |
| Welded | $\frac{h}{b} \leq 2$ | 100x55x4x6 * | 1.82 | 6 | 1 | 1 | 1 |
| | | 200x100x6x9 * | 2.00 | 9 | 1 | 1 | 1 |
| | | 240x120x6x10 * | 2.00 | 10 | 1 | 1 | 1 |
| | | 300x150x7x11 * | 2.00 | 11 | 1 | 2 | 3 |
| | | 432x307x21x40 | 1.41 | 40 | 1 | 1 | 1 |
| | | 524x306x21x40 | 1.71 | 40 | 1 | 1 | 1 |
| | | 390x300x11x19 | 1.30 | 19 | 3 | 3 | 3 |
| | | 400x300x14x24 | 1.33 | 24 | 1 | 1 | 3 |
| | | 600x300x16x30 | 2.00 | 30 | 1 | 1 | 1 |
| | | 300x300x11x19 | 1.00 | 19 | 3 | 3 | 3 |
| | | 200x200x9x15 * | 1.00 | 15 | 1 | 2 | 3 |
| | | 100x100x6x10 | 1.00 | 10 | 1 | 1 | 1 |
| | | 120x106x12x20 * | 1.13 | 20 | 1 | 1 | 1 |
| | | 340x310x21x39 | 1.10 | 39 | 1 | 1 | 1 |
| | | 114x120x5x8 * | 0.95 | 8 | 3 | 3 | 3 |
| | 455x418x42x68 | 1.09 | 68 | 1 | 1 | 1 | |
| | 465x421x45x72 | 1.10 | 72 | 1 | 1 | 1 | |
| | 474x424x48x77 | 1.12 | 77 | 1 | 1 | 1 | |
| | $\frac{h}{b} > 2$ | 400x180x9x14 * | 2.22 | 14 | 1 | 1 | 3 |
| | | 500x200x10x16 * | 2.50 | 16 | 1 | 1 | 3 |
| | | 600x220x12x19 * | 2.73 | 19 | 1 | 1 | 2 |
| | | 999x434x38x68 | 2.30 | 68 | 1 | 1 | 1 |
| | | 1068x417x39x70 | 2.56 | 70 | 1 | 1 | 1 |
| | | 1011x437x41x74 | 2.31 | 74 | 1 | 1 | 1 |
| | | 1056x314x36x64 | 3.36 | 64 | 1 | 1 | 1 |
| | | 993x322x36x65 | 3.08 | 65 | 1 | 1 | 1 |
| | | 711x347x39x69 | 2.05 | 69 | 1 | 1 | 1 |
| 1012x402x24x42 | | 2.52 | 42 | 1 | 1 | 1 | |
| 1020x404x25x46 | | 2.52 | 46 | 1 | 1 | 1 | |
| 965x425x28x51 | | 2.27 | 51 | 1 | 1 | 1 | |

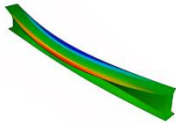

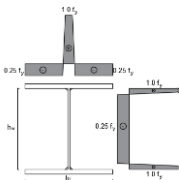
*- Sections used in bending moments distributions with fewer sections.

4.4.2.1. Hybrid beams

To extend the parametric study to hybrid beams, the previous parametric study was performed, changing the web's steel grade to S355 and maintaining the same conditions for the flanges steel grade. For a direct comparison with the results obtained in the parametric study for homogeneous beams, the parametric study for hybrid beams was performed using the

equivalent slenderness, aiming to obtain the same beam length both for hybrid and homogeneous beams (Table 4.14).

Table 4.14 – Parametric study for hybrid beams

| Fabrication | Imperfections | Normalized slenderness $\bar{\lambda}_{LT}$ | Material Properties f_y | Bending moment distribution ψ | Number of sections (simulations) |
|-------------|--|--|----------------------------------|---|----------------------------------|
| Welded | Geometrical imperfections  | Equivalent slenderness to the length used for homogeneous beams; $L_{homogeneous} = L_{hybrid}$ | EN10025: S460 S500 S690 |  $\psi = 1$ | 30 (1175) |
| | $L/100$ | | | | |
| | Residual stresses  | | | | |
| | ECCS | | | | |

4.4.3. Beam-Columns

The parametric study for beam-columns includes a total of 4512 simulations, for 4 different major axis bending moment distributions, varying the normalized slenderness ($\bar{\lambda}_z$), steel grade (f_y) and the parameter ϕ which represents the ratio $(M_{pl}/M)/(N_{pl}/N)$, as shown in Table 4.15.

The 4 welded cross-sections used in the parametric study are presented in Table 4.16, and are classified as class 2 or lower, under pure compression.

Table 4.15 – Parametric study for beam-columns

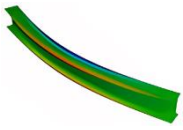

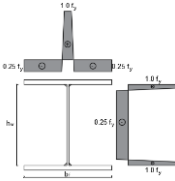
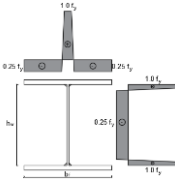

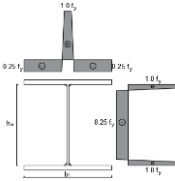

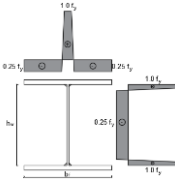

| Fabri- cation | Imperfections | Normalized slenderness $\bar{\lambda}_z$ | ϕ $\frac{M_{pl}}{M} / \frac{N_{pl}}{N}$ | Material Properties f_y | Bending moment distribution | Restraints | Number of sections simulations | | | |
|---|---|--|---|--|--|---|--------------------------------------|--|------------------------|---------|
| Welded | Geometrical imperfections  | $L/100$ | 0.4; 0.5; 0.6; 0.8; 1.0; 1.2; 1.4; 1.5; 1.6; 1.8; | EN10025: S460 S500 S690 |  | None | 4 (960) | | | |
| | | | | | | Minor axis (z-z) | 4 (288) | | | |
| | Residual stresses  | | | | ECCS |  | ECCS |  | None | 4 (960) |
| | | | | | | | | | Minor axis (z-z) | 4 (280) |
| |  | | | | ECCS | ECCS | ECCS |  | None | 4 (840) |
| | | | | | | | | | Minor axis (z-z) | 4 (270) |
|  | ECCS | ECCS | ECCS |  | None | 4 (914) | | | | |
| | | | | | Minor axis (z-z) | 4 (914) | | | | |

Table 4.16 – Sections for the parametric study for beam-columns

| Fabrication | Limits: EC3-1-1 | Sections | | | |
|-------------|-----------------|---|---------------|------------|----|
| | | Profile ($h \times b \times t_w \times t_f$) | h/b | t_f (mm) | |
| Welded | $h/b > 1.2$ | $t_f \leq 40$ mm | 390x300x16x25 | 1.30 | 25 |
| | | 40 mm $< t_f \leq 100$ mm | 500x300x21x28 | 1.67 | 28 |
| | $h/b \leq 1.2$ | 40 mm $< t_f \leq 100$ mm | 632x310x26x46 | 2.04 | 46 |
| | | 40 mm $< t_f \leq 100$ mm | 407x404x27x44 | 1.01 | 44 |

4.4.4. New residual stresses models

In order to study the influence of different residual stresses patterns in high strength steel members, the parametric studies performed above for columns and beams, were extended to the new residual stresses models proposed Schaper et al. [40] and presented in Chapter 2 for thermal cut plates and non-thermal cut plates.

Figure 4.43 shows the residual stresses values for a welded I-section, considering a steel grade S690, for the approaches considered (ECCS, thermal cut, and non-thermal cut). It is possible to have an overview of the differences in terms of the residual stresses' magnitude for the different patterns.

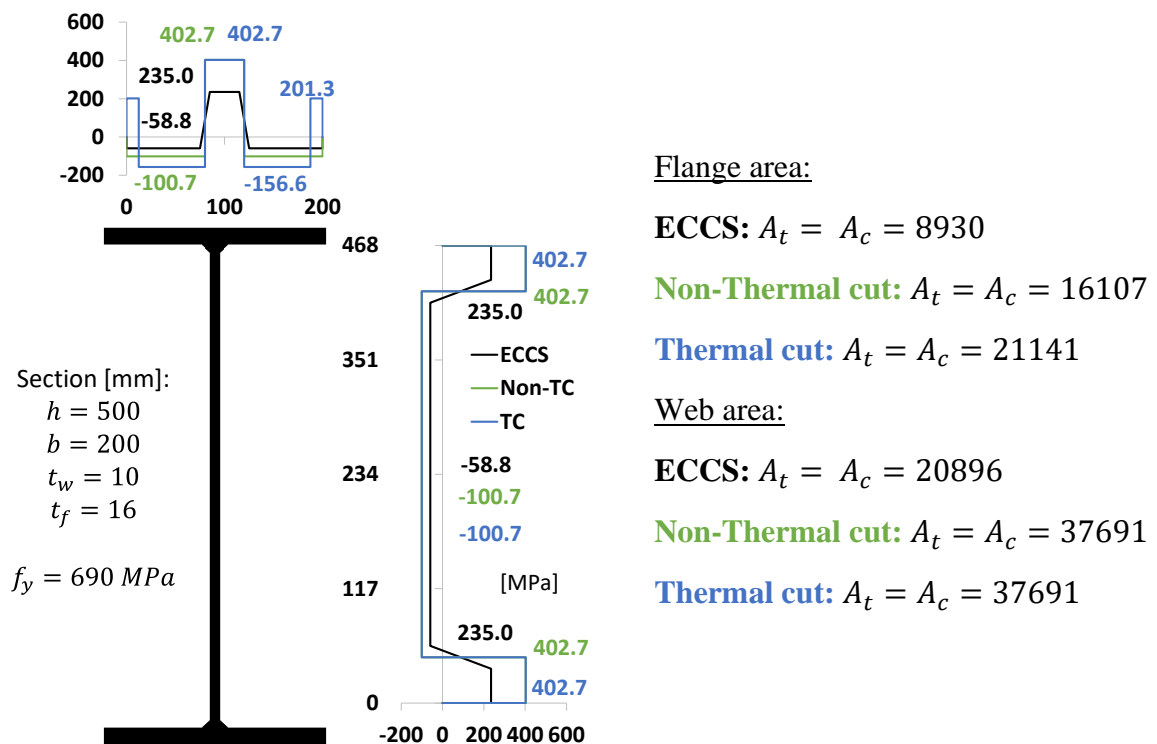


Figure 4.43 – Residual stresses patterns applied to a welded I-section

The thermal cut pattern (TC) has a higher tension in the flanges due to the tension in the flange tips. However, as a consequence of such higher tension, the TC has the highest compression value since the residual stresses must be in equilibrium in each plate. By not considering the tension in the flange tips, which is the case of the non-thermal cut pattern (NTC), the compression value of the residual stresses is reduced significantly in comparison to the thermal cut pattern. The ECCS residual stresses pattern has the lowest value for compression

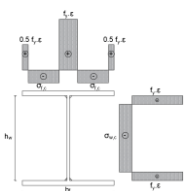

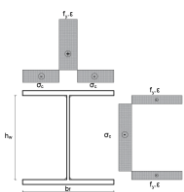
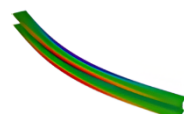
and also tension, since this model considers the value $f_y = 235 \text{ MPa}$, regardless of the plate steel grade.

For the web residual stresses pattern, both thermal cut and non-thermal cut patterns have the same configuration. Once more, the ECCS model has the lowest values of residual stresses for tension and compression.

4.4.4.1. Columns

The parametric study for columns with new residual stresses models presented in Table 4.17 was performed exactly as before, by changing the residual stresses patterns for the same slenderness, material properties, buckling mode, and sections.




Table 4.17 – Parametric study for columns with new residual stresses models

| Fabrication | Residual stresses | Normalized slenderness $\bar{\lambda}_{y z}$ | Material Properties f_y | Buckling mode | Number of sections (simulations) |
|-------------|---|--|----------------------------------|---|----------------------------------|
| Welded | Thermal cut:  | 0.5; 0.6; 0.7; 0.8; 0.9; 1.0; 1.2; 1.4; 1.5; 1.6; 1.8; 2.0; 2.5; | EN10025: S460 S500 S690 |  In plane (y-y) | 45 (1599) |
| | Non-Thermal cut:  | | |  Out plane (z-z) | 45 (1599) |

4.4.4.2. Beams

In the case of the parametric study for beams with new residual stresses models, the parametric study was performed once more for the same normalized slenderness, material properties and sections as before, but for less bending moment distributions. Three different bending moment distributions were considered: $\psi = 1$, $\psi = 0$, and $\psi = -1$ (Table 4.18).

Table 4.18 – Parametric study for beams with new residual stresses models

| Fabrication | Residual stresses | Normalized slenderness $\bar{\lambda}_{LT}$ | Material Properties f_y | Bending moment distribution | Number of sections (simulations) |
|-------------|-------------------|---|----------------------------------|--|----------------------------------|
| Welded | Thermal cut: | 0.4; 0.6; 0.8; 1.0; 1.1; 1.2; 1.3; 1.4; 1.5; 1.6; 1.7; 1.8; 2.0; 2.1; | EN10025: S460 S500 S690 |  $\psi = 1$ | 30 (970) |
| | Non-Thermal cut: | | |  $\psi = 0$ | 30 (769) |
| | | | |  $\psi = -1$ | 30 (634) |
| | | | | | |

4.5. Results

In this section, the results obtained in the numerical simulations (parametric study) are compared with current design recommendations for buckling resistance of members available in Eurocode 3 [1] and in the new version of Eurocode 3 [7].

4.5.1. Columns

The results for flexural buckling about major and minor axes are presented in Figure 4.44, together with the buckling curves given in the current code specifications. Curve b ($t_f \leq 40 \text{ mm}$) and curve c ($t_f > 40 \text{ mm}$) for major axis (y-y) flexural buckling, and curve c ($t_f \leq 40 \text{ mm}$) and curve d ($t_f > 40 \text{ mm}$) for minor axis (z-z) flexural buckling. Each point represents a single numerical case (the numerical reduction factor obtained for the flexural buckling of a specific column), and the results are also divided by steel grade. It is noted that the results are above the lowest buckling curve (more favourable), and the gap between the numerical results and the buckling curve tends to get bigger for $\bar{\lambda} > 0.7$ for both major and minor axes flexural buckling. It is also noticeable the shift of the numerical reduction factor when the steel grade gets higher.

Further illustration of the results is presented in Figure 4.45, where the vertical axis represents the reduction factor (χ_y and χ_z) according to Eurocode 3 [1], referred to as theoretical, and the horizontal axis represents the numerical reduction factor obtained in the simulations, referred to as numerical. This representation, further referred to as scatter plots, easily show and compare the relation between the Eurocode recommendations and the numerical results obtained. For the flexural buckling case, both for major and minor axes, the majority of the cases present a lower theoretical reduction factor compared to the numerical one, which means that the Eurocode provides a safe-sided estimate for the reduction factor, and the level of safety increases with the steel grade.

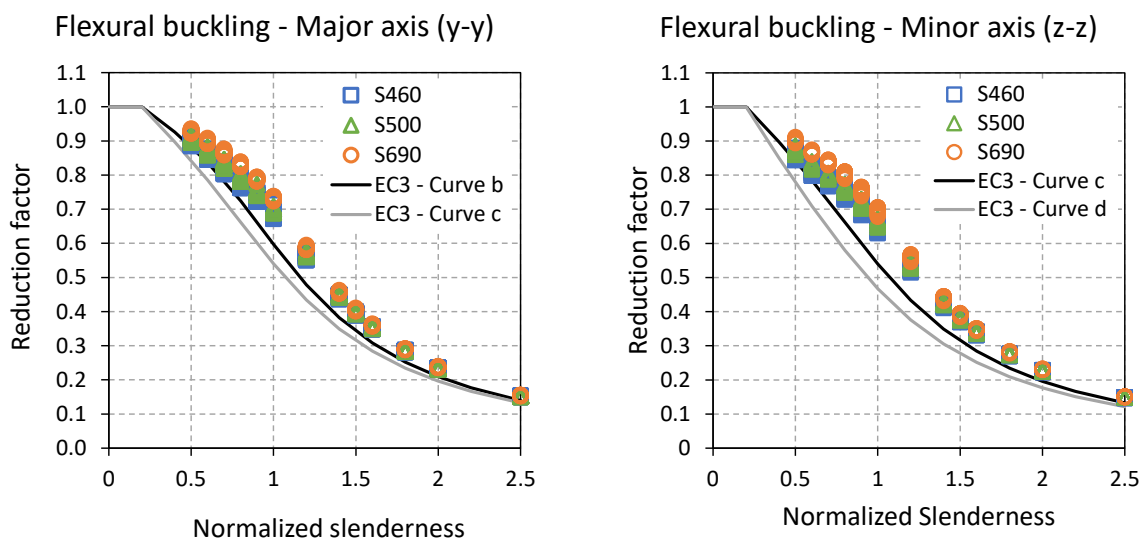


Figure 4.44 – Buckling curves for flexural buckling

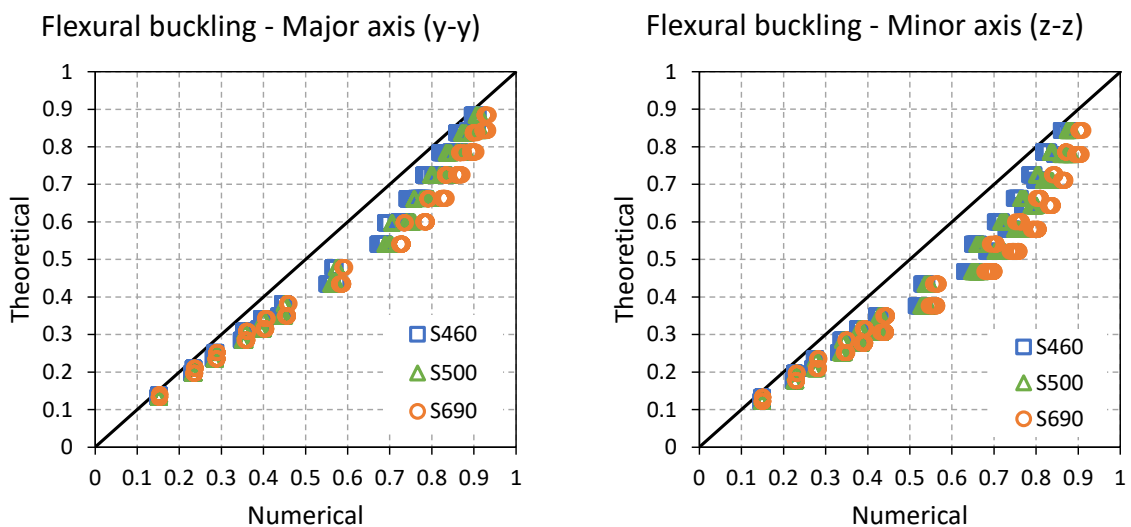


Figure 4.45 – Scatter plots for flexural buckling

The results are further analysed through the statistical parameters of the ratio r_e/r_t , where r_e is the numerical reduction factor and r_t is the theoretical reduction factor obtained using the Eurocode 3 [1] expressions for flexural buckling. These statistics are shown in Table 4.19, for all cases, divided into steel grades. For a good design rule, a mean value of around 1.0 or slightly higher than 1.0 is considered a safe estimate [70], where the safety is introduced by partial factors which include variability of the material and geometrical properties [22].

The results presented in Table 4.19 show a mean value significantly higher than 1.0, of approximately 18% for major axis and of 25% for minor axis, where the minimum values for the ratio are always higher than one and the maximum values are up to a difference of 50% higher (maximum of 1.502 obtained for minor axis FB).

The trend of increasing the reduction factor with the increase of the steel grade is also noted in the statistical parameters and is highlighted in Figure 4.46, showing the mean values obtained for the ratio r_e/r_t for flexural buckling. These indicators conclude that an adjustment of the design rules for the buckling resistance of members made of high strength steel in compression is possible and may lead to more economical solutions.

Table 4.19 – Statistical parameters – flexural buckling

| Design rule | Subset (steel grade) | Buckling axis | n | mean | cov | min | max | >1.1 | <0.97 |
|---------------------------|----------------------|---------------|------|-------|------|-------|-------|------|-------|
| Flexural buckling EC3-1-1 | All | y-y | 1599 | 1.180 | 6.7% | 1.013 | 1.358 | 1327 | 0 |
| | | z-z | 1599 | 1.257 | 8.8% | 1.020 | 1.502 | 1486 | 0 |
| | S460 | y-y | 585 | 1.160 | 6.3% | 1.013 | 1.326 | 447 | 0 |
| | | z-z | 585 | 1.229 | 8.3% | 1.020 | 1.425 | 519 | 0 |
| | S500 | y-y | 559 | 1.177 | 6.5% | 1.025 | 1.326 | 461 | 0 |
| | | z-z | 559 | 1.253 | 8.4% | 1.037 | 1.449 | 525 | 0 |
| | S690 | y-y | 455 | 1.210 | 6.7% | 1.048 | 1.358 | 419 | 0 |
| | | z-z | 455 | 1.299 | 8.7% | 1.070 | 1.502 | 442 | 0 |

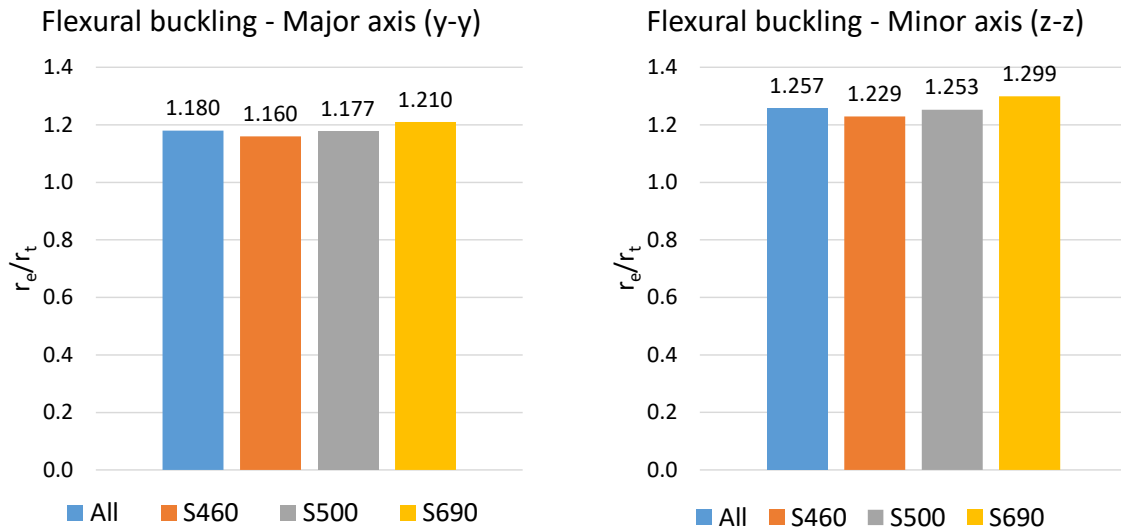


Figure 4.46 – Mean values of the safety factor using Eurocode 3 approach for flexural buckling

4.5.2. Beams

Considering the three methods presented in Section 2.4.2 to obtain the reduction factor χ_{LT} for lateral-torsional buckling, the numerical results obtained from the parametric study are plotted together with the theoretical ones according to the design method, general case, special case, and new EC3 case, respectively (Figure 4.47, Figure 4.48, and Figure 4.49). The scatter plots are divided into the cross-section class, where the approach described in Section 2.4.4 was used to obtain the reduction factor for class 3 sections.

For all the three methods, the trend of increasing the numerical reduction factor with the increase of the steel grade is also noted, as it was for the flexural buckling of columns. When comparing the three methods, the general case is the method that gives the lowest reduction factors, though on the other hand, the special case seems like the “unsafest method”, as some of the cases show a theoretical reduction factor higher than the numerical one. The new EC3 case is placed between the two methods (general case and special case), although with very few cases with a theoretical reduction factor higher than the numerical one. The results obtained are in line with previous assessments made for these design rules [14], [20], and [23].

These evidences can be verified through the statistical parameters for the ratio r_e/r_t ($\chi_{LT(numerical)}/\chi_{LT(theoretical)}$), presented in Table 4.20 for the general case, in Table 4.21 for the special case, and in Table 4.22 for the new EC3 case. The general case has 97% of the cases (4469 in 4595 cases) with a ratio higher than 1.1, with a mean value of 39% higher than 1.0 and the maximum value reaching 1.9.

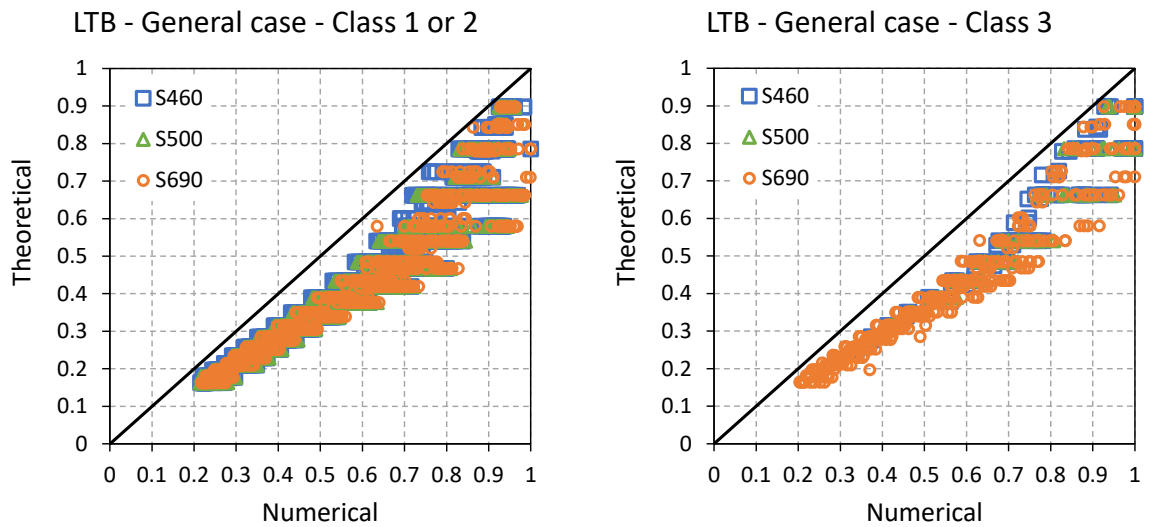


Figure 4.47 – Scatter plots for lateral-torsional buckling (all loading cases) – General case

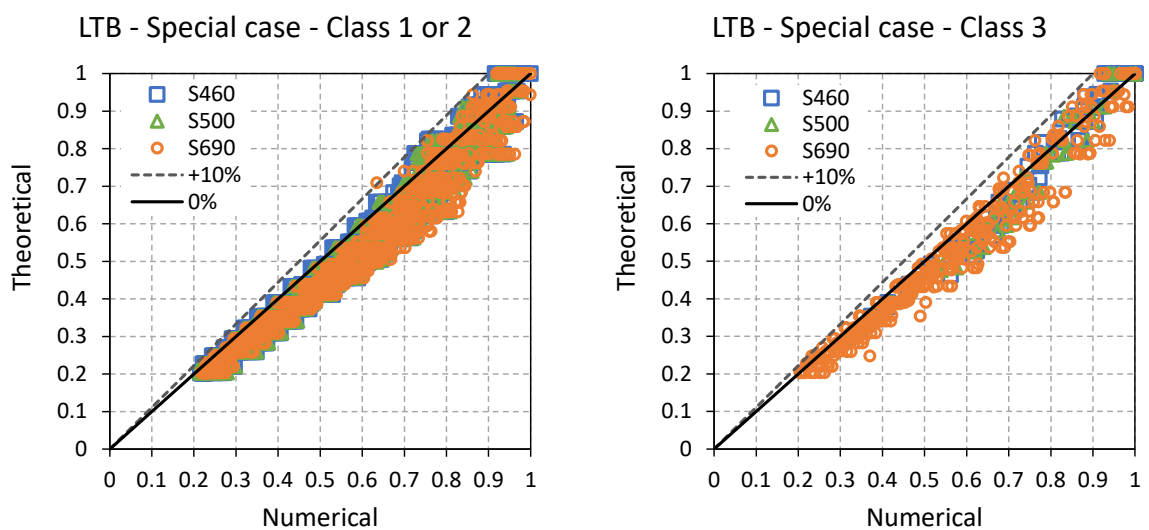


Figure 4.48 – Scatter plots for lateral-torsional buckling (all loading cases) – Special case

The statistics (Table 4.21) also prove that the special case is the unsafest method, with some cases ($\approx 4\%$) with a ratio lower than 0.97 and 40% of the cases in the range between 0.97 and 1.1. Nonetheless, the mean value is still 11% higher than 1.0.

The new EC3 case results in 2 cases lower than 0.97, nevertheless, 81% of the cases are higher than 1.1 (3731 in 4595), with a mean value at about 1.18. The new EC3 method presents the lowest coefficient of variation, meaning that it is the method with the lowest result dispersion.

The results obtained for the lateral-torsional buckling of beams indicate that a possible adjustment in the imperfection factors may lead to more economical designs, especially for the general case and the new EC3 case, since there is still a reservation in the resistance that can be exploited.

The mean values combined for the three methods are presented in Figure 4.50 and divided into steel grades, where it is possible to confirm the increase of the safety with the steel grade for the three methods.

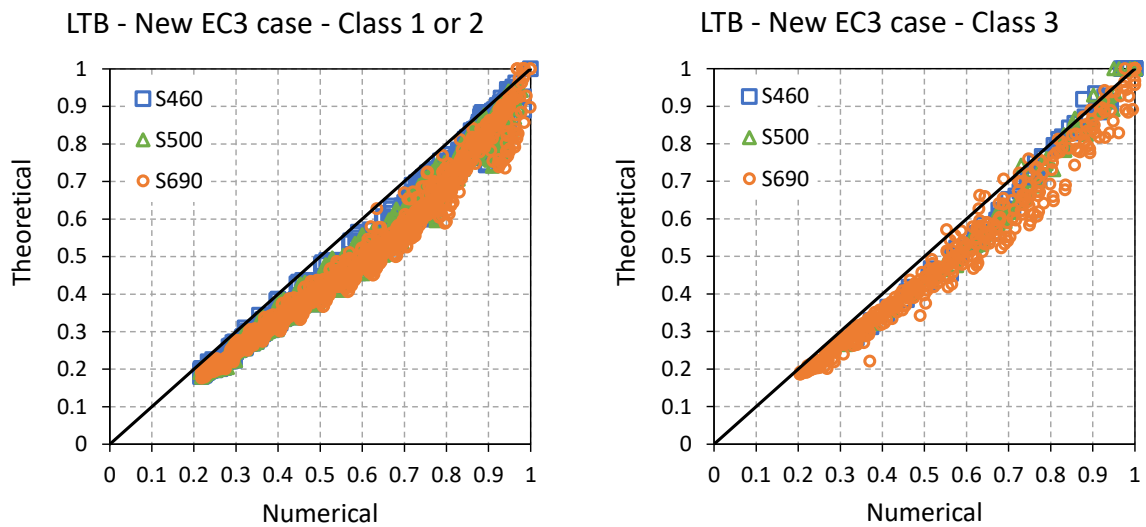


Figure 4.49 – Scatter plots for lateral-torsional buckling (all loading cases) – New EC3 case

Table 4.20 – Statistical parameters for lateral-torsional buckling – General case

| Design rule | Subset (steel grade) | n | mean | cov | min | max | >1.1 | <0.97 |
|--------------|----------------------|------|-------|-------|-------|-------|------|-------|
| General case | All | 4595 | 1.392 | 10.2% | 1.024 | 1.933 | 4469 | 0 |
| | S460 | 1508 | 1.367 | 10.0% | 1.031 | 1.713 | 1454 | 0 |
| | S500 | 1469 | 1.388 | 9.7% | 1.030 | 1.734 | 1434 | 0 |
| | S690 | 1618 | 1.419 | 10.3% | 1.024 | 1.933 | 1581 | 0 |

Table 4.21 – Statistical parameters for lateral-torsional buckling – Special case

| Design rule | Subset (steel grade) | n | mean | cov | min | max | >1.1 | <0.97 |
|--------------|----------------------|------|-------|------|-------|-------|------|-------|
| Special case | All | 4595 | 1.118 | 7.9% | 0.895 | 1.533 | 2579 | 178 |
| | S460 | 1508 | 1.100 | 7.5% | 0.916 | 1.354 | 743 | 75 |
| | S500 | 1469 | 1.112 | 7.5% | 0.920 | 1.380 | 799 | 58 |
| | S690 | 1618 | 1.139 | 8.2% | 0.895 | 1.533 | 1037 | 45 |

Table 4.22 – Statistical parameters for lateral-torsional buckling – New EC3 case

| Design rule | Subset (steel grade) | n | mean | cov | min | max | >1.1 | <0.97 |
|--------------|----------------------|------|-------|------|-------|-------|------|-------|
| New EC3 case | All | 4595 | 1.176 | 6.7% | 0.968 | 1.721 | 3731 | 2 |
| | S460 | 1508 | 1.155 | 6.0% | 1.000 | 1.353 | 1164 | 0 |
| | S500 | 1469 | 1.169 | 6.1% | 1.000 | 1.370 | 1185 | 0 |
| | S690 | 1618 | 1.202 | 7.2% | 0.968 | 1.721 | 1382 | 2 |

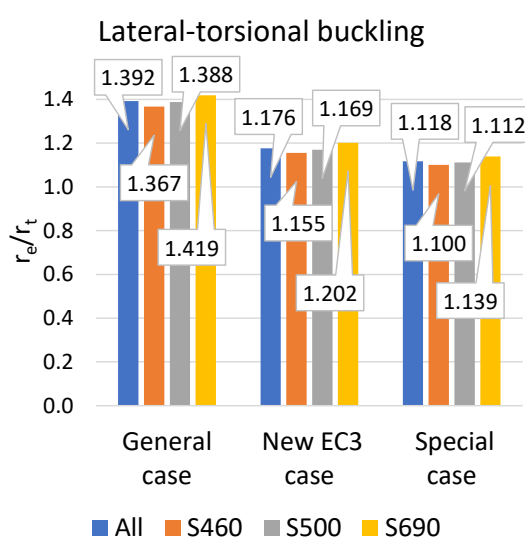


Figure 4.50 – Mean values of the safety factor for lateral-torsional buckling for all methods considered

4.5.2.1. Hybrid beams

As described in Section 4.4.2, for the assessment of the behaviour of hybrid beams, three steel grades were considered for the flanges, S460, S500 and S690 with the webs in steel grade S355. The assessment was performed only for constant bending moment, in order to exclude any interaction with shear force, as the objective was to assess the lateral-torsional buckling resistance of hybrid members.

Therefore, the results assessed are divided into two sets: i) how the current design rules for homogeneous beams perform for hybrid beams in high strength steel, and ii) aimed to assess whether the hybrid beams are capable to resist similarly to the homogenous beams.

In order to evaluate how the current design rules perform when applied to hybrid beams, similar analyses to those carried out for the homogenous beams were made. The scatter plots for the three methods considered, general case, special case, and new EC3 case are presented in Figure 4.51 and Figure 4.52, as well as the mean values for the ratio r_e/r_t , divided into the steel grades (Figure 4.52).

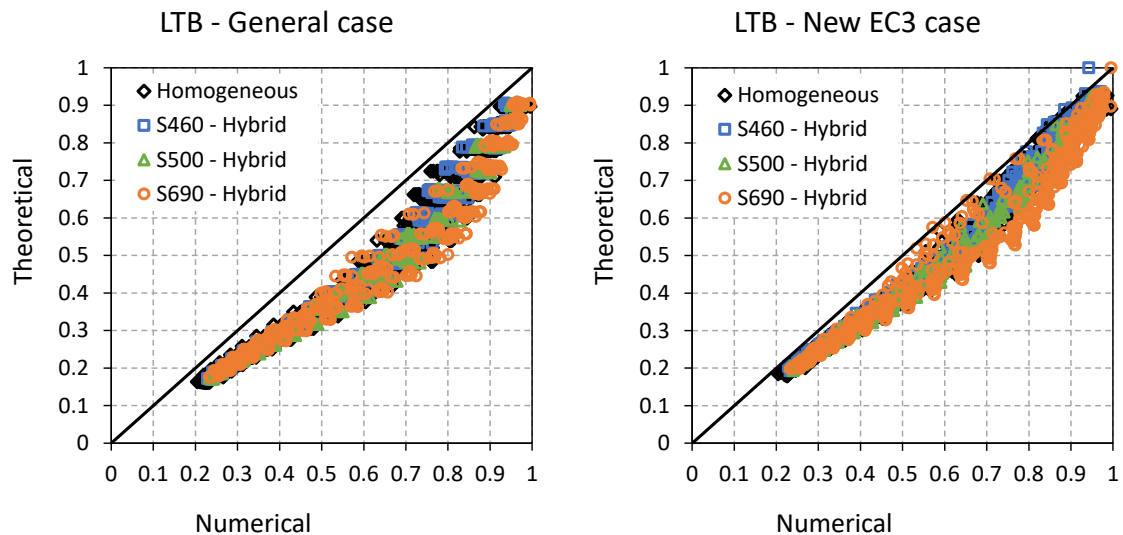


Figure 4.51 - Scatter plots for lateral-torsional buckling of hybrid beams – General case and New EC3 case

The statistical parameters for the ratio (r_e/r_t) are shown in Table 4.23, Table 4.24, and Table 4.25, for the general case, the special case, and the new EC3 case, respectively, for hybrid and homogeneous beams under constant bending moment, in subset by steel grade. The results show that in terms of safety (the difference between the numerical and theoretical reduction factor), the behaviour of hybrid and homogeneous beams are very similar when the lateral-torsional buckling is the governing buckling mode. The difference in the mean value between hybrid and homogeneous is on average less than 2%, considering all the three design methods.

Based on the analyses performed for hybrid beams, it is viable to say that a possible adjustment in the rules for lateral-torsional buckling of high strength steel beams can also be suitable to hybrid beams.

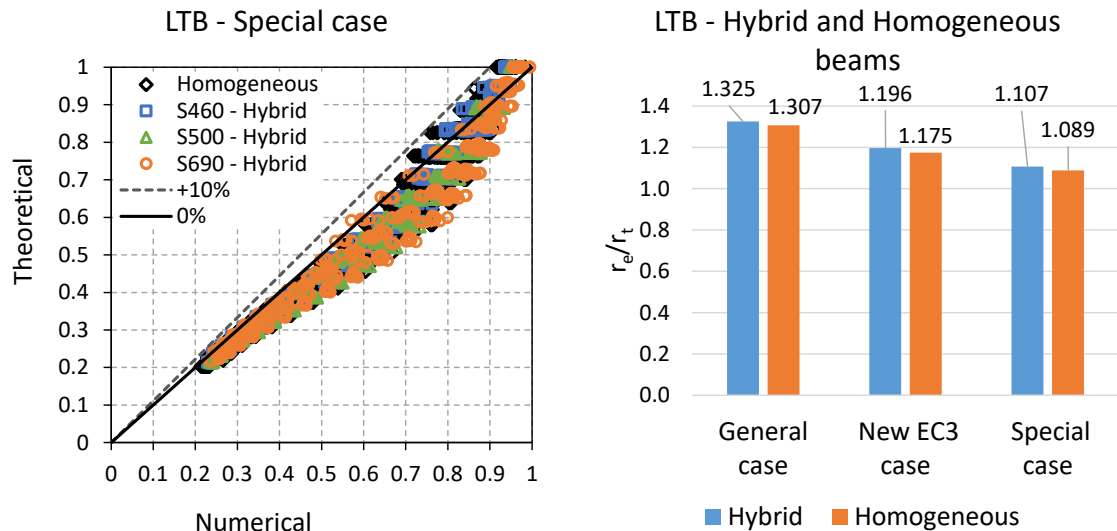


Figure 4.52 – Scatter plots for special case for LTB of hybrid beams and mean values

Table 4.23 – Statistical parameters for lateral-torsional buckling of hybrid beams – General case

| Design rule | Subset - Steel grade | Beams - Set | n | mean | cov | min | max | >1.1 | <0.97 |
|--------------|----------------------|-------------|------|-------|-------|-------|-------|------|-------|
| General case | All | Hybrid | 1175 | 1.325 | 10.4% | 1.031 | 1.634 | 1082 | 0 |
| | | Homog. | | 1.307 | 10.6% | 1.024 | 1.606 | 1031 | 0 |
| | S460 | Hybrid | 412 | 1.294 | 10.2% | 1.031 | 1.560 | 362 | 0 |
| | | Homog. | | 1.287 | 10.6% | 1.031 | 1.568 | 351 | 0 |
| | S500 | Hybrid | 320 | 1.340 | 10.0% | 1.048 | 1.587 | 297 | 0 |
| | | Homog. | | 1.316 | 10.1% | 1.030 | 1.558 | 282 | 0 |
| | S690 | Hybrid | 443 | 1.344 | 10.5% | 1.058 | 1.634 | 423 | 0 |
| | | Homog. | | 1.319 | 10.7% | 1.024 | 1.606 | 398 | 0 |

Table 4.24 – Statistical parameters for lateral-torsional buckling of hybrid beams – Special case

| Design rule | Subset - Steel grade | Beams - Set | n | mean | cov | min | max | >1.1 | <0.97 |
|--------------|----------------------|-------------|------|-------|------|-------|-------|------|-------|
| Special case | All | Hybrid | 1175 | 1.107 | 8.5% | 0.935 | 1.355 | 608 | 100 |
| | | Homog. | | 1.089 | 8.6% | 0.914 | 1.327 | 545 | 156 |
| | S460 | Hybrid | 412 | 1.083 | 7.9% | 0.935 | 1.290 | 182 | 52 |
| | | Homog. | | 1.076 | 8.3% | 0.916 | 1.296 | 174 | 64 |
| | S500 | Hybrid | 320 | 1.115 | 8.1% | 0.947 | 1.313 | 178 | 27 |
| | | Homog. | | 1.093 | 8.2% | 0.920 | 1.287 | 155 | 41 |
| | S690 | Hybrid | 443 | 1.123 | 8.9% | 0.955 | 1.355 | 248 | 21 |
| | | Homog. | | 1.098 | 8.9% | 0.914 | 1.327 | 216 | 51 |

Table 4.25 – Statistical parameters for lateral-torsional buckling of hybrid beams – New EC3 case

| Design rule | Subset - Steel grade | Beams - Set | n | mean | cov | min | max | >1.1 | <0.97 |
|--------------|----------------------|-------------|------|-------|------|-------|-------|------|-------|
| New EC3 case | All | Hybrid | 1175 | 1.196 | 8.0% | 0.942 | 1.478 | 948 | 1 |
| | | Homog. | | 1.175 | 7.2% | 1.000 | 1.393 | 889 | 0 |
| | S460 | Hybrid | 412 | 1.164 | 6.7% | 0.942 | 1.331 | 308 | 1 |
| | | Homog. | | 1.156 | 6.7% | 1.003 | 1.310 | 289 | 0 |
| | S500 | Hybrid | 320 | 1.203 | 7.0% | 1.019 | 1.381 | 267 | 0 |
| | | Homog. | | 1.177 | 6.7% | 1.000 | 1.337 | 251 | 0 |
| | S690 | Hybrid | 443 | 1.221 | 8.9% | 0.994 | 1.478 | 373 | 0 |
| | | Homog. | | 1.190 | 7.7% | 1.007 | 1.393 | 349 | 0 |

Figure 4.53 depicts the assessment of the resistance of the hybrid beams in relation to the homogeneous beams, where the vertical axis shows the ratio between the buckling bending moment resistance of a hybrid beam over the buckling bending moment resistance of a homogenous beam, the normalized slenderness is represented on the horizontal axis (left side) and the ratio between the bending moment resistance for the same beams (right side), plastic

bending moment resistance for class 1 or 2 sections ($M_{pl,Rd}$) and elasto-plastic bending moment resistance for class 3 sections ($M_{ep,Rd}$). These ratios are plotted for the numerical results (orange dots) and using the general case from Eurocode 3 [1] (blue dots). These representations show that, with the increase of the slenderness, the ratio between the buckling bending moment resistances is reduced (Figure 4.53 – left side), and also that, for a given ratio for the bending moment resistance of the hybrid and homogeneous beams, the buckling resistance is either equal to that moment ratio or higher, where this trend is shown for the majority of the cases (Figure 4.53 – right side).

The trend of decreasing the ratio of the buckling bending moment resistance between hybrid and homogeneous beams with the increase of the slenderness is also confirmed through the statistical parameters presented in Table 4.26, where the ratio $M_{b,Rd,Hybrid}/M_{b,Rd,homogeneous}$, is splitted into different levels of slenderness: i) low - $\bar{\lambda}_{LT} \leq 0.8$, ii) medium - $0.8 < \bar{\lambda}_{LT} \leq 1.2$, iii) high - $\bar{\lambda}_{LT} > 1.2$, and also divided into steel grades. The increase of the mean value for this ratio is slightly more noticeable into lower to medium slenderness (about 1% considering all steel grades) than medium to high slenderness (about 0.6% considering all steel grades). Once we split the ratio into steel grades, the difference in the mean value is higher for the S690 cases than for the lower steel grades, of approximately 2% for lower-to-high slenderness for S690 and of approximately 1%-1.5% for lower steel grades. Nonetheless, the mean value is higher for lower steel grades, which is due to the fact that the difference for the bending moment resistance ($M_{pl,Rd}$ or $M_{ep,Rd}$) between hybrid and homogeneous beams is higher for the higher steel grades. The majority of the cases (938 in 1175 cases) falls in the range between 0.95-1.0 for the ratio $M_{b,Rd,Hybrid}/M_{b,Rd,homogeneous}$, being the mean value for all the cases 0.987. The mean values are graphically represented in Figure 4.54.

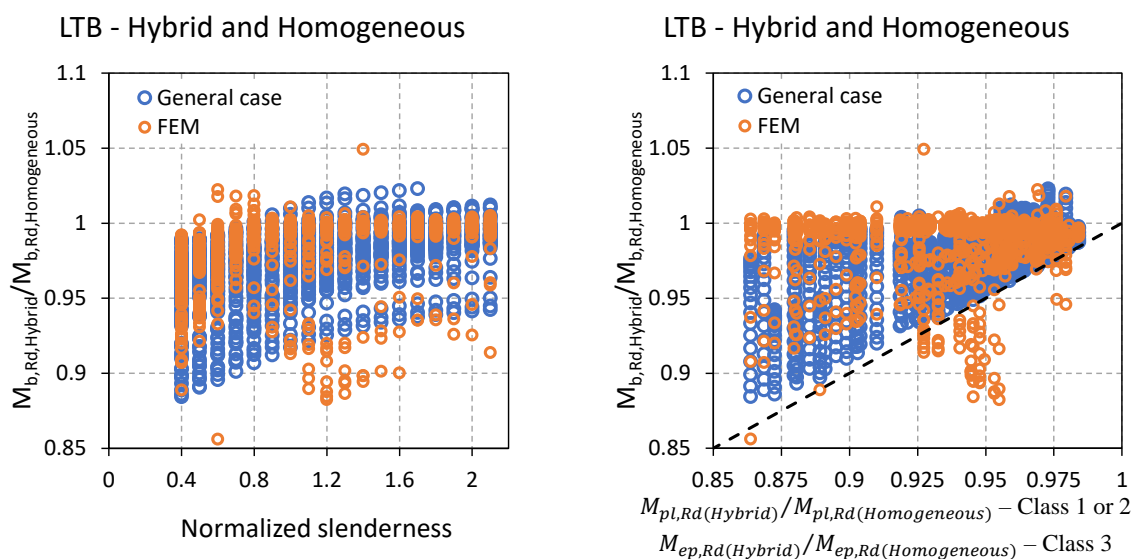
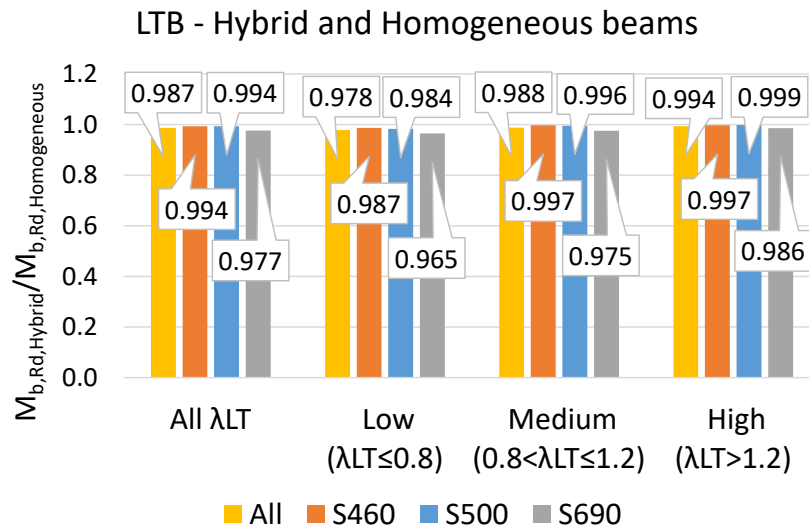


Figure 4.53 – Assessment of the resistance for hybrid beams

Table 4.26 – Statistical parameters for the ratio $M_{b,Rd,Hybrid}/M_{b,Rd,Homogeneous}$

| Steel grade | Slenderness | n | mean | cov | min | max | >1.0 | <0.95 |
|-------------|-------------|------|-------|------|-------|-------|------|-------|
| All | All | 1175 | 0.987 | 2.2% | 0.856 | 1.049 | 141 | 96 |
| | Low | 379 | 0.978 | 2.2% | 0.856 | 1.022 | 15 | 44 |
| | Medium | 289 | 0.988 | 2.5% | 0.882 | 1.011 | 26 | 26 |
| | High | 507 | 0.994 | 1.9% | 0.887 | 1.049 | 100 | 26 |
| S460 | All | 412 | 0.994 | 1.0% | 0.909 | 1.018 | 35 | 3 |
| | Low | 150 | 0.987 | 1.3% | 0.909 | 1.018 | 5 | 3 |
| | Medium | 101 | 0.997 | 0.5% | 0.969 | 1.003 | 12 | 0 |
| | High | 161 | 0.997 | 0.3% | 0.970 | 1.003 | 18 | 0 |
| S500 | All | 320 | 0.994 | 1.2% | 0.946 | 1.022 | 56 | 2 |
| | Low | 90 | 0.984 | 1.6% | 0.946 | 1.022 | 8 | 2 |
| | Medium | 76 | 0.996 | 0.7% | 0.975 | 1.001 | 4 | 0 |
| | High | 154 | 0.999 | 0.4% | 0.975 | 1.005 | 44 | 0 |
| S690 | All | 443 | 0.977 | 3.2% | 0.856 | 1.049 | 50 | 91 |
| | Low | 139 | 0.965 | 2.6% | 0.856 | 1.013 | 2 | 39 |
| | Medium | 112 | 0.975 | 3.6% | 0.882 | 1.011 | 10 | 26 |
| | High | 192 | 0.986 | 2.9% | 0.887 | 1.049 | 38 | 26 |

Figure 4.54 – Mean values for the ratio $M_{b,Rd,Hybrid}/M_{b,Rd,Homogeneous}$

4.5.3. Beam-Columns

The parametric study for members in bending and axial compression covered unrestrained members and minor axis restrained buckling members, both loaded with axial force and major axis bending moment. The restrained members are susceptible to major axis flexural buckling, and therefore, for determining the theoretical reduction factor (χ_y), the Eurocode 3 [1] approach for flexural buckling (described in Section 2.4.1) is used.

For the unrestrained members, prone to flexural buckling and lateral-torsional buckling, the determination of the theoretical reduction factors (χ_y , χ_z and χ_{LT}) is also based on the Eurocode 3 [1] approach for flexural buckling, and for the lateral-torsional buckling, the determination is performed first using the general case from Eurocode 3 [1] and then using the new EC3 case from the new version of the Eurocode 3 [7] (both described in Section 2.4.2).

The results for the beam-columns parametric study are assessed in terms of pairs (n, m) , where a pair represent the ratio $n = N/N_{pl}$ and $m = M/M_{pl}$. For the numerical results, N and M are the pair of axial force and bending moment obtained in the numerical analysis, and for the theoretical results, N and M represent the maximum pair of axial force and bending moment that can be applied using the interaction formula presented in Section 2.4.3. Figure 4.55 represent the interaction curve N-M with the representation of the pairs (n, m) .

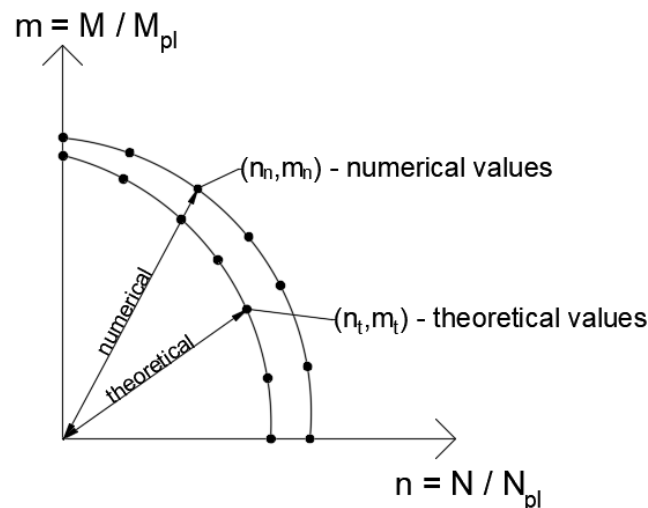


Figure 4.55 – Interaction N+M – representation of the results for beam-columns

The scatter plots, shown in Figure 4.56 for the unrestrained members and in Figure 4.57 for members with minor axis restrained, represent the distance of the obtained pair (n, m) to the central point $(0,0)$, where the vertical axis represent the theoretical values and the horizontal axis the numerical values.

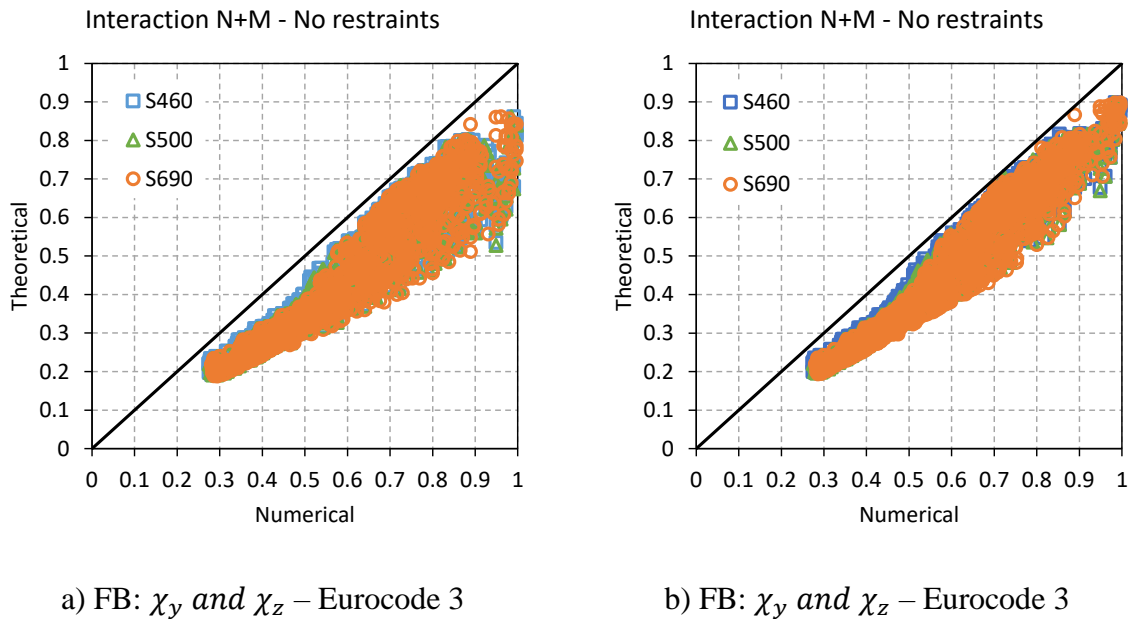


Figure 4.56 – Scatter plots for beam-columns without restraints (all loading cases)

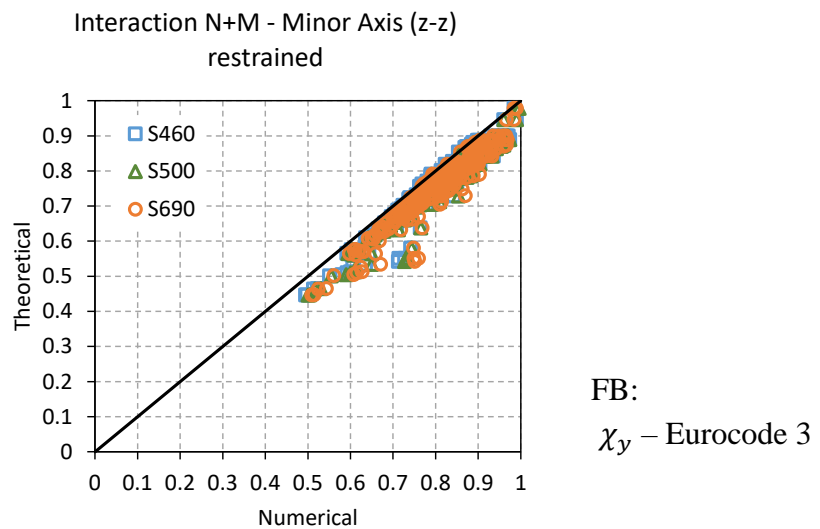


Figure 4.57 – Scatter plots for beam-columns with minor axis restrained (all loading cases)

The statistical parameters are assessed for the ratio $(n_n/m_n)/(n_t/m_t)$, and are given in Table 4.27 and Table 4.28 for unrestrained and restrained members, respectively. In both cases, the results are on the safe-side (with the numerical values being higher than the theoretical

ones). Nevertheless, it is noted that the unrestrained members exhibit an increased level of safety when compared to the unrestrained ones.

Table 4.27 – Statistical parameters for bending combined with axial compression without restrains

| Design rule | Subset (steel grade) | n | mean | cov | min | max | >1.1 | <0.97 |
|--|----------------------|------|-------|-------|-------|-------|------|-------|
| FB: EC3-1-1 and LTB: General case | All | 3674 | 1.345 | 11.5% | 1.057 | 1.806 | 3542 | 0 |
| | S460 | 1231 | 1.326 | 10.8% | 1.059 | 1.775 | 1187 | 0 |
| | S500 | 1227 | 1.340 | 11.3% | 1.061 | 1.799 | 1184 | 0 |
| | S690 | 1216 | 1.367 | 12.2% | 1.057 | 1.806 | 1171 | 0 |
| FB: EC3-1-1 and LTB: New EC3 case | All | 3674 | 1.276 | 10.1% | 1.024 | 1.597 | 3395 | 0 |
| | S460 | 1231 | 1.260 | 9.3% | 1.041 | 1.508 | 1137 | 0 |
| | S500 | 1227 | 1.272 | 9.9% | 1.024 | 1.531 | 1139 | 0 |
| | S690 | 1216 | 1.297 | 10.9% | 1.026 | 1.597 | 1119 | 0 |

Table 4.28 – Statistical parameters for bending combined with axial compression with minor axis (z-z) restrained

| Design rule | Subset (steel grade) | n | mean | cov | min | max | >1.1 | <0.97 |
|---------------------|----------------------|-----|-------|------|-------|-------|------|-------|
| FB (y-y): EC31-1 | All | 838 | 1.067 | 4.6% | 0.982 | 1.388 | 117 | 0 |
| | S460 | 285 | 1.064 | 4.2% | 0.994 | 1.321 | 36 | 0 |
| | S500 | 283 | 1.067 | 4.5% | 0.994 | 1.343 | 38 | 0 |
| | S690 | 270 | 1.072 | 5.0% | 0.982 | 1.388 | 43 | 0 |

For the unrestrained members, the difference between using the general case or the new EC3 case to obtain the reduction factor for lateral-torsional buckling (χ_{LT}) is of approximately 7%, being the reduction factor higher for the new EC3 case (able to resist to higher forces).

The trend of increasing the safety with the steel grade is also present in the unrestrained members, using the general case or the new EC3 case, and for the restrained members, as it can be seen from Figure 4.58, though not as pronounced as in the beams and columns buckling (only submitted to bending moment or axial force).

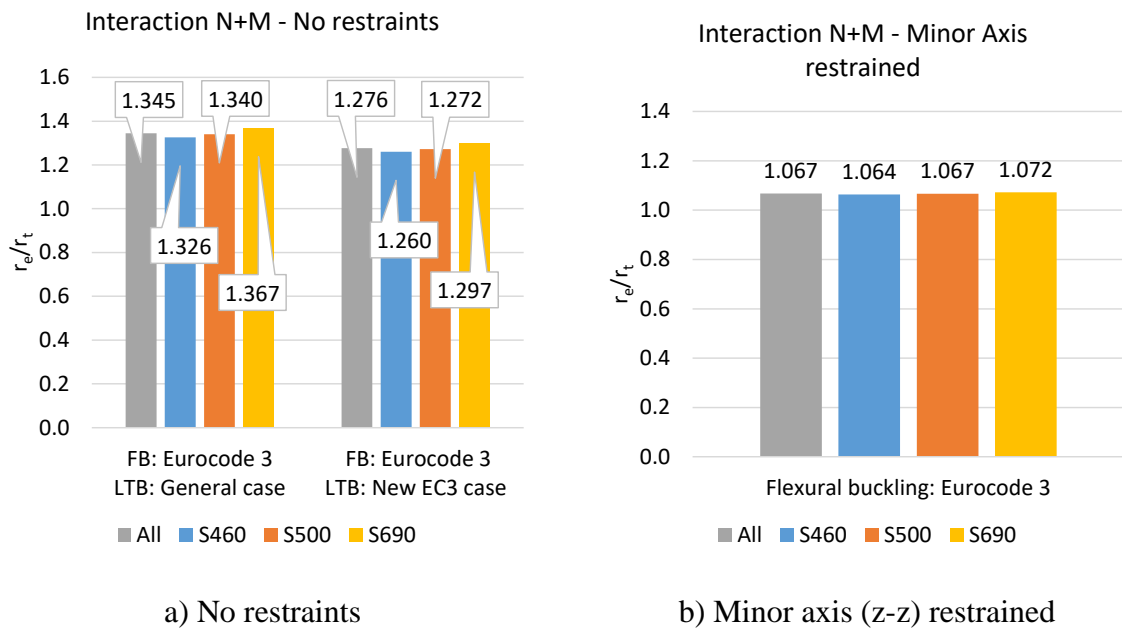


Figure 4.58 – Mean values of the safety factor for combined bending and axial compression

4.5.4. New residual stresses models

In this section, the results obtained in the numerical simulations with the residual stresses models with thermal cuts and non-thermal cuts (Section 4.4.4) are presented and compared with the recommendations of the Eurocode and with the numerical simulations using the ECCS residual stresses patterns.

4.5.4.1. Columns

The first set of results in Figure 4.59 and Figure 4.60 presents the comparison of the reduction factor for the different residual stresses models used in the parametric studies (ECCS, thermal cut and non-thermal cut), with the reduction factor given by the Eurocode 3 [1] design recommendations for flexural buckling.

The theoretical reduction factor (Eurocode 3) is associated with a buckling curve, where, for welded I-sections with a $t_f \leq 40 \text{ mm}$, curve b is for flexural buckling about major axis (y-y) and curve c for minor axis (z-z), if $t_f > 40 \text{ mm}$, then it is curve c for flexural buckling about major axis (y-y) and curve d for minor axis (z-z). These curves (b, c and d) are plotted in Figure

4.59 together with the numerical results in relation to the normalized slenderness. It is possible to note that most of the cases are under the lowest buckling curve (less conditioning), both for flexural buckling about major and minor axes, although this is more evident in the flexural buckling about minor axis.

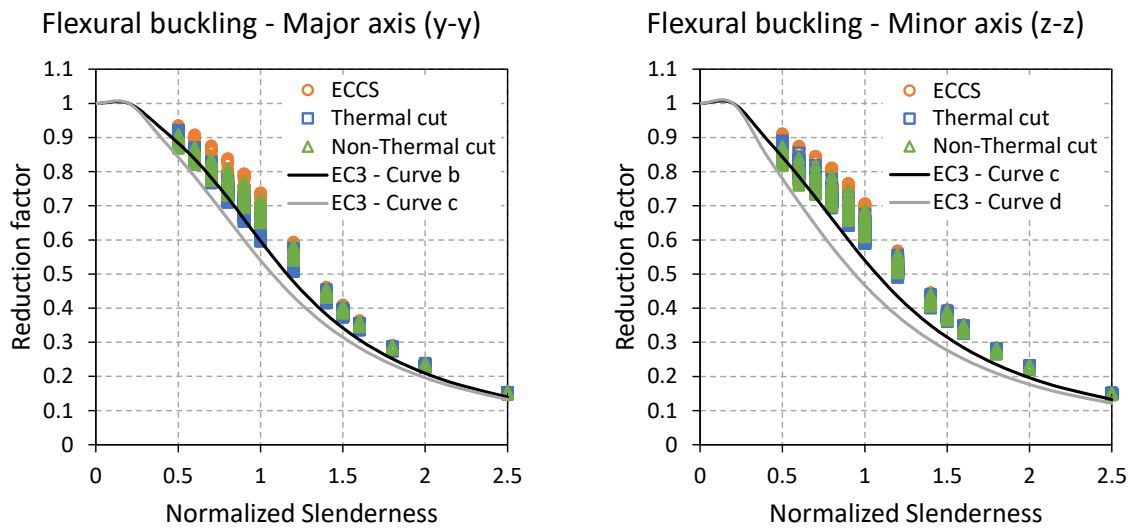


Figure 4.59 – Buckling curves for flexural buckling with new residual stresses models

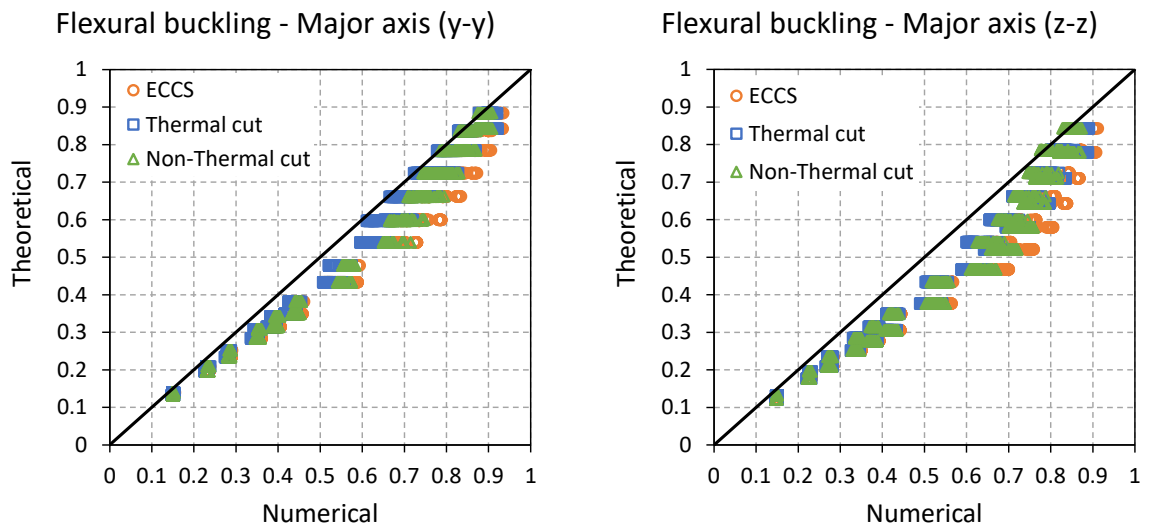


Figure 4.60 – Scatter plots for flexural buckling with new residual stresses models

In Figure 4.60, the numerical reduction factors ($\chi_{y|z(FEM)}$) are plotted in relation to the theoretical reduction factor ($\chi_{y|z(EC3)}$) for the same case (section, slenderness and steel grade),

since the theoretical reduction factor only depends on the buckling curve and slenderness, for different numerical reduction factors (ECCS, thermal cut and non-thermal cut), the corresponding theoretical reduction factor is the same. Given that it is possible to verify that the model which uses the ECCS residual stresses is the one showing higher numerical reduction factors and the model considering the thermal cut gives the lowest numerical reduction factor. However, all the residual stresses models have a higher reduction factor when compared to the theoretical reduction factor, meaning that the Eurocode remains safe-sided regardless of the residual stresses pattern used in the numerical analyses.

The scatter plots in Figure 4.60 are further analysed with the statistical parameters of the ratio r_e/r_t in Table 4.29 for flexural buckling about major axis and minor axis, where r_e is the numerical reduction factor and r_t is the theoretical reduction factor (obtained using Eurocode 3). The statistical parameters are divided into subsets according to the residual stresses model.

Table 4.29 - Statistical parameters for flexural buckling with new residual stresses models

| Design rule | Subset (residual stresses model) | Buckling axis | n | mean | cov | min | max | >1.1 | <0.97 |
|-----------------------------|----------------------------------|---------------|------|-------|------|-------|-------|------|-------|
| Flexural buckling - EC3-1-1 | ECCS | y-y | 1599 | 1.180 | 6.7% | 1.013 | 1.358 | 1327 | 0 |
| | | z-z | 1599 | 1.257 | 8.8% | 1.020 | 1.502 | 1486 | 0 |
| | Thermal cut | y-y | 1599 | 1.126 | 6.1% | 0.989 | 1.289 | 1037 | 0 |
| | | z-z | 1599 | 1.218 | 8.2% | 1.015 | 1.441 | 1400 | 0 |
| | Non-Thermal cut | y-y | 1599 | 1.151 | 7.0% | 0.988 | 1.326 | 1152 | 0 |
| | | z-z | 1599 | 1.223 | 9.2% | 0.982 | 1.462 | 1345 | 0 |

The results confirm that the majority of the cases have a numerical reduction factor higher than the theoretical ones, having no cases with a ratio lower than 0.97 for both major and minor axes flexural buckling (the lowest ratio obtained is 0.982 for minor axis flexural buckling with the non-thermal cut residual stresses model).

In terms of the mean value for the ratio r_e/r_t , for flexural buckling about major axis, all the approaches considered show a mean value higher than 1.0, where the ECCS model has the highest value, of approximately 18% higher than 1.0, followed by the non-thermal cut (15%

higher than 1.0) and then the thermal cut model with a mean value higher than 1.0 of approximately 12%, where 73% of the cases have a ratio higher than 1.1 (3516 in 4797 cases).

Regarding the statistical parameters about minor axis flexural buckling, the mean values are even higher, 25% higher than 1.0 for the ECCS model, 22% for the non-thermal cut model and 21% for the thermal cut model (4231 of the 4797 cases have a ratio higher than 1.1).

From Table 4.29, it is possible to confirm that regardless of the residual stresses model considered in the numerical model, the theoretical reduction factor for flexural buckling obtained by the Eurocode 3 [1], for both major and minor axes, is considerably lower when compared to the numerical reduction factor. This means that an adjustment of the design rules for flexural buckling of high strength steel columns is of interest.

Figure 4.61 shows the mean value for ratio r_e/r_t of the different residual stresses patterns used in the parametric study (ECCS, non-thermal cut, and thermal cut), divided into the steel grades considered (S460, S500, and S690). The trend of increasing the safety with the increasing of the steel grade is also noticeable in the new residual stresses models.

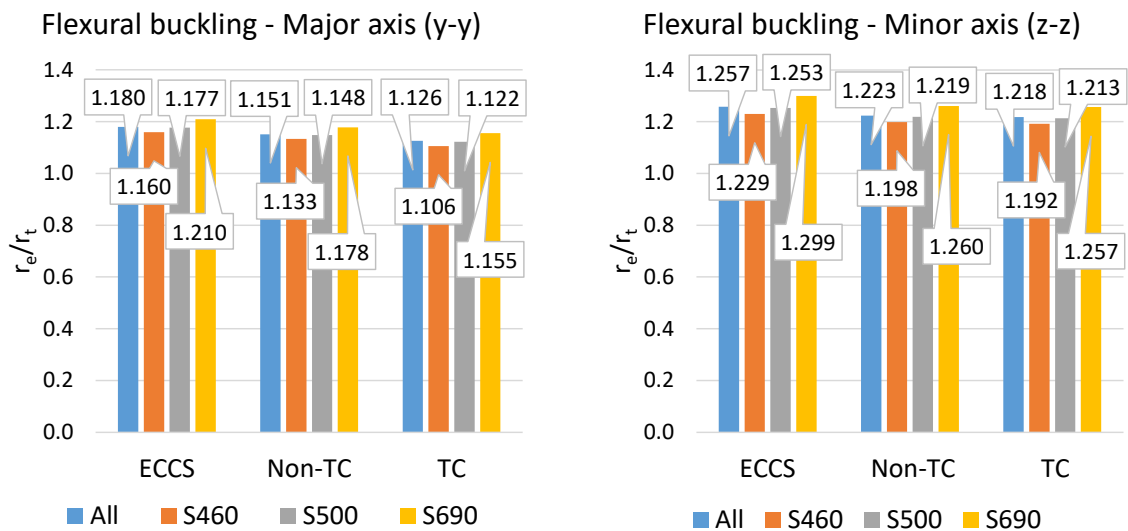


Figure 4.61 – Mean values for flexural buckling with new residual stresses models

Bearing in mind a direct comparison of the numerical reduction factors obtained using the different residual stresses models, in Figure 4.62, the numerical results using the new residual stresses models (thermal cut and non-thermal cut) are plotted in relation to the numerical results using the ECCS residual stresses model. From the results plotted in Figure 4.62, it is possible to identify a trend of having lower reduction factors when using the residual stresses model

with thermal cuts and having the highest reduction factors for the ECCS residual stresses model, both for flexural buckling about major and minor axes.

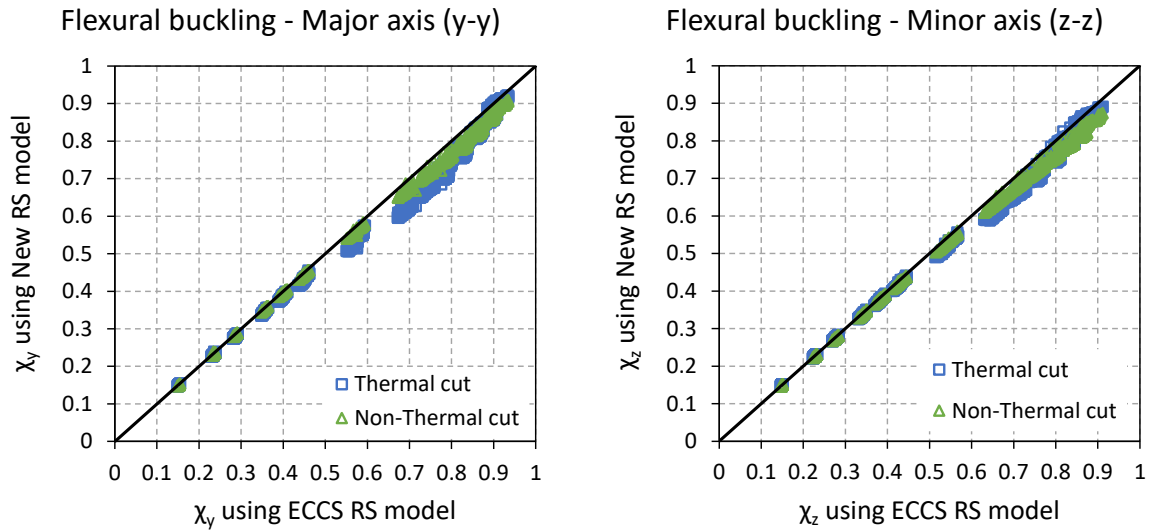


Figure 4.62 – Direct comparison between the reduction factors for flexural buckling with new residual stresses models

The trend observed in Figure 4.62 is confirmed through the statistical parameters for the ratio between the residual stresses model considered ($\chi_{y|z(FEMi)}/\chi_{y|z(FEMj)}$) presented in Table 4.30 for flexural buckling about major axis and Table 4.31 for minor axis.

Table 4.30 – Statistical parameters for the ratio between the reduction factors (flexural buckling – major axis)

| Subset (residual stresses model) | n | mean | cov | min | max | >1.0 | <0.95 |
|-----------------------------------|------|-------|------|-------|-------|------|-------|
| $\chi_{y(TC)}/\chi_{y(ECCS)}$ | 1599 | 0.955 | 3.2% | 0.877 | 1.013 | 10 | 557 |
| $\chi_{y(Non-TC)}/\chi_{y(ECCS)}$ | 1599 | 0.975 | 1.7% | 0.930 | 1.021 | 1 | 122 |
| $\chi_{y(TC)}/\chi_{y(Non-TC)}$ | 1599 | 0.979 | 2.4% | 0.916 | 1.028 | 175 | 263 |

Table 4.31 – Statistical parameters for the ratio between the reduction factors (flexural buckling – minor axis)

| Subset (residual stresses model) | n | mean | cov | min | max | >1.0 | <0.95 |
|-----------------------------------|------|-------|------|-------|-------|------|-------|
| $\chi_{z(TC)}/\chi_{z(ECCS)}$ | 1599 | 0.969 | 2.5% | 0.914 | 1.009 | 8 | 368 |
| $\chi_{z(Non-TC)}/\chi_{z(ECCS)}$ | 1599 | 0.972 | 1.9% | 0.936 | 1.000 | 0 | 257 |
| $\chi_{z(TC)}/\chi_{z(Non-TC)}$ | 1599 | 0.997 | 1.9% | 0.947 | 1.037 | 450 | 9 |

For flexural buckling about major axis, the difference between the ECCS model and thermal cut model is on average of approximately 5%, of approximately 3% for the ECCS and non-thermal cut model, and of approximately 2% between the new residual stresses models (thermal cut and non-thermal cut). These differences are slightly lower in the flexural buckling about minor axis, of approximately 3% on average between ECCS and thermal cut and non-thermal cut models, and almost no difference between the new residual stresses models.

In Figure 4.63 the mean values for the ratio between the reduction factors are plotted, divided into the steel grades (S460, S500 and S690). It is noted that there is no significant difference in the mean values ratios for the high strength steel grades considered.

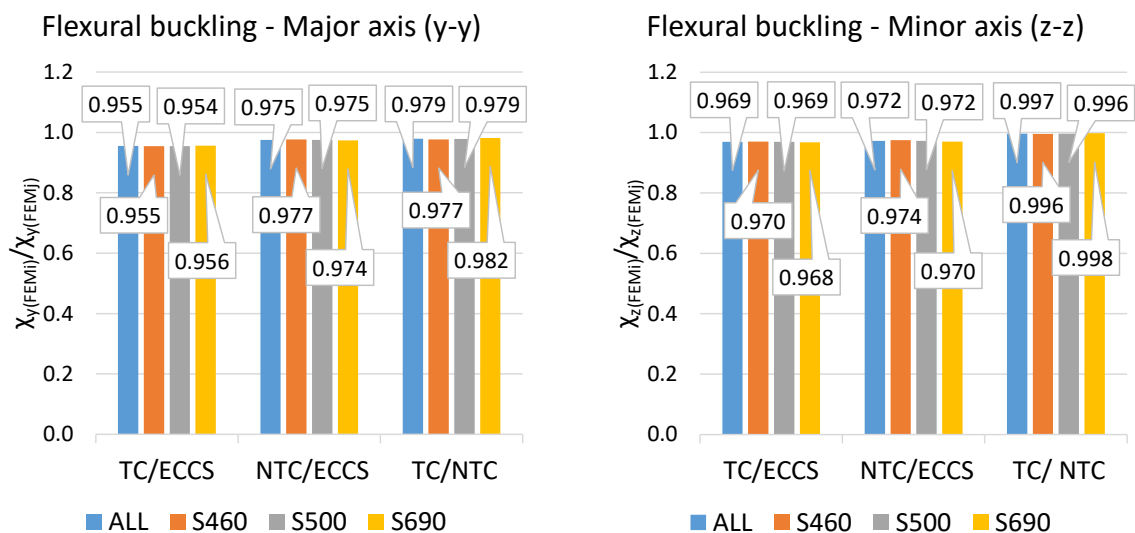


Figure 4.63 – Mean values for the ratio between the reduction factors for flexural buckling

4.5.4.2. Beams

Similar analyses were performed for lateral-torsional buckling of beams and then compared to the three methods currently available, the general case and special case from the current Eurocode 3 [1] and the new EC3 method from the new version of the Eurocode 3 [7]. The scatter plots for the numerical over the theoretical reduction factor for the three residual stresses models considered are given in Figure 4.64, Figure 4.65, and Figure 4.66, for the general case, new EC3 case, and special case. The results are plotted in relation to the numerical reduction factor ($\chi_{LT(FEM)}$) and the corresponding theoretical reduction factor ($\chi_{LT(design-rule)}$), similarly to what was previously done for flexural buckling.

The results (from Figure 4.64 to Figure 4.66), show that the ECCS residual stresses model gives the highest reduction factor (as in the flexural buckling), and the thermal cut tends to give the lowest reduction factor. When the three methods are compared, it is clear that the general case is the method that shows the highest difference (on the safe-side) in relation to the numerical reduction factor, regardless of the residual stresses model. The special case shows unsafe results for all the three residual stresses patterns considered, while the new EC3 method is the method which has the lowest difference between the numerical and theoretical reduction factor and being safe-sided at the same time, presenting a good balance between safety and accuracy, regardless of the residual stresses model used.

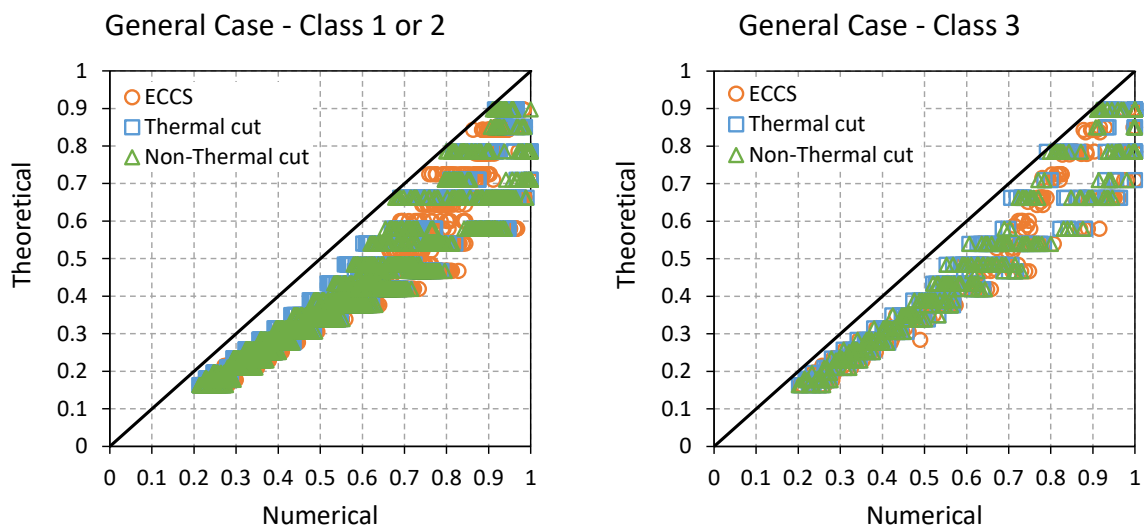


Figure 4.64 – Scatter plots for lateral-torsional buckling with new residual stresses models (all cases) – General case

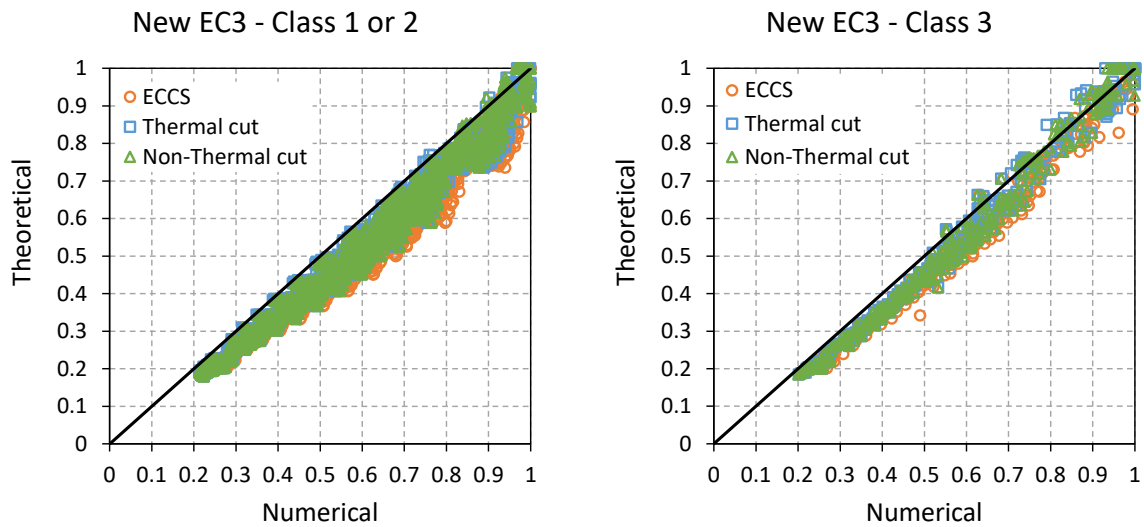


Figure 4.65 – Scatter plots for lateral-torsional buckling with new residual stresses models (all cases) – New EC3 case

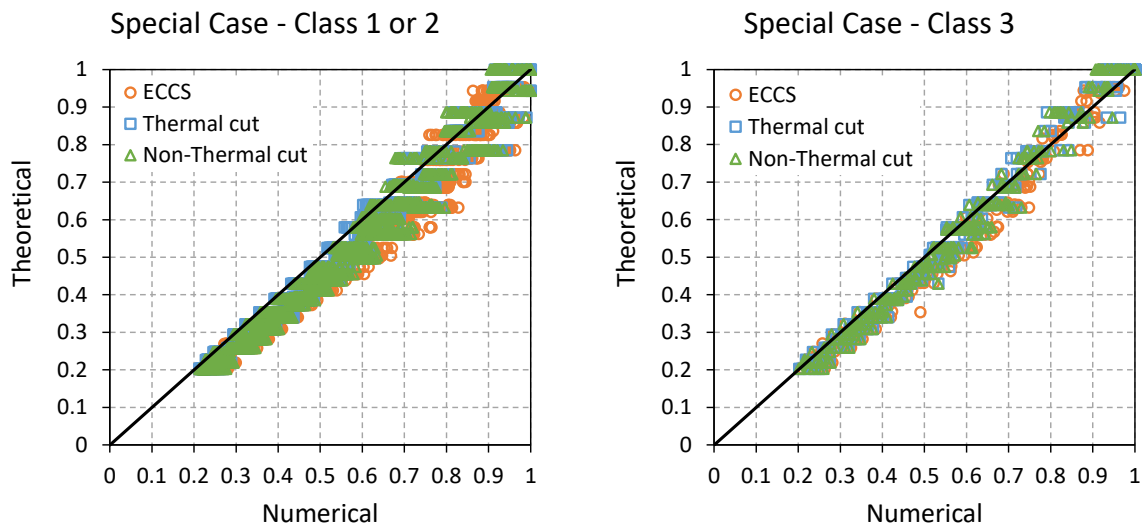


Figure 4.66 – Scatter plots for lateral-torsional buckling with new residual stresses models (all cases) – Special case

From the statistical parameters of the ratio r_e/r_t (where r_e is the numerical reduction factor and r_t is the theoretical reduction factor) presented in Table 4.32, Table 4.33, and Table 4.34, for the general case, the new EC3 case, and the special case, it is possible to confirm the trends verified in the scatter plots. The general case is the method with the highest mean value, approximately 35% higher than 1.0, regardless of the residual stresses model, and with more

than 95% of the cases having a ratio higher than 1.1 (7006 of 7324 cases) and no cases with a ratio lower than 0.97.

Table 4.32 – Statistical parameters for new residual stresses models (lateral-torsional buckling – general case)

| Design rule | Subset (residual stresses model) | n | mean | cov | min | max | >1.1 | <0.97 |
|-------------------------|----------------------------------|------|-------|-------|-------|-------|------|-------|
| General case EC3-1-1 | ECCS | 2578 | 1.388 | 11.7% | 1.024 | 1.773 | 2433 | 0 |
| | Thermal cut | 2373 | 1.367 | 10.7% | 1.007 | 1.687 | 2264 | 0 |
| | Non-Thermal cut | 2373 | 1.371 | 11.0% | 1.014 | 1.709 | 2236 | 0 |

Table 4.33 – Statistical parameters for new residual stresses models (lateral-torsional buckling – new EC3 case)

| Design rule | Subset (residual stresses model) | n | mean | cov | min | max | >1.1 | <0.97 |
|-------------------------|----------------------------------|------|-------|------|-------|-------|------|-------|
| New EC3 case EC3-1-1 | ECCS | 2578 | 1.156 | 7.4% | 0.950 | 1.433 | 1834 | 8 |
| | Thermal cut | 2373 | 1.129 | 6.5% | 0.926 | 1.336 | 1545 | 16 |
| | Non-Thermal cut | 2373 | 1.132 | 7.0% | 0.935 | 1.351 | 1539 | 19 |

Table 4.34 – Statistical parameters for new residual stresses models (lateral-torsional buckling – special case)

| Design rule | Subset (residual stresses model) | n | mean | cov | min | max | >1.1 | <0.97 |
|-------------------------|----------------------------------|------|-------|------|-------|-------|------|-------|
| Special case EC3-1-1 | ECCS | 2578 | 1.108 | 8.5% | 0.914 | 1.386 | 1313 | 166 |
| | Thermal cut | 2373 | 1.086 | 7.6% | 0.893 | 1.326 | 1006 | 188 |
| | Non-Thermal cut | 2373 | 1.090 | 8.2% | 0.888 | 1.360 | 1046 | 201 |

The special case has a mean value considerably lower when comparing to the general case, of approximately 1.08 for the special case and 1.36 for the general case, when using the thermal cut residual stresses (minimum values). Also, the special case has 7.5% of the cases with a ratio lower than 0.97 (555 in 7324 cases), exhibiting minimum ratio values in the order of 0.9.

Though the new EC3 case has a mean value closer to the special case when compared to the general case, the new EC3 is nevertheless considerably safer in comparison with the special case, with 43 cases with a ratio lower than 0.97 and more than 65% of the cases (4918 in 7324 cases) with a ratio higher than 1.1.

It is clear that an improvement in the general case is strongly recommended when applied to high strength steel beams, regardless of the residual stresses model used in the numerical models (mean values higher than 1.35). However, even though the new EC3 method significantly improves the results (mean values closer to 1.15), comparing to the general case, an adjustment in the imperfection factors when applied to high strength steel beams is possible.

The mean values are also plotted in Figure 4.67, where it is possible to observe the difference between the three design methods, regardless of the residual stresses model.

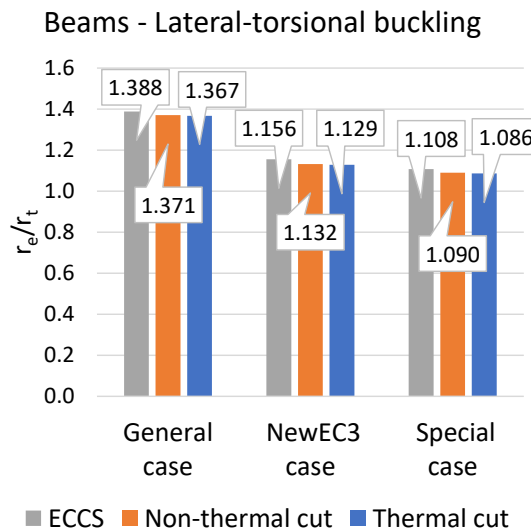


Figure 4.67 – Mean values for lateral-torsional buckling with new residual stresses models

A direct comparison of the numerical reduction factors obtained using the different residual stresses models is made in Figure 4.68. The numerical results using the different residual stresses models (ECCS, thermal cut, and non-thermal cut) are plotted in relation to the normalized slenderness ($\bar{\lambda}_{LT}$), together with the buckling curves from Eurocode 3 [1] for welded sections (curve c for sections with $h/b \leq 2$ and curve d for $h/b > 2$) on the left side of Figure 4.68. On the right side, the numerical results using the new residual stresses models (thermal

cut and non-thermal cut) are plotted in relation to the numerical results using the ECCS residual stresses model.

The majority of the cases are way above the lowest buckling curve (curve c), confirming what was previously said about the application of the general case to high strength steel beams, regardless of the residual stresses patterns used in the numerical model.

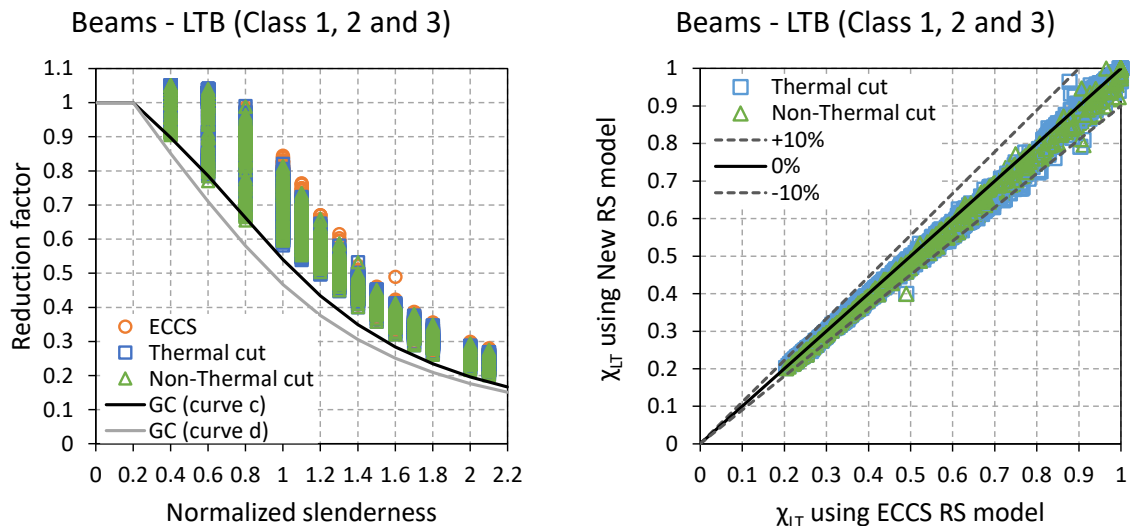


Figure 4.68 - Direct comparison between the reduction factors for lateral-torsional buckling using the new residual stresses models

From the results plotted in Figure 4.68 (right side) it is also possible to identify the trend of having lower reduction factors when using the residual stresses model with thermal cuts. However, this trend is not as pronounced as it was for example in the case of flexural buckling about major axis. This can be confirmed through the statistical parameters for the ratio between the residual stresses models ($\chi_{y|z(FEMi)}/\chi_{y|z(FEMj)}$), given in Table 4.35.

In the case of lateral-torsional buckling, the difference between the ECCS model and thermal cut model is on average about 2%, approximately the same for the difference between the ECCS and the non-thermal cut, since the mean value for the difference between the thermal cut and non-thermal cut is close to 1.0.

Likewise for flexural buckling, also for lateral-torsional buckling it was observed that there is no significant difference in the ratio when splitting the mean values in the different steel grades considered, as shown in Figure 4.69.

Table 4.35 – Statistical parameters for the ratio between the reduction factors (lateral-torsional buckling)

| Subset (residual stresses model) | n | mean | cov | min | max | >1.0 | <0.95 |
|-------------------------------------|------|-------|------|-------|-------|------|-------|
| $\chi_{LT(TC)}/\chi_{LT(ECCS)}$ | 2373 | 0.976 | 2.4% | 0.815 | 1.099 | 142 | 311 |
| $\chi_{LT(Non-TC)}/\chi_{LT(ECCS)}$ | 2373 | 0.978 | 1.6% | 0.815 | 1.044 | 19 | 105 |
| $\chi_{LT(TC)}/\chi_{LT(Non-TC)}$ | 2373 | 0.998 | 1.6% | 0.916 | 1.110 | 854 | 16 |

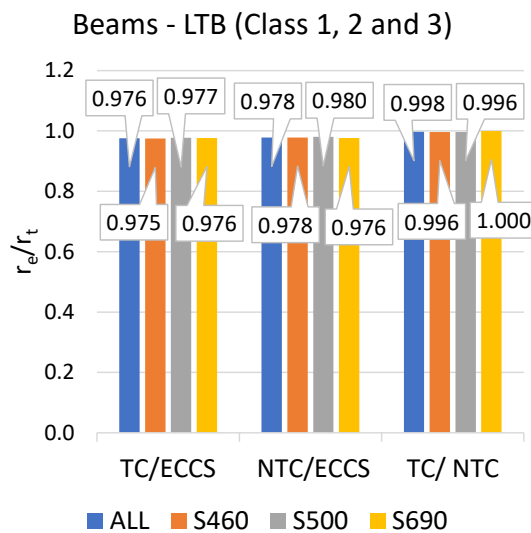


Figure 4.69 – Mean values for the ratio between the reductions factors for lateral-torsional buckling

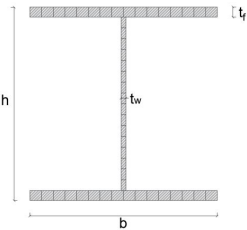
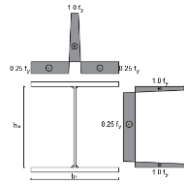
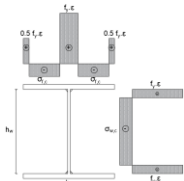
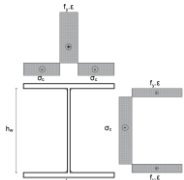

4.5.4.3. Discussion of results

The numerical results obtained when applying the new residual stresses models showed to be different than those obtained in [40], where these models were proposed. A trend to have lower reduction factors for the new residual stresses models was observed when comparing to the ECCS residual stresses model, contrary to what was obtained in [40] (higher reduction factors for the new residual stresses models than ECCS). However, this was observed using normal strength steels (S355) and for a single case.

Based on the simplified numerical model presented in Section 4.3 and used in the parametric study, additional numerical simulations were performed for the same conditions presented in [40] for further comparison.

The three residual stresses models (ECCS, thermal cut, and non-thermal cut) were applied to a welded-cross-section 410x350x8x20, made of steel grade S355, subjected to flexural buckling about major and minor axes and lateral-torsional buckling with constant bending moment ($\psi = 1$), the slenderness is equal to 1.0 ($\bar{\lambda}_y$, $\bar{\lambda}_z$, and $\bar{\lambda}_{LT}$), as presented in Table 4.36. Then, the same conditions were applied, however, changing the steel grade to high strength steels (S460, S500 and S690).

Table 4.36 – Additional numerical studies

| Fabrication and cross-section | Residual stresses | Material Properties f_y | Buckling mode and Slenderness $\bar{\lambda}$ |
|---|---|--|---|
| Welded: 410x350x8x20  $h = 410 \text{ mm}$ $b = 350 \text{ mm}$ $t_w = 8 \text{ mm}$ $t_f = 20 \text{ mm}$ | ECCS  | EN10025: S355 S460 S500 S690 | $\bar{\lambda}_y = 1.0$ Flexural Buckling Major axis (y-y) |
| | Thermal cut  | | $\bar{\lambda}_z = 1.0$ Flexural Buckling Minor axis (z-z) |
| | Non-Thermal cut  | | $\bar{\lambda}_{LT} = 1.0$ Lateral-torsional buckling  $\psi = 1$ |

The results obtained are presented and plotted together with the results available in [40]. For flexural buckling (Figure 4.70), the reduction factors (χ_y, χ_z) are plotted in relation to the mid-span deflection (w). In the case of lateral-torsional buckling, the reduction factor (χ_{LT}) is plotted in relation to the mid-span rotation (θ) in Figure 4.71. It is possible to observe that the

numerical models have the same initial stiffness for all the residual stresses approaches. Furthermore, the maximum reduction factors reached in both numerical models are close.

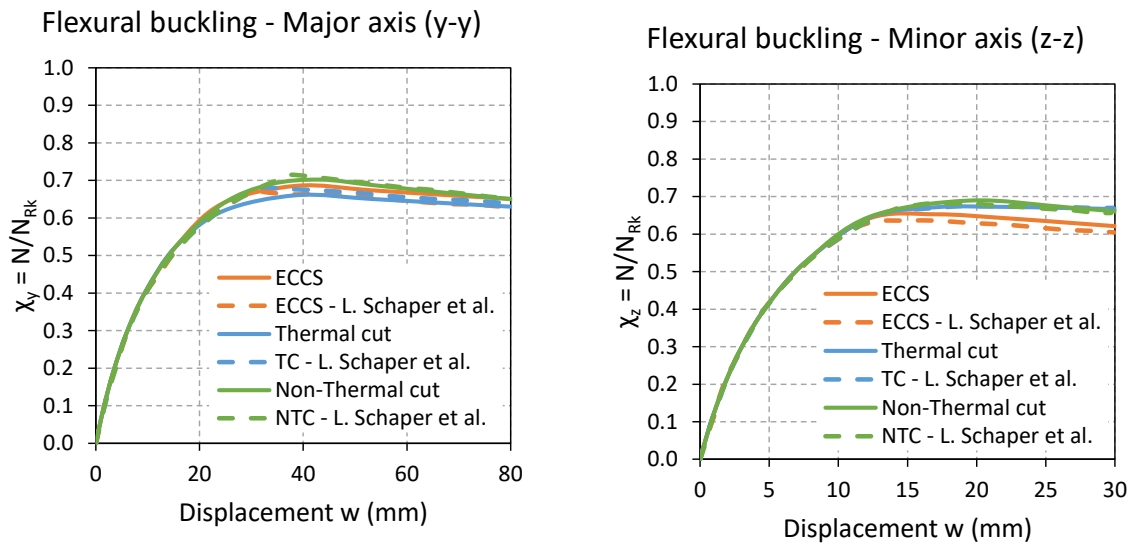


Figure 4.70 – Flexural buckling

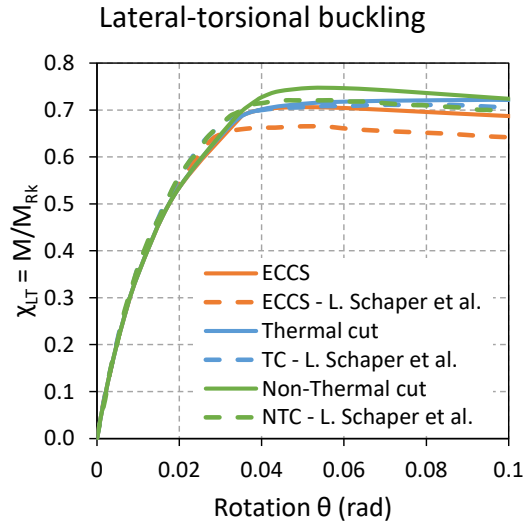


Figure 4.71 – Lateral-torsional buckling

Comparing the maximum reduction factors obtained from flexural buckling in Table 4.37 and lateral-torsional buckling in Table 4.38 with the reductions factors from [40], the overall difference is less than 3% with a maximum of 6%. The maximum difference is obtained for

lateral-torsional buckling with the ECCS model, although this difference does not affect the trend.

For the normal strength steel (S355), the trend observed is to have higher reduction factors for the non-thermal cut model and lower reduction factors for the ECCS model, which are in line with the results from [40]. The only case where this was not observed was for the major axis flexural buckling, where the thermal cut model gives the lowest reduction factor, though the non-thermal cut keeps providing the highest reduction factor.

Nevertheless, even though we are just analysing one separate case, as we move to high strength steel grades, the trend is not so evident, being the reduction factor for the ECCS model very close to the thermal cut model or higher, and close to the non-thermal cut. It can be observed that the difference between the reduction factor for the different residual stresses models tends to be smaller for high strength steels when comparing to normal strength steels.

Table 4.37 – Comparison of the reduction factors for flexural buckling

| Model | FB Major axis (y-y) - χ_y | | | FB Minor axis (z-z) - χ_z | | |
|---------------------|--------------------------------|-------|-------|--------------------------------|-------|--------|
| | ECCS | TC | NTC | ECCS | TC | NTC |
| FEM - S355 | 0.688 | 0.660 | 0.706 | 0.654 | 0.672 | 0.690 |
| Schaper et al. [40] | 0.669 | 0.679 | 0.714 | 0.636 | 0.673 | 0.681 |
| Difference (%) | -2.80% | 2.76% | 1.10% | -2.75% | 0.08% | -1.35% |
| FEM - S460 | 0.728 | 0.694 | 0.735 | 0.694 | 0.704 | 0.718 |
| FEM - S500 | 0.747 | 0.710 | 0.749 | 0.713 | 0.719 | 0.731 |
| FEM - S690 | 0.790 | 0.750 | 0.783 | 0.757 | 0.758 | 0.766 |

Table 4.38 – Comparison of the reduction factors for lateral-torsional buckling

| Model | Lateral-torsional buckling - χ_{LT} | | |
|---------------------|--|-------------|-----------------|
| | ECCS | Thermal cut | Non-thermal cut |
| FEM - S355 | 0.706 | 0.721 | 0.747 |
| Schaper et al. [40] | 0.664 | 0.711 | 0.722 |
| Difference (%) | -6.13% | -1.40% | -3.40% |
| FEM - S460 | 0.734 | 0.736 | 0.760 |
| FEM - S500 | 0.745 | 0.744 | 0.766 |
| FEM - S690 | 0.782 | 0.777 | 0.791 |

5. Development of stability design rules for high strength steel members

5.1. Calibration of design guidance

In the previous section (Section 4.5), it was seen that applying the current design recommendations available in the current version of Eurocode 3 [1] and also in the new version of the Eurocode 3 [7], for the buckling design of steel members made of high strength steel, can lead to over-conservative designs, and therefore, full advantage of the use of the high strength steels is not being taken into account.

In this chapter, the development of new design rules, based on the existing ones, more suitable to the buckling design of high strength steel members is presented. Focus is placed on columns and beams, flexural buckling and lateral-torsional buckling, where all the available methods (described in Section 2.4.2) are assessed for the lateral-torsional buckling case.

The adopted approach is based on the comparison of the generalized imperfections η , and the imperfection factors α , obtained using the current design rules from Eurocode 3 [1], [7] and those assessed through the numerical simulations carried out in the parametric study. Hence, it allows to obtain a numerical estimation of the required generalized imperfections η , and imperfection factors α that can be directly compared with the Eurocode [1], [7]. For this, the Ayrton-Perry equation [71] was adopted to obtain the numerical generalized imperfections η_{num} .

5.1.1. Design rules for members in compression

The Ayrton-Perry equation for members in compression submitted to flexural buckling is written in Equation (5.1), where the reduction factor χ_{num} refers to the reduction factor obtained in the numerical analysis and the normalized slenderness is equal to $\bar{\lambda} = \sqrt{Af_y/N_{cr}}$, regarding the relevant buckling mode. Therefore, the numerical generalized imperfection η_{num} , is obtained using the Equation (5.2).

$$\chi_{num} + \eta_{num} \cdot \frac{\chi_{num}}{1 - \bar{\lambda}^2 \cdot \chi_{num}} = 1.0 \quad (5.1)$$

$$\eta_{num} = \left(\frac{1}{\chi_{num}} - 1 \right) \times (1 - \bar{\lambda}^2 \cdot \chi_{num}) \quad (5.2)$$

The generalized imperfection recommended by the Eurocode η_{EC3} is obtained using Equation (5.3), based on the imperfection factor α and also the normalized slenderness. The recommended imperfection factor is presented in Table 2.4 and Table 2.5 for flexural buckling.

$$\eta_{EC3} = \alpha(\bar{\lambda} - 0.2) \quad (5.3)$$

Therefore, a direct comparison of the numerical (η_{num}) and theoretical (η_{EC3}) generalized imperfections is made in Figure 5.1 for major axis flexural buckling and in Figure 5.2 for minor axis flexural buckling split into the thickness flange, according to Eurocode 3 [1] provisions for flexural buckling of welded sections. For both cases (Figure 5.1 and Figure 5.2), the black line represents the current generalized imperfections recommended by the Eurocode, and the grey line represents the generalized imperfections using one curve lower than the current recommendations provided by the Eurocode. The dots represent the numerical cases obtained in the parametric study.

It is noted for both major and minor axes flexural buckling that the expression for the generalized imperfection factor follows closely the numerical demand at low slenderness, whereas for high slenderness the differences tends to get higher. This was previously observed [71], where imperfection factors with cut-off limit were proposed. Nonetheless, in the present study, it is aimed for simplicity and keeping the current design format with an adjustment of the imperfection factors.

Therefore, lowering the currently recommended buckling curves for flexural buckling seems to be a practicable proposal to be applied for high strength steels, according to the numerical imperfections observed in Figure 5.1 and Figure 5.2. Thus, the proposed imperfection factors for major and minor axes flexural buckling are summarized in Table 5.1.

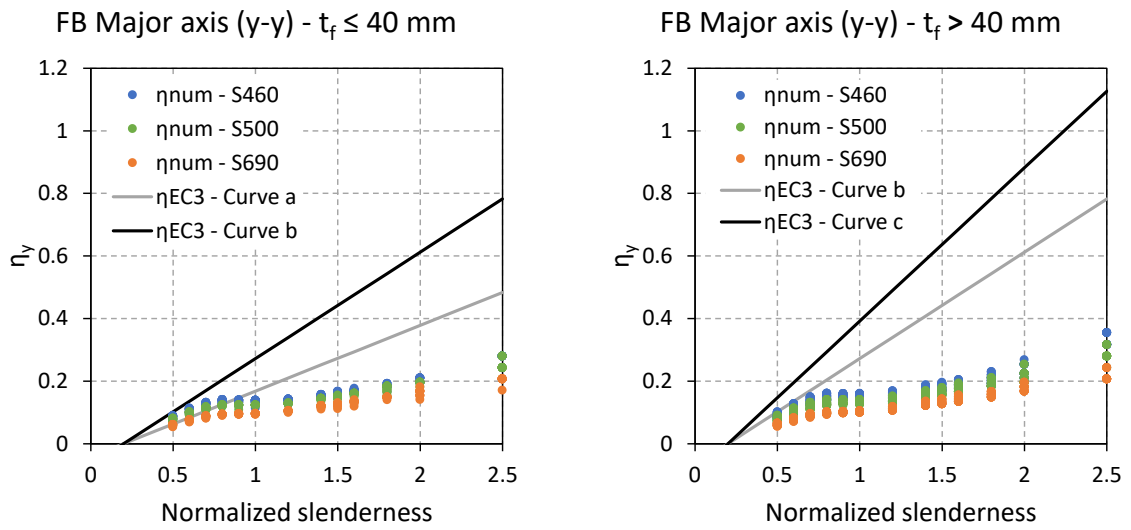


Figure 5.1 – Generalized imperfections for flexural buckling about major axis (y-y)

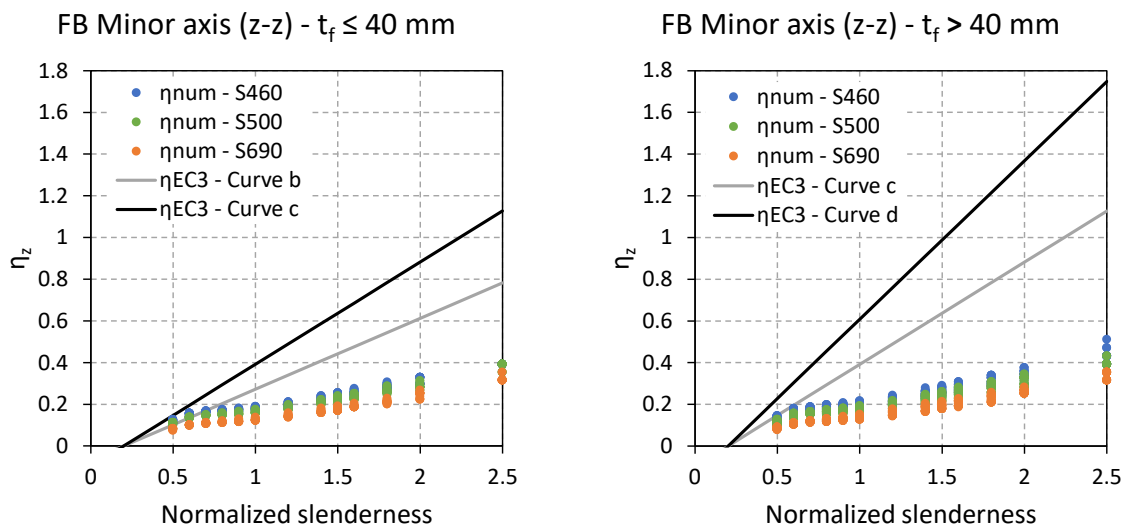
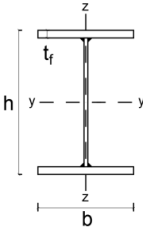


Figure 5.2 – Generalized imperfections for flexural buckling about minor axis (z-z)

Table 5.1 – Proposed imperfections for flexural buckling applied to high strength steels

| Cross-section | Limits | Buckling axis | Buckling curve | |
|--|--------------------------|---------------|----------------|--------------------------|
| | | | Current | Proposed S460 to S700 |
| Welded I-sections  | $t_f \leq 40 \text{ mm}$ | y – y | <i>b</i> | <i>a</i> |
| | | z – z | <i>c</i> | <i>b</i> |
| | $t_f > 40 \text{ mm}$ | y – y | <i>c</i> | <i>b</i> |
| | | z – z | <i>d</i> | <i>c</i> |

5.1.2. Design rules for members in bending

For members in bending subjected to lateral-torsional buckling, the same approach, that is using the Ayrton-Perry equation, is adopted. Nonetheless, it needs to be adjusted depending on the method used to assess the reduction factor for lateral-torsional buckling. Furthermore, the normalized slenderness is modified to the normalized slenderness for lateral-torsional buckling, where $\bar{\lambda}_{LT} = \sqrt{W_y f_y / M_{cr}}$.

5.1.2.1. General case

For the general case, the Ayrton-Perry equation is identical to the one used for columns, the only difference is that it applies the factors for the lateral-torsional buckling case (Equation (5.4)):

$$\chi_{num} + \eta_{num} \cdot \frac{\chi_{num}}{1 - \bar{\lambda}_{LT}^2 \cdot \chi_{num}} = 1.0 \quad (5.4)$$

Being the numerical generalized imperfection η_{num} equal to:

$$\eta_{num} = \left(\frac{1}{\chi_{num}} - 1 \right) \times (1 - \bar{\lambda}_{LT}^2 \cdot \chi_{num}) \quad (5.5)$$

The generalized imperfection recommended by the Eurocode for lateral-torsional buckling when using the general case η_{GC} , is based on the imperfection factor α_{LT} , presented in Table 2.6 and Table 2.7 and is obtained through Equation (5.6).

$$\eta_{GC} = \alpha_{LT}(\bar{\lambda}_{LT} - 0.2) \quad (5.6)$$

In Figure 5.3, the numerical (η_{num}) and theoretical (η_{GC}) generalized imperfections are plotted, similarly to what was done for the columns case, where the black line represents the current generalized imperfections recommended by the Eurocode, the grey line represents the generalized imperfections using one curve lower than the current, and the dots represent the numerical cases obtained in the parametric study. The cases are also split into the ratio h/b , according to Eurocode 3 [1] provisions for lateral-torsional buckling using the general case.

The same trend observed for columns is noted for the general case, where the theoretical generalized imperfection factors at low slenderness are more or less close to the numerical one, however, as we move towards medium-to-high slenderness, these differences become too great. Hence, the same approach is used, lowering the currently recommended buckling curves for lateral-torsional buckling, which allows to approximate the theoretical generalized imperfections to the numerical ones for medium slenderness, and reduces the differences for high slenderness levels. Consequently, the proposed imperfections factors α_{LT} , for lateral-torsional buckling when using the general case are presented in Table 5.2.

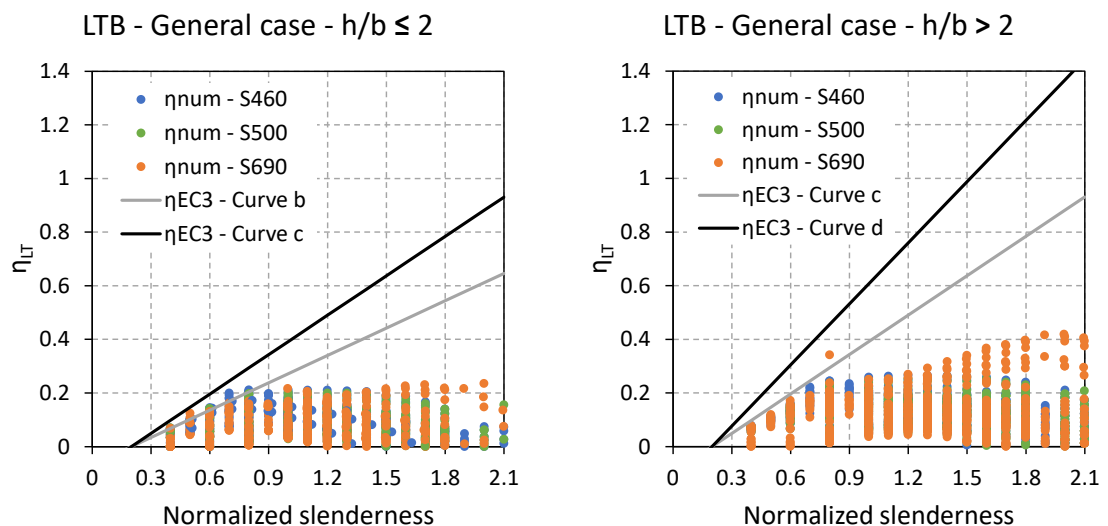
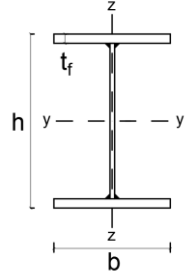


Figure 5.3 – Generalized imperfections for lateral-torsional buckling – General case

Table 5.2 – Proposed imperfections for the general case applied to high strength steels – lateral-torsional buckling

| Cross-section | Limits | Buckling curve | |
|--|--------------|----------------|--------------------------|
| | | Current | Proposed S460 to S700 |
| Welded I-sections  | $h/b \leq 2$ | <i>c</i> | <i>b</i> |
| | $h/b > 2$ | <i>d</i> | <i>c</i> |

5.1.2.2. Special case

For the special case, the above procedure needs to be slightly changed in order to take into account factor f , for the bending moment distribution, and also the introduction of parameter β , present in the special case. The equation applied to the special case, shall be as follows:

$$\chi_{num} \cdot f + \eta_{num} \cdot \frac{\chi_{num} \cdot f}{1 - \beta \cdot \bar{\lambda}_{LT}^2 \cdot \chi_{num} \cdot f} = 1.0 \quad (5.7)$$

Then, the numerical generalized imperfection η_{num} is equal to:

$$\eta_{num} = \left(\frac{1}{\chi_{num} \cdot f} - 1 \right) \times (1 - \beta \cdot \bar{\lambda}_{LT}^2 \cdot \chi_{num} \cdot f) \quad (5.8)$$

The theoretical generalized imperfection (Equation (5.9)) for lateral-torsional buckling when using the special case η_{SC} , is also based on the imperfection factor α_{LT} , with the introduction of parameter $\bar{\lambda}_{LT,0}$. The selection of the imperfection factor α_{LT} is presented in Table 2.7 and Table 2.8.

$$\eta_{SC} = \alpha_{LT}(\bar{\lambda}_{LT} - \bar{\lambda}_{LT,0}) \quad (5.9)$$

For $\bar{\lambda}_{LT,0}$ and β , the recommended values from Eurocode 3 [1] are: $\bar{\lambda}_{LT,0} = 0.4$ and $\beta = 0.75$. Factor f is based on the bending moment distribution (see Equation (2.16) and Table 2.9).

The results obtained for the numerical (η_{num}) and theoretical (η_{SC}) generalized imperfections are presented in Figure 5.4, where the black line represents the current generalized imperfections recommended by the Eurocode and the dots represent the numerical cases obtained in the parametric study. It is noted that a considerable number of cases are above the black line, especially in the subset of cross-sections with $h/b \leq 2.0$, where it is possible to find cases above the black line across all levels of slenderness. This means that the numerical imperfection obtained is higher than the recommended by the Eurocode and so a higher theoretical imperfection would be required.

The special case method has previously been found to be inconsistent [14], [21], and [23], and so, based on the results from Figure 5.4, it is considered that this method cannot be improved for high strength steel members, and consequently, no development of new design rules for this method are proposed.

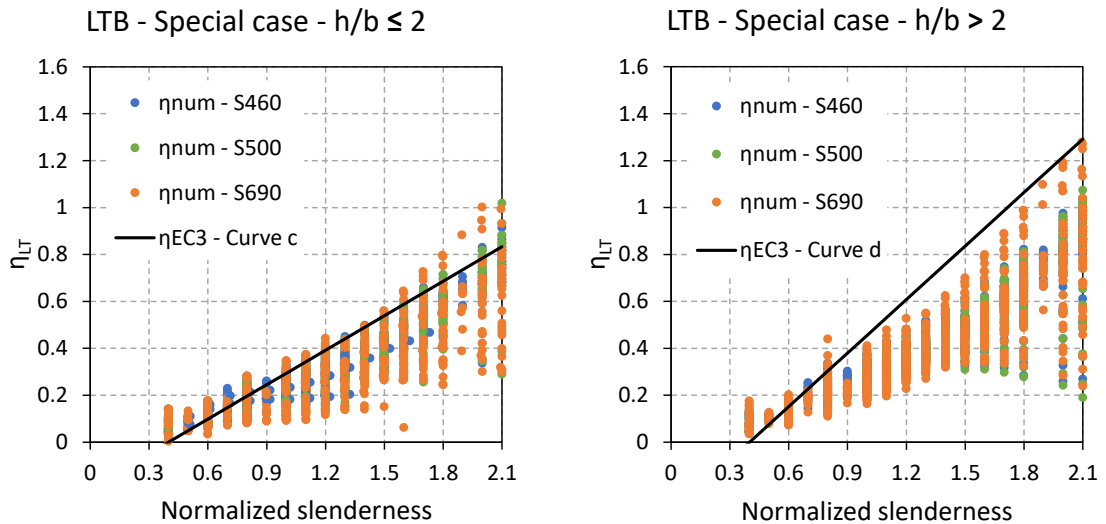


Figure 5.4 – Generalized imperfections for lateral-torsional buckling – Special case

5.1.2.3. New EC3 case

For the assessment of the numerical generalized imperfection η_{num} for the new EC3 case for H and I sections, the Equation (5.10) has to account for the bending moment distribution

with the introduction of the parameter f_M (described in Table 2.9), and also the introduction of the normalized slenderness for flexural buckling about minor axis ($\bar{\lambda}_z$). Hence, to obtain the η_{num} , Equation (5.11) is used.

$$\frac{\chi_{num}}{f_M} + \eta_{num} \cdot f_M \cdot \frac{\bar{\lambda}_{LT}^2}{\bar{\lambda}_z^2} \cdot \frac{\frac{\chi_{num}}{f_M}}{1 - \frac{\chi_{num}}{f_M} \cdot f_M \cdot \bar{\lambda}_{LT}^2} = 1.0 \quad (5.10)$$

$$\eta_{num} = \frac{(\chi_{num} - f_M)(\bar{\lambda}_{LT}^2 \cdot \chi_{num} - 1)\bar{\lambda}_z^2}{f_M \cdot \bar{\lambda}_{LT}^2 \cdot \chi_{num}} \quad (5.11)$$

The theoretical generalized imperfection (Equation (5.12)) for lateral-torsional buckling when using the new EC3 case η_{NewEC3} is based on normalized slenderness for flexural buckling about minor axis ($\bar{\lambda}_z$) and the imperfection factor α_{LT} . For the new EC3 case, the imperfection factor given in Equation (5.13) depends on the imperfection α_0 , which is a constant value and previously defined in Table 2.10, and also on the cross-section properties, and therefore the generalized imperfection (η_{NewEC3}) varies with the cross-section.

$$\eta_{NewEC3} = \alpha_{LT}(\bar{\lambda}_z - 0.2) \quad (5.12)$$

$$\alpha_{LT} = \alpha_0 \cdot \sqrt{\frac{W_{el,y}}{W_{el,z}}} \quad (5.13)$$

Since the generalized imperfection for the new EC3 case varies with the cross-section, the assessment is carried out on the basis of the imperfection α_0 , and also the imperfection factor α_{LT} , since the imperfection factor is defined with a cut-off limit (see Table 2.10). Therefore, based on the numerical generalized imperfection obtained (η_{num}), a numerical imperfection factor $\alpha_{LT,num}$ can be obtained through the use of the Equation (5.14) in order to be compared with the cut-off limit and then a numerical imperfection $\alpha_{0,num}$ can also be obtained (Equation (5.15)) and directly compared to the values defined by the new version of the Eurocode 3 [7] for welded sections (Table 2.10).

$$\alpha_{LT,num} = \frac{\eta_{num}}{(\bar{\lambda}_z - 0.2)} \quad (5.14)$$

$$\alpha_{0,num} = \frac{\alpha_{LT,num}}{\sqrt{W_{el,y}/W_{el,z}}} \quad (5.15)$$

The numerical estimation of the imperfection factor α_{LT} and imperfection α_0 is plotted in Figure 5.5 and Figure 5.6, respectively, for the two cases considered in the Eurocode ($t_f \leq 40 \text{ mm}$ and $t_f > 40 \text{ mm}$). In Figure 5.6, the black line represents the current imperfections recommended by the Eurocode ($\alpha_0 = 0.21$ for $t_f \leq 40 \text{ mm}$ and $\alpha_0 = 0.25$ for $t_f > 40 \text{ mm}$), and in Figure 5.5 the black line represents the cut-off limit considered in the Eurocode ($\alpha_{LT} \leq 0.49$ for $t_f \leq 40 \text{ mm}$ and $\alpha_{LT} \leq 0.64$ for $t_f > 40 \text{ mm}$). For both cases, the dots represent the numerical cases obtained in the parametric study.

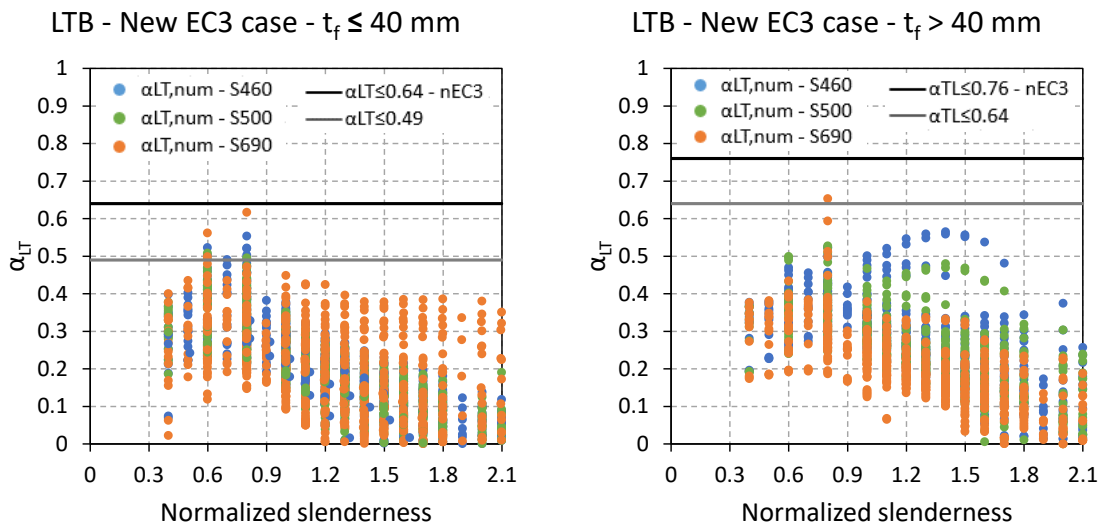
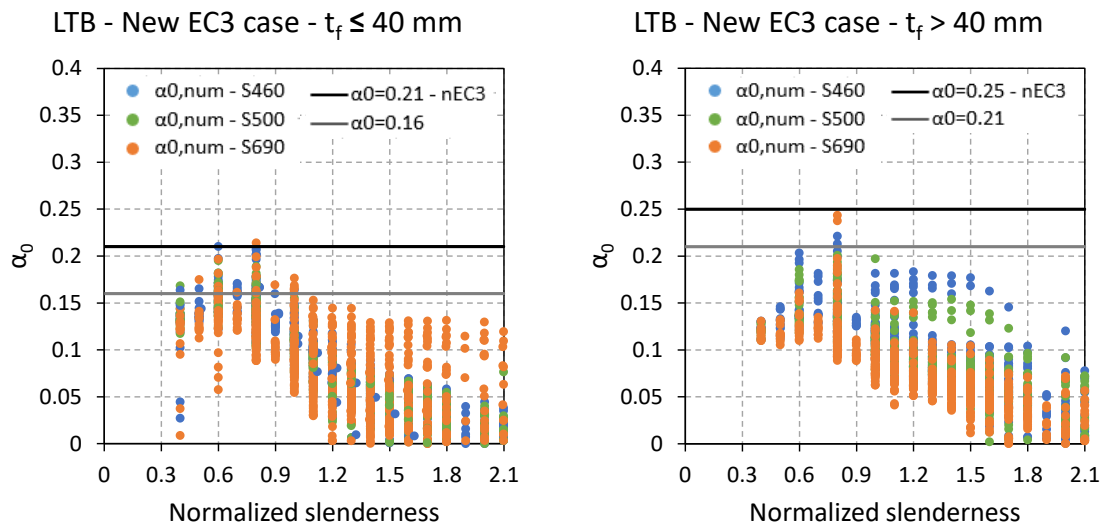


Figure 5.5 – Estimation for the imperfection factor α_{LT} – New EC3 case

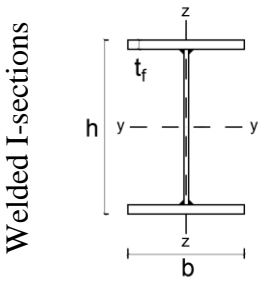

 Figure 5.6 – Estimation for the imperfection α_0 – New EC3 case

The numerical imperfection α_0 is generally lower than the suggested value, especially for high slenderness ($\bar{\lambda}_{LT} > 1.2$), where the difference between the numerical and theoretical imperfection is higher. On the other hand, the smallest difference is found in the range between 0.6 to 0.9. Even so, it is found that just a few cases are close to the current recommended value, and that the majority of them are way below this value. Hence, it is considered possible to slightly reduce the imperfections for high strength steel members, from 0.21 to 0.16 for $t_f \leq 40$ mm and from 0.25 to 0.21 for $t_f > 40$ mm, these values are represented with grey lines in Figure 5.6.

In terms of the cut-off limits for the imperfection factor α_{LT} , the same trend is observed to some extent, though with higher differences for high and also low slenderness and lower differences for the range between 0.6 to 0.9. In this case, there are no numerical cases close to the actual limits (touching the black line of Figure 5.5). Consequently, it is also possible to reduce the actual limits, from 0.64 to 0.49 for $t_f \leq 40$ mm and from 0.76 to 0.64 for $t_f > 40$ mm, when applied to lateral-torsional buckling of high strength steel members. These limits are represented with grey lines in Figure 5.5.

Table 5.3 summarises the proposal for the new EC3 case available in the new version of Eurocode 3 [7], for the buckling design of members subjected to lateral-torsional buckling, applied to high strength steel.

Table 5.3 – Proposed imperfections for the new EC3 case applied to high strength steels – lateral-torsional buckling

| Cross-section | Limits | α_{LT} | |
|--|--------------------------|---|---|
| | | Current | Proposed S460 to S700 |
| Welded I-sections  | $t_f \leq 40 \text{ mm}$ | $0.21 \sqrt{\frac{W_{el,y}}{W_{el,z}}} \leq 0.64$ | $0.16 \sqrt{\frac{W_{el,y}}{W_{el,z}}} \leq 0.49$ |
| | $t_f > 40 \text{ mm}$ | $0.25 \sqrt{\frac{W_{el,y}}{W_{el,z}}} \leq 0.76$ | $0.21 \sqrt{\frac{W_{el,y}}{W_{el,z}}} \leq 0.64$ |

5.2. Validation of the stability design rules for high strength steel members

In this section, the proposed imperfections/buckling curves are applied in the respective design method for the same cases considered in the parametric studies, so as to obtain the theoretical reduction factor based on the proposed imperfections/buckling curves. This approach is performed for all members considered in the parametric studies: i) columns, ii) beams – hybrid-beams, and iii) beam-columns.

And then, the theoretical reduction factors obtained for the proposed imperfections/buckling curves are confronted with the numerical reduction factors and also compared with the current theoretical reduction factors (presented in Section 4.5), in order to validate the proposed stability design rules for high strength steel members.

5.2.1. Columns

The assessment of the proposals for flexural buckling is performed similarly to what was previously done in Section 4.5. The scatter plots presented in Figure 5.7 for major and minor axes flexural buckling, shows the theoretical reduction factor using the proposed buckling curves (proposal) and the current buckling curves (EC3) in relation to the numerical reduction factor.

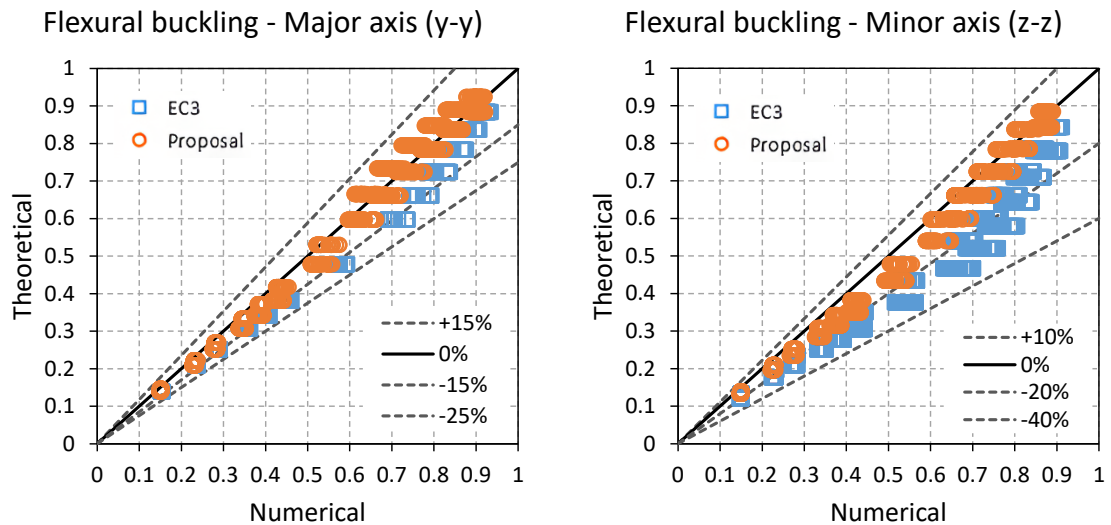


Figure 5.7 – Scatter plots for proposal for flexural buckling

From Figure 5.7, it is noted that the new proposals for the flexural buckling design of high strength steel members are safe-sided, and significantly reduce the cases with over conservative results, where the numerical reduction factor was considerably higher than the theoretical one. This can be seen through the lines represented in grey, where they define the difference between the numerical and theoretical case (theoretical factor higher – positive side, numerical factor higher – negative side). For major axis flexural buckling, the current design leads to differences of approximately -25%, by using the proposed curves, these differences are reduced to -15%. In the minor axis flexural buckling, the reduction is even higher from cases with almost -40% to a difference of -20%. This is also confirmed through the statistical parameters for the ratio r_e/r_t , presented in Table 5.4.

The statistical parameters using the proposed buckling curves (Table 5.4), are directly comparable with the statistics presented in Table 4.19 (Section 4.5.1), using the current buckling curves. In both buckling modes (major and minor axes), the mean value and the coefficient of variation have reduced. It is noted that the minor axis flexural buckling is slightly “safer” than the major axis.

The reduction of the mean value is of approximately 9% for major axis and of approximately 12.5% for minor axis, and it is verified across all the steel grades.

The differences in the mean values between the current buckling curves and the proposed buckling curves for flexural buckling are presented in Figure 5.8.

For major axis flexural buckling, changing the buckling curve led to a few cases with a ratio lower than 0.97 (16 in 1599 cases), nonetheless, they are close to 0.97, since the minimum value

is 0.965. They are found for steel grade S460, where the impact of the residual stresses is higher in relation to the other steel grades considered.

For the minor axis flexural buckling, no cases were found below 0.97, yet some are also found in the range between 0.97 and 1.0 for the steel grades S460 and S500.

Table 5.4 – Statistical parameters for proposal for flexural buckling

| Design rule | Subset (steel grade) | Buckling axis | n | mean | cov | min | max | >1.1 | <0.97 |
|------------------------------|----------------------|---------------|------|-------|------|-------|-------|------|-------|
| Flexural buckling - Proposal | All | y-y | 1599 | 1.090 | 5.7% | 0.965 | 1.232 | 674 | 16 |
| | | z-z | 1599 | 1.132 | 6.4% | 0.973 | 1.303 | 1086 | 0 |
| | S460 | y-y | 585 | 1.071 | 5.4% | 0.965 | 1.203 | 199 | 16 |
| | | z-z | 585 | 1.108 | 6.0% | 0.973 | 1.236 | 338 | 0 |
| | S500 | y-y | 559 | 1.087 | 5.5% | 0.979 | 1.203 | 218 | 0 |
| | | z-z | 559 | 1.128 | 6.0% | 0.988 | 1.256 | 373 | 0 |
| | S690 | y-y | 455 | 1.117 | 5.5% | 1.003 | 1.232 | 257 | 0 |
| | | z-z | 455 | 1.168 | 6.2% | 1.020 | 1.303 | 375 | 0 |

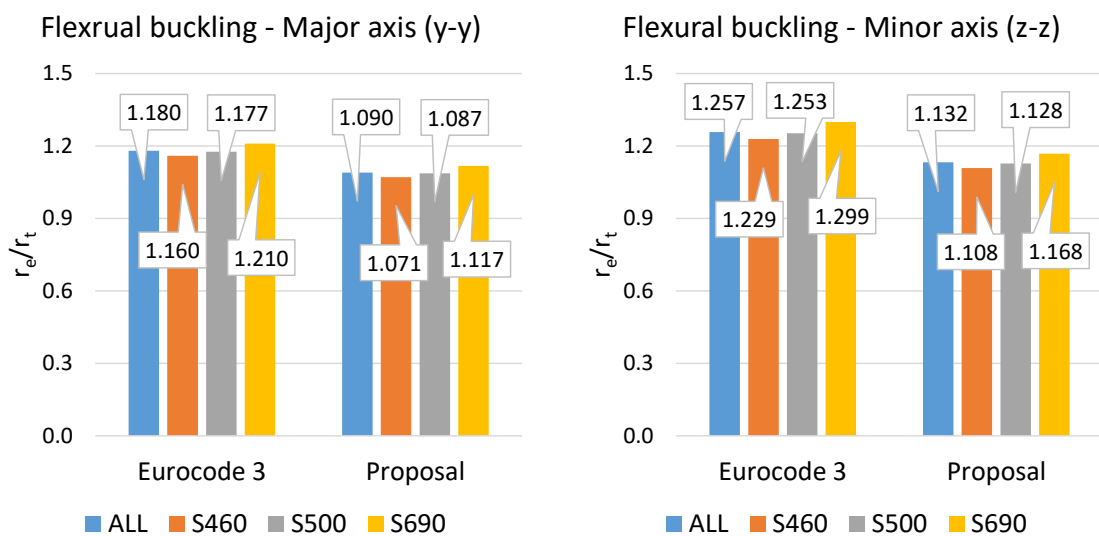


Figure 5.8 – Comparison of the mean values between Eurocode 3 and proposal for flexural buckling

5.2.2. Beams

The same assessment is performed for members in bending submitted to lateral-torsional buckling using the general case and the new EC3 case. The special case is not presented here, since no improvement in the buckling curves was possible to justify for this method.

The scatter plots with the proposed design rules (orange dots) are presented in Figure 5.9 for the general case (left side) and new EC3 case (right side), together with the current design rules (blue dots). It is possible to note that the over conservative design is considerably reduced for the general case, where most of the cases show a theoretical reduction factor not higher than 35% in relation to the numerical reduction factor (orange dots above the grey line shown as -35%). For the new EC3 case, the over conservative design is also slightly reduced, in which most of the cases have a theoretical reduction factor higher than the numerical one, at a maximum of 25%.

Through the statistical parameters for the new curves, presented in Table 5.5 (directly comparable with Table 4.20 for the current design rules) for the general case, and in Table 5.6 for the new EC3 case (directly comparable with Table 4.22 for the current design rules), it is possible to show that the new design rules for LTB provide safe-sided results. For both methods (general case and new EC3 case), there are very few cases with a ratio lower than 1.0 (and only 12 cases below 0.97). There is a reduction in the mean values (see Figure 5.10), of approximately 14% for the general case and of approximately 5% for the new EC3 case and also a reduction in the coefficient of variation (approximately 2%) in comparison to the current design rules for both methods.

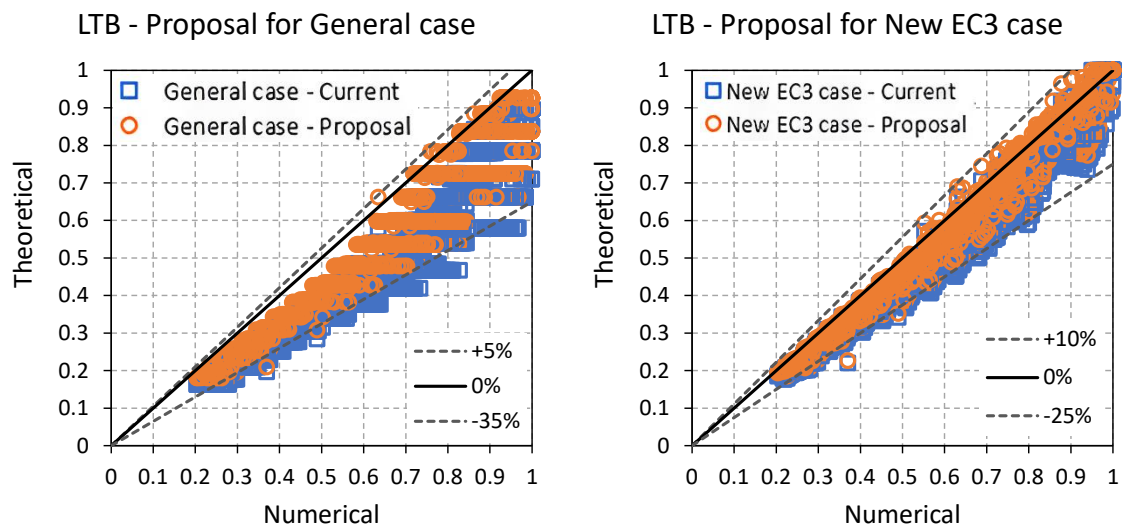


Figure 5.9 – Scatter plots for proposals for lateral-torsional buckling

Table 5.5 – Statistical parameters for proposal for general case – lateral-torsional buckling

| Design rule | Subset (steel grade) | n | mean | cov | min | max | >1.1 | <0.97 |
|------------------------------------|----------------------|------|-------|------|-------|-------|------|-------|
| LTB: General case - Proposal | All | 4595 | 1.254 | 8.4% | 0.959 | 1.811 | 4169 | 2 |
| | S460 | 1508 | 1.231 | 8.2% | 0.968 | 1.514 | 1326 | 1 |
| | S500 | 1469 | 1.249 | 7.9% | 0.993 | 1.553 | 1346 | 0 |
| | S690 | 1618 | 1.279 | 8.6% | 0.959 | 1.811 | 1497 | 1 |

Table 5.6 – Statistical parameters for proposal for new EC3 case – lateral-torsional buckling

| Design rule | Subset (steel grade) | n | mean | cov | min | max | >1.1 | <0.97 |
|------------------------------------|----------------------|------|-------|------|-------|-------|------|-------|
| LTB: New EC3 case - Proposal | All | 4595 | 1.127 | 6.1% | 0.935 | 1.674 | 3142 | 10 |
| | S460 | 1508 | 1.107 | 5.4% | 0.961 | 1.300 | 909 | 5 |
| | S500 | 1469 | 1.120 | 5.4% | 0.980 | 1.338 | 988 | 0 |
| | S690 | 1618 | 1.152 | 6.6% | 0.935 | 1.674 | 1245 | 5 |

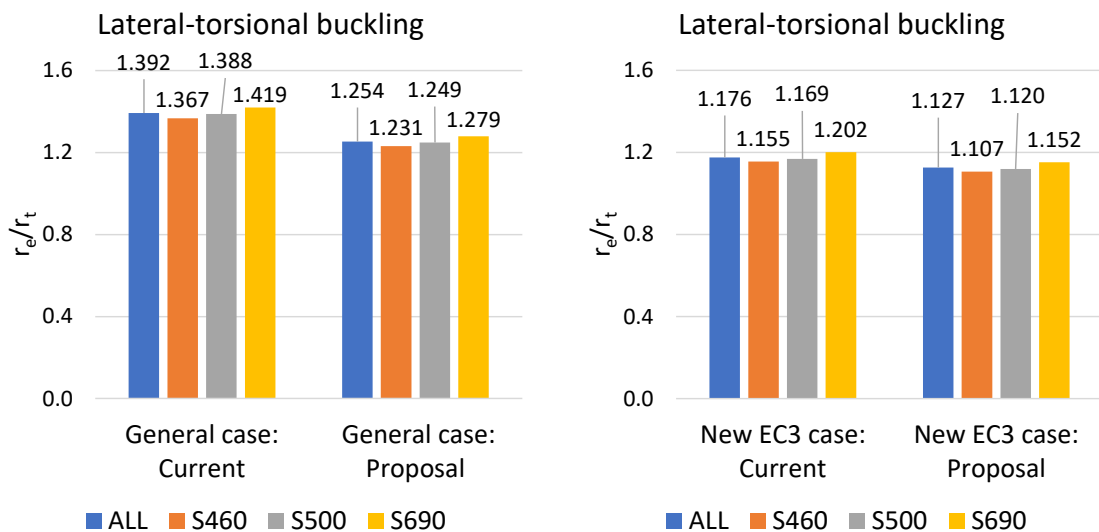


Figure 5.10 – Comparison of the mean values between the current design and proposals

5.2.2.1. Hybrid beams

The proposed design curves for lateral-torsional buckling (general case and new EC3 case) were also applied to hybrid beams, in order to assess if they are suitable or not.

The scatter plots for the same set of hybrid beams and homogeneous beams, under constant bending moment ($\psi = 1$) and using the new design rules for the general case (left side) and new EC3 case (right side) are presented in Figure 5.11. The results show that, in terms of safety, the resistance of hybrid (orange dots) and homogenous (blue dots) beams are very similar when submitted to lateral-torsional buckling. The range of the reduction factors obtained for hybrid and homogenous beams is very close, as it can be seen in Figure 5.11, for both methods.

In terms of the difference between the current design rules and the proposed design rules for lateral-torsional buckling, Table 5.7 (general case) and Table 5.8 (new EC3 case) present the statistical parameters for the ratio between the numerical and theoretical reduction factor (r_e/r_t), using the proposed design rules, which are directly comparable with Table 4.23 and Table 4.24, respectively (statistics for the ratio r_e/r_t , using the current design rules). As observed for the homogenous beams, also for hybrid beams, there is a reduction in the mean value (see Figure 5.12) of approximately 13% for the general case and of approximately 5% for the new EC3 and of 2.5% in the coefficient of variation for the general case, and of 1% for the new EC3 case. No cases lower than 0.97 are found for the general case and only 9 for the new EC3 case. Most of the cases have a ratio higher than 1.1 (more than 70% for the general case, and close to 70% for the new EC3 case).

Based on the analyses performed, it can be concluded that the rules proposed for the design of lateral-torsional buckling of beams are also suitable for the lateral-torsional buckling design of hybrid beams, which comply with the requirements of EN 1993-1-5 [73].

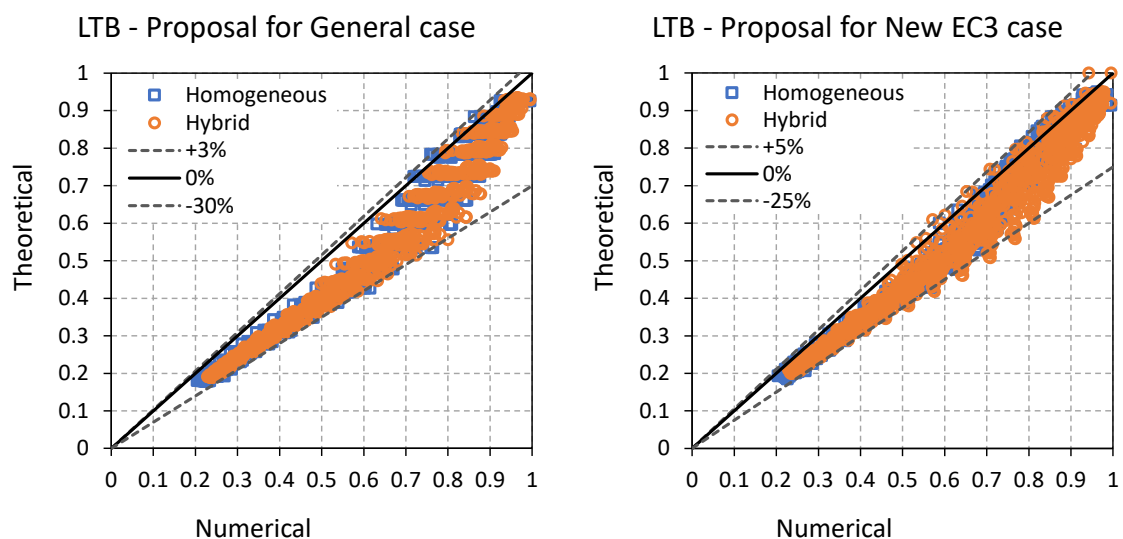


Figure 5.11 – Scatter plots for proposals for lateral-torsional buckling of hybrid beams

Table 5.7 – Statistical parameters for lateral-torsional buckling of hybrid beams – Proposal for general case

| Design rule | Subset (steel grade) | n | mean | cov | min | max | >1.1 | <0.97 |
|--|----------------------|------|-------|------|-------|-------|------|-------|
| Proposal for General case – Hybrid beams | All | 1175 | 1.198 | 8.0% | 0.993 | 1.439 | 908 | 0 |
| | S460 | 412 | 1.170 | 7.9% | 0.993 | 1.362 | 286 | 0 |
| | S500 | 320 | 1.209 | 7.6% | 1.018 | 1.375 | 262 | 0 |
| | S690 | 443 | 1.215 | 8.0% | 1.027 | 1.439 | 360 | 0 |

Table 5.8 – Statistical parameters for lateral-torsional buckling of hybrid beams – Proposal for new EC3 case

| Design rule | Subset (steel grade) | n | mean | cov | min | max | >1.1 | <0.97 |
|--|----------------------|------|-------|------|-------|-------|------|-------|
| Proposal for New EC3 case – Hybrid beams | All | 1175 | 1.142 | 7.2% | 0.938 | 1.397 | 812 | 9 |
| | S460 | 412 | 1.113 | 6.0% | 0.942 | 1.263 | 251 | 3 |
| | S500 | 320 | 1.149 | 6.2% | 0.984 | 1.308 | 240 | 0 |
| | S690 | 443 | 1.166 | 8.1% | 0.938 | 1.397 | 321 | 6 |

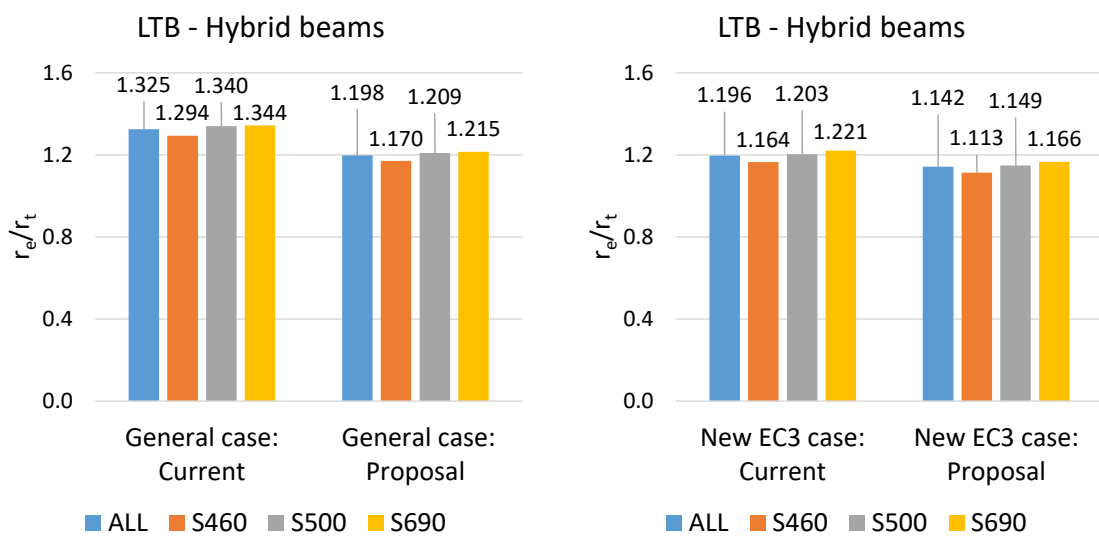


Figure 5.12 – Comparison of the mean values between the current design and proposals applied to hybrid beams

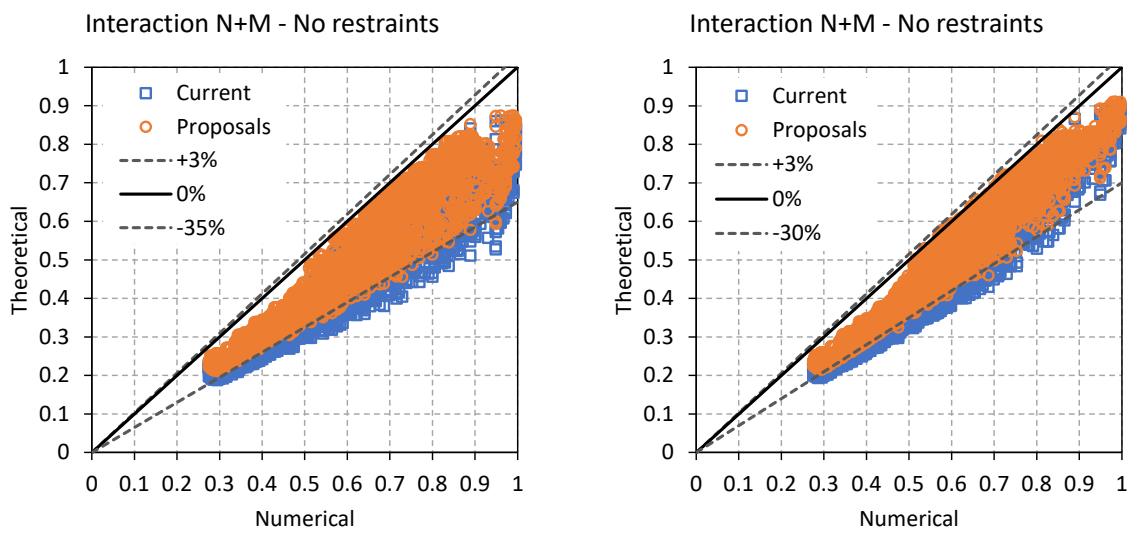
5.2.3. Beam-Columns

The buckling design of members in bending and axial compression (beam-columns) was also assessed against the current buckling curves and the proposed ones.

The results are assessed in terms of the distance of each pair (n, m) to the central point $(0,0)$, for the numerical and theoretical cases, as it was previously defined and done in Section 4.5.3.

Figure 5.13 shows the scatter plots for the unrestrained members, subjected to flexural buckling and lateral-torsional buckling. On the left side of Figure 5.13, the theoretical reduction factor (χ_{LT}) for lateral torsional buckling to apply in the interaction formula (Equation (2.19) and Equation (2.20)) is based on the general case. On the right side (Figure 5.13), the theoretical reduction factor (χ_{LT}) , is based on the new EC3 case. In both cases, the theoretical reduction factors $(\chi_y$ and $\chi_z)$ for flexural buckling are obtained based on current and proposed design rules for flexural buckling about major and minor axes, respectively.

The results show that using the new curves does not impact on the safety of the beam-columns, and that a reduction in the over-conservative design cases is observed through the comparison of the cases with the proposal design rules (orange dots) and the cases with the current rules (blue dots). This is also proved through the statistical parameters presented in Table 5.9 (directly comparable with Table 4.27 – for current design rules), using the same conditions (design rules) as described above. There are no cases with a ratio lower than 0.97 (neither using the general case nor using the new EC3 case), where the minimum value is found for the new EC3 case with a ratio 0.998.



a) FB: χ_y and χ_z – Eurocode 3

b) FB: χ_y and χ_z – Eurocode 3

LTB: χ_{LT} – General case

LTB: χ_{LT} – New EC3 case

Figure 5.13 – Scatter plots for proposals for beam-columns without restraints

Table 5.9 – Statistical parameters for proposals for bending combined with axial compression without restrains

| Design rule | Subset (steel grade) | n | mean | cov | min | max | >1.1 | <0.97 |
|------------------|----------------------|------|-------|------|-------|-------|------|-------|
| FB: | All | 3674 | 1.229 | 9.3% | 1.025 | 1.602 | 3117 | 0 |
| EC3-1-1 and LTB: | S460 | 1231 | 1.214 | 8.7% | 1.025 | 1.581 | 1033 | 0 |
| General case | S500 | 1227 | 1.225 | 9.1% | 1.025 | 1.600 | 1042 | 0 |
| | S690 | 1216 | 1.248 | 9.9% | 1.027 | 1.602 | 1042 | 0 |
| FB: | All | 3674 | 1.184 | 7.9% | 0.998 | 1.492 | 2974 | 0 |
| EC3-1-1 and LTB: | S460 | 1231 | 1.170 | 7.1% | 0.998 | 1.389 | 987 | 0 |
| New EC3 case | S500 | 1227 | 1.181 | 7.6% | 1.002 | 1.412 | 989 | 0 |
| | S690 | 1216 | 1.203 | 8.5% | 1.003 | 1.492 | 998 | 0 |

Comparing the mean value between using the current design rules for flexural buckling and lateral-torsional buckling (general case and new EC3 case) and the proposed ones (Figure 5.14), it is possible to observe a decrease of the mean value of about 12% when using the general case to obtain the reduction factor for LTB and of about 9% when using the new EC3 case.

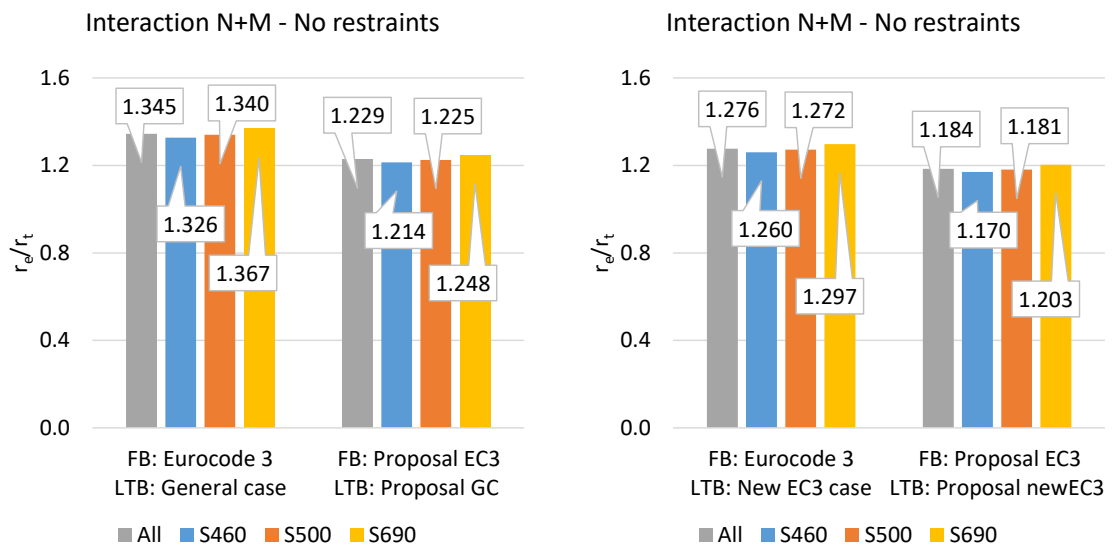


Figure 5.14 – Mean values of the safety factor for combined bending and axial compression without restraints

Regarding the minor axis restrained members, the same assessments between the current design rules and the proposed design rules were made. Nonetheless, as in this case the member is restrained about the minor axis, the interaction formula (Equation (2.19) and Equation (2.20)), only accounts for the reduction factor for flexural buckling about major axis (χ_y). Then, the comparison is made using the current and the proposed design rules for flexural buckling about major axis.

Figure 5.15 represents the scatter plots (left side) and the difference between the mean values using the current design rules and the proposed ones (right side). The statistical parameters are presented in Table 5.10 (directly comparable with Table 4.28 – statistics for current design rules). It is found that applying the proposed design rules does not affect the safety of the beam-columns (likewise for the unrestrained members), with no cases with a ratio lower than 0.97 and a mean value higher than 1.0. Nonetheless, although the mean value and the coefficient of variation have decreased compared to the current design rules, this is the case where the reduction of these values is the lowest, of approximately 1.6% in terms of the mean value and of 1% for the coefficient of variation.

Even though the new design rules have the least impact in this case, they can still be applied with safety and with slight improvements in terms of the buckling resistance of beam-columns with minor axis restrained.

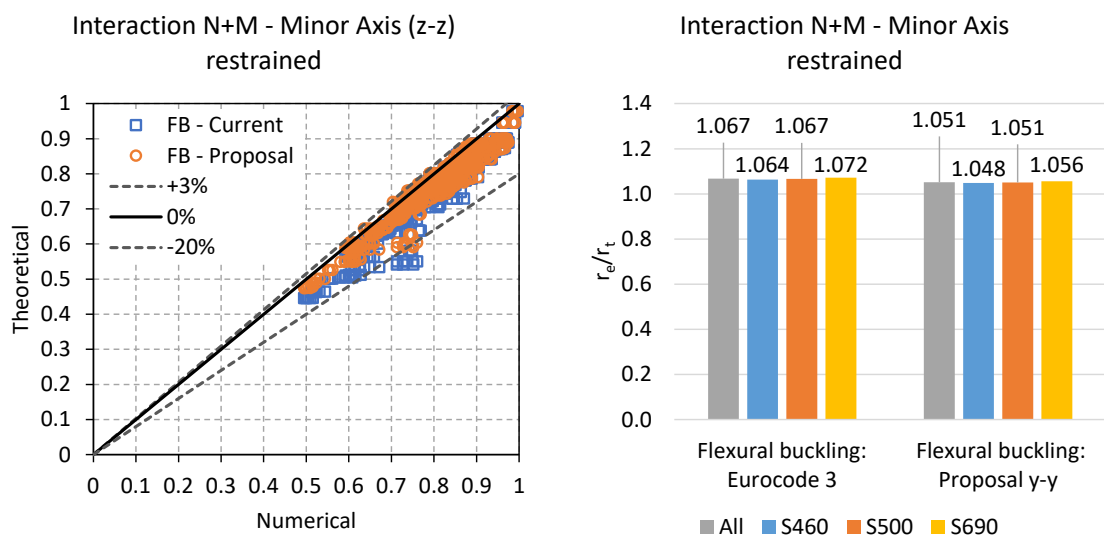


Figure 5.15 – Scatter plots and mean values for proposal for beam-columns with minor axis restrained

Table 5.10 – Statistical parameters for proposal for bending combined with axial compression with minor axis restrained

| Design rule | Subset (steel grade) | n | mean | cov | min | max | >1.1 | <0.97 |
|-----------------------|----------------------|-----|-------|------|-------|-------|------|-------|
| | All | 838 | 1.051 | 3.6% | 0.978 | 1.273 | 58 | 0 |
| Proposal for FB (y-y) | S460 | 285 | 1.048 | 3.4% | 0.978 | 1.218 | 17 | 0 |
| | S500 | 283 | 1.051 | 3.5% | 0.984 | 1.233 | 18 | 0 |
| | S690 | 270 | 1.056 | 3.7% | 0.982 | 1.273 | 23 | 0 |

5.2.4. New residual stresses models

This section presents the comparison between the theoretical reduction factors from the current buckling curves (Eurocode 3) with the buckling curves proposed in Section 5.1.1 and 5.1.2. In addition, these theoretical results are presented together with the numerical results, using different residual stresses models (ECCS [24], thermal cut, and non-thermal cut [40]).

5.2.4.1. Columns

Figure 5.16 depicts the scatters plots for major and minor axes flexural buckling using the buckling curves proposed in Section 5.1.1. The theoretical reduction factors obtained using the proposed buckling curves are plotted in relation to the numerical reduction factors for the different residual stresses models (ECCS, thermal cut, and non-thermal cut).

The chart shows that the proposals for both major and minor axes flexural buckling remain safe-sided regardless of the residual stresses model applied to obtain the numerical reduction factor. Although there are some cases that fall into the unsafe side, this is more pronounced for major axis flexural buckling, which can be confirmed by the statistical parameters presented in Table 5.11 for major and minor axes flexural buckling. About 8% (416 in 4797 cases) of the cases have a ratio lower than 0.97 for the major axis, while for minor axis this percentage is less than 3% (137 in 4797 cases). Most of these cases occur for residual stresses models with thermal cut and non-thermal cut (only 16 cases for the ECCS model). As it was previously noted, they result in lower reduction factors.

In terms of the mean value, there is a decrease in the value of about 10% for all the numerical approaches for both major and minor axes flexural buckling when comparing to the current buckling curves from Eurocode 3, as it can be seen in Figure 5.17. There is also a decrease in the coefficient of variation (cov), meaning that the dispersion of the results is lower.

The mean value stays above 1.0 for all the residual stresses models, whereby the proposal for flexural buckling is safe-sided. However, and as mentioned earlier, there is a significant difference between major and minor axes, where the mean value tends to be about 5% higher for all the residual stresses models for the minor axis flexural buckling in comparison to major axis flexural buckling.

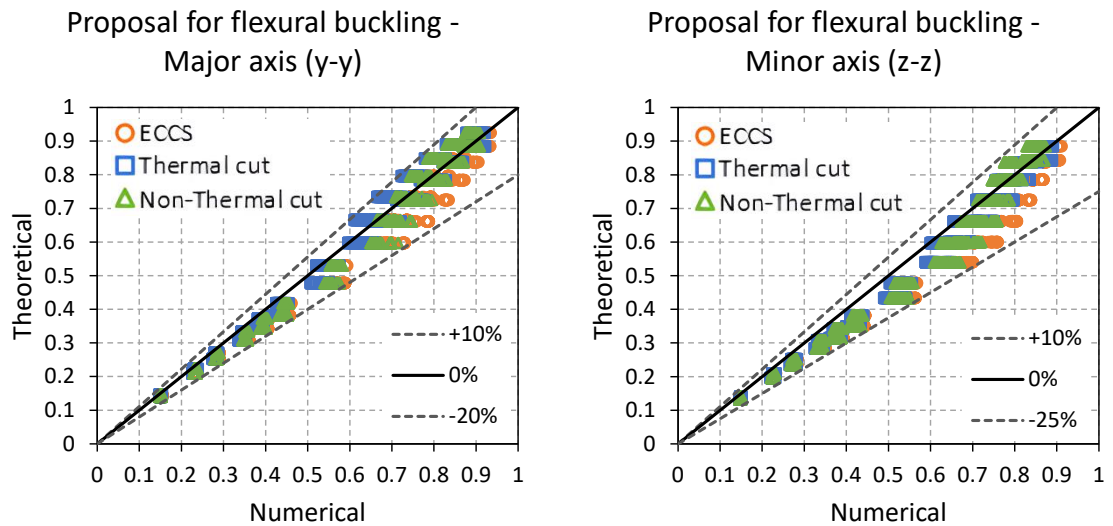


Figure 5.16 – Scatter plots with new residual stresses models and proposals for flexural buckling

Table 5.11 - Statistical parameters for proposal for flexural buckling with new residual stresses models

| Design rule | Subset (residual stresses model) | Buckling axis | n | mean | cov | min | max | >1.1 | <0.97 |
|--|----------------------------------|---------------|------|-------|------|-------|-------|------|-------|
| Proposal for flexural buckling - EC3-1-1 | ECCS | y-y | 1599 | 1.090 | 5.7% | 0.965 | 1.232 | 674 | 16 |
| | | z-z | 1599 | 1.132 | 6.4% | 0.973 | 1.303 | 1086 | 0 |
| | Thermal cut | y-y | 1599 | 1.040 | 5.8% | 0.906 | 1.169 | 318 | 232 |
| | | z-z | 1599 | 1.097 | 6.2% | 0.955 | 1.250 | 758 | 35 |
| | Non-Thermal cut | y-y | 1599 | 1.063 | 6.3% | 0.925 | 1.203 | 506 | 168 |
| | | z-z | 1599 | 1.101 | 7.1% | 0.926 | 1.268 | 849 | 102 |

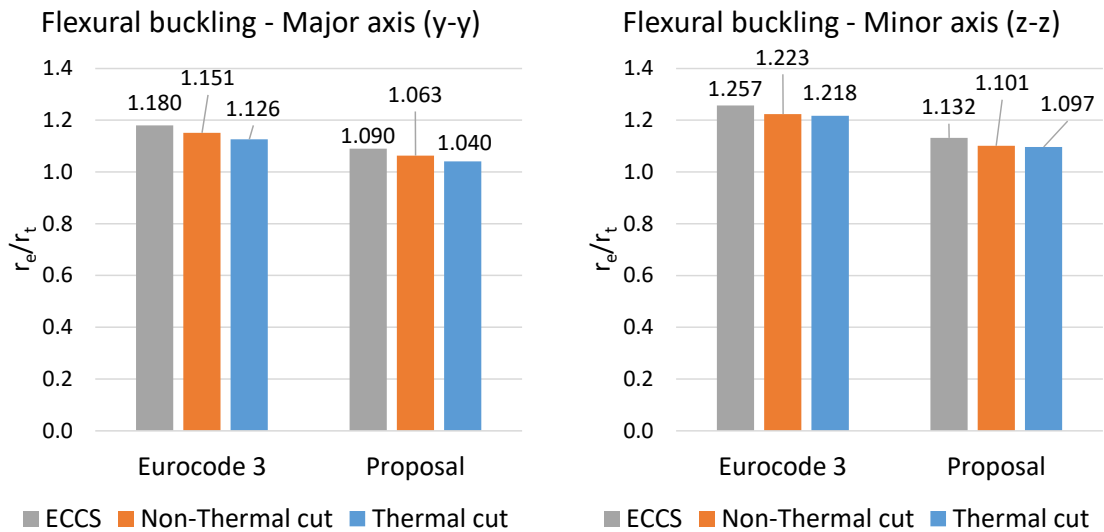


Figure 5.17 – Mean values with new residual stresses models and proposals for flexural buckling (major and minor axes)

5.2.4.2. Beams

For members subjected to lateral-torsional buckling, a similar assessment was performed. The numerical results using different residual stresses models were compared to the buckling curves proposed in Section 5.1.2 for the general case and new EC3 case since, for the special case, no improvement in the buckling curves was proposed.

Figure 5.18 shows the scatter plots for the numerical results using both proposals (proposal for general case and new EC3 method), in relation to the numerical results using the residual stresses models.

Table 5.12 and Table 5.13 summarise the statistical parameters for the proposals for the general case and the new EC3 case, respectively.

Both proposals fall on the safe-side, with less than 1% of the cases with a ratio lower than 0.97 for the proposal for general case and less than 2.5% for the proposal for the new EC3 case (22 for general case and 177 for new EC3 case in 7324 cases). Nonetheless, the general case keeps providing way more dispersion in the results regardless of the residual stresses model, comparing to the new EC3 case, as it can be observed in Figure 5.18.

Even though the new residual stresses models (thermal cut and non-thermal cut) result in lower reduction factors compared to the ECCS model, they also result in a slightly lower coefficient of variation, also in comparison to the ECCS model.

The buckling curves proposed for lateral-torsional buckling result in an improvement observed in all the residual stresses models, of about 13% for the general case and of 4% for

the new EC3 case, when compared to the current buckling curves, as it can be seen in Figure 5.19.

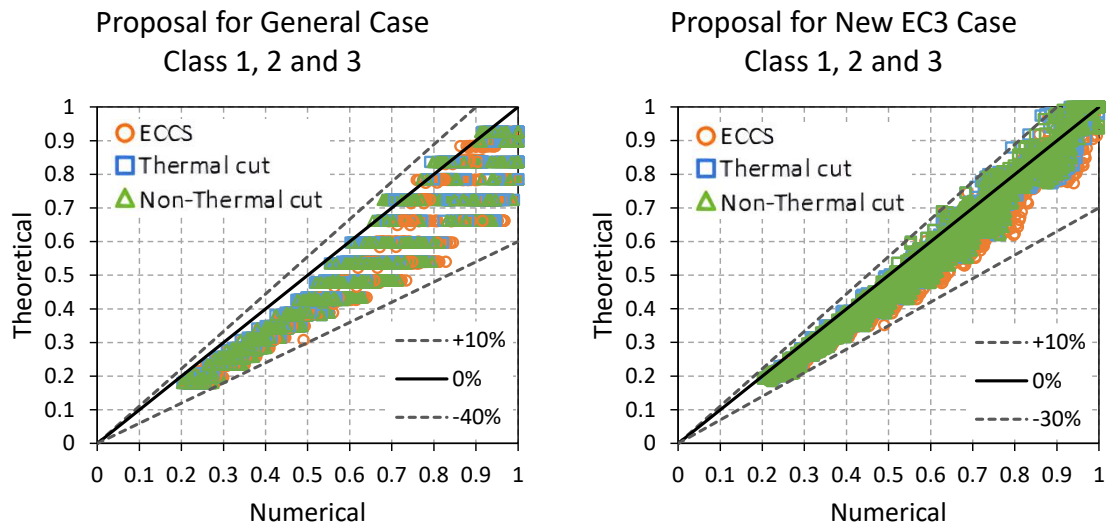


Figure 5.18 – Scatter plots for lateral-torsional buckling with new residual stresses models and proposals (all cases) – General case and New EC3 case

Table 5.12 – Statistical parameters for new residual stresses models and proposal for general case (lateral-torsional buckling)

| Design rule | Subset (residual stresses model) | n | mean | cov | min | max | >1.1 | <0.97 |
|--|----------------------------------|------|-------|------|-------|-------|------|-------|
| Proposal for General case EC3-1-1 | ECCS | 2578 | 1.252 | 9.4% | 0.968 | 1.591 | 2227 | 1 |
| | Thermal cut | 2373 | 1.233 | 8.6% | 0.945 | 1.492 | 2059 | 6 |
| | Non-Thermal cut | 2373 | 1.236 | 8.9% | 0.936 | 1.531 | 2076 | 15 |

Table 5.13 – Statistical parameters for new residual stresses models and proposal for new EC3 case (lateral-torsional buckling)

| Design rule | Subset (residual stresses model) | n | mean | cov | min | max | >1.1 | <0.97 |
|-----------------------------------|----------------------------------|------|-------|------|-------|-------|------|-------|
| Proposal for New EC3 case EC3-1-1 | ECCS | 2578 | 1.112 | 6.7% | 0.911 | 1.392 | 1451 | 28 |
| | Thermal cut | 2373 | 1.087 | 6.0% | 0.884 | 1.302 | 1017 | 65 |
| | Non-Thermal cut | 2373 | 1.090 | 6.4% | 0.901 | 1.319 | 1100 | 84 |

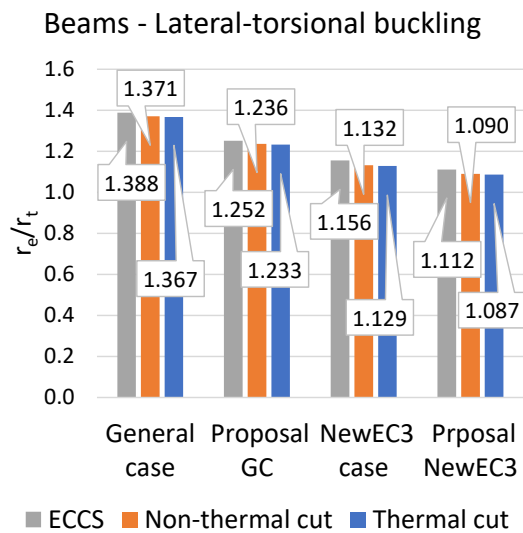


Figure 5.19 – Mean values with new residual stresses models and proposals for lateral-torsional buckling

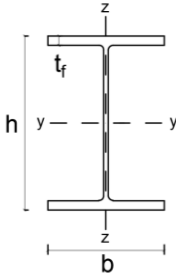
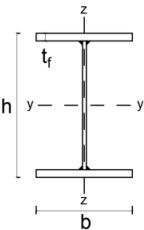
5.3. Recommendations

Based on the calibration of the design rules presented in Section 5.1, the validation of the design rules in Section 5.2, and the assessment of the safety of the developed design rules in terms of the partial safety factor performed in [74], this section comprises the developed and proposed buckling curves and imperfection factors applicable to the buckling design of high strength steel members.

5.3.1. Members in compression

The selection of the buckling curve for members in compression subjected to flexural buckling about major and minor axes is presented in Table 5.14. The developed design recommendations for welded sections made of high strength steel are highlighted.

Table 5.14 – Selection of a buckling curve for a cross-section for flexural buckling

| Cross section | Limits | Buckling about axis | Buckling Curve | | |
|--|--------------------------------|---------------------------|------------------------|-----------------|-----------------------|
| | | | S235; S275; S355; S420 | S460 up to S700 | |
| Rolled sections  | $h/b > 1.2$ | $t_f \leq 40 \text{ mm}$ | y – y | <i>a</i> | <i>a</i> ₀ |
| | | | z – z | <i>b</i> | <i>a</i> |
| | $40 \text{ mm} < t_f \leq 100$ | y – y | <i>b</i> | <i>a</i> | |
| | | z – z | <i>c</i> | <i>b</i> | |
| | $h/b \leq 1.2$ | $t_f \leq 100 \text{ mm}$ | y – y | <i>b</i> | <i>a</i> |
| | | | z – z | <i>c</i> | <i>b</i> |
| | $t_f > 100 \text{ mm}$ | y – y | <i>d</i> | <i>c</i> | |
| | | z – z | <i>d</i> | <i>c</i> | |
| Welded I-sections  | $t_f \leq 40 \text{ mm}$ | y – y | <i>b</i> | <i>a</i> | |
| | | z – z | <i>c</i> | <i>b</i> | |
| | $t_f > 40 \text{ mm}$ | y – y | <i>c</i> | <i>b</i> | |
| | | z – z | <i>d</i> | <i>c</i> | |

5.3.2. Members in bending

As previously described, for members in bending subjected to lateral-torsional buckling, there are currently two approaches available in the current Eurocode 3 [1], called the general case and the special case, and a new approach is available in the new version of the Eurocode [7], which was referred to in this document as the new EC3 case.

For the general case and new EC3 case, it was possible to justify, develop and apply new improvements in the design rules when applied to high strength steel members, contrary to the

special case, where it was not possible to justify new design rules, considering that the same levels of safety must be preserved.

5.3.2.1. General case

The selection of the buckling curve to obtain the reduction factor for lateral-torsional buckling when using the general case is presented in Table 5.15. The buckling curves developed are introduced into the table by adding a new column, for welded sections made of high strength steels, dependent on the ratio h/b .

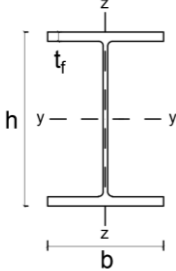
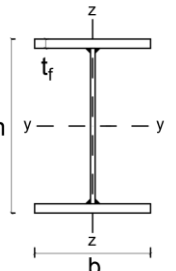
Table 5.15 – Recommend values for lateral-torsional buckling curves for cross-sections using the general case

| Cross-section | Limits | Buckling curve | |
|----------------------|--------------|---------------------------|-------------------------|
| | | S235; S275; S355; S420 | S460 to S700 |
| Rolled I-sections | $h/b \leq 2$ | <i>a</i> | - |
| | $h/b > 2$ | <i>b</i> | - |
| Welded I-sections | $h/b \leq 2$ | <i>c</i> | <i>b</i> |
| | $h/b > 2$ | <i>d</i> | <i>c</i> |
| Other cross-sections | - | <i>d</i> | - |

5.3.2.2. New EC3 case

The reduction factor for lateral-torsional buckling when using the new EC3 case is based on the imperfection factor α_{LT} . The imperfection factor is dependent on the flange thickness, where the developed design rules are added into a new column to account for the buckling design of welded sections made of high strength steel, as presented in Table 5.16.

Table 5.16 – Imperfection factor α_{LT} for lateral-torsional buckling of doubly symmetric I- and H-sections using the new EC3 method

| Cross-section | Limits | α_{LT} | | |
|---|--------------------------|---|---|---|
| | | S235 to S420 | S460 to S700 | |
| Rolled I-sections  | $h/b > 1.2$ | $t_f \leq 40 \text{ mm}$ | $0.12 \sqrt{\frac{W_{el,y}}{W_{el,z}}} \leq 0.34$ | - |
| | $h/b > 1.2$ | $t_f > 40 \text{ mm}$ | $0.16 \sqrt{\frac{W_{el,y}}{W_{el,z}}} \leq 0.49$ | - |
| | $h/b \leq 1.2$ | - | $0.16 \sqrt{\frac{W_{el,y}}{W_{el,z}}} \leq 0.49$ | - |
| Welded I-sections  | $t_f \leq 40 \text{ mm}$ | $0.21 \sqrt{\frac{W_{el,y}}{W_{el,z}}} \leq 0.64$ | $0.16 \sqrt{\frac{W_{el,y}}{W_{el,z}}} \leq 0.49$ | |
| | $t_f > 40 \text{ mm}$ | $0.25 \sqrt{\frac{W_{el,y}}{W_{el,z}}} \leq 0.76$ | $0.21 \sqrt{\frac{W_{el,y}}{W_{el,z}}} \leq 0.64$ | |

5.3.3. Members in bending and axial compression

The buckling design of members in bending and axial compression is based on the interaction formulas (Equation (2.19) and Equation (2.20)), as presented in Section 2.4.3.

For welded sections made of high strength steels, the selection of the buckling curve to obtain the reduction factors for flexural buckling (χ_y and χ_z) should be done using Table 5.14. To obtain the reduction factor for lateral-torsional buckling (χ_{LT}), the selection of the buckling curve should be done using Table 5.15 if the general case is used, or Table 5.16 to obtain the imperfection factor (α_{LT}), if the method used is the new EC3 case.

6. Conclusions and further research

6.1. Conclusions

The goal of this thesis was to contribute towards increasing the knowledge of the structural buckling behaviour of steel members made of high strength steel through an assessment of the current design procedures available for the stability design of steel members. The goal was achieved through the following steps: (i) assessment of the experimental buckling behaviour of high strength steel beams; (ii) extension of the scope of the buckling resistance of HSS members through advanced numerical analyses; (iii) assessment of the current stability design rules provided by Eurocode 3 Part 1-1 [1], [7]; (iv) development of stability design rules for HSS members; and (v) validation of the stability design rules for HSS members.

Regarding the first step, twelve full-scale tests on the lateral-torsional buckling of high strength steel beams were performed, including different steel grades, member slenderness, cross-section class, hybrid and homogeneous sections, double-symmetric and monosymmetric sections, and welded and rolled sections. For a complete characterization of the HSS beams, the experimental tests were completed with the characterization of the material properties (tensile coupon tests), measurement of geometrical properties, and measurement of residual stresses. At this stage, it was concluded that:

- The material overstrength is also observed in the high strength steels, at about 12%, according to the material properties characterization;
- The residual stresses were measured for all cross-section typologies, showing that the cross-section dimensions, flange width and section depth had a major impact on the distribution and magnitude of the residual stresses in comparison with the steel grade. The compressive and tensile residual stresses were constant to some extent, regardless of the steel grade, and showed mean values similar to the ECCS residual stress pattern in the case of the flanges;
- Most of the specimens showed imperfection values lower than the usual limits of $L/1000$ considered for the geometrical imperfections, showing that the consideration of a geometrical amplitude of $L/1000$ is usually a safe estimate for the geometrical imperfections;

- All the beams failed in the expected buckling mode, where the maximum load was reached for the homogenous beam in steel grade S690 for each group of cross-sections as expected. On average, the gain in terms of resistance of a homogeneous beam in steel grade S690 in relation to the same cross-section of a homogeneous beam in steel grade S460 was 39%. The difference between a welded section and the equivalent rolled section was of approximately 7% due to the slightly higher cross-section area of the rolled section. Small differences were found between homogenous and hybrid beams, showing that the HSS hybrid beams can be competitive compared to the homogeneous solution;
- A preliminary comparison between the obtained experimental buckling resistance and the buckling resistance provided by Eurocode 3 showed that the code underestimates the buckling resistance of high strength steel members by about 30%.

In order to further assess the buckling resistance of the high strength members, the scope of the buckling resistance of the HSS members was extended through advanced numerical analyses and validated against the experimental results:

- Small differences were obtained between the maximum loads obtained experimentally and numerically, on average smaller than 5%, except for beam B14 (11%), which is attributed to the residual stresses that were not measured specifically for this specimen and were used as mean values of the other measurements in the numerical model;
- In terms of initial stiffness, there was a good agreement between experimental and numerical behaviour, for all tests; furthermore, the numerical vertical and horizontal displacements closely followed the measured experimental displacements;
- Similar lateral-torsional buckling modes were observed numerically and experimentally, with large lateral displacements after reaching the maximum load;
- A comparison between different modelling assumptions for the members' imperfections, residual stresses, and geometrical imperfections showed that the assumption of an amplitude of $L/1000$ for the geometrical imperfections combined with the ECCS residual stress pattern is a safe-sided estimation, leading to values that are about 10% on the safe-side. Whereas the assumption of the ECCS residual stress pattern combined with real geometrical imperfections follows the experimental results quite closely.

Based on the validated advanced numerical models, a simplified numerical model was adopted for standard conditions in terms of material properties, boundary conditions, geometrical imperfections, and residual stress distributions. Furthermore, an extensive parametric study was carried out, including more than 20000 simulations covering different members, columns (flexural buckling), beams (lateral-torsional buckling), beam-columns

(flexural and lateral-torsional buckling), cross-section dimensions, steel grade, normalized slenderness, loading conditions, and residual stress distributions. The results obtained in the parametric study were further compared with the current stability design rules from Eurocode 3 Part 1-1 [1], and it was concluded that:

- It is clear that as steel grade increases, so does safety, as confirmed in all of the different members studied (columns, beams, and beam-columns), implying that using the same rules and specifications for high strength steels and normal strength steels is not cost-effective;
- Applying the current Eurocode 3 rules to high strength steels leads to a significant underestimation of the buckling resistance. On average, 20% in the case of flexural buckling and about 40% on average for lateral-torsional buckling are observed when using the general case. The special case is inaccurate in some cases, and the new EC3 case leads to better results than the general case, but it still underestimates the buckling resistance by about 18% on average;
- The lateral-torsional buckling resistance of hybrid beams is not influenced by the lower steel grade of the web, showing that the use of HSS beams can be cost-effective compared to homogeneous HSS beams, where the highest difference in terms of buckling resistance was about 15%;
- The most recent and accurate residual stress patterns proposed by Schaper et al. [40] lead to slightly more conservative results compared to the ECCS model, on average of approximately 3% for flexural buckling and of approximately 2% for lateral-torsional buckling.

Finally, based on the calibration of the generalized imperfection factor, it was possible to develop stability design rules more suitable for high strength steel members. Significant improvements can be achieved for flexural buckling about both buckling axes and for lateral-torsional buckling when using the general case applied to high strength steels by just selecting a better buckling curve based on the existing ones. For the new EC3 case, better accuracy of the buckling resistance can be obtained through a slight adjustment of the imperfection factor.

Design recommendations applicable to welded sections made of high strength steels ranging from S460 up to S700 for members in compression (flexural buckling) and for members in bending (lateral-torsional buckling) when using the general case and the new EC3 case were proposed. These proposed design recommendations were based on the selection of appropriate buckling curves based on the existing ones and the adjustment of the imperfection factor in the new EC3 case, since the objective was also to keep the design procedures as simple as they are in Eurocode 3.

The proposed stability design rules for HSS members were further validated against the results obtained from the extensive parametric study carried out. The results showed that these design rules are not too conservative, but also not unsafe, with mean values for the ratio between the theoretical and numerical reduction factors higher than 1.0. The results also show that these rules can be applied to HSS hybrid solutions and to the design of members in bending and axial compression to obtain the reduction factors for flexural buckling and lateral-torsional buckling.

6.2. Future research

The research conducted in the scope of this thesis investigated the lateral-torsional buckling resistance of high strength steel beams, and the parametric study extended the research to the buckling resistance of high strength steel columns and the combined flexural and lateral-torsional buckling of HSS beam-columns.

Nonetheless, the parametric study was limited to classes 1 to 3 sections for both columns and beams and classes 1 to 2 sections for beam-columns, which were all limited to double-symmetric cross-sections. Whereby it would be valuable to extend the parametric study to the following: (i) flexural buckling of class 4 section columns; (ii) lateral-torsional buckling of class 4 section beams; (iii) combined flexural and lateral-torsional buckling of class 3 and 4 section beam-columns; and (iv) monosymmetric cross-sections, including hybrid solutions.

6.3. Publications

The research carried out in the scope of this thesis has resulted in the following publications so far:

Journals

- Tankova T., Rodrigues F., Leitão C., Martins C., Simões da Silva L. “Lateral-torsional buckling of high strength steel beams: Experimental resistance”, *Thin-Walled Structures*, vol. 164, 2021.
- Tankova T., Simões da Silva L., Rodrigues F. “Buckling curve selection for HSS welded I-section members”, *Thin-Walled Structures*, vol. 177, 2022.

Conference Proceedings

- Rodrigues F., Tankova T., Simões da Silva L. “Tensões residuais em elementos de aço de alta resistência”, XII Congresso de Construção Metálica e Mista, Coimbra, Portugal, Novembro 2019.
- Tankova T., Simões da Silva L., Rodrigues F. “Stability Design of High Strength Steel Beams”, Eurosteel 2021, vol. 4, pp. 1624-1629, September, 2021.
- Rodrigues F., Tankova T., Simões da Silva L. “Vigas constituídas por aços de alta resistência: investigação experimental e numérica”, XIII Congresso de Construção Metálica e Mista, Congresso on-line, Novembro de 2021.
- Simões da Silva L., Tankova T., Rodrigues F. “Design Buckling Resistance of High Strength Steel Members”, The International Colloquium on Stability and Ductility of Steel Structures (SDSS), vol. 5, pp. 364-369, Aveiro, Portugal, September, 2022.
- Ferreira Filho J., Tankova T., Carvalho H., Rodrigues F., Simões da Silva L. “Numerical Study on the Buckling Resistance of High Strength Steel Columns and Beam-columns”, The International Colloquium on Stability and Ductility of Steel Structures (SDSS), vol. 5, pp. 527-536, Aveiro, Portugal, September, 2022.

REFERENCES

- [1] EN 1993-1-1. “Eurocode 3: Design of steel structures – Part 1-1: General rules and rules for buildings”, CEN, Brussels, 2005.
- [2] EN 1993-1-12. “Eurocode 3: Design of steel structures – Part 1-12: Additional rules for the extension of EN 1993 up to steel grades S700”, CEN, Brussels 2007.
- [3] High Strength Steel Market by Type (High Strength Low Alloy, Dual Phase, Bake Hardenable, Carbon Manganese), End-Use Industry (Automotive, Yellow Goods & Mining Equipment, Construction, Aviation & Marine), and Region - Global Forecast to 2023.
- [4] World steel Association, <https://www.worldsteel.org>.
- [5] EN 10025. “Hot rolled products of structural steels”, CEN, Brussels, 2004.
- [6] EN 1090-1. “Execution of steel structures and aluminium structures – Part 1: Requirements for conformity assessment of structural components”, CEN, Brussels, 2009.
- [7] CEN/TC 250/SC 3/WG 1. “Eurocode 3: Design of steel structures – Part 1-1: General rules and rules for buildings”, CEN/TC 250/SC n 2532 – prEN1993-1-1 – final draft, 2020.
- [8] CEN/TC 250/SC 3/WG 12. “Evolution of EN 1993-1-12 – High strength steels”, CEN/TC 250/SC 3 n 3080, report on WG EN1993-1-12, 2020.
- [9] Simões da Silva L., Tankova T., Marques L., Rebelo C. “Safety assessment of Eurocode 3 stability design rules for the flexural buckling of columns”, *Advanced Steel Construction*, vol. 12, pp. 328-358, 2016.
- [10] Sfintesco D. “Fondement expérimental des courbes européennes de flambement”, *Construction Métallique*, no. 3, pp. 5-12, 1970.
- [11] Beer H., Schulz G. “Bases théoriques des courbes européennes de flambement”, *Construction Métallique*, no. 3, pp. 37-57, 1970.
- [12] Strating J., Vos H. “Simulation sur ordinateur de la courbe C.E.E.M de flambement à l’aide de la méthode de Monte-Carlo”, *Construction Métallique*, no. 2, pp. 23-39, 1973.
- [13] Maquoi R., Rondal J. “Mise en équations des nouvelles courbes européennes de flambement”, *Construction Métallique*, no. 1, pp. 17-30, 1978.

- [14] Rebelo C., Lopes N., Simões da Silva L., Nethercot D., Vila Real P. M. M. “Statistical evaluation of the lateral-torsional buckling resistance of steel I-beams, Part 1: Variability of the Eurocode 3 resistance model”, *Journal of Constructional Steel Research*, vol. 65, pp. 818-831, 2009.
- [15] Greiner R., Kaim P. “Comparison of LT-buckling curves with test results”, ECCS TC 8, Supplementary Report, no. 2003-10, European Convention for Constructional Steelwork, 2003.
- [16] Byfield M. P., Nethercot D. A. “An analysis of the true bending strength of steel beams”, *Proceedings of the Institution of Civil Engineers – Structures and Buildings*, vol. 128, pp. 188-197, 1998.
- [17] Salzgeber G. “LT-buckling curves”, ECCS TC 8, Report, no. 2000-001, European Convention for Constructional Steelwork, 2000.
- [18] Janss J., Maquoi R. “Evaluation of test results on lateral torsional buckling in order to obtain strength function and suitable model factor”, Background Report to Eurocode 3.
- [19] ENV 1993-1-1. “Eurocode 3: Design of steel structures – Part 1-1: General rules and rules for buildings”, CEN, Brussels, 1992.
- [20] Snijder H. H., Hoenderkamp J. C. D. “Buckling curves for lateral torsional buckling of unrestrained beams”, *Proceedings of the Hommages a Rene Maquoi Birthday Anniversary*, pp. 239-248, Universite de Liege, Belgium, 2007.
- [21] Taras A., Greiner R. “New design curves for lateral-torsional buckling – Proposal based on a consistent derivation”, *Journal of Constructional Steel Research*, vol. 66, pp. 648-663, 2010.
- [22] Simões da Silva L., Tankova T., Marques L., Rebelo C., Kuhlmann U., Kleiner A., Spiegler J., Snijder H. H., Dekker R., Dehan V., Taras A., Haremza C., Cajot L. G., Vassart O., Popa N. “Standardization of Safety Assessment Procedures across Brittle to Ductile Failure Modes (SAFEBRITILE)”, RFSR-CT-2013-00023, Final report, 2017.
- [23] Simões da Silva L., Tankova T., Marques L., Rebelo C., Taras A. “Safety assessment of Eurocode 3 stability design rules for the lateral-torsional buckling of prismatic beams”, *Advanced Steel Construction*, vol. 14, pp. 668-693, 2018.
- [24] ECCS. “Ultimate limit state calculation of sway frames with rigid joints. 1st Ed. N°33. ECCS – Technical Committee 8 – Structural Stability, European Convention of Constructional Steelwork, 1984.
- [25] CEN/TC 250/SC 3/WG 22. “Eurocode 3: Design of steel structures – Part 1-14: Design assisted by finite element analysis”, CEN/TC 250/SC n 3296 – prEN1993-1-14 – draft version, 2021.
- [26] Tankova T., Simões da Silva L., Balakrishnam M., Rodrigues D., Launert B., Pasternak H., Tun T. “Residual stresses in welded I section steel members”, *Engineering Structures*, vol. 197, 2019.

-
- [27] Liu X., Chung KF. “Experimental and numerical investigation into temperature histories and residual stresses distributions of high strength steel S690 welded H-sections”, *Journal of Constructional Steel Research*, vol. 165, pp. 396-411, 2018.
- [28] Rasmussen K. J. R., Hancock G. J. “Test of high strength steel columns”, *Journal of Constructional Steel Research*, vol. 34, pp. 27-52, 1995.
- [29] Liu X. “Structural effects of welding onto high strength S690 steel plates and welded sections”, The Hong Kong Polytechnic University, PhD Thesis, 2017.
- [30] Wang K. “Study on structural behaviour of high strength steel S690 welded H- and I-sections”, The Hong Kong Polytechnic University, PhD Thesis, 2018.
- [31] Wang Y-B., Li G-Q., Chen S-W. “Residual stresses in welded flame-cut high strength steel H-sections”, *Journal of Constructional Steel Research*, vol. 79, pp. 159-165, 2012.
- [32] Ban H., Shi G., Bai Y., Shi Y., Wang Y. “Residual stress of 460 MPa high strength steel welded I section: Experimental investigation and modeling”, *International Journal of Steel Structures*, vol. 13, pp. 691-705, 2013.
- [33] Yang B., Nie S., Xiong G., Hu Y., Bai J., Zhang W., Dai G. “Residual stresses in welded I-shaped sections fabricated from Q460GK structural steel plates”, *Journal of Constructional Steel Research*, vol. 122, pp. 261-273, 2016.
- [34] Unsworth D., Driver R., Li L. “Measurement and prediction of residual stresses in welded girders”, *Journal of Constructional Steel Research*, vol. 169, 2020.
- [35] Unsworth D., Driver R. G., Twizell S., Imanpour A. “Characterization of residual stresses for LTB simulations of modern welded girders”, *Journal of Constructional Steel Research*, vol. 183, 2021.
- [36] Schaper L., Winkler R., Jörg F., Kuhlmann U., Knobloch M. “Experimental study on LTB behaviour and residual stresses of welded I-section members”, *Conference: The International Colloquium on Stability and Ductility of Steel Structures*, Prague, Czech Republic, 2019.
- [37] Schaper L., Jörg F., Winkler R., Kuhlmann U., Knobloch M. “The simplified method of the equivalent compression flange – development based on LTB tests and residual stress measurements”, *Steel Construction*, vol. 12, pp. 264-277, 2019.
- [38] Ban H., Shi G., Shi Y., Wang Y. “Residual stress of 460 MPa high strength steel welded box section: Experimental investigation and modeling”, *Thin-Walled Structures*, vol. 64, pp. 73-82, 2013.
- [39] Yang B., Zhu Q., Nie S., Elchalakani M., Xiong G. “Experimental and model investigation on residual stresses in Q460GJ thick-walled I-shaped sections”, *Journal of Constructional Steel Research*, vol. 145, pp. 489-503, 2018.
- [40] Schaper L., Tankova T., Simões da Silva L., Knobloch M. “A novel residual stress model for welded I-sections”, *Journal of Constructional Steel Research*, vol. 188, 2022.
-

- [41] Somodi B., Kövesdi B. “Residual stress measurements on welded square box sections using steel grades of S235-S960”, *Thin-Walled Structures*, vol. 123, pp. 142-154, 2018.
- [42] Launert B., Rhode M., Pasternak H., Kannengiesser T. “Welding residual stresses in high strength steel. Experimental results”, *Proceedings of the International Colloquium on Stability and Ductility of Steel Structures*, pp. 517-414, Romania, 2016.
- [43] Launert B., Pasternak H. “Welded residual stresses effects in the design of welded plate girders: Simulation and Implementation”, *Ce/Papers, Proceedings of Eurosteel*, vol. 1, pp. 1039-1047, 2017.
- [44] Li T-J., Li G-Q., Wang Y-B. “Residual stress tests of welded Q690 high-strength steel box- and H-sections”, *Journal of Constructional Steel Research*, vol. 115, pp. 283-289, 2015.
- [45] Yang Z., Wang W., Zhang J., Xu L. “Effect of fire exposure on residual stresses relief in welded high strength steel sections”, *Journal of Constructional Steel Research*, vol. 177, 2021.
- [46] Le T., Paradowska A., Brandford M., Liu X., Valipour H. “Residual stresses in welded high-strength steel I-Beams”, *Journal of Constructional Steel Research*, vol. 167, 2020.
- [47] Li D., Paradowska A., Uy B., Wang J., Khan M. “Residual stresses of box and I-shaped columns fabricated from S960 ultra-high-strength steel”, *Journal of Constructional Steel Research*, vol. 166, 2020.
- [48] Su A., Sun Y., Liang Y., Zhao O. “Membrane residual stresses and local buckling of S960 ultra-high strength steel welded I-section stub columns”, *Thin-Walled Structures*, vol. 161, 2021.
- [49] Wang F., Lui E. “Experimental investigation of post-fire residual stresses in Q690 welded I-sections”, *Thin-Walled Structures*, vol. 163, 2021.
- [50] Cao X., Xu Y., Kong Z., Shen H., Zhong W. “Residual stress of 800 MPa high strength steel welded T section: Experimental study”, *Journal of Constructional Steel Research*, vol. 131, pp. 30-37, 2017.
- [51] Wang Y-B., Li G-Q., Chen S-W., Sun F-F. “Experimental and numerical study on the behaviour of axially compressed high strength steel columns with H-section”, *Engineering Structures*, vol. 43, pp. 149-159, 2012.
- [52] Shi G., Ban H., Bijlaard F. S. K. “Tests and numerical study of ultra-high strength steel columns with end restraints”, *Journal of Constructional Steel Research*, vol. 70, pp. 236-247, 2012.
- [53] Ban H., Shi G., Shi Y., Wang Y. “Overall buckling behaviour of 460 MPa high strength steel columns: Experimental investigation and design method”, *Journal of Constructional Steel Research*, vol. 74, pp. 140-150, 2012.
- [54] Feng R., Zhan H., Meng S., Zhu J. “Experiments on H-shaped high-strength steel beams with perforated web”, *Engineering Structures*, vol. 177, pp. 374-394, 2018.

-
- [55] Feng R., Liu J., Chen Z., Roy K., Chen B., Lim J. “Numerical investigation and design rules for flexural capacities of H-section high-strength steel beams with and without web openings”, *Engineering Structures*, vol. 225, 2020.
- [56] Yang Y., Bradford M., Liu X. “Strength design of welded high-strength steel beams considering coupled local and global buckling”, *Thin-Walled Structures*, vol. 149, 2020.
- [57] Nethercot D. A. “Buckling of welded hybrid steel I-beams”, *Journal of the Structural Division*, vol. 102, 1976.
- [58] Veljkovic M., Johansson B. “Design of hybrid steel girders”, *Journal of Constructional Steel Research*, vol. 60, pp. 535-547, 2004.
- [59] Shokouhian M., Shi Y. “Flexural strength of hybrid steel I-beams based on slenderness”, *Engineering Structures*, vol. 93, pp. 114-128, 2015.
- [60] Le.T., Bradford M., Liu X., Valipour H. “Buckling of welded high-strength steel I-beams”, *Journal of Constructional Steel Research*, vol. 168, 2020.
- [61] Yan X-L., Li G-Q., Wang Y-B., Jiang J. “Experimental and numerical investigation on flexural-torsional buckling of Q460 steel beams”, *Journal of Constructional Steel Research*, vol. 174, 2020.
- [62] Wang K., Xiao M., Chung K-F., Nethercot D. “Lateral torsional buckling of partially restrained beams of high strength S690 welded I-sections”, *Journal of Constructional Steel Research*, vol. 184, 2021.
- [63] Xiong G., Feng Y., Peng Q., Kang S-B., Zhang Y., Fan Y-L. “Lateral-torsional buckling behaviour of 690 MPa high strength steel beams”, *Structures*, vol. 33, pp. 3999-4010, 2021.
- [64] Xiong G., Feng Y., Liao X-D., Gu Y., Kang S-B. “Lateral-torsional buckling behaviour of welded Q690 steel I-beams with double lateral restraints along the length”, *Thin-Walled Structures*, vol. 170, 2022.
- [65] ISO 6892-1:2009. “Metallic materials – Tensile testing – Part 1: Method of test at room temperature”, International Organization for Standardization, 2009.
- [66] Spoorenberg R. C., Snijder H. H., Hoenderkamp J. C. D. “Experimental investigation of residual stresses in roller bent wide flange steel sections”, *Journal of Constructional Steel Research*, vol. 66, pp. 737-747, 2010.
- [67] Galéa Y. “Moment critique de déversement élastique de poutres fléchies, Présentation du logiciel LTBEAM”, *Revue de la Construcion Métallique* n. 2, CTICM, 2003.
- [68] ABAQUS. v.6.18, Dassault Systems/Simulia, Providence, RI, USA, 2018.
- [69] MATLAB. Version 9.7 (R2019b), Natick, Massachusetts, The MathWorks Inc, 2019.
-

[70] Simões da Silva L., Rebelo C., Nethercot D., Marques L., Simões R., Vila Real P. M. M. “Statistical evaluation of the lateral-torsional buckling resistance of steel I-beams, Part 2: Variability of steel properties”, *Journal of Constructional Steel Research*, vol. 65, pp. 832-849, 2009.

[71] Marques L., Taras A., Simões da Silva L., Greiner R., Rebelo C. “Development of a consistent buckling design procedure for tapered columns”, *Journal of Constructional Steel Research*, vol. 72, pp. 61-74, 2012.

[72] EN 1990. “Eurocode – Basis of structural design”, CEN, Brussels, 2002.

[73] EN 1993-1-5. “Eurocode 3 – Design of steel structures – Part 1-5: Plated structural elements”, CEN, Brussels, 2006.

[74] Tankova T., Simões da Silva L., Rodrigues F. “Buckling curve selection for HSS welded I-section members”, *Thin-Walled Structures*, vol. 177, 2022.

Annex A – Geometrical imperfections

The geometrical imperfections measurements for the web and flanges performed for each specimen are presented in this annex.

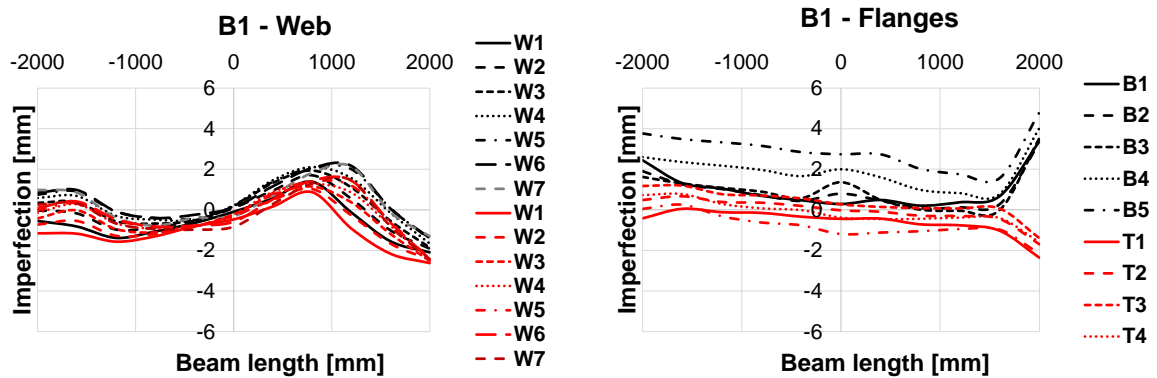


Figure A.1 – Geometrical imperfections for specimen B1

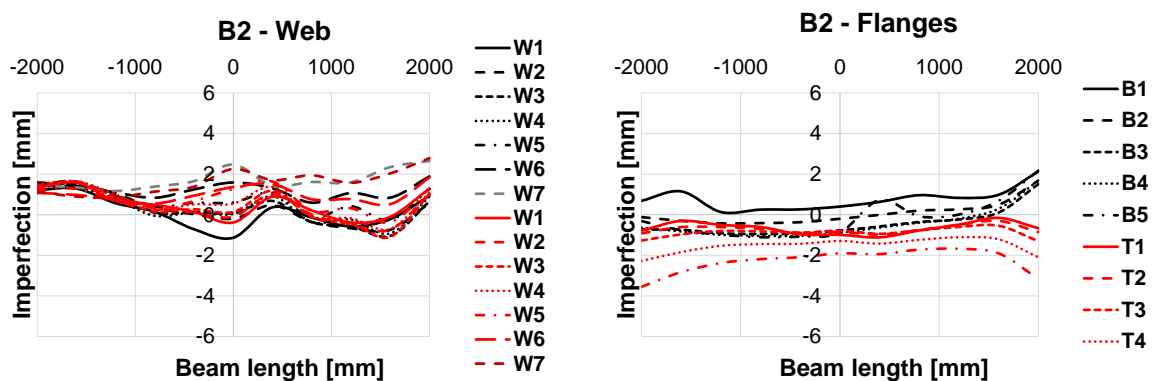


Figure A.2 – Geometrical imperfections for specimen B2

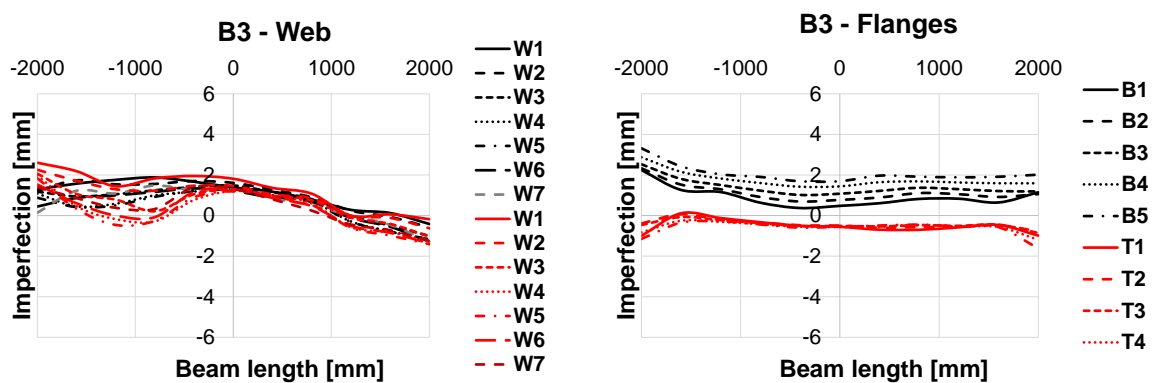


Figure A.3 – Geometrical imperfections for specimen B3

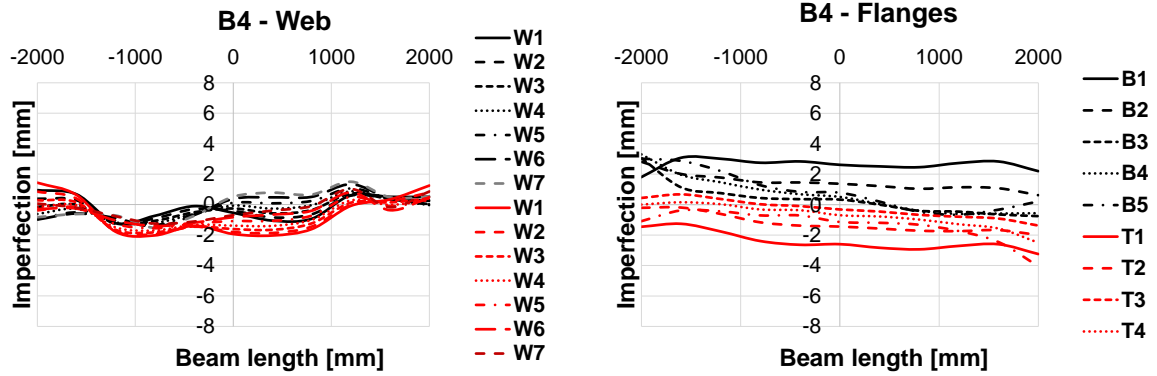


Figure A.4 – Geometrical imperfections for specimen B4

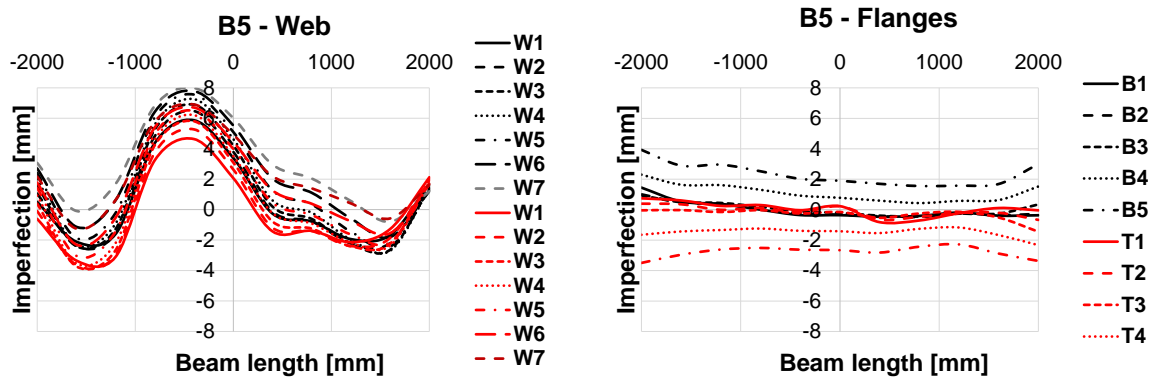


Figure A.5 – Geometrical imperfections for specimen B5

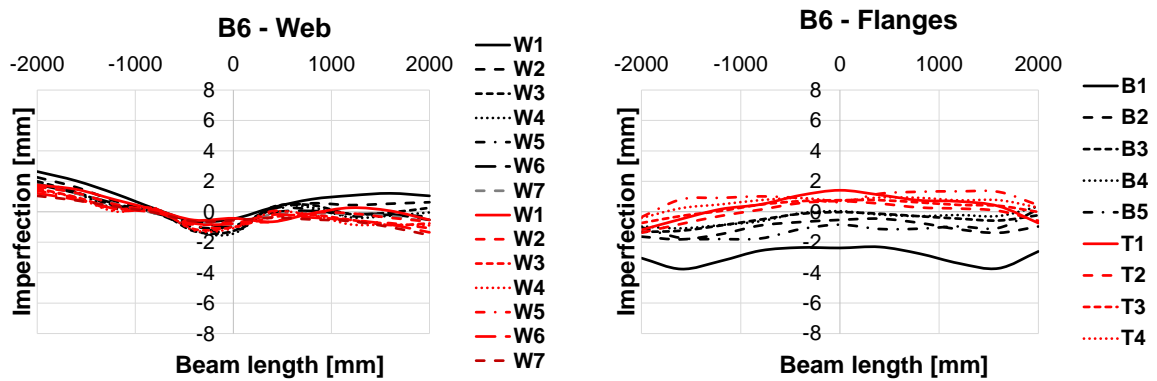


Figure A.6 – Geometrical imperfections for specimen B6

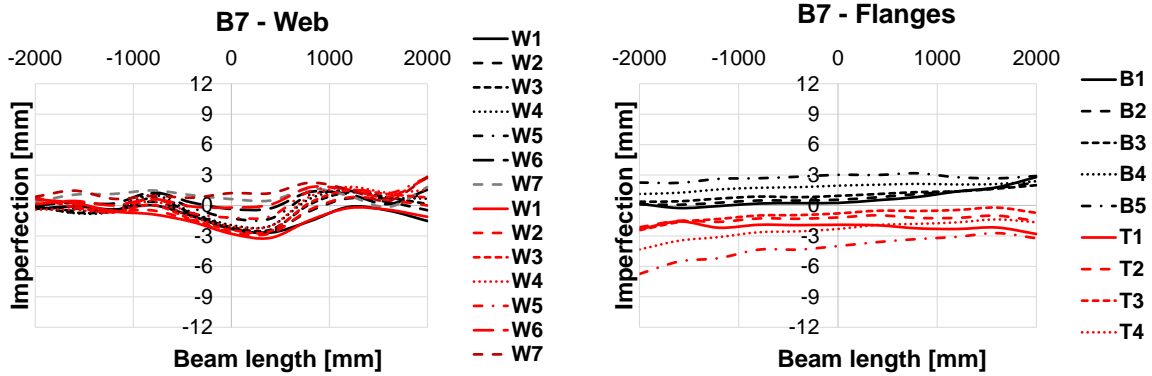


Figure A.7 – Geometrical imperfections for specimen B7

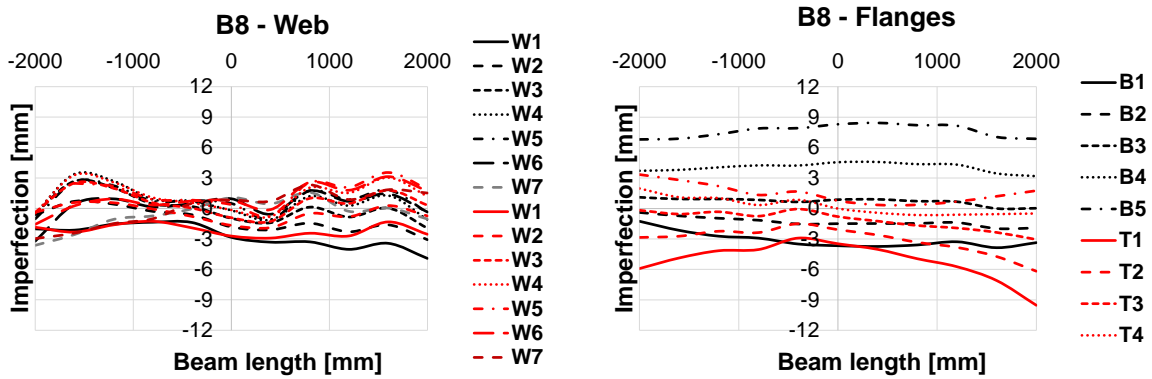


Figure A.8 – Geometrical imperfections for specimen B8

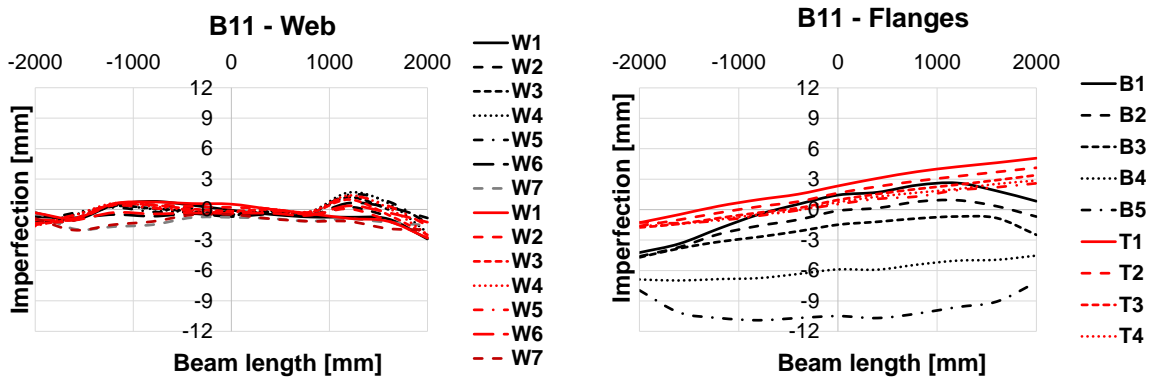


Figure A.9 – Geometrical imperfections for specimen B11

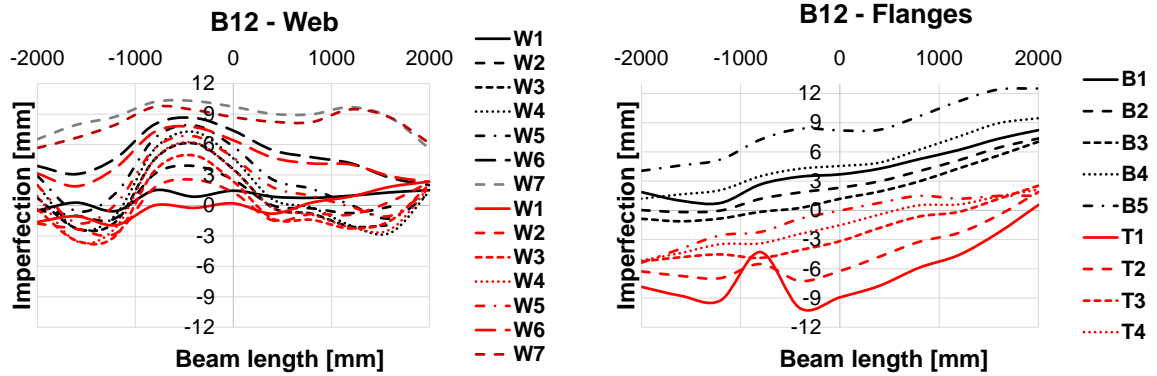


Figure A.10 – Geometrical imperfections for specimen B12

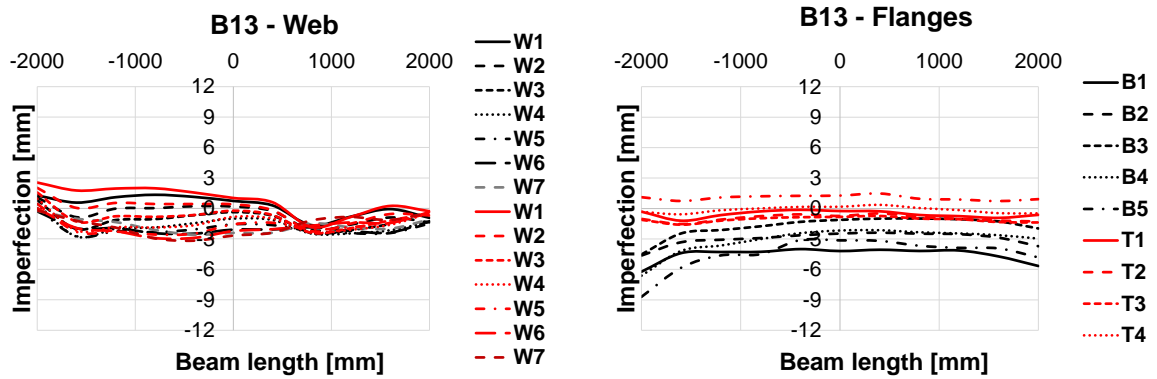


Figure A.11 – Geometrical imperfections for specimen B13

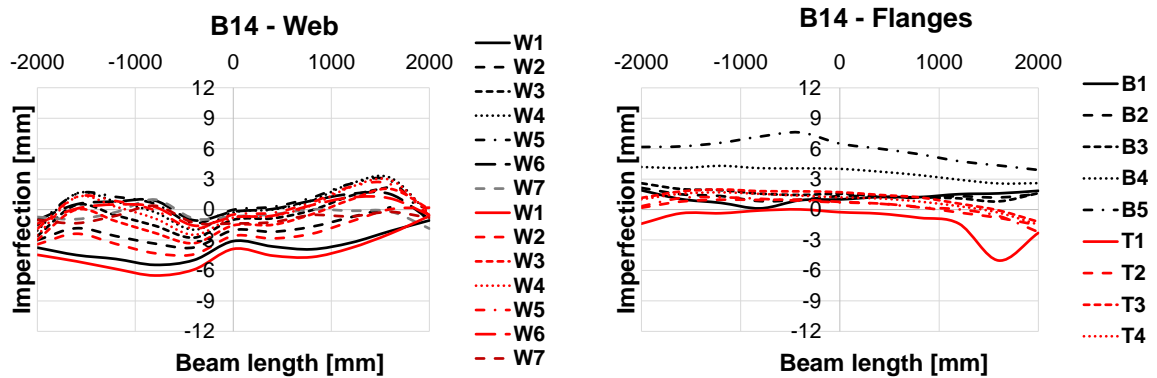


Figure A.12 – Geometrical imperfections for specimen B14

Annex B – Members in bending (beams)

In this annex, the results obtained for the different bending moment distributions considered in the parametric study for beams (members subjected to lateral-torsional buckling) are presented separately, in terms of the numerical result (r_e) over the theoretical (r_t) design resistance according to the Eurocode 3 methods (general case, special case, and new EC3 case), as well as the statistical parameters for the ratio (r_e/r_t).

B.1 Constant bending moment – $\psi = 1$

Table B.1 – Statistical parameters: constant bending moment $\psi = 1$ – Class 1 or 2

| Design rule | Steel grade | n | mean | cov | min | max | >1.1 | <0.97 |
|---------------------------|-------------|------|-------|-------|-------|-------|------|-------|
| General case | All | 1008 | 1.316 | 10.6% | 1.024 | 1.606 | 890 | 0 |
| | S460 | 379 | 1.292 | 10.5% | 1.031 | 1.568 | 328 | 0 |
| | S500 | 295 | 1.322 | 10.0% | 1.030 | 1.558 | 263 | 0 |
| | S690 | 334 | 1.336 | 10.9% | 1.024 | 1.606 | 299 | 0 |
| Proposal for General case | All | 1008 | 1.188 | 8.6% | 0.968 | 1.441 | 743 | 1 |
| | S460 | 379 | 1.167 | 8.5% | 0.968 | 1.366 | 258 | 1 |
| | S500 | 295 | 1.192 | 7.9% | 0.993 | 1.391 | 228 | 0 |
| | S690 | 334 | 1.207 | 8.9% | 0.976 | 1.441 | 257 | 0 |
| Special case | All | 1008 | 1.095 | 8.7% | 0.914 | 1.327 | 502 | 126 |
| | S460 | 379 | 1.078 | 8.3% | 0.916 | 1.296 | 165 | 55 |
| | S500 | 295 | 1.096 | 8.2% | 0.920 | 1.287 | 150 | 36 |
| | S690 | 334 | 1.114 | 9.1% | 0.914 | 1.327 | 187 | 35 |
| New EC3 case | All | 1008 | 1.183 | 7.1% | 1.015 | 1.393 | 784 | 0 |
| | S460 | 379 | 1.162 | 6.5% | 1.024 | 1.310 | 275 | 0 |
| | S500 | 295 | 1.183 | 6.5% | 1.015 | 1.337 | 236 | 0 |
| | S690 | 334 | 1.207 | 7.6% | 1.023 | 1.393 | 273 | 0 |
| Proposal for New EC3 case | All | 1008 | 1.131 | 6.6% | 0.985 | 1.320 | 680 | 0 |
| | S460 | 379 | 1.111 | 6.1% | 0.987 | 1.246 | 226 | 0 |
| | S500 | 295 | 1.131 | 5.9% | 0.985 | 1.268 | 215 | 0 |
| | S690 | 334 | 1.156 | 6.9% | 0.989 | 1.320 | 239 | 0 |

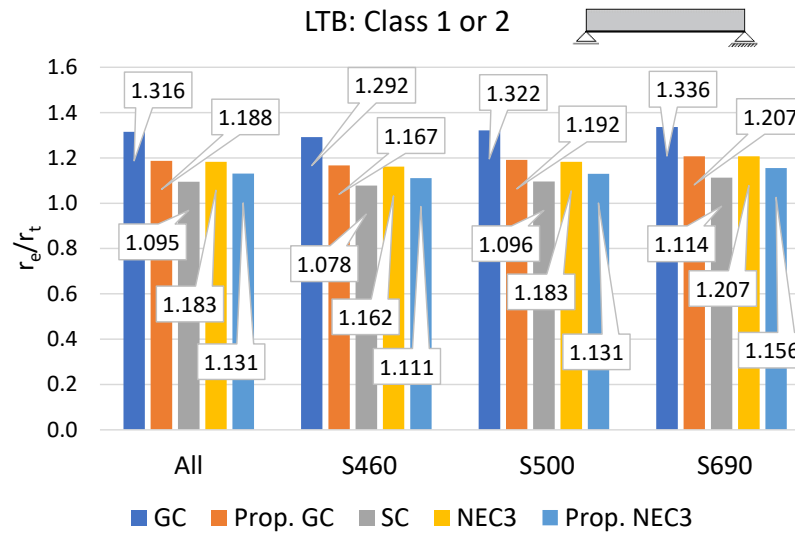

 Figure B.1 – Mean values for ratio r_e/r_t for constant bending moment $\psi = 1$ – Class 1 or 2

 Table B.2 – Statistical parameters: constant bending moment $\psi = 1$ – Class 3

| Design rule | Steel grade | n | mean | cov | min | max | >1.1 | <0.97 |
|---------------------------|-------------|-----|-------|-------|-------|-------|------|-------|
| General case | All | 167 | 1.257 | 9.4% | 1.032 | 1.489 | 141 | 0 |
| | S460 | 33 | 1.232 | 11.3% | 1.035 | 1.484 | 23 | 0 |
| | S500 | 25 | 1.249 | 9.9% | 1.042 | 1.430 | 19 | 0 |
| | S690 | 109 | 1.266 | 8.7% | 1.032 | 1.489 | 99 | 0 |
| Proposal for General case | All | 167 | 1.148 | 8.3% | 0.993 | 1.391 | 112 | 0 |
| | S460 | 33 | 1.136 | 9.8% | 0.997 | 1.353 | 17 | 0 |
| | S500 | 25 | 1.150 | 8.4% | 0.994 | 1.298 | 16 | 0 |
| | S690 | 109 | 1.152 | 7.8% | 0.993 | 1.391 | 79 | 0 |
| Special case | All | 167 | 1.051 | 6.9% | 0.917 | 1.214 | 43 | 30 |
| | S460 | 33 | 1.049 | 8.1% | 0.928 | 1.214 | 9 | 9 |
| | S500 | 25 | 1.053 | 6.8% | 0.935 | 1.182 | 5 | 5 |
| | S690 | 109 | 1.052 | 6.7% | 0.917 | 1.211 | 29 | 16 |
| New EC3 case | All | 167 | 1.124 | 6.6% | 1.000 | 1.336 | 105 | 0 |
| | S460 | 33 | 1.096 | 7.2% | 1.003 | 1.238 | 14 | 0 |
| | S500 | 25 | 1.108 | 6.2% | 1.000 | 1.188 | 15 | 0 |
| | S690 | 109 | 1.136 | 6.3% | 1.007 | 1.336 | 76 | 0 |
| Proposal for New EC3 case | All | 167 | 1.070 | 6.3% | 0.967 | 1.299 | 55 | 5 |
| | S460 | 33 | 1.048 | 6.8% | 0.967 | 1.186 | 10 | 3 |
| | S500 | 25 | 1.058 | 5.7% | 0.967 | 1.149 | 9 | 2 |
| | S690 | 109 | 1.079 | 6.2% | 0.976 | 1.299 | 36 | 0 |

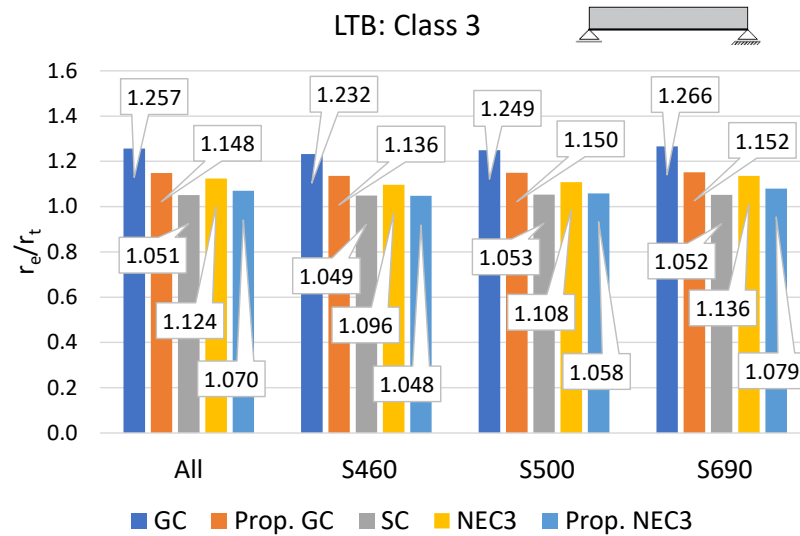


Figure B.2 – Mean values for the ratio r_e/r_t for constant bending moment $\psi = 1$ – Class 3

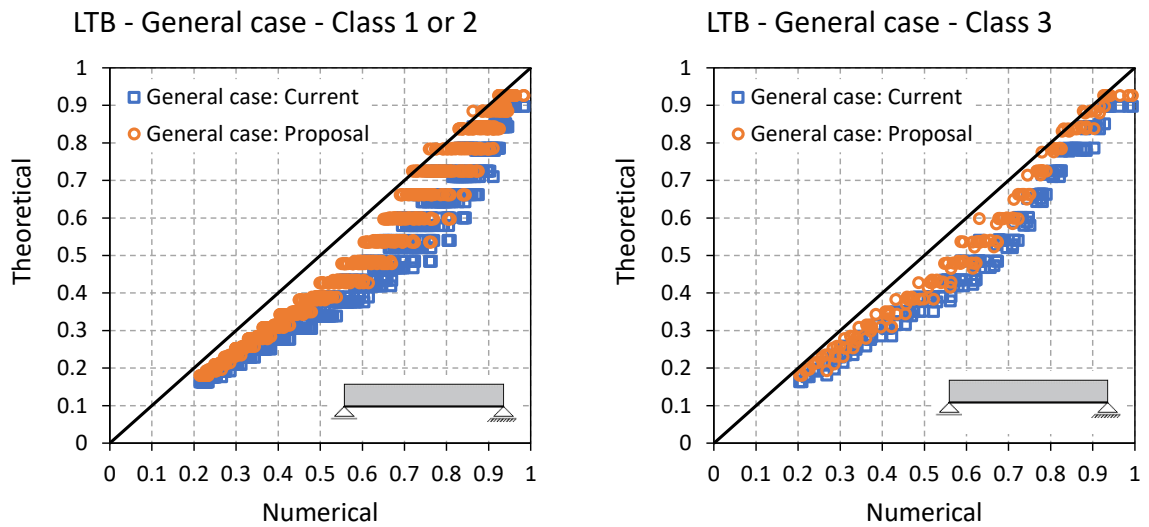


Figure B.3 – Scatter plots for LTB with constant bending moment $\psi = 1$ – General case

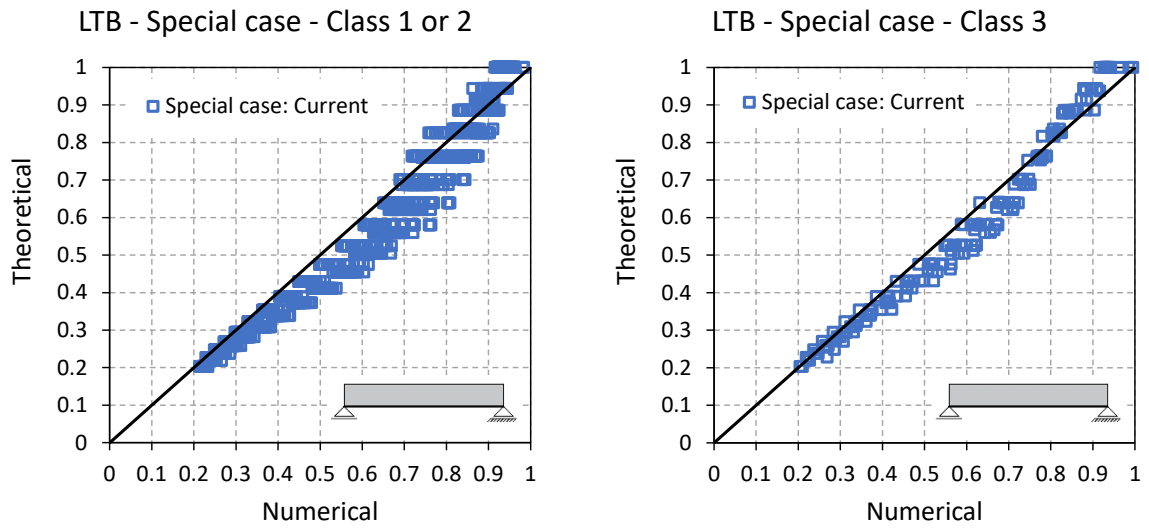


Figure B.4 – Scatter plots for LTB with constant bending moment $\psi = 1$ – Special case

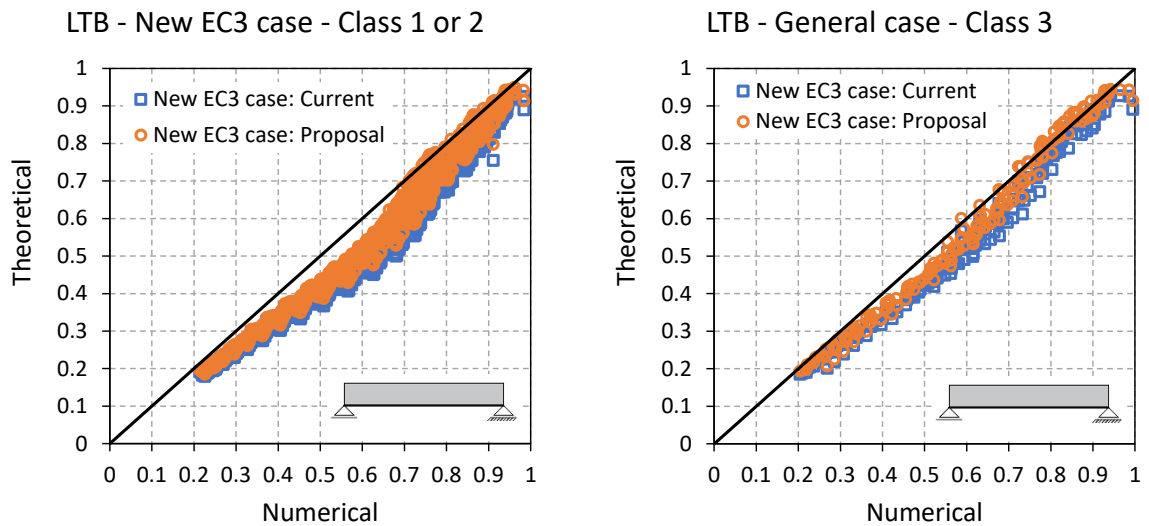


Figure B.5 – Scatter plots for LTB with constant bending moment $\psi = 1$ – New EC3 case

B.2 Linear bending moment – $\psi = 0$

Table B.3 – Statistical parameters: linear bending moment $\psi = 0$ – Class 1 or 2

| Design rule | Steel grade | n | mean | cov | min | max | >1.1 | <0.97 |
|---------------------------|-------------|-----|-------|------|-------|-------|------|-------|
| General case | All | 684 | 1.464 | 9.6% | 1.148 | 1.773 | 684 | 0 |
| | S460 | 228 | 1.453 | 9.4% | 1.148 | 1.713 | 228 | 0 |
| | S500 | 239 | 1.464 | 9.6% | 1.148 | 1.734 | 239 | 0 |
| | S690 | 217 | 1.476 | 9.8% | 1.148 | 1.773 | 217 | 0 |
| Proposal for General case | All | 684 | 1.317 | 6.8% | 1.112 | 1.534 | 684 | 0 |
| | S460 | 228 | 1.306 | 6.5% | 1.112 | 1.482 | 228 | 0 |
| | S500 | 239 | 1.317 | 6.7% | 1.112 | 1.500 | 239 | 0 |
| | S690 | 217 | 1.328 | 7.0% | 1.112 | 1.534 | 217 | 0 |
| Special case | All | 684 | 1.149 | 7.0% | 0.971 | 1.310 | 451 | 0 |
| | S460 | 228 | 1.139 | 6.8% | 1.000 | 1.296 | 137 | 0 |
| | S500 | 239 | 1.149 | 6.9% | 1.010 | 1.291 | 155 | 0 |
| | S690 | 217 | 1.159 | 7.2% | 0.971 | 1.310 | 159 | 0 |
| New EC3 case | All | 684 | 1.162 | 6.9% | 0.985 | 1.353 | 527 | 0 |
| | S460 | 228 | 1.146 | 6.3% | 1.000 | 1.306 | 167 | 0 |
| | S500 | 239 | 1.162 | 6.6% | 1.010 | 1.332 | 187 | 0 |
| | S690 | 217 | 1.178 | 7.4% | 0.985 | 1.353 | 173 | 0 |
| Proposal for New EC3 case | All | 684 | 1.122 | 5.9% | 0.961 | 1.299 | 452 | 2 |
| | S460 | 228 | 1.107 | 5.3% | 0.961 | 1.272 | 134 | 2 |
| | S500 | 239 | 1.121 | 5.5% | 0.994 | 1.299 | 158 | 0 |
| | S690 | 217 | 1.139 | 6.5% | 0.971 | 1.287 | 160 | 0 |

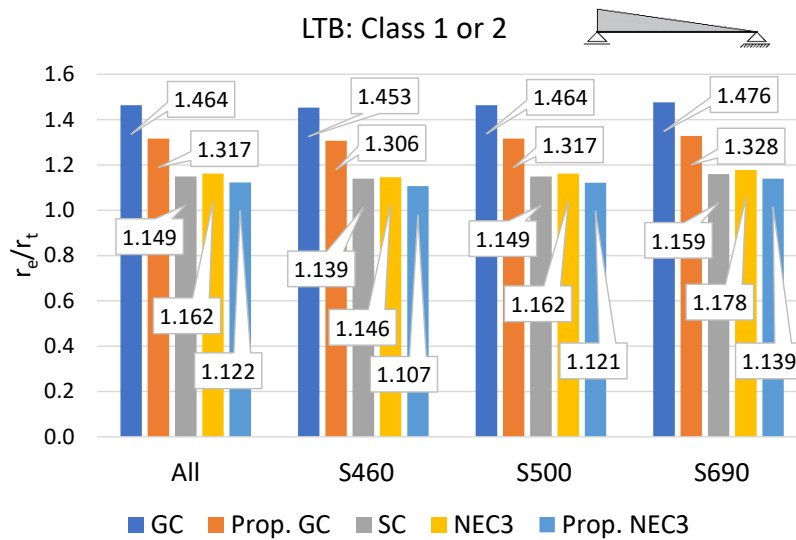

 Figure B.6 – Mean values for the ratio r_e/r_t for linear bending moment $\psi = 0$ – Class 1 or 2

 Table B.4 – Statistical parameters: linear bending moment $\psi = 0$ – Class 3

| Design rule | Steel grade | n | mean | cov | min | max | >1.1 | <0.97 |
|---------------------------|-------------|----|-------|------|-------|-------|------|-------|
| General case | All | 85 | 1.336 | 9.7% | 1.088 | 1.723 | 84 | 0 |
| | S460 | 12 | 1.283 | 9.7% | 1.114 | 1.439 | 12 | 0 |
| | S500 | 13 | 1.281 | 9.1% | 1.114 | 1.416 | 13 | 0 |
| | S690 | 60 | 1.358 | 9.4% | 1.088 | 1.723 | 59 | 0 |
| Proposal for General case | All | 85 | 1.218 | 7.2% | 1.055 | 1.591 | 73 | 0 |
| | S460 | 12 | 1.193 | 7.1% | 1.080 | 1.302 | 9 | 0 |
| | S500 | 13 | 1.187 | 6.5% | 1.080 | 1.290 | 10 | 0 |
| | S690 | 60 | 1.230 | 7.2% | 1.055 | 1.591 | 54 | 0 |
| Special case | All | 85 | 1.055 | 7.0% | 0.950 | 1.386 | 26 | 5 |
| | S460 | 12 | 1.018 | 4.0% | 0.968 | 1.083 | 0 | 1 |
| | S500 | 13 | 1.013 | 3.9% | 0.950 | 1.088 | 0 | 2 |
| | S690 | 60 | 1.072 | 7.3% | 0.953 | 1.386 | 26 | 2 |
| New EC3 case | All | 85 | 1.074 | 7.9% | 0.950 | 1.433 | 39 | 6 |
| | S460 | 12 | 1.017 | 5.8% | 0.956 | 1.121 | 2 | 2 |
| | S500 | 13 | 1.018 | 5.8% | 0.950 | 1.128 | 2 | 2 |
| | S690 | 60 | 1.098 | 7.5% | 0.952 | 1.433 | 35 | 2 |
| Proposal for New EC3 case | All | 85 | 1.036 | 7.2% | 0.911 | 1.392 | 11 | 15 |
| | S460 | 12 | 0.991 | 5.0% | 0.911 | 1.073 | 0 | 4 |
| | S500 | 13 | 0.991 | 5.0% | 0.925 | 1.085 | 0 | 5 |
| | S690 | 60 | 1.054 | 7.2% | 0.914 | 1.392 | 11 | 6 |

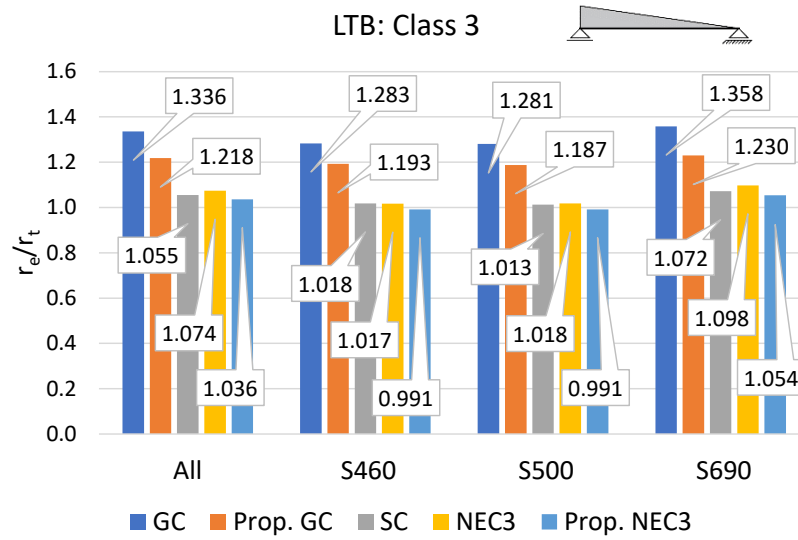


Figure B.7 – Mean values for the ratio r_e/r_t for linear bending moment $\psi = 0$ – Class 3

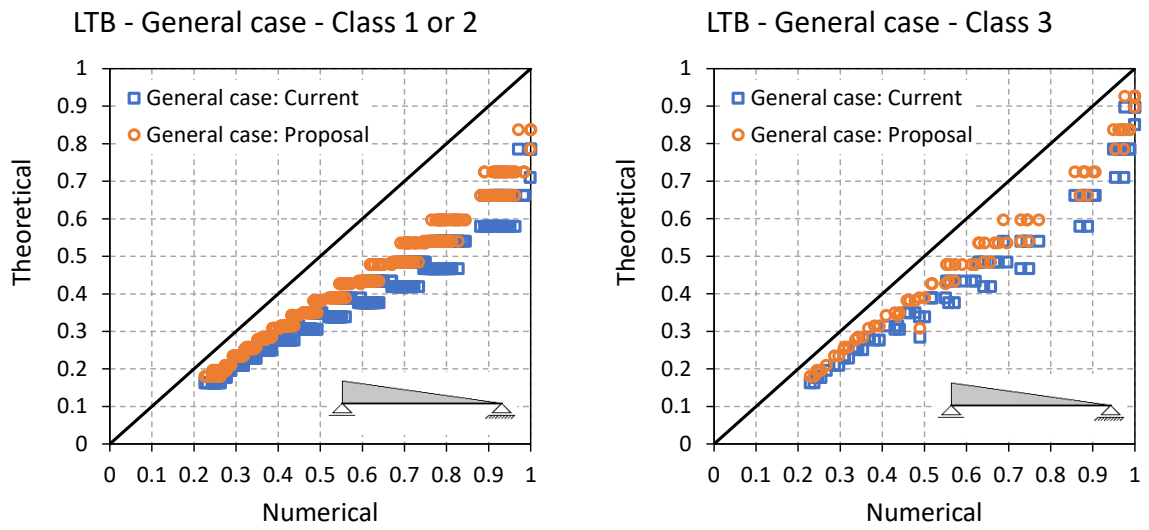


Figure B.8 – Scatter plots for LTB with linear bending moment $\psi = 0$ – General case

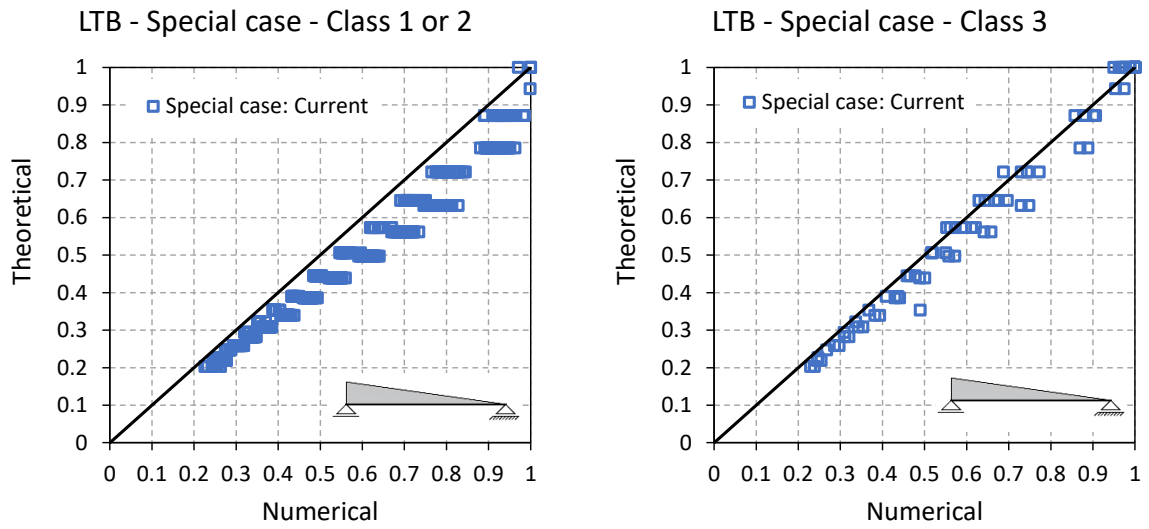


Figure B.9 – Scatter plots for LTB with linear bending moment $\psi = 0$ – Special case

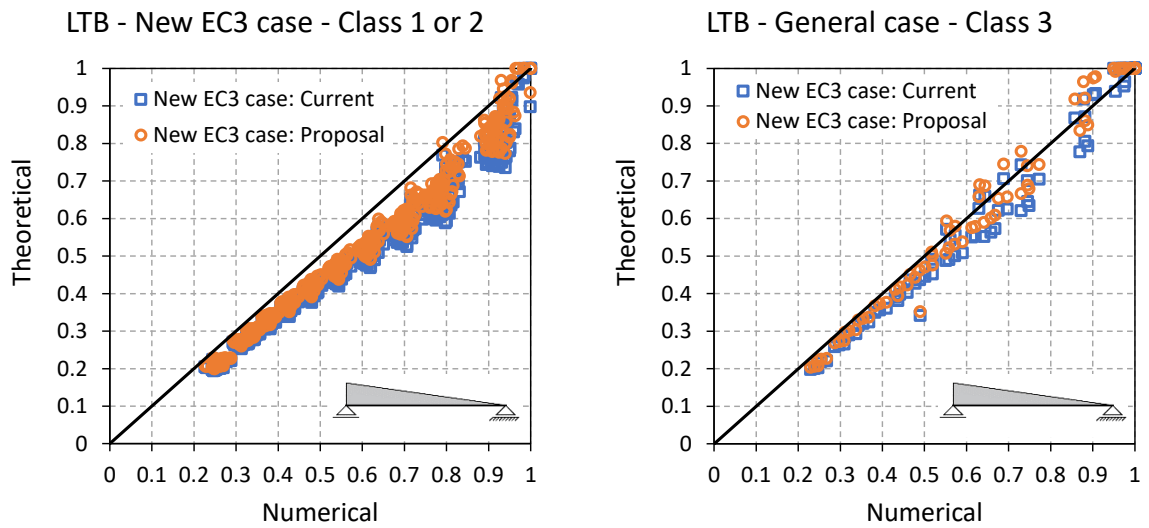


Figure B.10 – Scatter plots for LTB with linear bending moment $\psi = 0$ – New EC3 case

B.3 Linear bending moment – $\psi = -1$

Table B.5 – Statistical parameters: linear bending moment $\psi = -1$ – Class 1 or 2

| Design rule | Steel grade | n | mean | cov | min | max | >1.1 | <0.97 |
|---------------------------|-------------|-----|-------|-------|-------|-------|------|-------|
| General case | All | 557 | 1.474 | 10.2% | 1.126 | 1.719 | 557 | 0 |
| | S460 | 178 | 1.458 | 9.9% | 1.159 | 1.681 | 178 | 0 |
| | S500 | 193 | 1.474 | 10.2% | 1.148 | 1.718 | 193 | 0 |
| | S690 | 186 | 1.491 | 10.3% | 1.126 | 1.719 | 186 | 0 |
| Proposal for General case | All | 557 | 1.325 | 7.4% | 1.079 | 1.553 | 550 | 0 |
| | S460 | 178 | 1.310 | 7.0% | 1.123 | 1.514 | 178 | 0 |
| | S500 | 193 | 1.323 | 7.4% | 1.112 | 1.553 | 193 | 0 |
| | S690 | 186 | 1.339 | 7.7% | 1.079 | 1.525 | 179 | 0 |
| Special case | All | 557 | 1.114 | 8.4% | 0.968 | 1.380 | 272 | 2 |
| | S460 | 175 | 1.100 | 8.2% | 0.987 | 1.354 | 73 | 0 |
| | S500 | 193 | 1.112 | 8.5% | 0.994 | 1.380 | 49 | 0 |
| | S690 | 186 | 1.130 | 8.4% | 0.968 | 1.355 | 109 | 2 |
| New EC3 case | All | 557 | 1.131 | 6.7% | 0.968 | 1.370 | 350 | 2 |
| | S460 | 178 | 1.115 | 6.1% | 1.007 | 1.330 | 97 | 0 |
| | S500 | 193 | 1.128 | 6.5% | 1.010 | 1.370 | 118 | 0 |
| | S690 | 186 | 1.148 | 7.2% | 0.968 | 1.366 | 135 | 2 |
| Proposal for New EC3 case | All | 557 | 1.096 | 6.0% | 0.968 | 1.338 | 238 | 3 |
| | S460 | 178 | 1.080 | 5.4% | 0.968 | 1.300 | 57 | 1 |
| | S500 | 193 | 1.093 | 5.8% | 0.984 | 1.338 | 79 | 0 |
| | S690 | 186 | 1.115 | 6.4% | 0.968 | 1.331 | 102 | 2 |

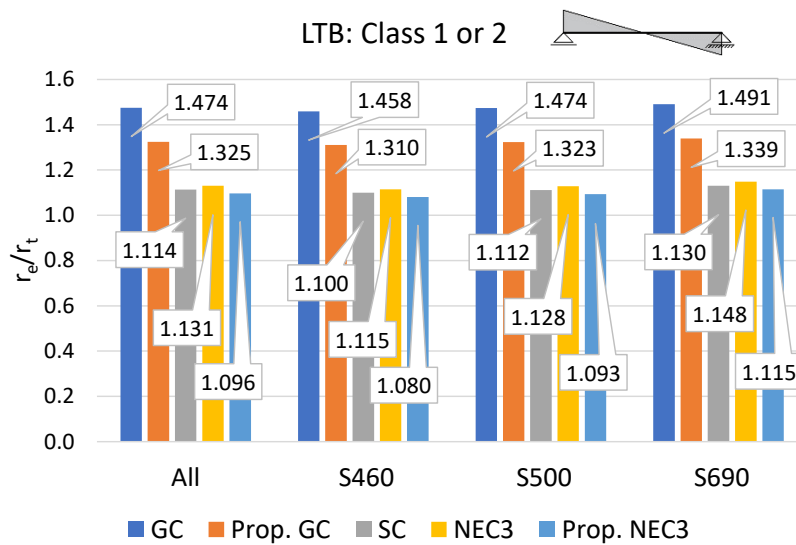

 Figure B.11 – Mean values for ratio r_e/r_t for linear bending moment $\psi = -1$ – Class 1 or 2

 Table B.6 – Statistical parameters: linear bending moment $\psi = -1$ – Class 3

| Design rule | Steel grade | n | mean | cov | min | max | >1.1 | <0.97 |
|---------------------------|-------------|----|-------|-------|-------|-------|------|-------|
| General case | All | 77 | 1.379 | 10.7% | 1.114 | 1.611 | 77 | 0 |
| | S460 | 8 | 1.254 | 10.7% | 1.114 | 1.450 | 8 | 0 |
| | S500 | 10 | 1.302 | 11.9% | 1.114 | 1.495 | 10 | 0 |
| | S690 | 59 | 1.409 | 9.7% | 1.114 | 1.611 | 59 | 0 |
| Proposal for General case | All | 77 | 1.257 | 7.9% | 1.080 | 1.456 | 65 | 0 |
| | S460 | 8 | 1.179 | 8.0% | 1.080 | 1.311 | 5 | 0 |
| | S500 | 10 | 1.215 | 9.2% | 1.080 | 1.352 | 7 | 0 |
| | S690 | 59 | 1.275 | 7.2% | 1.080 | 1.456 | 53 | 0 |
| Special case | All | 77 | 1.057 | 8.7% | 0.955 | 1.294 | 19 | 3 |
| | S460 | 8 | 0.999 | 0.4% | 0.989 | 1.001 | 0 | 0 |
| | S500 | 10 | 1.007 | 1.6% | 0.995 | 1.042 | 0 | 0 |
| | S690 | 59 | 1.073 | 9.3% | 0.955 | 1.294 | 19 | 3 |
| New EC3 case | All | 77 | 1.078 | 7.0% | 0.984 | 1.270 | 29 | 0 |
| | S460 | 8 | 1.015 | 2.7% | 1.000 | 1.065 | 0 | 0 |
| | S500 | 10 | 1.030 | 4.5% | 1.000 | 1.112 | 2 | 0 |
| | S690 | 59 | 1.095 | 6.9% | 0.984 | 1.270 | 27 | 0 |
| Proposal for New EC3 case | All | 77 | 1.046 | 6.3% | 0.942 | 1.244 | 15 | 3 |
| | S460 | 8 | 1.002 | 0.5% | 1.000 | 1.015 | 0 | 0 |
| | S500 | 10 | 1.011 | 2.7% | 0.976 | 1.065 | 0 | 0 |
| | S690 | 59 | 1.058 | 6.7% | 0.942 | 1.244 | 15 | 3 |

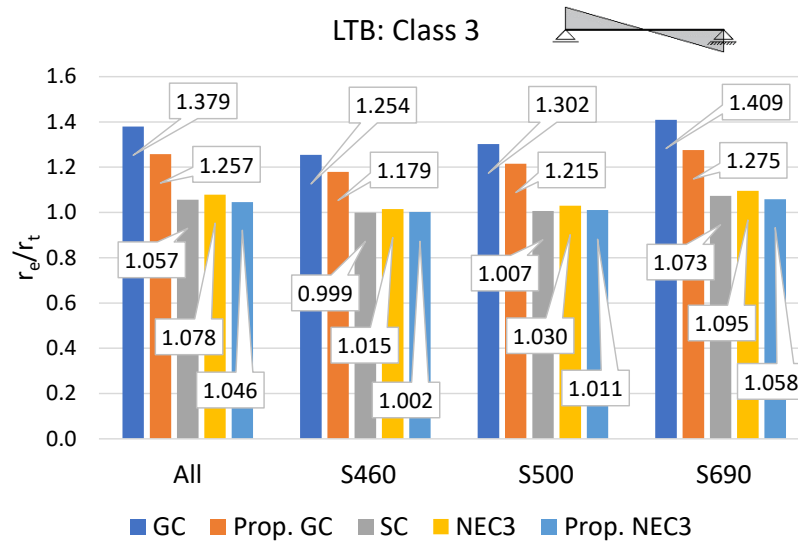


Figure B.12 – Mean values for ratio r_e/r_t for linear bending moment $\psi = -1$ – Class 3

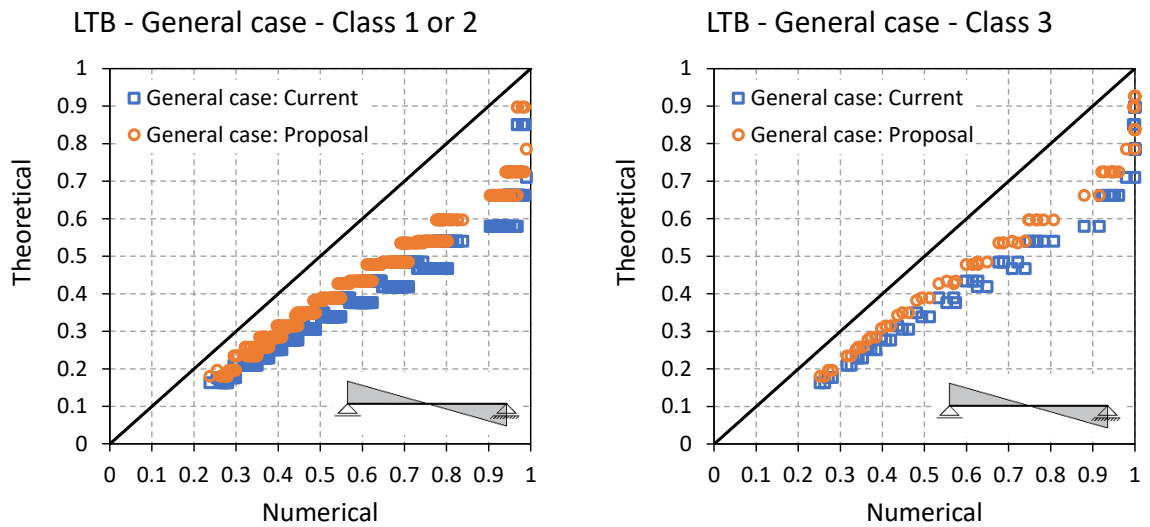


Figure B.13 – Scatter plots for LTB with linear bending moment $\psi = -1$ – General case

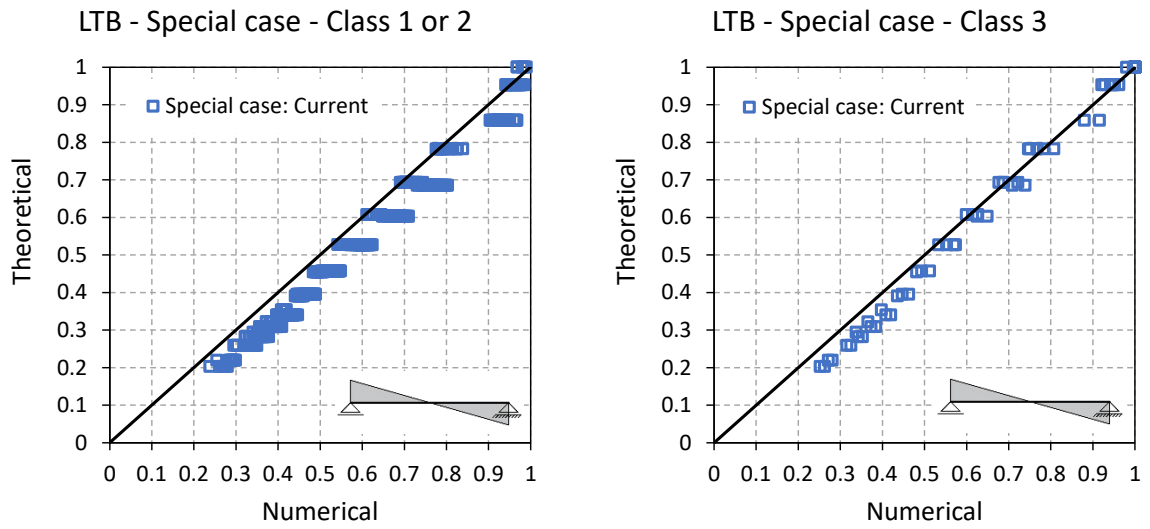


Figure B.14 – Scatter plots for LTB with linear bending moment $\psi = -1$ – Special case

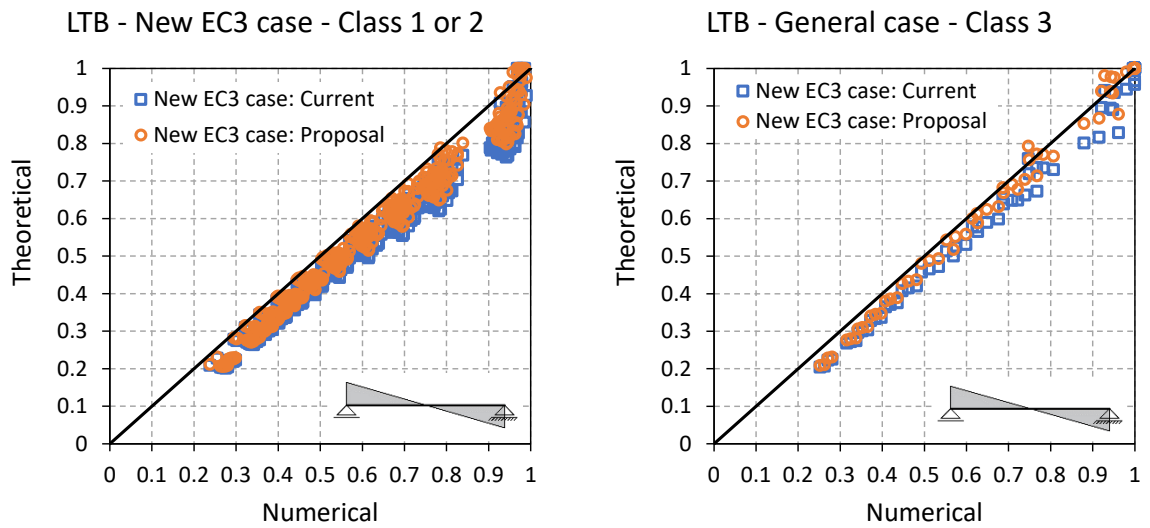


Figure B.15 – Scatter plots for LTB with linear bending moment $\psi = -1$ – New EC3 case

B.4 Uniform distributed load – applied in the middle of the web

Table B.7 – Statistical parameters: uniform distributed load (center) – Class 1 or 2

| Design rule | Steel grade | n | mean | cov | min | max | >1.1 | <0.97 |
|---------------------------|-------------|-----|-------|------|-------|-------|------|-------|
| General case | All | 715 | 1.373 | 7.4% | 1.084 | 1.618 | 711 | 0 |
| | S460 | 249 | 1.355 | 7.2% | 1.094 | 1.563 | 248 | 0 |
| | S500 | 256 | 1.364 | 7.4% | 1.084 | 1.576 | 254 | 0 |
| | S690 | 210 | 1.404 | 6.9% | 1.098 | 1.618 | 209 | 0 |
| Proposal for General case | All | 715 | 1.230 | 6.0% | 1.017 | 1.468 | 671 | 0 |
| | S460 | 249 | 1.214 | 5.7% | 1.019 | 1.380 | 229 | 0 |
| | S500 | 256 | 1.223 | 6.0% | 1.017 | 1.391 | 237 | 0 |
| | S690 | 210 | 1.258 | 5.7% | 1.030 | 1.468 | 205 | 0 |
| Special case | All | 715 | 1.118 | 6.7% | 0.934 | 1.310 | 434 | 18 |
| | S460 | 249 | 1.104 | 6.4% | 0.937 | 1.265 | 140 | 7 |
| | S500 | 256 | 1.111 | 6.7% | 0.934 | 1.276 | 150 | 10 |
| | S690 | 210 | 1.142 | 6.4% | 0.946 | 1.310 | 144 | 1 |
| New EC3 case | All | 715 | 1.186 | 5.4% | 1.005 | 1.336 | 632 | 0 |
| | S460 | 249 | 1.166 | 4.9% | 1.005 | 1.276 | 214 | 0 |
| | S500 | 256 | 1.180 | 5.2% | 1.014 | 1.300 | 221 | 0 |
| | S690 | 210 | 1.217 | 5.3% | 1.029 | 1.336 | 197 | 0 |
| Proposal for New EC3 case | All | 715 | 1.133 | 5.3% | 0.972 | 1.274 | 549 | 0 |
| | S460 | 249 | 1.113 | 4.8% | 0.972 | 1.214 | 174 | 0 |
| | S500 | 256 | 1.127 | 5.1% | 0.985 | 1.235 | 189 | 0 |
| | S690 | 210 | 1.164 | 5.0% | 1.001 | 1.274 | 186 | 0 |

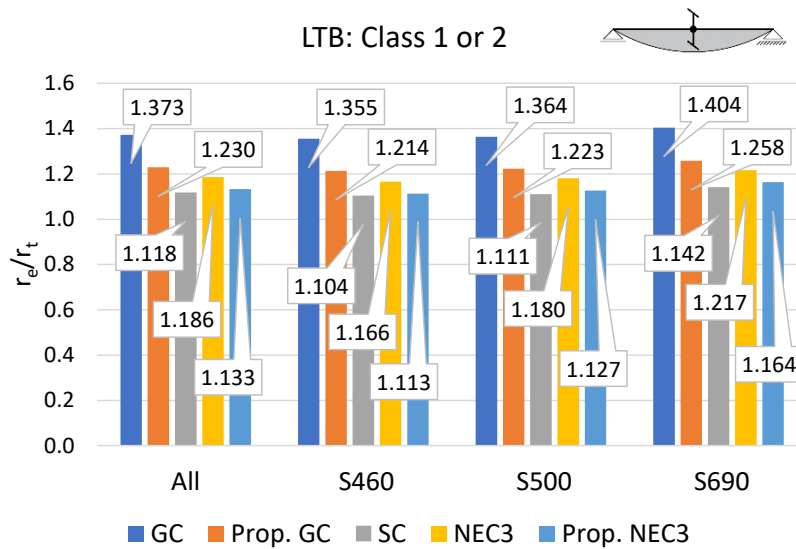

 Figure B.16 – Mean values for ratio r_e/r_t for uniform distributed load (center) – Class 1 or 2

Table B.8 – Statistical parameters: uniform distributed load (center) – Class 3

| Design rule | Steel grade | n | mean | cov | min | max | >1.1 | <0.97 |
|---------------------------|-------------|-----|-------|-------|-------|-------|------|-------|
| General case | All | 122 | 1.341 | 9.4% | 1.084 | 1.884 | 121 | 0 |
| | S460 | 18 | 1.281 | 7.0% | 1.120 | 1.422 | 18 | 0 |
| | S500 | 21 | 1.329 | 7.5% | 1.144 | 1.482 | 21 | 0 |
| | S690 | 83 | 1.358 | 10.0% | 1.084 | 1.884 | 82 | 0 |
| Proposal for General case | All | 122 | 1.219 | 9.4% | 1.017 | 1.765 | 111 | 0 |
| | S460 | 18 | 1.171 | 6.1% | 1.051 | 1.290 | 14 | 0 |
| | S500 | 21 | 1.215 | 6.7% | 1.074 | 1.350 | 19 | 0 |
| | S690 | 83 | 1.230 | 10.3% | 1.017 | 1.765 | 78 | 0 |
| Special case | All | 122 | 1.096 | 8.5% | 0.934 | 1.494 | 45 | 6 |
| | S460 | 18 | 1.056 | 5.1% | 0.965 | 1.151 | 4 | 2 |
| | S500 | 21 | 1.092 | 5.7% | 0.986 | 1.196 | 7 | 0 |
| | S690 | 83 | 1.106 | 9.3% | 0.934 | 1.494 | 34 | 4 |
| New EC3 case | All | 122 | 1.155 | 7.8% | 1.008 | 1.678 | 95 | 0 |
| | S460 | 18 | 1.088 | 4.5% | 1.019 | 1.154 | 9 | 0 |
| | S500 | 21 | 1.130 | 5.0% | 1.033 | 1.214 | 15 | 0 |
| | S690 | 83 | 1.176 | 8.1% | 1.008 | 1.678 | 71 | 0 |
| Proposal for New EC3 case | All | 122 | 1.098 | 8.1% | 0.957 | 1.631 | 42 | 2 |
| | S460 | 18 | 1.037 | 4.4% | 0.963 | 1.101 | 1 | 1 |
| | S500 | 21 | 1.077 | 5.0% | 0.997 | 1.164 | 9 | 0 |
| | S690 | 83 | 1.117 | 8.6% | 0.957 | 1.631 | 32 | 1 |

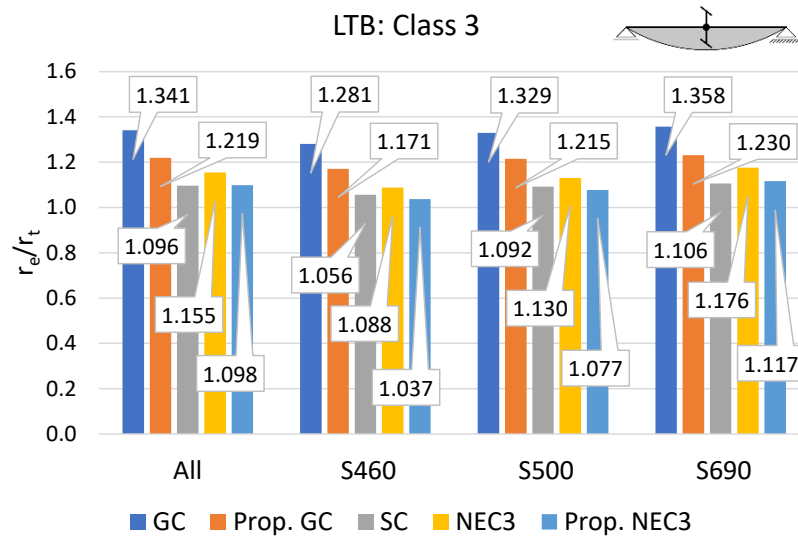


Figure B.17 – Mean values for ratio r_e/r_t for uniform distributed load (center) – Class 3

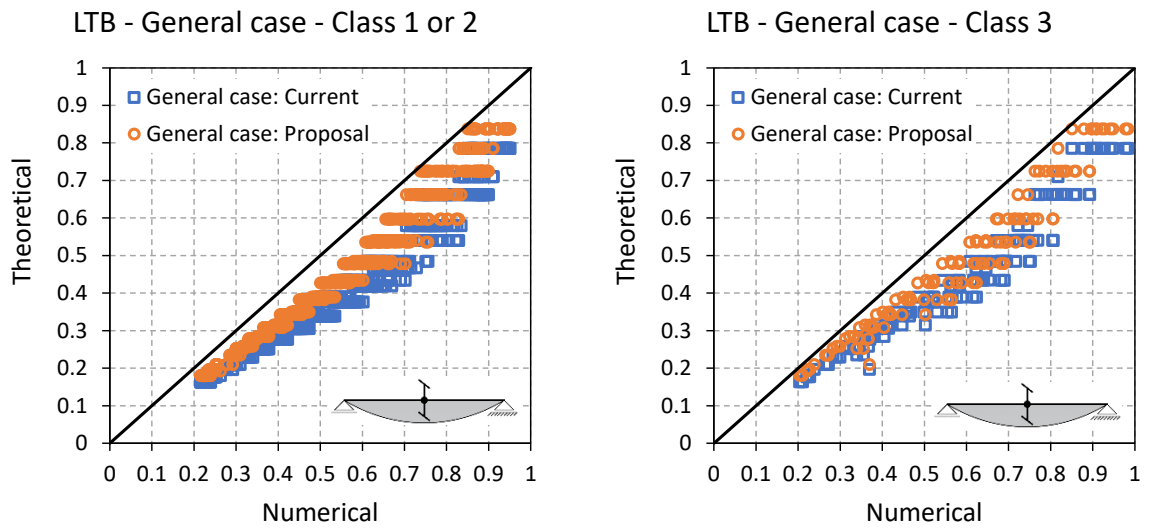


Figure B.18 – Scatter plots for LTB with uniform distributed load (center) – General case

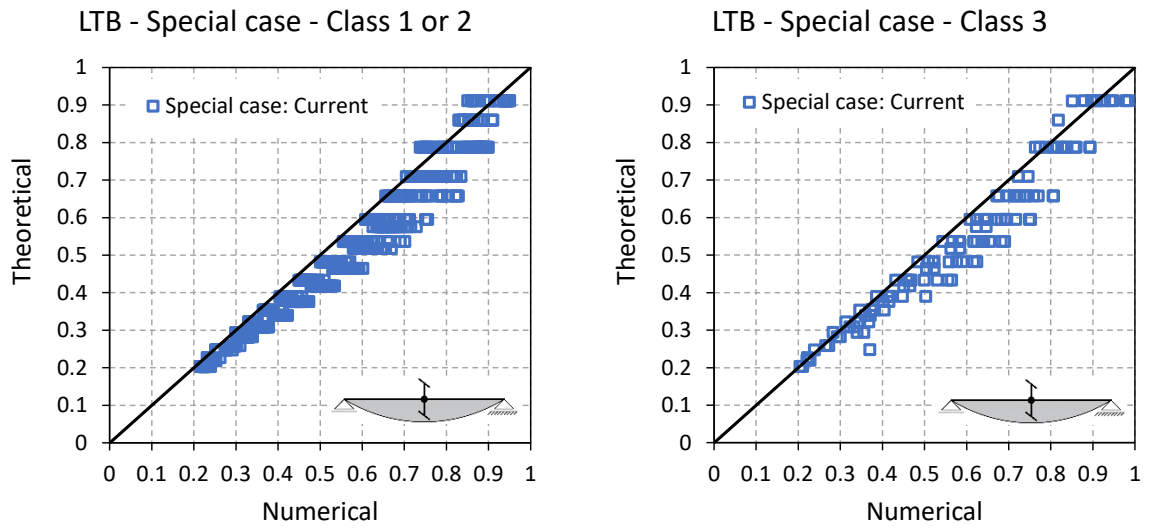


Figure B.19 – Scatter plots for LTB with uniform distributed load (center) – Special case

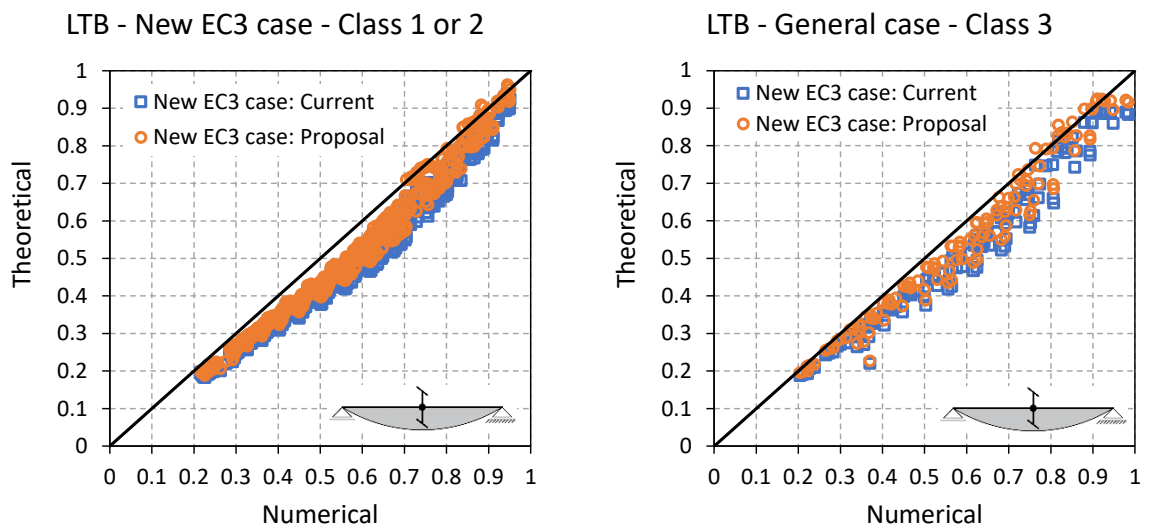


Figure B.20 – Scatter plots for LTB with uniform distributed load (center) – New EC3 case

B.5 Uniform distributed load – applied on the top flange and bottom flange

Table B.9 – Statistical parameters: uniform distributed load (top) – Class 1 or 2

| Design rule | Steel grade | n | mean | cov | min | max | >1.1 | <0.97 |
|---------------------------|-------------|-----|-------|------|-------|-------|------|-------|
| General case | All | 238 | 1.291 | 6.0% | 1.070 | 1.524 | 234 | 0 |
| | S460 | 93 | 1.287 | 6.2% | 1.087 | 1.507 | 91 | 0 |
| | S500 | 94 | 1.294 | 6.3% | 1.070 | 1.507 | 93 | 0 |
| | S690 | 51 | 1.293 | 5.2% | 1.095 | 1.524 | 50 | 0 |
| Proposal for General case | All | 238 | 1.169 | 5.4% | 0.959 | 1.379 | 208 | 1 |
| | S460 | 93 | 1.163 | 5.4% | 1.001 | 1.373 | 80 | 0 |
| | S500 | 94 | 1.170 | 5.5% | 1.004 | 1.373 | 81 | 0 |
| | S690 | 51 | 1.176 | 5.2% | 0.959 | 1.379 | 47 | 1 |
| Special case | All | 238 | 1.048 | 5.6% | 0.895 | 1.252 | 50 | 11 |
| | S460 | 93 | 1.045 | 5.7% | 0.921 | 1.216 | 20 | 5 |
| | S500 | 94 | 1.051 | 5.7% | 0.922 | 1.216 | 23 | 4 |
| | S690 | 51 | 1.048 | 5.1% | 0.895 | 1.252 | 7 | 2 |
| New EC3 case | All | 238 | 1.201 | 4.4% | 1.009 | 1.293 | 221 | 0 |
| | S460 | 93 | 1.189 | 4.2% | 1.009 | 1.243 | 85 | 0 |
| | S500 | 94 | 1.200 | 4.3% | 1.023 | 1.293 | 88 | 0 |
| | S690 | 51 | 1.223 | 4.7% | 1.012 | 1.282 | 48 | 0 |
| Proposal for New EC3 case | All | 238 | 1.129 | 4.3% | 0.935 | 1.260 | 194 | 1 |
| | S460 | 93 | 1.119 | 4.0% | 0.975 | 1.189 | 72 | 0 |
| | S500 | 94 | 1.129 | 4.2% | 0.988 | 1.260 | 78 | 0 |
| | S690 | 51 | 1.150 | 4.5% | 0.935 | 1.245 | 44 | 1 |

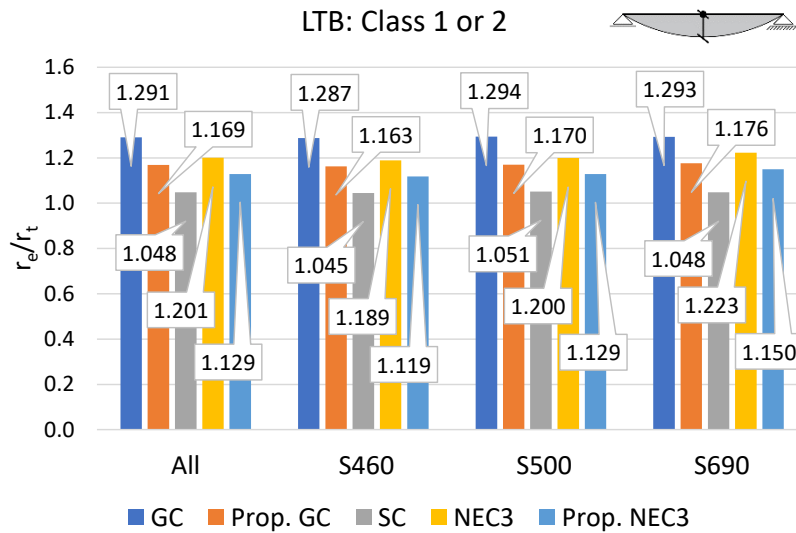

 Figure B.21 – Mean values for ratio r_e/r_t for uniform distributed load (top) – Class 1 or 2

Table B.10 – Statistical parameters: uniform distributed load (bottom) – Class 1 or 2

| Design rule | Steel grade | n | mean | cov | min | max | >1.1 | <0.97 |
|---------------------------|-------------|-----|-------|------|-------|-------|------|-------|
| General case | All | 245 | 1.352 | 7.3% | 1.103 | 1.543 | 245 | 0 |
| | S460 | 95 | 1.345 | 7.4% | 1.103 | 1.509 | 95 | 0 |
| | S500 | 95 | 1.354 | 7.4% | 1.106 | 1.521 | 95 | 0 |
| | S690 | 55 | 1.361 | 6.9% | 1.123 | 1.543 | 55 | 0 |
| Proposal for General case | All | 245 | 1.224 | 6.0% | 1.035 | 1.401 | 218 | 0 |
| | S460 | 95 | 1.215 | 6.0% | 1.035 | 1.353 | 84 | 0 |
| | S500 | 95 | 1.223 | 6.0% | 1.038 | 1.366 | 85 | 0 |
| | S690 | 55 | 1.240 | 6.0% | 1.054 | 1.401 | 49 | 0 |
| Special case | All | 245 | 1.100 | 6.4% | 0.951 | 1.267 | 112 | 9 |
| | S460 | 95 | 1.094 | 6.5% | 0.951 | 1.223 | 40 | 4 |
| | S500 | 95 | 1.101 | 6.5% | 0.954 | 1.233 | 41 | 3 |
| | S690 | 55 | 1.107 | 5.9% | 0.968 | 1.267 | 31 | 2 |
| New EC3 case | All | 245 | 1.173 | 5.5% | 1.000 | 1.325 | 203 | 0 |
| | S460 | 95 | 1.160 | 5.2% | 1.000 | 1.218 | 77 | 0 |
| | S500 | 95 | 1.170 | 5.3% | 1.007 | 1.228 | 77 | 0 |
| | S690 | 55 | 1.200 | 5.8% | 1.022 | 1.325 | 49 | 0 |
| Proposal for New EC3 case | All | 245 | 1.115 | 5.6% | 0.969 | 1.293 | 181 | 1 |
| | S460 | 95 | 1.103 | 5.4% | 0.969 | 1.172 | 68 | 1 |
| | S500 | 95 | 1.112 | 5.4% | 0.980 | 1.171 | 69 | 0 |
| | S690 | 55 | 1.141 | 5.8% | 0.976 | 1.293 | 44 | 0 |

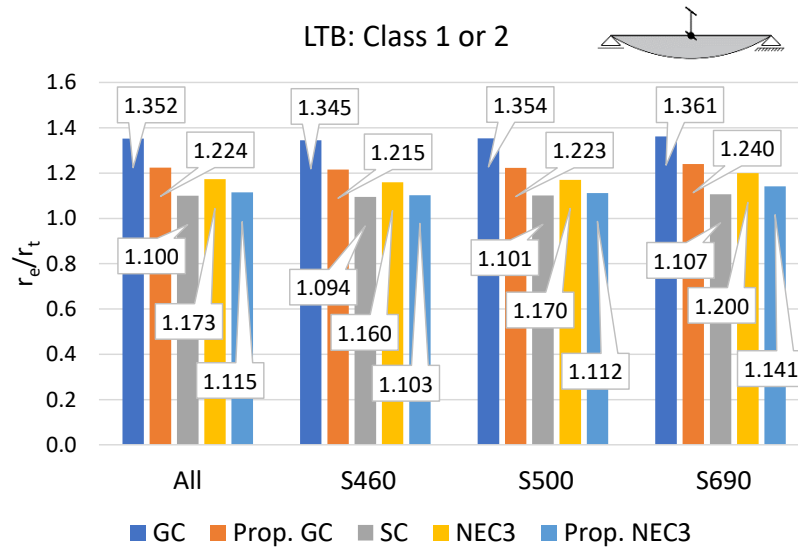


Figure B.22 – Mean values for ratio r_e/r_t for uniform distributed load (bottom) – Class 1 or 2

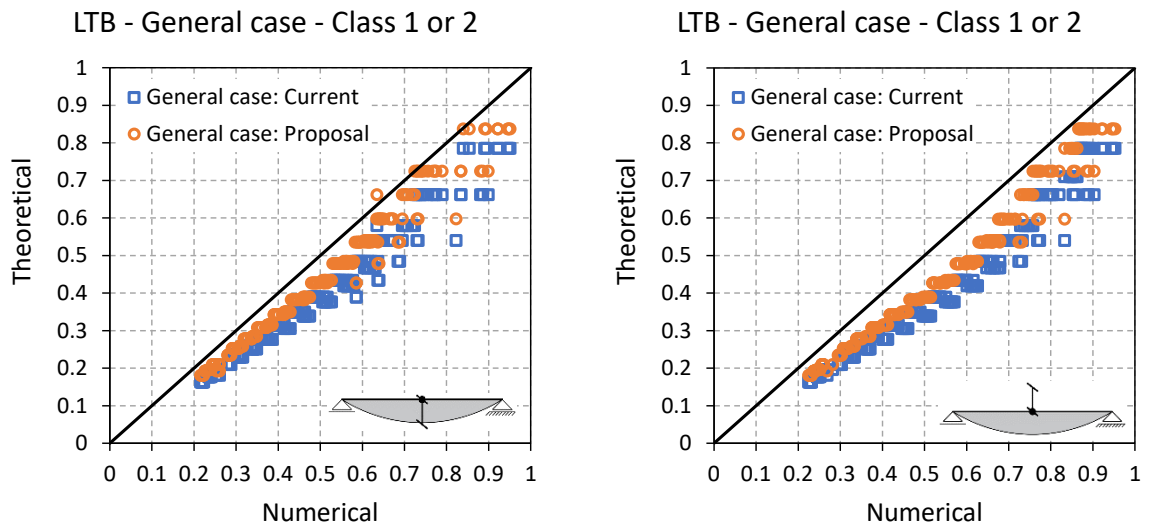


Figure B.23 – Scatter plots for LTB with uniform distributed load (load applied at top and bottom flange) – General case

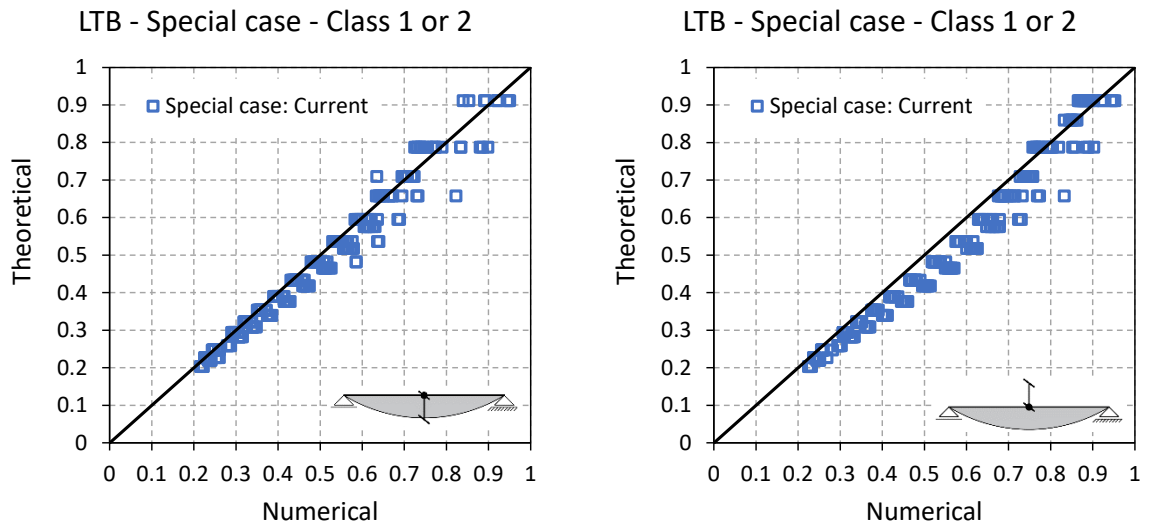


Figure B.24 – Scatter plots for LTB with uniform distributed load (load applied at top and bottom flange) – Special case

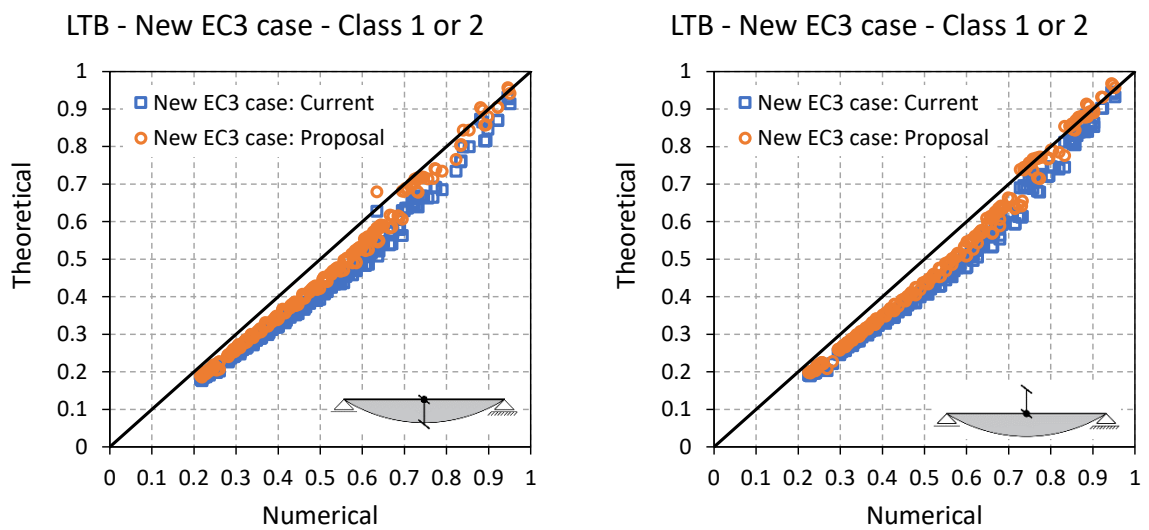


Figure B.25 – Scatter plots for LTB with uniform distributed load (load applied at top and bottom flange) – New EC3 case

B.6 Concentrated load at L/2 – applied in the middle of the web

Table B.11 – Statistical parameters: concentrated load (center) – Class 1 or 2

| Design rule | Steel grade | n | mean | cov | min | max | >1.1 | <0.97 |
|---------------------------|-------------|-----|-------|------|-------|-------|------|-------|
| General case | All | 607 | 1.405 | 6.3% | 1.139 | 1.626 | 607 | 0 |
| | S460 | 204 | 1.392 | 6.1% | 1.140 | 1.587 | 204 | 0 |
| | S500 | 216 | 1.402 | 6.2% | 1.149 | 1.599 | 216 | 0 |
| | S690 | 187 | 1.423 | 6.4% | 1.139 | 1.626 | 187 | 0 |
| Proposal for General case | All | 607 | 1.254 | 4.8% | 1.041 | 1.454 | 594 | 0 |
| | S460 | 204 | 1.241 | 4.5% | 1.042 | 1.373 | 199 | 0 |
| | S500 | 216 | 1.252 | 4.6% | 1.050 | 1.384 | 212 | 0 |
| | S690 | 187 | 1.272 | 5.1% | 1.041 | 1.454 | 183 | 0 |
| Special case | All | 607 | 1.121 | 6.2% | 0.918 | 1.272 | 382 | 12 |
| | S460 | 204 | 1.110 | 6.1% | 0.919 | 1.245 | 117 | 4 |
| | S500 | 216 | 1.118 | 6.1% | 0.927 | 1.255 | 137 | 5 |
| | S690 | 187 | 1.136 | 6.3% | 0.918 | 1.272 | 128 | 3 |
| New EC3 case | All | 607 | 1.172 | 4.4% | 1.032 | 1.307 | 554 | 0 |
| | S460 | 204 | 1.156 | 3.8% | 1.038 | 1.250 | 185 | 0 |
| | S500 | 216 | 1.169 | 4.0% | 1.032 | 1.277 | 197 | 0 |
| | S690 | 187 | 1.193 | 4.7% | 1.032 | 1.307 | 172 | 0 |
| Proposal for New EC3 case | All | 607 | 1.122 | 4.3% | 0.969 | 1.246 | 446 | 1 |
| | S460 | 204 | 1.106 | 3.7% | 0.969 | 1.191 | 133 | 1 |
| | S500 | 216 | 1.118 | 3.9% | 0.984 | 1.216 | 153 | 0 |
| | S690 | 187 | 1.144 | 4.5% | 0.975 | 1.246 | 160 | 0 |

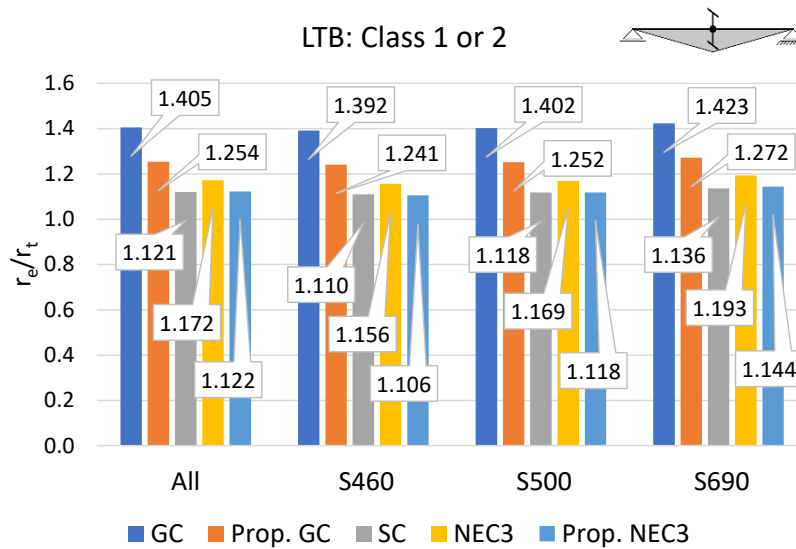

 Figure B.26 – Mean values for ratio r_e/r_t for concentrated load (center) – Class 1 or 2

Table B.12 – Statistical parameters: concentrated load (center) – Class 3

| Design rule | Steel grade | n | mean | cov | min | max | >1.1 | <0.97 |
|---------------------------|-------------|----|-------|------|-------|-------|------|-------|
| General case | All | 90 | 1.365 | 7.2% | 1.151 | 1.620 | 90 | 0 |
| | S460 | 11 | 1.333 | 4.1% | 1.231 | 1.422 | 11 | 0 |
| | S500 | 12 | 1.366 | 4.0% | 1.256 | 1.464 | 12 | 0 |
| | S690 | 67 | 1.369 | 8.0% | 1.151 | 1.620 | 67 | 0 |
| Proposal for General case | All | 90 | 1.234 | 7.3% | 1.052 | 1.470 | 88 | 0 |
| | S460 | 11 | 1.212 | 3.8% | 1.125 | 1.286 | 11 | 0 |
| | S500 | 12 | 1.242 | 3.7% | 1.148 | 1.324 | 12 | 0 |
| | S690 | 67 | 1.236 | 8.2% | 1.052 | 1.470 | 65 | 0 |
| Special case | All | 90 | 1.086 | 6.8% | 0.928 | 1.275 | 32 | 2 |
| | S460 | 11 | 1.059 | 3.6% | 0.992 | 1.119 | 2 | 0 |
| | S500 | 12 | 1.086 | 3.4% | 1.013 | 1.152 | 3 | 0 |
| | S690 | 67 | 1.091 | 7.5% | 0.928 | 1.275 | 27 | 2 |
| New EC3 case | All | 90 | 1.134 | 5.6% | 1.005 | 1.302 | 63 | 0 |
| | S460 | 11 | 1.079 | 2.7% | 1.034 | 1.110 | 4 | 0 |
| | S500 | 12 | 1.115 | 3.1% | 1.058 | 1.150 | 9 | 0 |
| | S690 | 67 | 1.146 | 5.8% | 1.005 | 1.302 | 50 | 0 |
| Proposal for New EC3 case | All | 90 | 1.078 | 6.0% | 0.938 | 1.250 | 20 | 1 |
| | S460 | 11 | 1.026 | 2.9% | 0.977 | 1.066 | 0 | 0 |
| | S500 | 12 | 1.061 | 3.4% | 1.000 | 1.107 | 1 | 0 |
| | S690 | 67 | 1.090 | 6.2% | 0.938 | 1.250 | 19 | 1 |

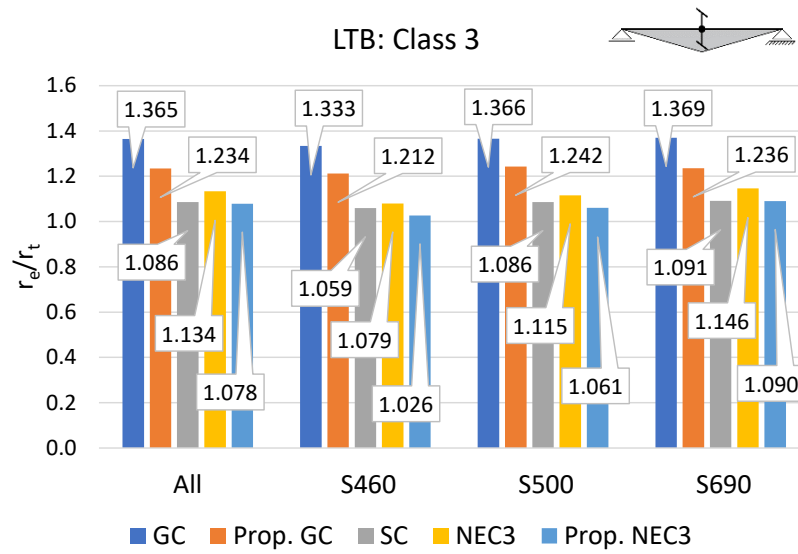


Figure B.27 – Mean values for ratio r_e/r_t for concentrated load (center) – Class 3

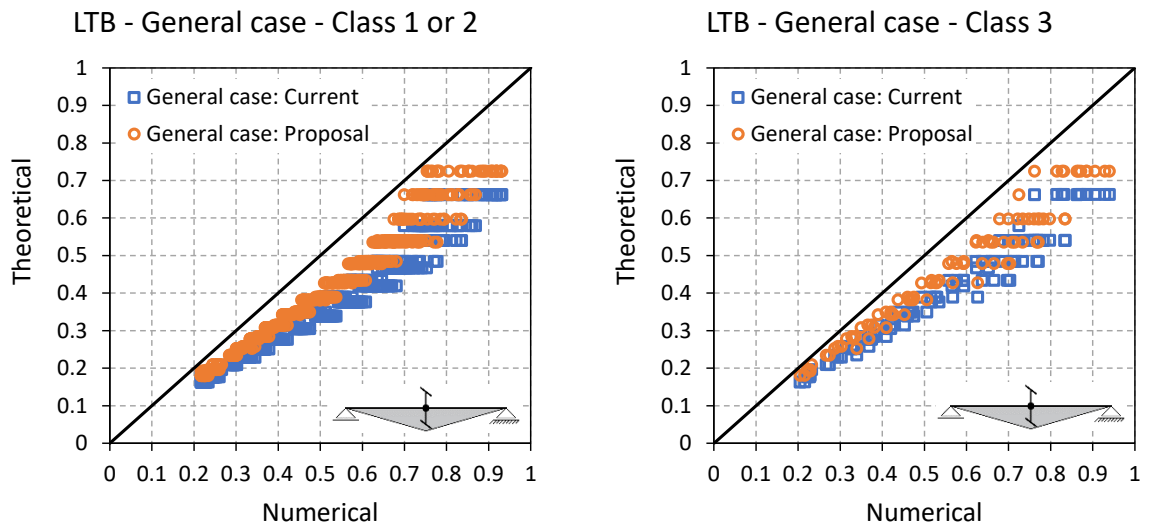


Figure B.28 – Scatter plots for LTB with concentrated load (center) – General case

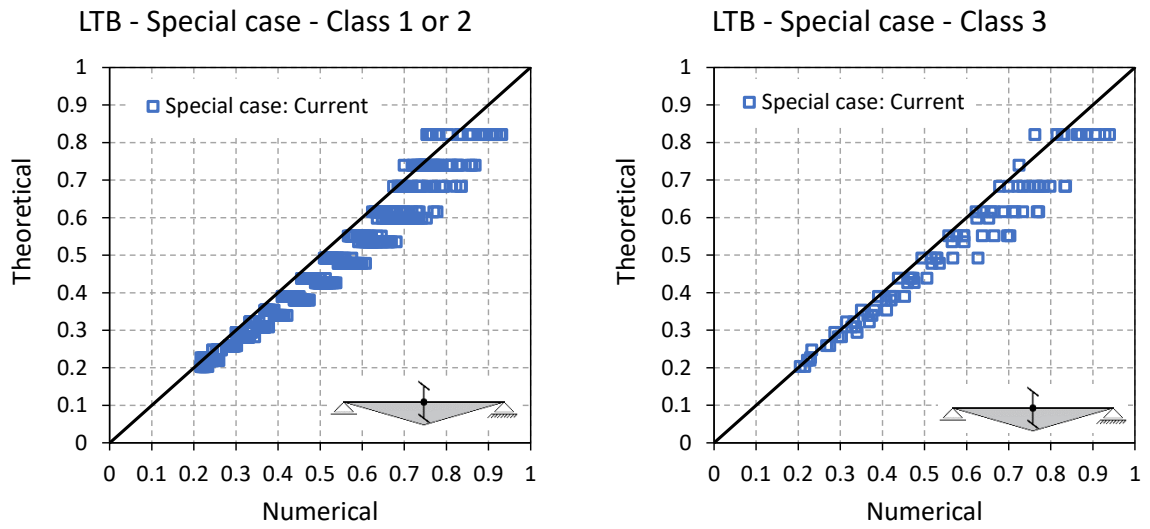


Figure B.29 – Scatter plots for LTB with concentrated load (center) – Special case

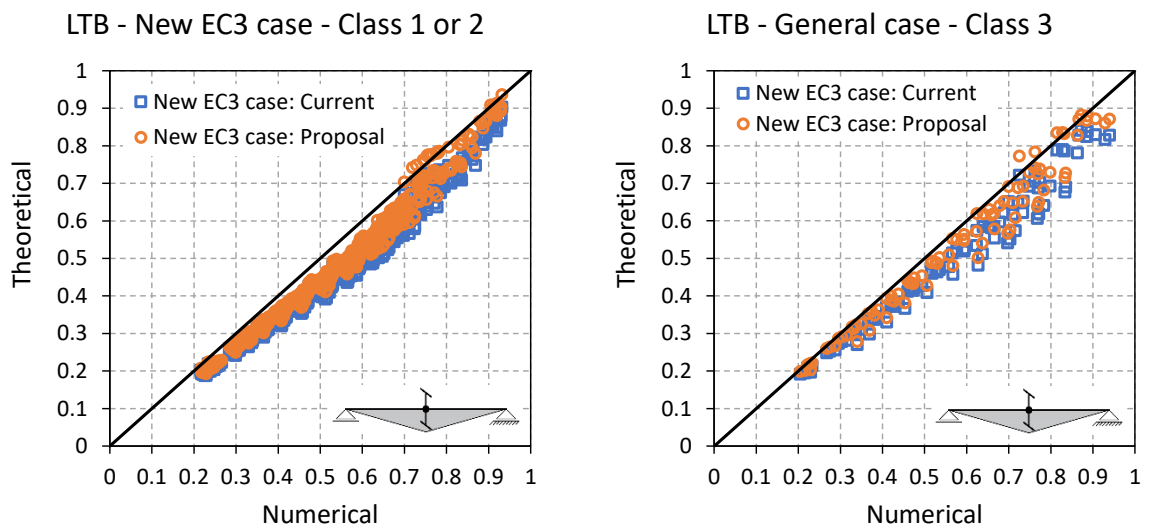


Figure B.30 – Scatter plots for LTB with concentrated load (center) – New EC3 case

Annex C – Members in bending and axial compression (beam-columns)

The results obtained for the different bending moment distributions considered in the parametric study for beam-columns (members subjected to lateral-torsional buckling and flexural buckling) are presented separately in this annex. The results are shown in terms of the numerical result (r_e) over the theoretical (r_t) design resistance according to Eurocode 3, using the general case and the new EC3 case for lateral-torsional buckling and the Eurocode 3 method for flexural buckling. Also, the statistical parameters for the ratio (r_e/r_t) are presented.

C.1 Constant bending moment – $\psi = 1$

- No restraints:

Table C.1 – Statistical parameters – beam-columns: constant bending moment $\psi = 1$ – no restraints

| Design rule | Steel grade | n | mean | cov | min | max | >1.1 | <0.97 |
|-----------------|-------------|-----|-------|-------|-------|-------|------|-------|
| FB and LTB | All | 960 | 1.301 | 11.9% | 1.059 | 1.806 | 877 | 0 |
| - General case: | S460 | 320 | 1.282 | 11.0% | 1.059 | 1.600 | 291 | 0 |
| Current | S500 | 320 | 1.296 | 11.7% | 1.061 | 1.698 | 295 | 0 |
| | S690 | 320 | 1.323 | 12.8% | 1.068 | 1.806 | 291 | 0 |
| FB and LTB | All | 960 | 1.185 | 9.4% | 1.025 | 1.566 | 675 | 0 |
| - General case: | S460 | 320 | 1.169 | 8.4% | 1.025 | 1.408 | 224 | 0 |
| Proposals | S500 | 320 | 1.181 | 9.1% | 1.025 | 1.475 | 224 | 0 |
| | S690 | 320 | 1.204 | 10.2% | 1.027 | 1.566 | 227 | 0 |
| FB and LTB | All | 960 | 1.255 | 10.6% | 1.057 | 1.597 | 826 | 0 |
| – New EC3 case: | S460 | 320 | 1.237 | 9.7% | 1.057 | 1.492 | 274 | 0 |
| Current | S500 | 320 | 1.251 | 10.4% | 1.060 | 1.530 | 279 | 0 |
| | S690 | 320 | 1.278 | 11.5% | 1.059 | 1.597 | 273 | 0 |
| FB and LTB | All | 960 | 1.164 | 8.6% | 0.998 | 1.492 | 660 | 0 |
| – New EC3 case: | S460 | 320 | 1.148 | 7.6% | 0.998 | 1.357 | 219 | 0 |
| Proposals | S500 | 320 | 1.160 | 8.3% | 1.006 | 1.411 | 219 | 0 |
| | S690 | 320 | 1.184 | 9.4% | 1.011 | 1.492 | 222 | 0 |

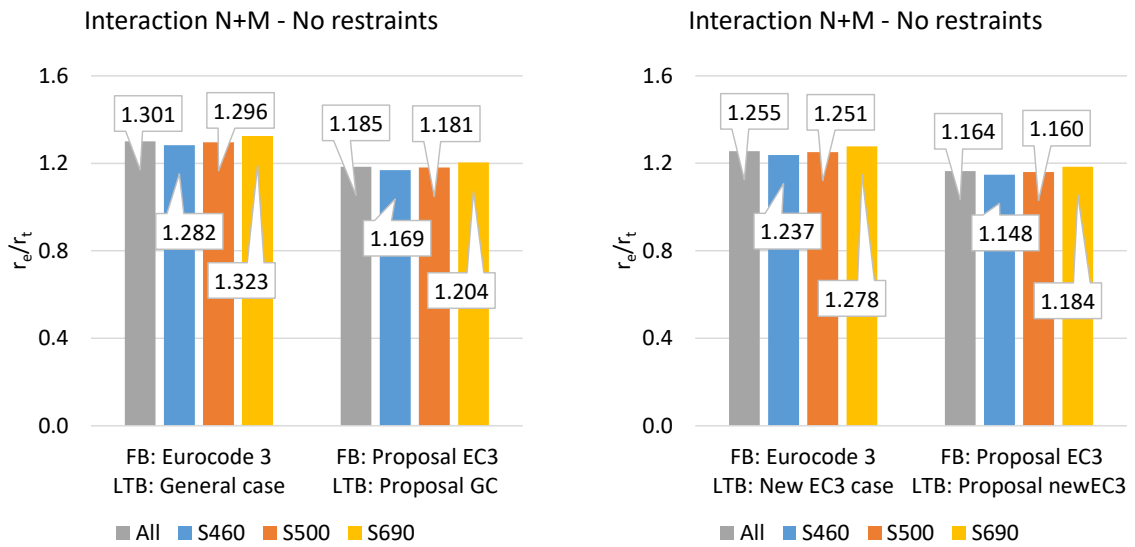
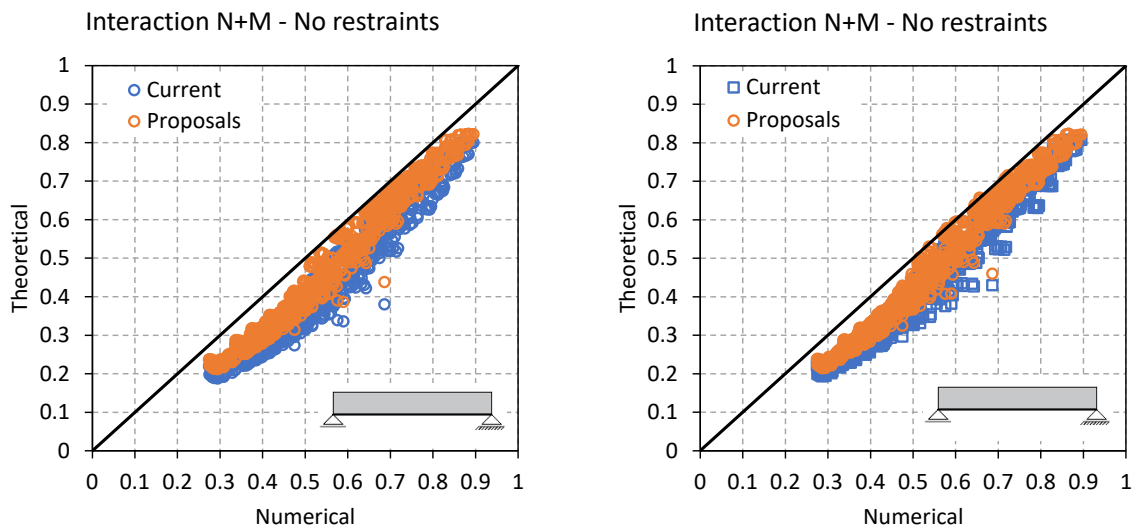


Figure C.1 – Mean values for ratio r_e/r_t for constant bending moment $\psi = 1$



a) FB: χ_y and χ_z – Eurocode 3

b) FB: χ_y and χ_z – Eurocode 3

LTB: χ_{LT} – General case

LTB: χ_{LT} – New EC3 case

Figure C.2 - Scatter plots – beam-columns: constant bending moment – $\psi = 1$

- **Minor axis (z-z) restrained:**

Table C.2 – Statistical parameters – beam-columns: constant bending moment $\psi = 1$ – minor axis restrained

| Design rule | Steel grade | n | mean | cov | min | max | >1.1 | <0.97 |
|-----------------------|-------------|-----|-------|------|-------|-------|------|-------|
| FB (y-y): Current | All | 288 | 1.069 | 3.0% | 1.000 | 1.205 | 39 | 0 |
| | S460 | 96 | 1.064 | 2.7% | 1.000 | 1.149 | 9 | 0 |
| | S500 | 96 | 1.068 | 2.9% | 1.001 | 1.169 | 11 | 0 |
| | S690 | 96 | 1.074 | 3.2% | 1.006 | 1.205 | 19 | 0 |
| FB (y-y): Proposal | All | 288 | 1.049 | 2.8% | 0.978 | 1.143 | 14 | 0 |
| | S460 | 96 | 1.045 | 2.8% | 0.978 | 1.123 | 3 | 0 |
| | S500 | 96 | 1.048 | 2.7% | 0.991 | 1.125 | 3 | 0 |
| | S690 | 96 | 1.055 | 2.8% | 1.003 | 1.143 | 8 | 0 |

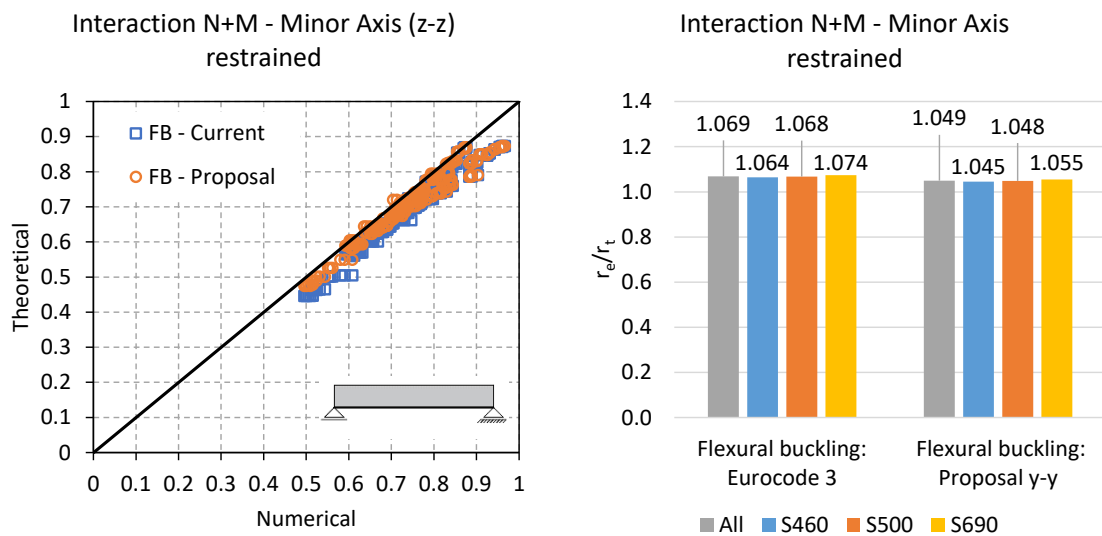


Figure C.3 – Scatter plots and mean values: constant bending moment – $\psi = 1$

C.2 Linear bending moment – $\psi = 0$

- No restraints:

Table C.3 – Statistical parameters – beam-columns: linear bending moment $\psi = 0$ – no restraints

| Design rule | Steel grade | n | mean | cov | min | max | >1.1 | <0.97 |
|-----------------|-------------|-----|-------|-------|-------|-------|------|-------|
| FB and LTB | All | 960 | 1.390 | 10.9% | 1.057 | 1.792 | 958 | 0 |
| - General case: | S460 | 320 | 1.374 | 10.3% | 1.101 | 1.737 | 320 | 0 |
| Current | S500 | 320 | 1.386 | 10.7% | 1.105 | 1.759 | 320 | 0 |
| | S690 | 320 | 1.410 | 11.6% | 1.057 | 1.792 | 318 | 0 |
| FB and LTB | All | 960 | 1.277 | 8.3% | 1.043 | 1.569 | 938 | 0 |
| - General case: | S460 | 320 | 1.263 | 7.8% | 1.070 | 1.534 | 311 | 0 |
| Proposals | S500 | 320 | 1.273 | 8.1% | 1.073 | 1.552 | 314 | 0 |
| | S690 | 320 | 1.293 | 8.9% | 1.043 | 1.569 | 313 | 0 |
| FB and LTB | All | 960 | 1.296 | 9.1% | 1.026 | 1.578 | 956 | 0 |
| – New EC3 case: | S460 | 320 | 1.283 | 8.3% | 1.096 | 1.508 | 319 | 0 |
| Current | S500 | 320 | 1.293 | 8.8% | 1.100 | 1.531 | 320 | 0 |
| | S690 | 320 | 1.313 | 9.8% | 1.026 | 1.578 | 317 | 0 |
| FB and LTB | All | 960 | 1.208 | 6.4% | 1.022 | 1.416 | 924 | 0 |
| – New EC3 case: | S460 | 320 | 1.196 | 5.8% | 1.066 | 1.362 | 306 | 0 |
| Proposals | S500 | 320 | 1.205 | 6.1% | 1.070 | 1.387 | 308 | 0 |
| | S690 | 320 | 1.222 | 7.0% | 1.022 | 1.416 | 310 | 0 |

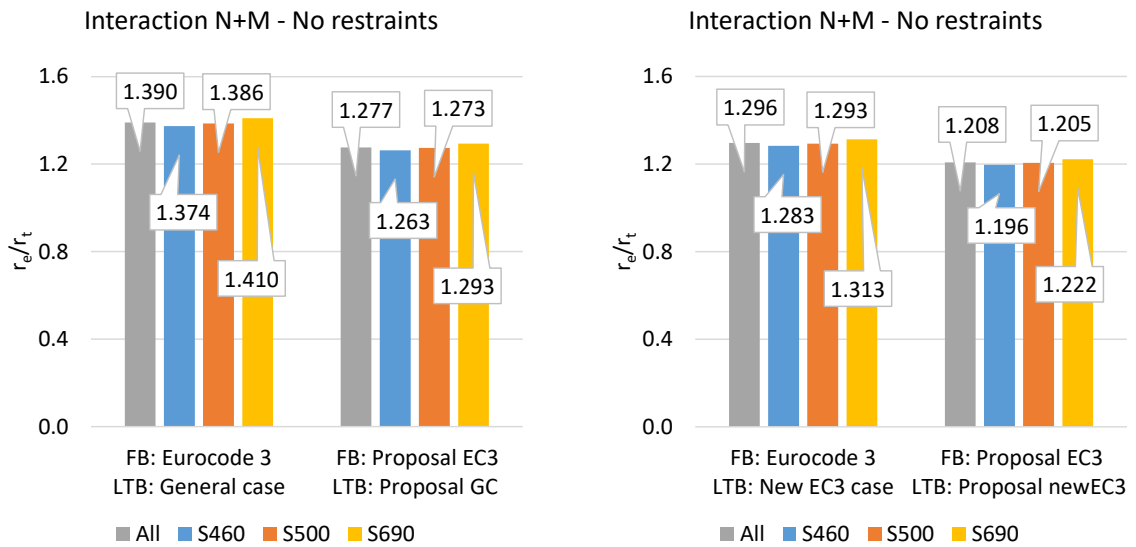
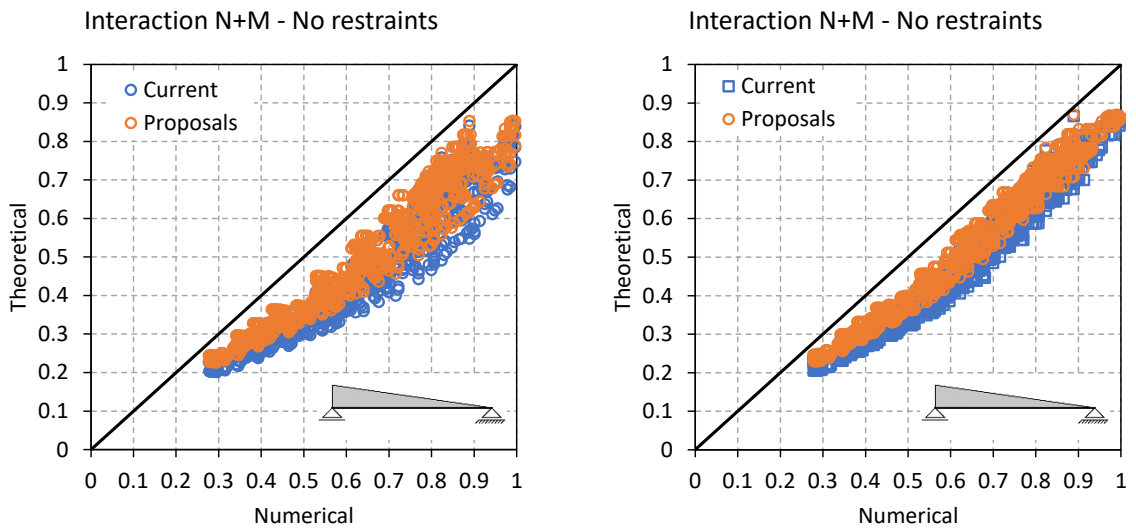


Figure C.4 – Mean values for ratio r_e/r_t for linear bending moment $\psi = 0$



a) FB: χ_y and χ_z – Eurocode 3

LTB: χ_{LT} – General case

Figure C.5 - Scatter plots – beam-columns: linear bending moment – $\psi = 0$

b) FB: χ_y and χ_z – Eurocode 3

LTB: χ_{LT} – New EC3 case

- **Minor axis (z-z) restrained:**

Table C.4 – Statistical parameters – beam-columns: linear bending moment $\psi = 0$ – minor axis restrained

| Design rule | Steel grade | n | mean | cov | min | max | >1.1 | <0.97 |
|-----------------------|-------------|-----|-------|------|-------|-------|------|-------|
| FB (y-y): Current | All | 280 | 1.054 | 4.2% | 0.982 | 1.257 | 28 | 0 |
| | S460 | 96 | 1.050 | 3.8% | 0.994 | 1.191 | 9 | 0 |
| | S500 | 96 | 1.053 | 4.1% | 0.994 | 1.217 | 10 | 0 |
| | S690 | 88 | 1.059 | 4.7% | 0.982 | 1.257 | 9 | 0 |
| FB (y-y): Proposal | All | 280 | 1.038 | 3.1% | 0.981 | 1.150 | 7 | 0 |
| | S460 | 96 | 1.035 | 3.0% | 0.981 | 1.101 | 1 | 0 |
| | S500 | 96 | 1.038 | 3.0% | 0.984 | 1.113 | 2 | 0 |
| | S690 | 88 | 1.041 | 3.3% | 0.982 | 1.150 | 4 | 0 |

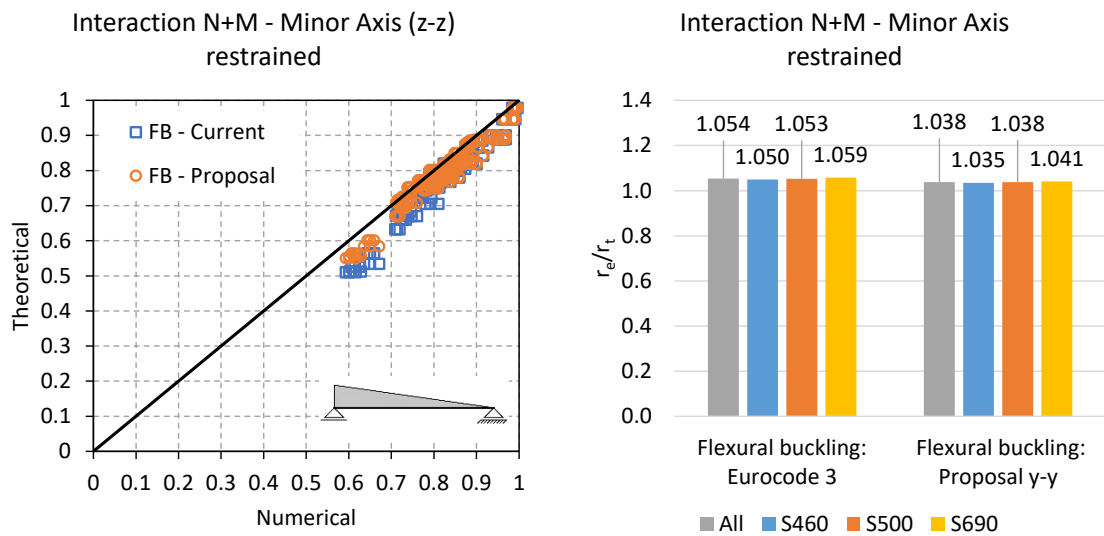


Figure C.6 – Scatter plots and mean values: linear bending moment – $\psi = 0$

C.3 Linear bending moment – $\psi = -1$

- No restraints:

Table C.5 – Statistical parameters – beam-columns: linear bending moment $\psi = -1$ – no restraints

| Design rule | Steel grade | n | mean | cov | min | max | >1.1 | <0.97 |
|-----------------|-------------|-----|-------|-------|-------|-------|------|-------|
| FB and LTB | All | 840 | 1.369 | 10.7% | 1.103 | 1.804 | 840 | 0 |
| - General case: | S460 | 280 | 1.351 | 10.0% | 1.125 | 1.775 | 280 | 0 |
| Current | S500 | 280 | 1.365 | 10.4% | 1.138 | 1.799 | 280 | 0 |
| | S690 | 280 | 1.392 | 11.3% | 1.103 | 1.804 | 280 | 0 |
| FB and LTB | All | 840 | 1.256 | 8.6% | 1.062 | 1.602 | 823 | 0 |
| - General case: | S460 | 280 | 1.240 | 8.1% | 1.062 | 1.581 | 273 | 0 |
| Proposals | S500 | 280 | 1.252 | 8.4% | 1.082 | 1.600 | 276 | 0 |
| | S690 | 280 | 1.275 | 9.1% | 1.086 | 1.602 | 274 | 0 |
| FB and LTB | All | 840 | 1.298 | 9.8% | 1.069 | 1.579 | 828 | 0 |
| – New EC3 case: | S460 | 280 | 1.282 | 8.9% | 1.096 | 1.506 | 279 | 0 |
| Current | S500 | 280 | 1.295 | 9.4% | 1.090 | 1.527 | 279 | 0 |
| | S690 | 280 | 1.316 | 10.7% | 1.069 | 1.579 | 270 | 0 |
| FB and LTB | All | 840 | 1.203 | 7.1% | 1.058 | 1.441 | 777 | 0 |
| – New EC3 case: | S460 | 280 | 1.190 | 6.3% | 1.058 | 1.389 | 260 | 0 |
| Proposals | S500 | 280 | 1.200 | 6.7% | 1.073 | 1.412 | 259 | 0 |
| | S690 | 280 | 1.219 | 7.9% | 1.062 | 1.441 | 258 | 0 |

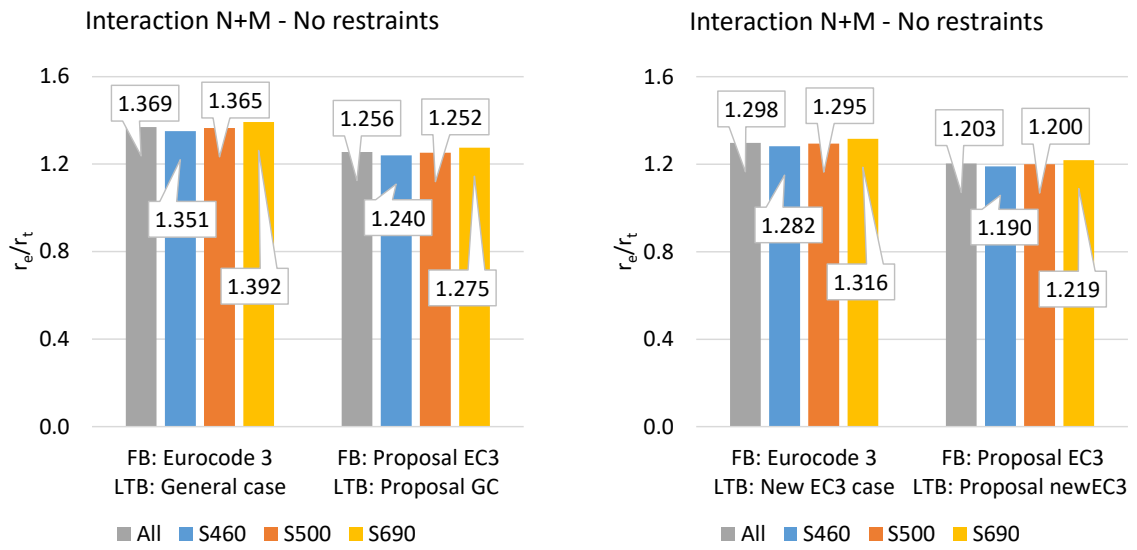
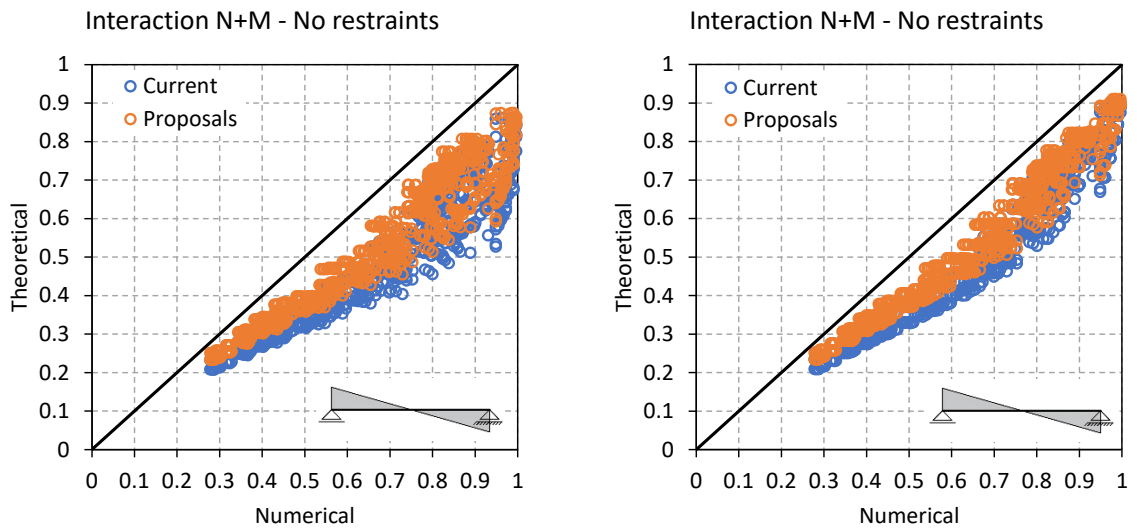


Figure C.7 – Mean values for ratio r_e/r_t for linear bending moment $\psi = -1$



a) FB: χ_y and χ_z – Eurocode 3

LTB: χ_{LT} – General case

b) FB: χ_y and χ_z – Eurocode 3

LTB: χ_{LT} – New EC3 case

Figure C.8 - Scatter plots – beam-columns: linear bending moment – $\psi = -1$

- **Minor axis (z-z) restrained:**

Table C.6 – Statistical parameters – beam-columns: linear bending moment $\psi = -1$ – minor axis restrained

| Design rule | Steel grade | n | mean | cov | min | max | >1.1 | <0.97 |
|-----------------------|-------------|-----|-------|------|-------|-------|------|-------|
| FB (y-y): Current | All | 270 | 1.080 | 5.8% | 1.006 | 1.388 | 50 | 0 |
| | S460 | 93 | 1.077 | 5.4% | 1.006 | 1.321 | 18 | 0 |
| | S500 | 91 | 1.080 | 5.7% | 1.012 | 1.343 | 17 | 0 |
| | S690 | 86 | 1.084 | 6.5% | 1.006 | 1.388 | 15 | 0 |
| FB (y-y): Proposal | All | 270 | 1.068 | 4.1% | 1.002 | 1.273 | 37 | 0 |
| | S460 | 93 | 1.066 | 3.8% | 1.002 | 1.218 | 13 | 0 |
| | S500 | 91 | 1.068 | 4.0% | 1.005 | 1.233 | 13 | 0 |
| | S690 | 86 | 1.071 | 4.5% | 1.006 | 1.273 | 11 | 0 |

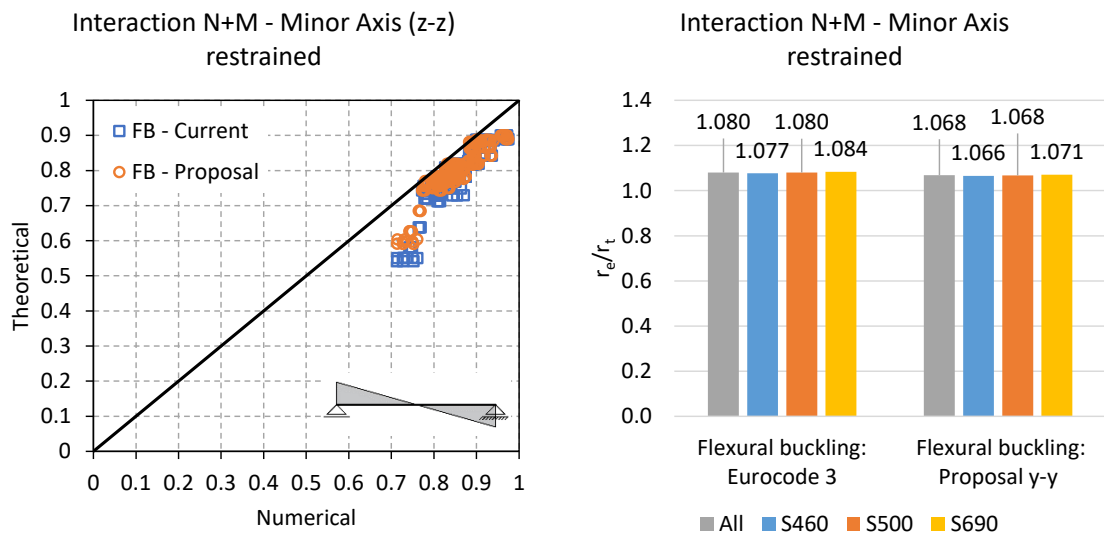


Figure C.9 – Scatter plots and mean values: linear bending moment – $\psi = -1$

C.4 Uniform distributed load

- No restraints:

Table C.7 – Statistical parameters – beam-columns: uniform distributed load – no restraints

| Design rule | Steel grade | n | mean | cov | min | max | >1.1 | <0.97 |
|-------------|-------------|-----|-------|-------|-------|-------|------|-------|
| FB and LTB | All | 914 | 1.320 | 11.3% | 1.061 | 1.656 | 867 | 0 |
| - General | S460 | 311 | 1.301 | 10.5% | 1.063 | 1.599 | 296 | 0 |
| case: | S500 | 307 | 1.315 | 11.1% | 1.061 | 1.624 | 289 | 0 |
| Current | S690 | 296 | 1.346 | 11.9% | 1.068 | 1.656 | 282 | 0 |
| FB and LTB | All | 914 | 1.201 | 8.8% | 1.031 | 1.454 | 681 | 0 |
| - General | S460 | 311 | 1.186 | 8.0% | 1.031 | 1.408 | 225 | 0 |
| case: | S500 | 307 | 1.197 | 8.6% | 1.034 | 1.429 | 228 | 0 |
| Proposals | S690 | 296 | 1.222 | 9.5% | 1.033 | 1.454 | 228 | 0 |
| FB and LTB | All | 914 | 1.258 | 10.6% | 1.024 | 1.558 | 785 | 0 |
| - New EC3 | S460 | 311 | 1.240 | 9.8% | 1.041 | 1.490 | 265 | 0 |
| case: | S500 | 307 | 1.253 | 10.4% | 1.024 | 1.514 | 261 | 0 |
| Current | S690 | 296 | 1.284 | 11.2% | 1.032 | 1.558 | 259 | 0 |
| FB and LTB | All | 914 | 1.164 | 8.5% | 1.002 | 1.398 | 613 | 0 |
| - New EC3 | S460 | 311 | 1.148 | 7.6% | 1.017 | 1.350 | 202 | 0 |
| case: | S500 | 307 | 1.159 | 8.3% | 1.002 | 1.367 | 203 | 0 |
| Proposals | S690 | 296 | 1.186 | 9.3% | 1.003 | 1.398 | 208 | 0 |

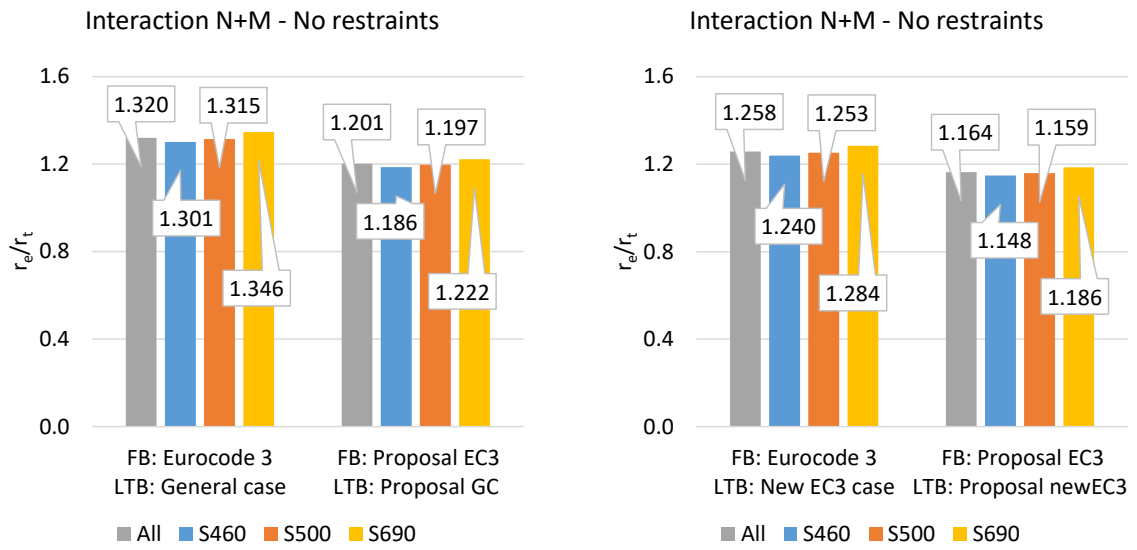
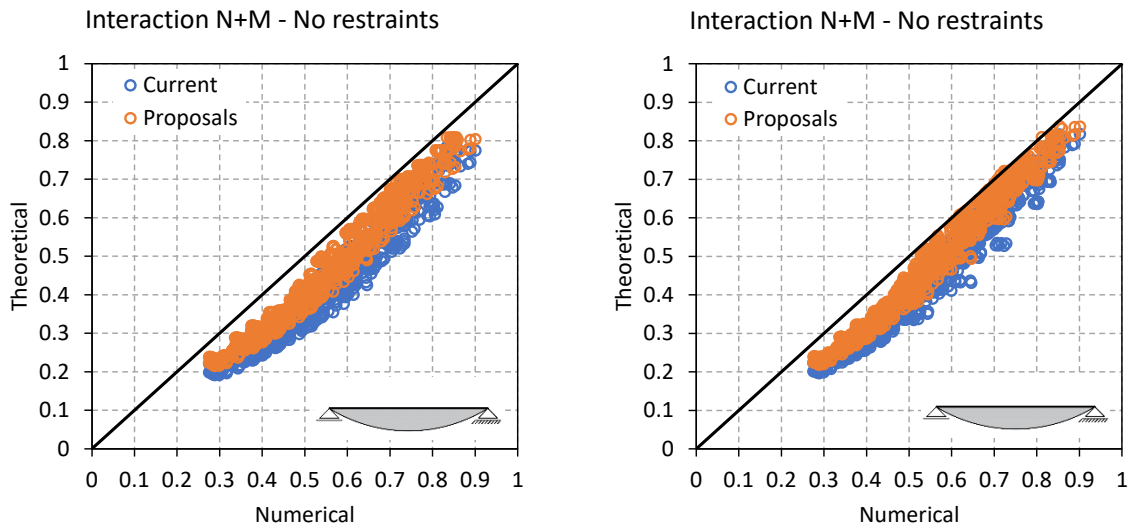


Figure C.10 – Mean values for ratio r_e/r_t for uniform distributed load



a) FB: χ_y and χ_z – Eurocode 3

b) FB: χ_y and χ_z – Eurocode 3

LTB: χ_{LT} – General case

LTB: χ_{LT} – New EC3 case

Figure C.11 - Scatter plots – beam-columns: uniform distributed load

Annex D – New Residual stress models

This annex presents the results obtained for the parametric study for beams with new residual stresses models (ECCS, thermal cut, and non-thermal cut), for the different bending moment distributions considered separately. The results are presented in terms of the numerical result (r_e) over the theoretical (r_t) design resistance according to the Eurocode 3 methods (general case, special case, and new EC3 case) and the statistical parameters for the ratio (r_e/r_t).

D.1 Constant bending moment – $\psi = 1$

Table D.1 – Statistical parameters: constant bending moment $\psi = 1$ – Class 1, 2 and 3

| Design rule | Subset - Residual stresses model | n | mean | cov | min | max | >1.1 | <0.97 |
|---------------------------|----------------------------------|------|-------|-------|-------|-------|------|-------|
| General case | ECCS | 1175 | 1.307 | 10.6% | 1.024 | 1.606 | 1031 | 0 |
| | Thermal cut | 970 | 1.278 | 9.2% | 1.007 | 1.526 | 863 | 0 |
| | Non-Thermal cut | 970 | 1.287 | 10.1% | 1.014 | 1.539 | 835 | 0 |
| Proposal for General case | ECCS | 1175 | 1.182 | 8.6% | 0.968 | 1.441 | 855 | 1 |
| | Thermal cut | 970 | 1.155 | 7.5% | 0.945 | 1.396 | 687 | 6 |
| | Non-Thermal cut | 970 | 1.162 | 8.2% | 0.936 | 1.396 | 704 | 15 |
| New EC3 case | ECCS | 1175 | 1.175 | 7.2% | 1.000 | 1.393 | 889 | 0 |
| | Thermal cut | 970 | 1.144 | 6.4% | 0.931 | 1.332 | 685 | 4 |
| | Non-Thermal cut | 970 | 1.151 | 6.9% | 0.955 | 1.348 | 701 | 3 |
| Proposal for New EC3 case | ECCS | 1175 | 1.123 | 6.8% | 0.967 | 1.320 | 735 | 5 |
| | Thermal cut | 970 | 1.093 | 6.2% | 0.899 | 1.265 | 476 | 29 |
| | Non-Thermal cut | 970 | 1.100 | 6.6% | 0.923 | 1.278 | 540 | 44 |
| Special case | ECCS | 1175 | 1.089 | 8.6% | 0.914 | 1.327 | 545 | 156 |
| | Thermal cut | 970 | 1.061 | 7.2% | 0.893 | 1.242 | 347 | 159 |
| | Non-Thermal cut | 970 | 1.068 | 8.2% | 0.888 | 1.272 | 387 | 164 |

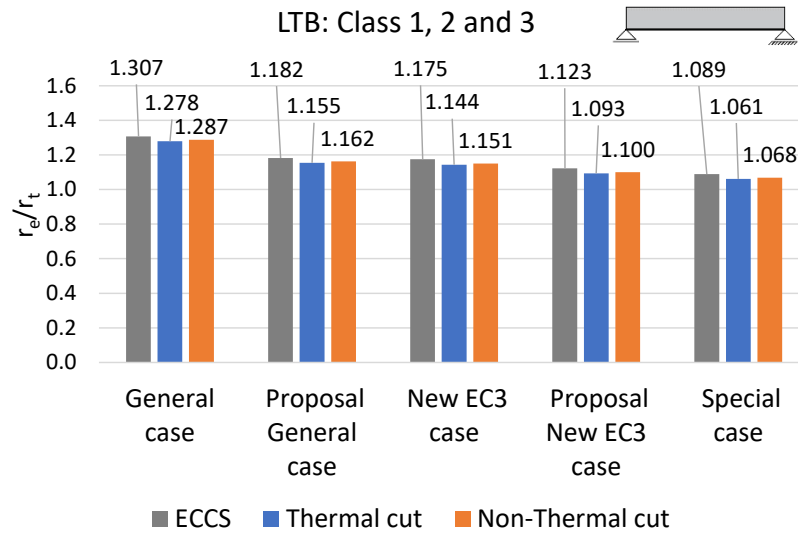


Figure D.1 – Mean values for ratio r_e/r_t for constant bending moment $\psi = 1$

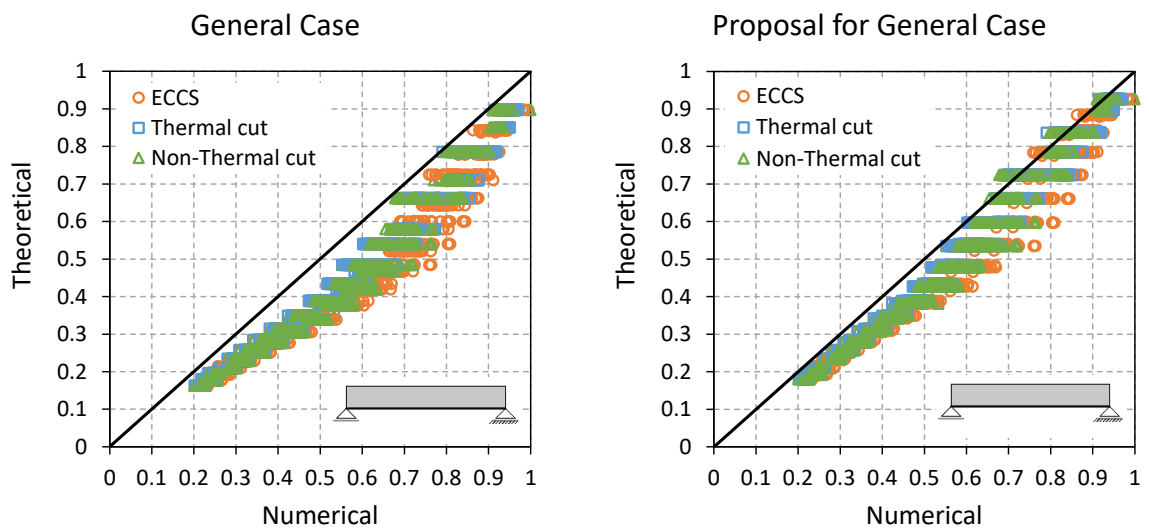
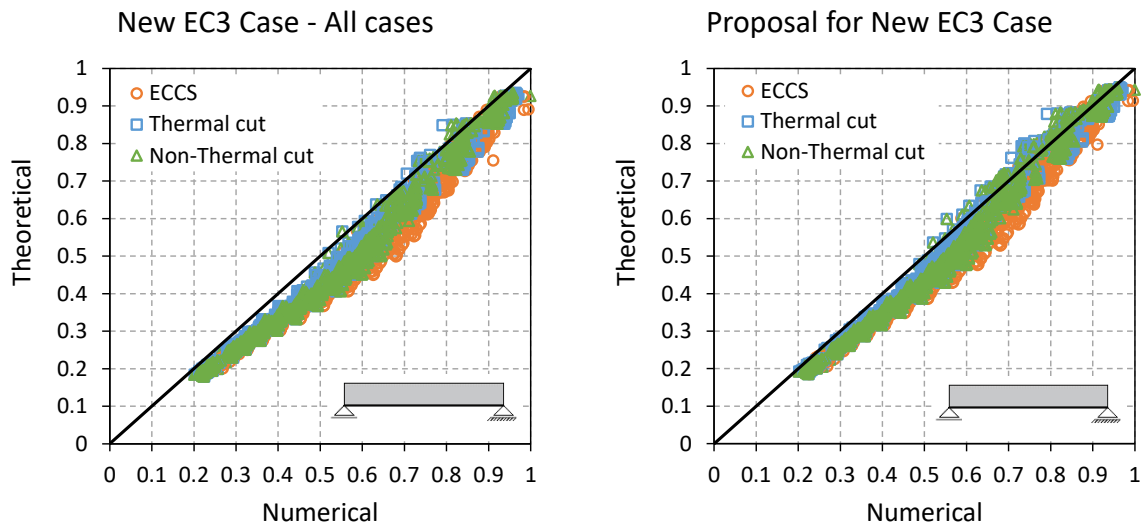


Figure D.2 – Scatter plots for LTB with constant bending moment $\psi = 1$ – General case

Figure D.3 – Scatter plots for LTB with constant bending moment $\psi = 1$ – New EC3 case

D.2 Linear bending moment – $\psi = 0$

Table D.2 – Statistical parameters: linear bending moment $\psi = 0$ – Class 1, 2 and 3

| Design rule | Subset - Residual stresses model | n | mean | cov | min | max | >1.1 | <0.97 |
|---------------------------|----------------------------------|-----|-------|-------|-------|-------|------|-------|
| General case | ECCS | 769 | 1.450 | 10.0% | 1.088 | 1.773 | 768 | 0 |
| | Thermal cut | 769 | 1.423 | 9.0% | 1.068 | 1.687 | 767 | 0 |
| | Non-Thermal cut | 769 | 1.425 | 9.4% | 1.079 | 1.709 | 767 | 0 |
| Proposal for General case | ECCS | 769 | 1.306 | 7.2% | 1.055 | 1.591 | 757 | 0 |
| | Thermal cut | 769 | 1.282 | 6.1% | 1.035 | 1.459 | 757 | 0 |
| | Non-Thermal cut | 769 | 1.284 | 6.6% | 1.045 | 1.479 | 757 | 0 |
| New EC3 case | ECCS | 769 | 1.152 | 7.4% | 0.950 | 1.433 | 566 | 6 |
| | Thermal cut | 769 | 1.131 | 6.5% | 0.926 | 1.295 | 530 | 11 |
| | Non-Thermal cut | 769 | 1.132 | 6.8% | 0.935 | 1.317 | 522 | 13 |
| Proposal for New EC3 case | ECCS | 769 | 1.113 | 6.5% | 0.911 | 1.392 | 463 | 17 |
| | Thermal cut | 769 | 1.092 | 5.8% | 0.884 | 1.264 | 362 | 23 |
| | Non-Thermal cut | 769 | 1.094 | 6.2% | 0.901 | 1.285 | 393 | 27 |
| Special case | ECCS | 769 | 1.139 | 7.5% | 0.950 | 1.386 | 477 | 5 |
| | Thermal cut | 769 | 1.118 | 6.7% | 0.930 | 1.269 | 416 | 11 |
| | Non-Thermal cut | 769 | 1.120 | 7.2% | 0.935 | 1.281 | 419 | 12 |

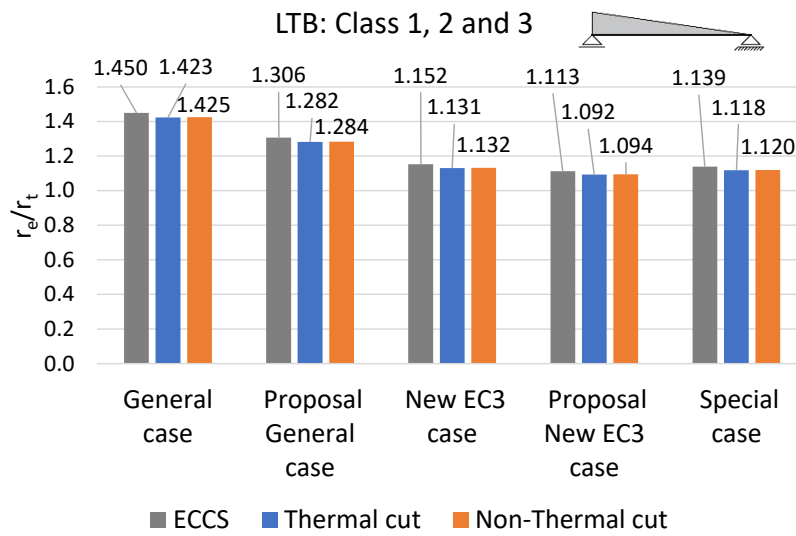


Figure D.4 – Mean values for ratio r_e/r_t for linear bending moment $\psi = 0$

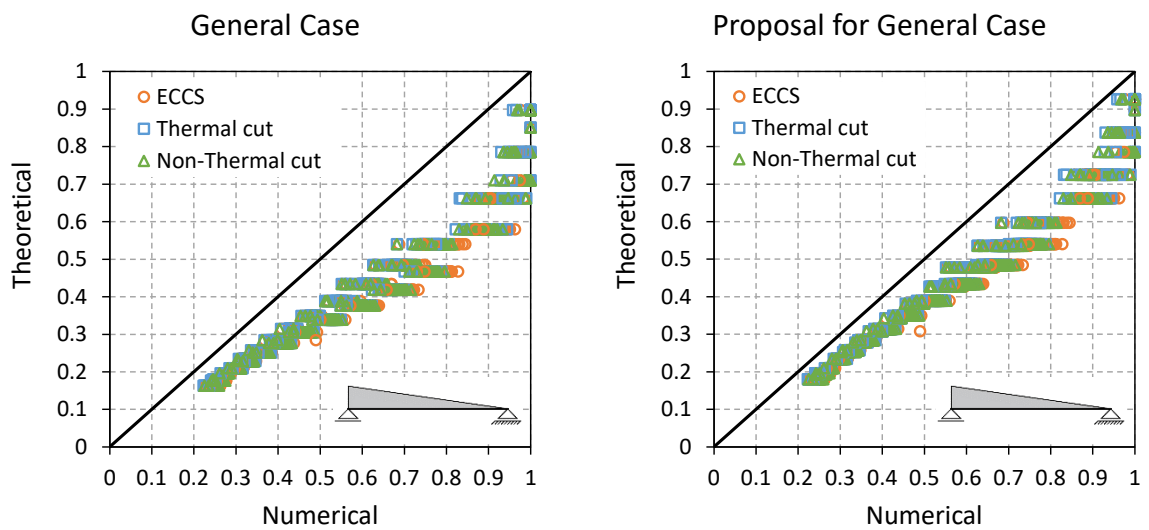
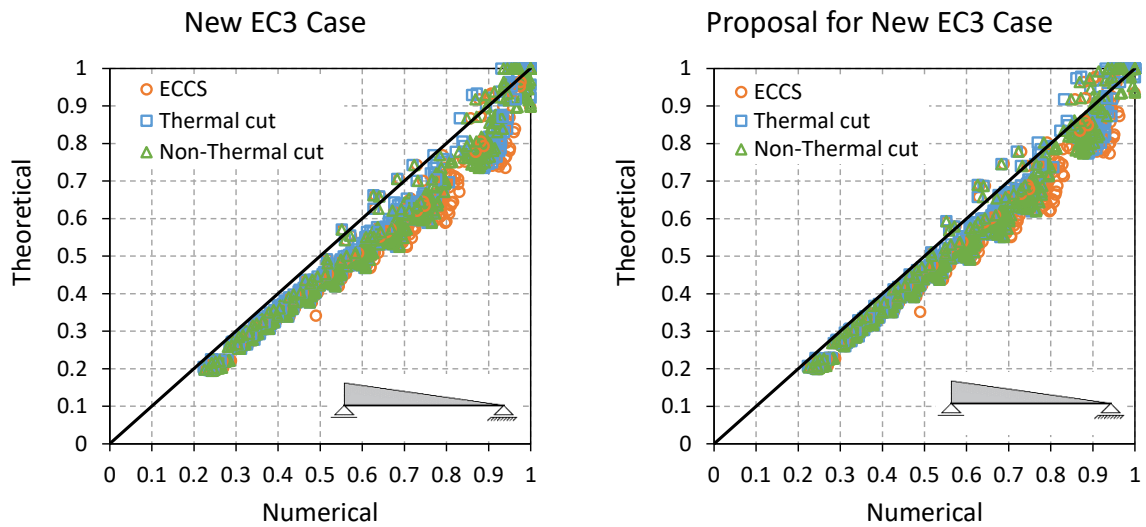


Figure D.5 – Scatter plots for LTB with linear bending moment $\psi = 0$ – General case

Figure D.6 – Scatter plots for LTB with linear bending moment $\psi = 0$ – New EC3 case

D.3 Linear bending moment – $\psi = -1$

Table D.3 – Statistical parameters: linear bending moment $\psi = -1$ – Class 1, 2 and 3

| Design rule | Subset - Residual stresses model | n | mean | cov | min | max | >1.1 | <0.97 |
|---------------------------|----------------------------------|-----|-------|-------|-------|-------|------|-------|
| General case | ECCS | 634 | 1.463 | 10.4% | 1.114 | 1.719 | 634 | 0 |
| | Thermal cut | 634 | 1.436 | 9.6% | 1.114 | 1.655 | 634 | 0 |
| | Non-Thermal cut | 634 | 1.435 | 9.7% | 1.114 | 1.693 | 634 | 0 |
| Proposal for General case | ECCS | 634 | 1.316 | 7.6% | 1.079 | 1.553 | 615 | 0 |
| | Thermal cut | 634 | 1.293 | 6.8% | 1.079 | 1.492 | 615 | 0 |
| | Non-Thermal cut | 634 | 1.292 | 6.9% | 1.078 | 1.531 | 615 | 0 |
| New EC3 case | ECCS | 634 | 1.124 | 6.9% | 0.968 | 1.370 | 379 | 2 |
| | Thermal cut | 634 | 1.104 | 6.2% | 0.939 | 1.336 | 330 | 3 |
| | Non-Thermal cut | 634 | 1.104 | 6.5% | 0.954 | 1.351 | 316 | 3 |
| Proposal for New EC3 case | ECCS | 634 | 1.090 | 6.2% | 0.942 | 1.338 | 253 | 6 |
| | Thermal cut | 634 | 1.071 | 5.7% | 0.902 | 1.302 | 179 | 13 |
| | Non-Thermal cut | 634 | 1.070 | 6.0% | 0.915 | 1.319 | 167 | 13 |
| Special case | ECCS | 634 | 1.107 | 8.6% | 0.955 | 1.380 | 291 | 5 |
| | Thermal cut | 634 | 1.087 | 8.1% | 0.925 | 1.326 | 243 | 18 |
| | Non-Thermal cut | 634 | 1.087 | 8.5% | 0.934 | 1.360 | 240 | 25 |

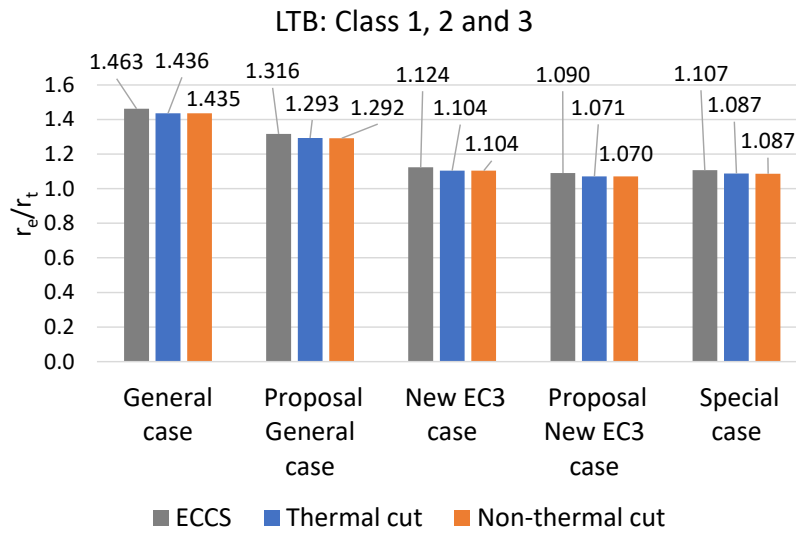


Figure D.7 – Mean values for ratio r_e/r_t for linear bending moment $\psi = -1$

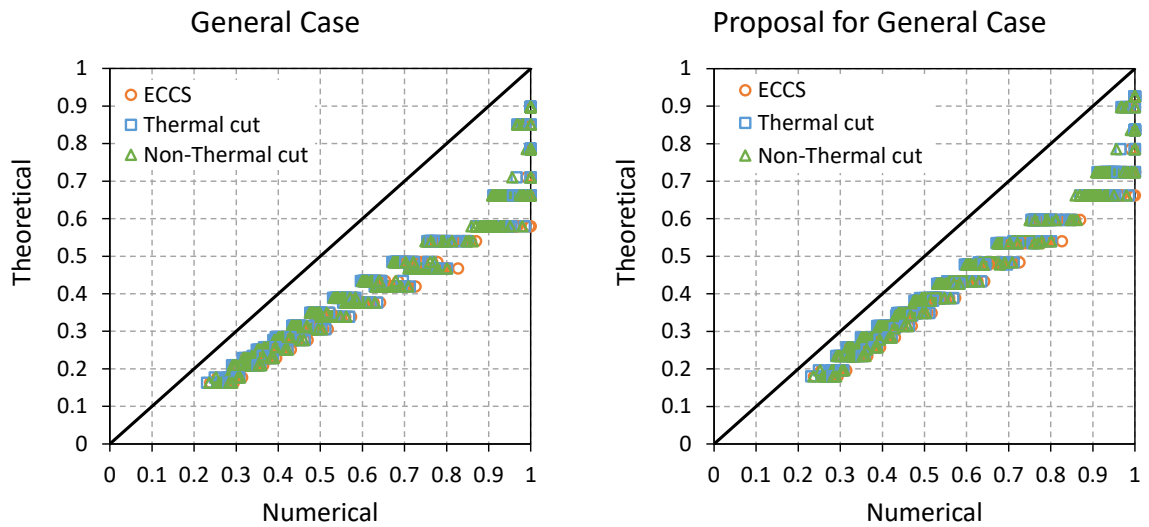


Figure D.8 – Scatter plots for LTB with linear bending moment $\psi = -1$ – General case

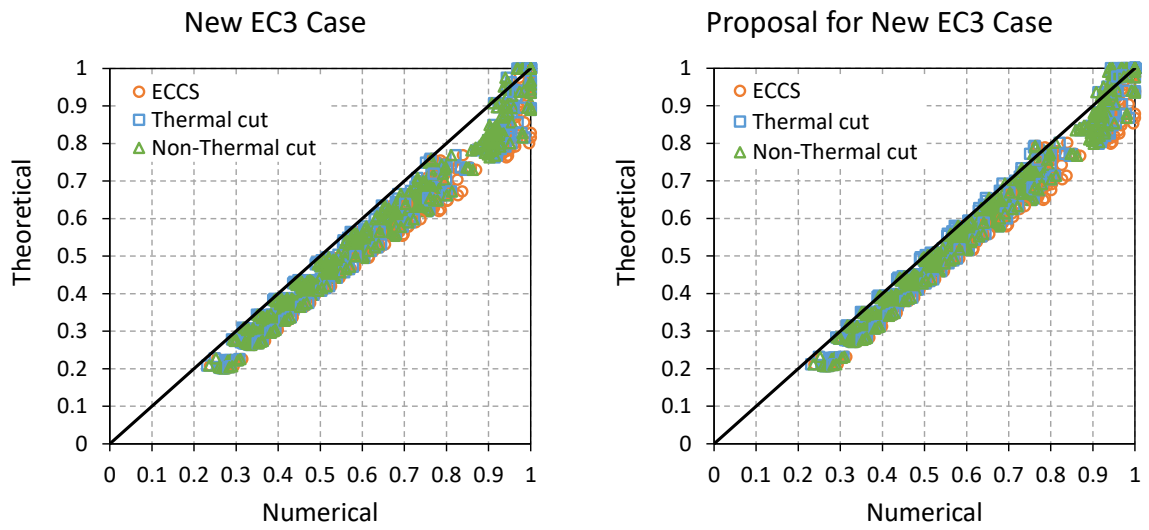


Figure D.9 – Scatter plots for LTB with linear bending moment $\psi = -1$ – New EC3 case